

STUDIES OF CONJUGATED SMALL MOLECULES, POLYMERS AND ORGANIC-  
INORGANIC HYBRID MATERIALS FOR PHOTOVOLTAIC APPLICATIONS

A DISSERTATION IN  
Chemistry  
and  
Pharmaceutical Sciences

Presented to the Faculty of the University  
of Missouri-Kansas City in partial fulfillment of  
the requirements for the degree

DOCTOR OF PHILOSOPHY

by  
LU JIN  
M.S. University of Missouri-Kansas City, 2015  
B. Med. Anhui Medical University, 2010

Kansas City, Missouri  
2015

© 2015

LU JIN

ALL RIGHTS RESERVED

STUDIES OF CONJUGATED SMALL MOLECULES, POLYMERS AND ORGANIC-  
INORGANIC HYBRID MATERIALS FOR PHOTOVOLTAIC APPLICATIONS

Lu Jin, Candidate for the Doctor of Philosophy Degree

University of Missouri-Kansas City, 2015

ABSTRACT

This dissertation focuses on the photophysical properties and device studies of three different types of materials, namely polyoxometalate (POM)-containing organic-inorganic hybrids, near-IR absorbing conjugated polymers and discotic polycyclic aromatic hydrocarbons. POM-containing organic-inorganic hybrids are interesting because of the potential roles, such as electron acceptors and electron transporters, that POM clusters may be able to play. A molecular hybrid (**Mo6-Fe**) containing a hexamolybdate cluster on one end, a ferrocenyl unit on the other and a conjugated bridge has been explored for photovoltaic applications. This hybrid shows direct charge transfer absorption in its UV-vis absorption spectrum. While the hybrid itself show very poor photovoltaic properties, solar cells fabricated from its PCBM blends show attractive device performance with power conversion efficiencies up to 1.8%. To develop a POM-containing hybrid system that exhibits the desired morphologies for solar cells, three POM-containing rod-coil hybrid diblock copolymers (**PS-Mo6-PT1-3**) with different rod block lengths have been carefully studies on their optical, electrochemical, morphological and photovoltaic properties. Solar cells fabricated from these hybrid diblock copolymers (without added PCBM) did show photovoltaic effects with around 0.01% power conversion efficiency. While good open circuit voltage (1.25 V) is observed for the pristine film, the short circuit

photocurrent is dismally low. Annealing improves the photocurrent by one order of magnitude and also the fill factor, presumably due to the formation of desired phase-separated domains. The overall photocurrent is still very low, likely due to the poor photoinduced charge transfer from the PT backbone to the POM cluster, which is corroborated by femtosecond time-resolved fluorescence studies. Two new POM-containing main-chain conjugated polymers (**P10** and **P11**) have been synthesized and characterized in detail. Simple single layer solar cells based on **P10** show respectable power conversion efficiencies up to 0.31%. Incident photo-to-current conversion efficiency measurements have confirmed the photocurrent contribution of both the organic  $\pi$ -segments and the POM clusters.

Near infrared (NIR) absorbing conjugated polymers combining alkoxy-substituted bithiophene units with different comonomers have been synthesized. Due to the electron-donating properties of the alkoxy substituents and the near planar structure of the bithiophene unit, conjugated polymers containing 3,3'-dialkoxy bithiophene units show strong propensity towards electrophiles such as  $H^+$ . The protonated polymers show strong NIR absorptions due to intra-chain charge transfer. The strength and the wavelengths of the NIR absorption depend on the comonomers as well. Comonomers with stronger electron donating properties (such as NDT over INDT) lead to more intense NIR absorptions and longer NIR absorption wavelengths. The protonation process is found to follow the first order reaction kinetics. While the NIR-absorbing polymers, when blended with PC<sub>71</sub>BM, show photovoltaic properties, only the absorptions in the UV-visible range are able to produce photocurrent.

Three PAH molecules, all based on the TBP core but with different peripheral substituents, have been studied as hole transporting materials. The SCLC hole mobility of compounds **1a-1c** pristine films deposited by spin-coating were measured to be  $8.58 \times 10^{-4} \text{ cm}^2 \text{ V}^{-1} \text{ s}^{-1}$ ,  $5.42 \times 10^{-3} \text{ cm}^2 \text{ V}^{-1} \text{ s}^{-1}$ , and  $2.30 \times 10^{-4} \text{ cm}^2 \text{ V}^{-1} \text{ s}^{-1}$ , respectively, which are typical for solution-processed organic thin films. Thermal annealing improved the mobility of all three compounds with compound **1b** showing the largest increase and an appealing SCLC hole mobility of  $3.63 \times 10^{-2} \text{ cm}^2 \text{ V}^{-1} \text{ s}^{-1}$  was obtained. The XRD studies of thin films before and after annealing suggest better molecule orders for both **1a** and **1b** after thermal annealing, which is likely responsible for their improved hole mobility.

The abstract of 556 words is approved as to form and content.

## APPROVAL PAGE

The faculty listed below, appointed by the Dean of the School of Graduate Studies have examined a dissertation titled “Studies of Conjugated Small Molecules, Polymers and Organic-Inorganic Hybrid Materials for Photovoltaic Applications”, presented by Lu Jin, candidate for the Doctor of Philosophy degree, and certify that in their opinion it is worthy of acceptance.

### Supervisory Committee

Zhonghua Peng, Ph.D., Committee Chair  
Department of Chemistry

James R. Durig, Ph.D.  
Department of Chemistry

Nathan A. Oyler, Ph.D.  
Department of Chemistry

Da-Ming Zhu, Ph.D.  
Department of Physics

Kun Cheng, Ph.D.  
Department of Pharmaceutical Sciences

## CONTENTS

ABSTRACT .....	iii
ILLUSTRATIONS .....	x
TABLES .....	xvii
ABBREVIATIONS .....	xviii
ACKNOWLEDGEMENTS .....	xx
1 INTRODUCTION OF ORGANIC PHOTOVOLTAIC DEVICES .....	1
1.1. Development of organic photovoltaic devices .....	1
1.2. Theory .....	4
1.2.1. Device operating principle .....	4
1.2.2. Characteristics of organic PV devices .....	12
1.3. Objective .....	22
2 POLYOXOMETALATE CONTAINING ORGANIC-INORGANIC HYBRID MATERIALS FOR PHOTOVOLTAIC APPLICATIONS.....	24
2.1 Introduction .....	24
2.2 Objective .....	27
2.3 Small molecular POM-containing hybrid .....	29
2.4 Dendrimer-PDI charge transfer molecule .....	34
2.5 POM-containing rod-coil diblock copolymers.....	41
2.5.1 Electrochemistry study.....	44

2.5.2	Photovoltaic devices .....	47
2.5.3	Steady fluorescence .....	53
2.5.4	Dynamic fluorescence study .....	55
2.6	Main chain POM containing donor-acceptor hybrid conjugated polymers .....	64
2.6.1	Structure characteristics .....	66
2.6.2	Optical properties .....	70
2.6.3	Electrochemical properties .....	74
2.6.4	Photovoltaic properties .....	76
2.7	Conclusions .....	82
2.8	Methods .....	85
3	NEAR INFRARED ABSORPTION POLYMERS WITH 3, 3'-DIALKOXY SUBSTITUTED BITHIOPHENE UNITS .....	90
3.1.	Introduction .....	90
3.2.	Objective .....	91
3.3.	Results .....	93
3.3.1.	Synthesis .....	93
3.3.2.	Theoretical calculation .....	98
3.3.3.	Electrochemical Properties .....	102
3.3.4.	Optical properties .....	103
3.3.5.	Photostability .....	122

3.3.6.	Photovoltaic properties .....	124
3.3.7.	Mobility.....	129
3.4.	Conclusions .....	131
3.5.	Methods .....	132
4	HOLE MOBILITY STUDIES OF SELECTED POLYCYCLIC AROMATIC HYDROCARBONS .....	136
4.1.	Introduction .....	136
4.2.	Methods in organic semiconductor mobility measurement .....	138
4.3.	Device design for SCLC measurements.....	143
4.4.	Objective .....	146
4.5.	Materials.....	147
4.6.	Result and discuss .....	148
4.6.1	Theoretical calculation.....	148
4.6.2	Electrochemical properties.....	152
4.6.3	Mobility.....	155
4.6.4	X-ray diffraction pattern .....	158
4.7.	Conclusions .....	160
4.8	Methods.....	160
	REFERENCES .....	163
	VITA.....	177

## ILLUSTRATIONS

Figure	Page
1-1. Device configurations of Schottky-barrier organic solar cell (a), bi-layer donor/acceptor solar cell (b), bulk heterojunction donor/acceptor solar cell (c), tri-layer p-i-n heterojunction solar cell (d), multilayer heterojunction solar cell (e) and tandem solar cell(f).....	6
1-2. Energy level diagram of a single layer organic solar cell.....	7
1-3. Photon-electron conversion process in a bilayer organic solar cell structure.....	10
1-4. Typical current density-voltage (J-V) curve.....	13
1-5. <i>J-V</i> curve obtained in space charge limited current mobility measurement. S-shape curve appeared when charge accumulated.....	15
1-6. Energy diagram of open circuit voltage.....	16
1-7. Energy diagram of charge separation and transportation.....	20
1-8. Architecture of ideal donor-acceptor organic solar cell.....	21
2-1. SEM of ZnO nanorods cross-section (left) and top view (right).....	25
2-2. Molecule structures of PC <sub>61</sub> BM (top left), hexamolybdate cluster (top right), monofunctionalized (bottom left) and bifunctionalized (bottom right) clusters....	26
2-3. Models of the three hybrid POM systems .....	28
2-4. Molecule structure of <b>Mo6-Fe</b> .....	29
2-5. UV-vis absorption spectra of <b>Mo6-Fe</b> in <i>o</i> -dichlorobenzene solution.....	30
2-6. Cyclic voltammograms of <b>Mo6-Fe</b> in acetonitrile solution.....	31
2-7. UV-vis absorption spectra of <b>Mo6-Fe</b> (right) and <b>Mo6-Fe/PC61BM</b> (1:1 wt ratio, left) in <i>o</i> -dichlorobenzene solutions (black) and films before (blue) and after (red) thermal annealing.....	33

2-8.	Device architecture (left) and $J-V$ curve (right, blue triangle line: dark; red ball lines: illuminated) of the photovoltaic devices of ITO/PEDOT:PSS/ <b>MoO6-Fe:PCBM</b> /Ca/Al with the thermal annealing treatment under 1-sun air mass 1.5 global illumination.....	33
2-9.	Hypothetic module of molecule stacking in <b>G0-PDI</b> , <b>G1-PDI</b> and <b>G1-O-PDI</b> ...35	
2-10.	Molecule structures of <b>G0-PDI</b> , <b>G1-PDI</b> and <b>G1-O-PDI</b> .....	36
2-11.	Cyclic voltammograms of <b>G0-PDI</b> , <b>G1-PDI</b> and <b>G1-O-PDI</b> thin films.....	37
2-12.	(a-c) UV-vis absorption spectra and (d-f) $J-V$ curve of the devices based on <b>G0-PDI</b> , <b>G1-PDI</b> and <b>G1-O-PDI</b> before (black) and after thermal annealing (red).....	39
2-13.	Molecule structures of <b>PS-Mo6-PT1-3</b> .....	42
2-14.	Hypothetic module of polymer stacking and charge transfer process in <b>PS-Mo6-PT1-3</b> .....	43
2-15.	Cyclic voltammograms of <b>PS-PT1-3</b> and <b>PS-Mo6-PT1-3</b> in films.....	46
2-16.	UV-vis absorption spectra of pristine (a, c) and blend film (b, d) of <b>PS-PT2</b> and <b>PS-Mo6-PT2</b> in solutions (black) and as films (blue: unannealed films; red: annealed films).....	48
2-17.	$J-V$ curve of device fabricated from <b>PT1/PC<sub>61</sub>BM</b> solution after thermally annealed, under 1-sun air mass 1.5 global illumination and in dark.....	49
2-18.	$J-V$ curve of the device based on <b>PS-PT2</b> (left) and <b>PS-PT2/PCBM</b> (right) before (black) or after (red) thermal annealed at 120 °C for 10 min, under 1-sun air mass 1.5 global illumination (solid line) and in dark (dash line).....	51

2-19.	<i>J-V</i> curve of the device based on <b>PS-Mo6-PT2</b> (left) and <b>PS-Mo6-PT2/PCBM</b> (right) before (black) or after (red) thermal annealed at 120 °C for 10 min, under 1-sun air mass 1.5 global illumination (solid line) and in dark (dash line).....	51
2-20.	Absorption (olive lines) and emission spectra (red lines) with excitation wavelength at 400 nm and excitation spectra with emission wavelengths at 580 nm (black lines) and 620 nm (blue lines) of <b>PS-Mo6-PT1-3</b> solutions (0.5 mg mL <sup>-1</sup> concentration) in CHCl <sub>3</sub> . The vertical black dashed line serves as an eye-guiding line through the data points at 620 nm.....	54
2-21.	Fluorescence dynamics of the <b>PS-Mo6-PT1-3</b> solutions (~0.5 mg mL <sup>-1</sup> ) in CHCl <sub>3</sub> with excitation at 400 nm and emission at (a-c) 580 nm and (d-f) 620 nm, respectively. The red lines are the plotted instrument response function, and the blue ones are the fitted curves.....	57
2-22.	Schematic illustration of the association mechanisms of <b>PS-Mo6-PT1-3</b> molecules in solution.....	60
2-23.	Anisotropy decay profiles of the <b>PS-Mo6-PT1-3</b> solutions (~0.5 mg mL <sup>-1</sup> ) in CHCl <sub>3</sub> for the emission at 580 nm (a-c) and 620 nm (d-f), respectively, under the excitation of 400 nm. ....	63
2-24.	Synthesis of main chain POM-containing hybrid conjugated copolymer <b>P10</b> and <b>P11</b> .....	65
2-25.	<sup>1</sup> H NMR spectrum of <b>P10</b> in CDCl <sub>3</sub> . The insert in rectangle displays the region of interest of the <sup>1</sup> H NMR of <b>P11</b> in CDCl <sub>3</sub> .....	67
2-26.	FT-IR spectra of <b>PBOR, 3, P10</b> and <b>P11</b> .....	70

2-27.	Normalized UV-vis-NIR absorption (a, b) and fluorescence emission spectra (c and d, excited at the wavelength of maximum absorption) and excitation spectra (e and f, monitored at the wavelength of maximum emission) of dilute solutions of <b>PBOR</b> , <b>P10</b> and <b>P11</b> in THF (a- c) and CHCl <sub>3</sub> (d-f).....	73
2-28.	Cyclic voltammograms of <b>PBOR</b> , <b>P10</b> , <b>P11</b> and <b>3</b> thin films prepared from CHCl <sub>3</sub> solutions.....	75
2-29.	(a) Normalized absorption spectra of <b>PBOR</b> , <b>P10</b> and <b>P11</b> thin films before (solid line) and after (dot line) thermal annealing at 120 °C for 10 min under nitrogen atmosphere; (b-d) Typical <i>J-V</i> curve (empty circle: in dark; sphere: under 1-sun air mass 1.5 global illumination) of the single –component photovoltaic cells of (b) <b>PBOR</b> , (c) <b>P10</b> and (d) <b>P11</b> with structure of ITO/PEDOT:PSS/polymer/Ca/Al (100nm).....	77
2-30.	<i>J-V</i> curves (empty circles: in dark; spheres: under illumination) of the highest-performing cells of ITO/PEDOT:PSS/ <b>P10</b> /Ca (50 nm)/Al (100 nm).....	79
2-31.	IPCE spectra of the devices of <b>P10</b> and <b>P11</b> with structure of ITO/PEDOT:PSS/polymer/Ca (50 nm)/Al (100 nm) before (sphere) and after (empty circle) thermally annealed at 120 °C for 15 min.....	81
2-32.	Schematic representation of a new hybrid diblock copolymer containing a bridging POM cluster to facilitate initial charge transfer and the scheme of hypothetical polymer stacking.....	84
3-1.	Structures of conjugated copolymer <b>PTR</b> , <b>PTOR</b> , <b>PTD</b> , <b>PDR</b> and <b>PBOR</b> .....	92
3-2.	Synthetic route of polymers <b>PTR</b> , <b>PTOR</b> and <b>PTD</b> .....	94
3-3.	<sup>1</sup> H NMR spectra of <b>PTR</b> .....	95

3-4.	<sup>1</sup> H NMR spectra of <b>PTOR</b> .....	96
3-5.	<sup>1</sup> H NMR spectra of <b>PTD</b> .....	97
3-6.	Energy minimized structures of <b>PTR</b> , <b>PTOR</b> and <b>PTD</b> from different views obtained from DFT calculations at the B3LYP/6-31G(d) level.....	99
3-7.	Schemes of dihedral angles of trimers.....	100
3-8.	Simulation HOM/LUMO energy levels of <b>PTR</b> , <b>PTOR</b> and <b>PTD</b> from different views obtained from DFT calculations at the B3LYP/6-31G(d) level.....	101
3-9.	Cyclic voltammograms of polymer thin films, scale corrected based on Fc/Fc <sup>+</sup> .....	102
3-10.	Normalized UV-vis absorption spectra in chloroform solutions (solid lines) and as thin films (short dots).....	105
3-11.	Emission spectra of <b>PTR</b> , <b>PTOR</b> and <b>PTD</b> (excited at 544/594, 386/390, and 480/494nm for <b>PTD</b> , <b>PTR</b> and <b>PTOR</b> solution/film, respectively) in solutions (solid lines) and as films (dash lines).....	108
3-12.	UV- vis- NIR absorption spectra of <b>PTOR</b> (up) and <b>PTD</b> (down) in different solvents.....	109
3-13.	Emission and excitation spectra of <b>PTOR</b> in CHCl <sub>3</sub> (a-c) and THF (d-f).....	110
3-14.	Emission (black) and excitation (red or green) spectra of <b>PTD</b> (left) and <b>PTR</b> (right) in THF or chloroform solutions .....	111
3-15.	UV-vis-NIR absorption spectra of <b>PTOR</b> (black), <b>PTOR</b> with addition of TSOH (blue) and then neutralized with base (red).....	113
3-16.	UV-vis-NIR absorption spectra of <b>PTD</b> before (red) and after addition of TSOH (black).....	113

3-17.	UV-vis-NIR absorption spectra of <b>PTOR</b> , <b>PBOR</b> , <b>PTD</b> , <b>PTR</b> and <b>PDR</b> with different polymer: TSOH ratio.....	115
3-18.	Color change in <b>PTOR</b> dilute THF solution before (left) and after (right) addition of TSOH.....	116
3-19.	Color change in <b>PTD</b> dilute THF solution before (left) and after (right) addition of TSOH.....	116
3-20.	Scheme of protonation in <b>PTOR</b> .....	118
3-21.	UV-vis-NIR absorbance ratio as a function of the reaction time at selected wavelengths in protonation process of <b>PTOR</b> and <b>PTD</b> at different polymer: acid ratio. ....	119
3-22.	Fluorescence intensity vs. time of <b>PTOR</b> (top) and <b>PTD</b> (bottom) at certain acid concentrations.....	120
3-23.	UV-vis-NIR absorption spectra of <b>PTOR</b> in chloroform (A) and THF (B) solution illuminated by a solar simulator.....	123
3-24.	Energy level diagram (a) and device structure (b) of blend films of <b>PTOR</b> :PC <sub>71</sub> BM (1:1 wt. ratio).....	125
3-25.	UV-vis-NIR absorption spectra of blend films of <b>PTOR</b> :PC <sub>71</sub> BM (1:1 wt. ratio) fabricated from CHCl <sub>3</sub> and ODCB with or without acid.....	126
3-26.	<i>J-V</i> curve of device fabricated from <b>PTOR</b> :PC <sub>71</sub> BM (1:1 wt. ratio) CHCl <sub>3</sub> and ODCB solution in dark (empty circle) and under illumination (sphere).....	126
3-27.	External quantum efficiency of <b>PTOR</b> :PC <sub>71</sub> BM blends in ODCB (black, thermal annealed film), in chloroform before (red) or after (blue) thermal annealing at 120 °C for 10 min, and in chloroform with acid addition (green).....	128

3-28.	(a) Experimental (blue circle) and fitted (red line) current density –voltage curve of ITO/PEDOT:PSS/ <b>PTOR</b> :PC <sub>71</sub> BM/MoO <sub>3</sub> /Au, (b) device architecture for mobility test.....	130
4-1.	Structures of rubrene, <b>C6STP</b> , hexabenzocoronene, and <b>DAT</b> .....	137
4-2.	Setup of time of flight charge carrier mobility measurements.....	139
4-3.	Device structures of metal-insulator-semiconductor field-effect transistor (a) and Organic field effect transistors with bottom contact (b) or top contact (c).....	140
4-4.	Typical current density-voltage curve in Ohmic and SCLC regions.....	141
4-5.	Device structures of hole-only device and electron-only device in SCLC measurements.....	144
4-6.	Structures of compounds <b>1a-c</b> .....	147
4-7.	Model structure used for describing molecular twist.....	148
4-8.	The energy minimized structures of <b>1a-1c</b> from different views obtained from Gaussian 03w at B3LYP 631G(d) level.....	150
4-9.	Visualized HOMO/LUMO orbitals of <b>1a-1c</b> obtained from Gaussian 03 at B3LYP 631G(d) level.....	151
4-10.	Cyclic voltammograms of <b>1a-1c</b> thin films drop casted on Pt plate.....	153
4-11.	Current density –voltage curve of hole only devices for <b>1a-1c</b> before (blue) or after (red) thermal annealing process (experimental data: empty circles; fitting curve: black line.).....	157
4-12.	XRD patterns of <b>1a-1c</b> thin films spin-coated on Si zero-diffraction plates.....	159

## TABLES

Table	Page
2-1 Parameters of the photovoltaic cells under 1-sun air mass 1.5 global illumination....	40
2-2 Parameters of the photovoltaic cells under 1-sun air mass 1.5 global illumination.....	52
2-3 Biexponential fitting parameters for the fluorescence dynamics of the <b>PS-Mo6-PT1-3</b> solutions (~0.5 mg mL <sup>-1</sup> ) in CHCl <sub>3</sub> with excitation of 400 nm.....	56
2-4 Optical and redox properties of the polymers.....	72
2-5 Photovoltaic Parameters of <b>PBOR</b> , <b>P10</b> and <b>P11</b> under illumination.....	80
3-1 Calculated dihedral angles and S-O short contact distances.....	100
3-2 Optoelectronic properties of <b>PTR</b> , <b>PTOR</b> and <b>PTD</b> .....	106
3-3 Photovoltaic performance under 1-sun air mass 1.5 global illumination.....	127
4-1 Optoelectronic properties of <b>1a</b> , <b>1b</b> and <b>1c</b> .....	154
4-2 SCLC hole mobility of compound <b>1a</b> , <b>1b</b> and <b>1c</b> .....	156

## ABBREVIATIONS

AFM	Atomic force microscopy
BHJ	Bulk heterojunction
Bu	Butyl group
CELIV	Charge extraction in a linearly increasing voltage
CS-AFM	Current-sensing atomic force microscopy
CV	Cyclic voltammetry
DFT	Density functional theory
DSC	Differential scanning calorimetry
EET	Excitation energy transfer
EH	2-Ethylhexyl group
EQE	External quantum efficiency
Fc	Ferrocene
FF	Fill factor
FFU	Femtosecond fluorescence up-conversion
GPC	Gel permeation chromatography
HDCP	Hybrid diblock copolymer
HOMO	Highest occupied molecule orbital
INDT	Imide-functionalized naphthodithiophene building block
IPCE	Incident photon-to-electron conversion efficiency
$I_{sc}$	Short circuit current
ITO	Indium tin oxide
$J_{sc}$	Short circuit current density
LMCT	Ligand-to-metal charge-transfer transition
LUMO	Lowest unoccupied molecule orbital
MALDI-TOF	Matrix Assisted Laser Desorption/Ionization time-of-flight
MEH-PPV	Poly[2-methoxy-5-(2-ethylhexyloxy)-1,4-phenylenevinylene]
Mo <sub>6</sub>	Hexamolybdate cluster

NDT	Naphthodithiophene building block
NIR	Near-infrared
ODCB	<i>o</i> -Dichlorobenzene
OFET	Organic field effect transistor
OPV	Organic photovoltaic
P3HT	Poly(3-hexylthiophene-2,5-diyl)
PAH	Polycyclic aromatic hydrocarbons
PCBM	[6,6]-phenyl-C <sub>61</sub> -butyric acid methyl ester
PC <sub>61</sub> BM	[6,6]-phenyl-C <sub>61</sub> -butyric acid methyl ester
PC <sub>71</sub> BM	[6,6]-phenyl -C <sub>71</sub> -butyric acid methyl ester
PCE	Power conversion efficiency
PEDOT:PSS	Poly(3,4-ethylenedioxythiophene)-poly(styrenesulfonate)
PDI	Perylenediimide
POM	Polyoxometalates
PS	Polystyrene
PT	Polythiophene
PV	Photovoltaic
SCLC	Space charge limited current
TBAPF	Tetra-n-butylammoniumhexafluorophosphate
TBP	Tribenzopentaphene
TFA	Trifluoroacetic acid
THF	Tetrahydrofuran
TOF	Time of flight
TPA	Triphenyleneacetylenes
TSOH	<i>p</i> -Toluenesulfonic acid
$V_{oc}$	Open circuit voltage
$V_{TFL}$	Trap-free voltage limit
XRD	X-ray diffraction

## ACKNOWLEDGEMENTS

I would like to express my deepest appreciation and sincerest gratitude to my advisor and the chair of my committee Dr. Zhonghua Peng for his continuous support and encouragement throughout my PhD study. I have been amazingly fortunate to have an advisor like him. Before join Dr. Peng's group, I have no experience in any kind of research work. It is him who trained and taught me how to question thought and express my idea. This dissertation would not have been possibly done without his guidance and persistent help.

I would also like to extend my thanks to other dissertation committee members, Professor James R. Durig, Professor Nathan A. Oyler, Professor Da-Ming Zhu, and Professor Kun Cheng, for their professional guidance and valuable support in reviewing my dissertation.

I would like to express my gratitude to my colleges who provide inestimable assistance and effort to support my work. I specially wish to express my earnest thanks to Dr. Yong Li at the Department of Chemistry, UMKC. He has been paying great effort in helping and teaching me with photovoltaic device study. I'm very much grateful to Dr. James Murowchick at the School of Geosciences, UMKC, for his kind assistance with XRD and SEM measurements, and Dr. David van Horn, for his support in profiler measurements.

I must express my thanks to all my past and present group members: Dr. Sanjiban Chakraborty, Dr. Ching-En Chou, Dr. Tanmoy Dutta, Dr. Yong Li, Dr. Shaohua Li, Mr. Kuldeep Shetye and Mr. John Oster. I would have not been able to achieve my accomplishments without their kindness help and support. I want to thank all the staff of

the Department of Chemistry: Ms. Josephine Maningat, Ms. Florence Middleton, Ms. Asia Williams, Mr. Michael Sykora, Mr. John Whitchurch and Ms. Kathy Garrison.

Finally, I would like to express my heart-felt gratitude to my parents for their unconditional support and care which help me to face all the difficulties and stay focused on my study. Without their priceless love, it would have been impossible to reach this far.

Dedicated to my parents

## CHAPTER 1

### INTRODUCTION OF ORGANIC PHOTOVOLTAIC DEVICES

#### 1.1. Development of organic photovoltaic devices

Due to the ever-increasing demand for energy and the serious concern of environment pollution caused by traditional energy resources, scientists have been seeking renewable and environmentally friendly energy sources, of which solar energy is the most appealing. In 1839, French physicist A. E. Becquerel observed that when a cell was exposed to light, there was a voltage or electrical current produced across the cell, demonstrating the first photovoltaic (PV) effect.<sup>1-4</sup> This observation has made solar electricity a reality.

Current solar cell market is dominated by inorganic semiconductors which possess high charge generation efficiency and environmental stability.<sup>5</sup> The power conversion efficiencies of solar cells based on crystalline silicon have reached 25.6%.<sup>6,7</sup> The high manufacturing cost has, however, prevented them from becoming a common energy source that is competitive with fuel. First, higher power conversion efficiency requires better quality in crystalline order and higher purity of silicon material.<sup>8</sup> For example, the 25% efficiency is based on silicon of 99% purity.<sup>8</sup> Second, there is significant unavoidable waste of materials during the production of the silicon wafer slides (the so-called kerf loss).<sup>9</sup> Third, crystalline silicon is an indirect band gap semiconductor, which leads to low absorption of light. In order to achieve sufficient light absorption, films up to several hundred micrometers thick are required.<sup>6</sup> Thin film inorganic solar cells have been developed which are based on direct bandgap semiconductors such as cadmium telluride (CdTe), gallium arsenide (GaAs), and amorphous silicon (a-Si:H).<sup>10-13</sup> With direct bandgap, it is possible to harvest enough photons with only a few nanometer thickness.<sup>12</sup>

The efficiency of this kind solar cell has reached up to 28.1% for GaAs single junction devices and 42.3% for GaAs triple-junction metamorphic cell.<sup>12-14</sup> Such solar cells, however, have so far found only limited applications, mainly in special projects. Their broader applications have been hampered by the high fabrication cost. A single-crystal GaAs devices costs about \$10000 per square meter which is not viable for commercial use.<sup>13</sup> Besides the requirement of expensive equipment and technologies in production, the toxicity and scarcity of these materials are also concerns for terrestrial applications.<sup>12,14</sup> Therefore, there is an urgent need in finding substitute materials for low-cost solar cells.

The pursuit of organic-based PV cells has been ongoing ever since the investigation of the first organic solar cells in early 1970s.<sup>15,16</sup> Compare to inorganic PV devices, besides the low fabrication cost offered by the well-developed, convenient processing techniques such as roll-to-roll coating and doctor-blading, organic-based PV cells enjoy other advantages as well, such as light weight, substrate flexibility, good mechanical properties, environmental-friendly, good substantiality, etc.<sup>14-21</sup> Moreover, high absorption coefficient ( $\sim 10^5 \text{ cm}^{-1}$ ) of organic materials allow the capture of sufficient photons with films only a few hundred nanometer thick.<sup>18</sup> Besides, the energy level of semiconducting polymers can be easily tuned by modifying the skeletons or their side groups.<sup>17,18,22-24</sup> The first generation of organic solar cell was made by simply sandwiching a layer of organic dye between a low work function metal (aluminum) and a high work function metal (gold or silver) electrodes.<sup>15,16,18</sup> Because of oxidization on the low work function metal surface, its electronic behavior is similar to metal-insulator-semiconductor structure.<sup>18</sup> The performance of this kind of solar cell is poor with low power conversion efficiencies (normally  $<10^{-3}$ ). In 1985, Tang reported a bilayer solar cell with a power conversion

efficiency raised up to  $\sim 1\%$  and a fill factor of 0.65.<sup>25</sup> A layer of copper phthalocyanine (CuPc) (as an electron donor) and a layer of perylene tetracarboxylic derivative (as an electron acceptor) were deposited successively through vacuum evaporation.<sup>25</sup> Unlike the single layer solar cells where charges are generated at the metal/organic contact, the bilayer devices have charges generated at the organic interface. Since then, many types of organic solar cells have been developed based on the idea of donor-acceptor interfaces. In 1995, Heeger's group mixed MEH-PPV (donor) with C<sub>60</sub> (acceptor) to form the active layer, which led to devices with two order of magnitude increase in power conversion efficiency over those of MEH-PPV.<sup>14,26,27</sup> This method turns out to be the most successful one and the device structure is called bulk heterojunction device.<sup>20</sup> Bulk heterojunction is usually formed by blending two materials, one as electron donor and the other as electron acceptor. The different electron affinities of the two materials create a strong driving force in splitting photogenerated electron-hole pairs from excitons. The nanoscale distribution of the two materials provides the large interface area between the donor and the acceptor, which can improve device efficiencies by orders of magnitude. Some of the most promising heterojunction devices reported so far are based on  $\pi$ -conjugated polymers blended with a fullerene derivative. Power conversion efficiencies over 8% have been achieved.<sup>17</sup>

Although organic PV devices enjoy tremendous advantages, the efficiency of organic solar cells is still too low to be competitive with inorganic ones. Some limiting factors include low dielectric constant (usually 3-5 compare to  $\sim 10$  for inorganic materials),<sup>28-30</sup> short exciton diffusion length ( $\sim 10$  nm),<sup>28,31-33</sup> narrow absorption wavelength range,<sup>18,19</sup> unstable film morphology,<sup>34</sup> etc.. There are clearly significant

challenges and issues that need to be resolved before organic PV devices can become a commercial reality.

## 1.2. Theory

### 1.2.1. Device operating principle

In organic PV devices, the following processes are involved in the PV effect: photons with energy higher than the band gap of the organic semiconductors are absorbed to form excitons; these excitons travel to an interface where the built-in electric field is large enough to split excitons (electron-hole pairs) into free charge carriers; the resulting free charge carrier transport to respective electrodes.<sup>35</sup>

Solar cells can be classified into three categories according to the materials used in the active layer: small molecule solar cells, polymer solar cells, and organic-inorganic hybrid solar cells. In small molecule and polymer solar cells, there is at least one component in the active layer that is a conjugated molecule or polymer which plays the role as light absorber and the electron-donor. For organic-inorganic hybrid solar cells both organic and inorganic materials are incorporated in the active layer. Usually, the organic component serves as the electron donor and hole transporter while the inorganic component accepts and transports electrons.<sup>21</sup>

Based on the device architecture, solar cells can be classified into six categories:

- 1) Single layer solar cells, which is also called Schottky-barrier organic solar cells.<sup>16</sup> In this type of cells, a layer of a single component organic semiconductors is sandwiched between the two electrodes.
- 2) Bi-layer donor/acceptor solar cells, where the active layer between the two electrodes includes one layer of electron donating material and another layer of an electron accepting material.
- 3) Bulk heterojunction donor/acceptor solar cells, where the

active layer is made from a mixture of donor and acceptor materials. 4) Tri-layer p-i-n heterojunction solar cells, which is similar to bi-layer donor/acceptor solar cells but it has an extra layer inserted between the donor and the acceptor layers with a mixture of these two components.<sup>36</sup> 5) Multilayer heterojunction solar cells, whose active layers are consisted of three or more layers. And 6) tandem solar cells, where two or more sub solar cells are stacked into a tandem structure.<sup>37</sup> Figure 1-1 shows the schemes of the six types of solar cell structures. The first three are the most common configurations used for PV device studies, and their device principles are thus further discussed.

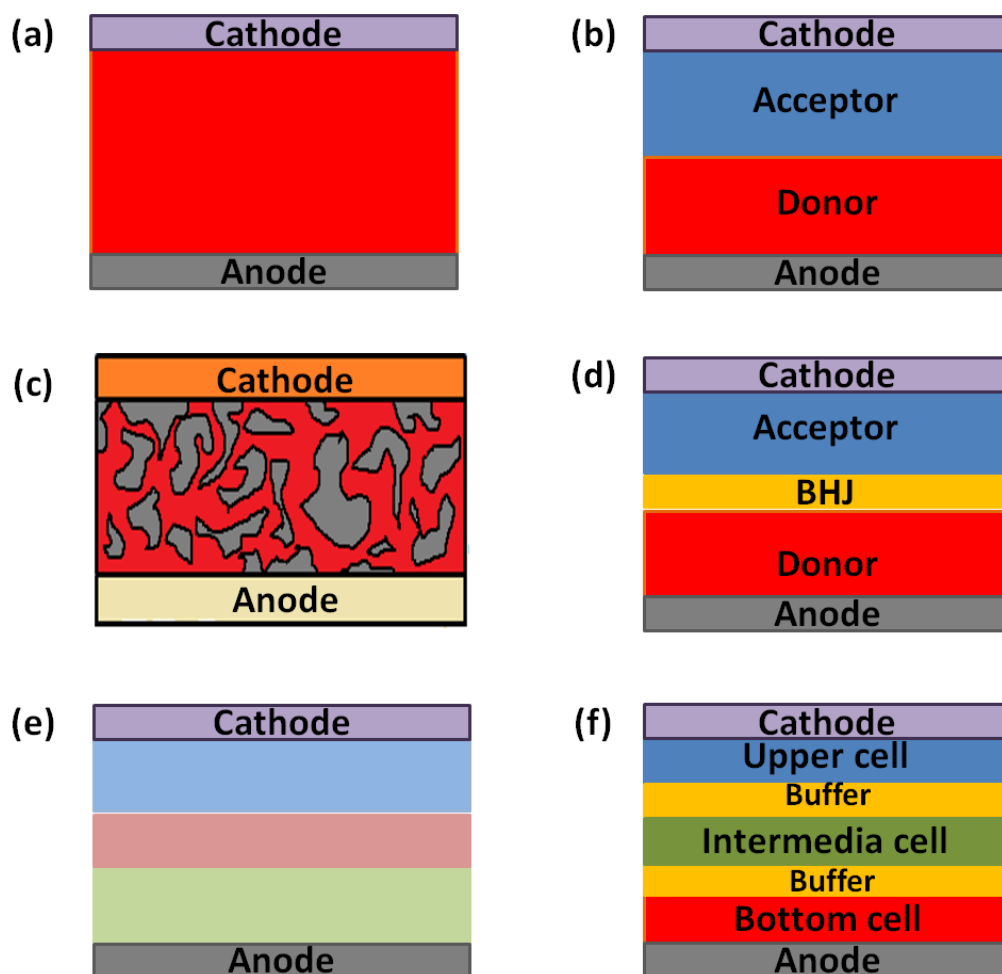


Figure 1-1 Device configurations of Schottky-barrier organic solar cell (a), bi-layer donor/acceptor solar cell (b), bulk heterojunction donor/acceptor solar cell (c), tri-layer p-i-n heterojunction solar cell (d), multilayer heterojunction solar cell (e) and tandem solar cell (f).

a) Single layer solar cells

Single layer solar cells is the simplest type of organic solar cells. It is also called Schottky barrier organic solar cells because a Schottky contact is formed at one of the organic/electrode interfaces, which shows rectifying characteristics. The other

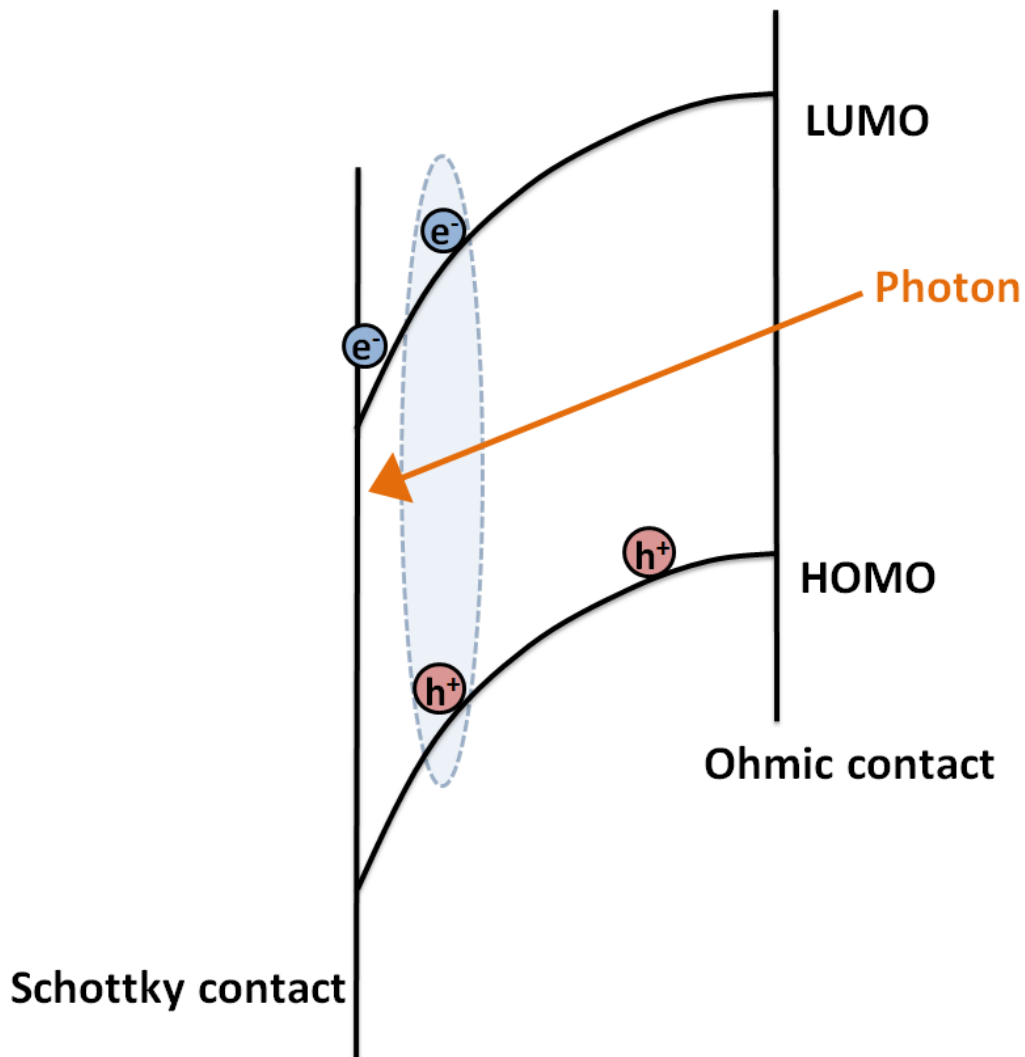


Figure 1-2 Energy level diagram of a single layer organic solar cell.

semiconductor/electrode interface shows Ohmic contact.<sup>35</sup> Figure 1-2 shows the energy level diagram of a single layer solar cell. The organic film is sandwiched between a transparent conducting substrate, usually ITO glass, and an electrode, such as Al or other low work function metals. Photons go through the transparent electrode and are absorbed by the organic film generating excitons. Some unabsorbed photons may travel through the organic film and are then reflected back to the organic film by the metal electrode before leaving the device, which offers a second chance for photon absorption. The exciton separation step only occurs at the Schottky contact where a rectifying Schottky barrier introduces an electric field large enough to produce free carriers. In order to ensure sufficient photon absorption, thick film is preferred. However, due to the low dielectric constant and high exciton binding energy, the photogenerated electron-hole pairs cannot be separated by the built-in electric field as in inorganic materials. Excitons can only be separated at the interface of the electrode/active layer where the electric field is large enough. In this type of configuration, there is only one interface where exciton can be separated into free charge carrier. All the excitons have to travel to this interface for charge dissociation. The diffusion length of organic exciton is usually shorter than 10 nm. In other words, only the excitons generated near the Schottky contact can be converted to free charges, the others will be reverted back to the ground state, which leads to low quantum yields and poor device performance. Besides, both kinds of charge carriers travel in the same material, and thus have a good chance to recombine, which further decreases the power conversion efficiency.<sup>18,35</sup>

b) Bi-layer heterojunction solar cells

The active layer in bilayer heterojunction solar cell is consisted of one donor layer and one acceptor layer as shown in Figure 1-1(b). This configuration has been used extensively in evaluating photovoltaic performance of various organic donor-acceptor pairs. The PV effect in this device configuration involves five steps as shown in Figure 1-3,<sup>23</sup> 1) the absorption of photons by electron donating materials to generate excitons; 2) the diffusion of excitons to the donor/acceptor interface; 3) the separation of excitons to free charge carriers at the donor-acceptor interface; 4) the migration of free charge carriers to their respective electrodes; 5) the collection of free carriers at the electrodes. The major difference in device operating principles between the single layer and the bilayer devices is that the separation of exciton is now occurring at the donor-acceptor interface instead of the semiconductor/electrode interface. The significant difference in electron affinity between the donor and acceptor materials can create a strong driving force which is capable of splitting photogenerated excitons in nearly 100% efficiency.<sup>18,20,25</sup> Another advantage of the bilayer configuration is that positive and negative charge carriers travel through different materials to their respective electrodes. The separated charge transporting pathways reduce the possibility of charge recombination.<sup>25</sup> As a result, the quantum yields and their power conversion efficiencies of bilayer PV devices are significantly improved. However, the limited donor/acceptor interface area is still an issue. As mentioned earlier, organic excitons have typical diffusion lengths of only around 10 nm, indicating that only those excitons generated in the donor layer within 10 nm of the donor/acceptor interface have a chance to reach the interface.

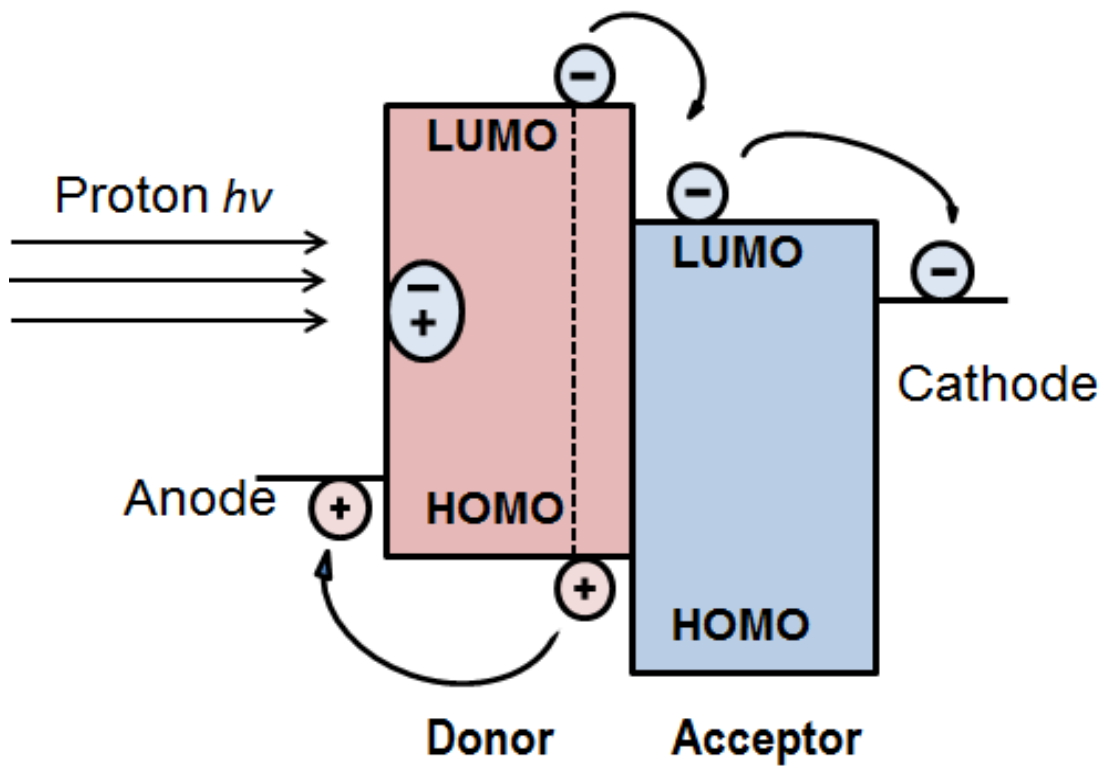


Figure 1-3 Photon-electron conversion process in a bilayer organic solar cell.

### c) Bulk heterojunction solar cells

The operating principle of bulk heterojunction solar cells is similar to bi-layer solar cells. It also requires an electron donating material and an electron accepting material. The difference is that, in bulk heterojunction solar cells, the donors and the acceptors, instead of forming two separated layers, are mixed together so that the donor and the acceptor regions are distributed throughout the device.<sup>27</sup> Numerous donor-acceptor interfaces are thus formed, resulting in a large interface area. In addition, by controlling the donor domain sizes to be in the nanometer range, there are donor-acceptor interfaces within the diffusion length of any excitons, thus significantly improving the photocharge generation quantum yields.<sup>27</sup>

The major drawback in this configuration is the randomly distributed donor/acceptor regions. The active layer of this configuration is usually fabricated by spin-coating from a solution of donor/acceptor mixture or co-evaporation techniques, which are generally lack of control on the molecular packing and morphology.<sup>34,38-40</sup> One solution is to use block copolymers. The covalently bonded two distinct blocks can result in a phase-separated supermolecular nano-domain structures.<sup>41-45</sup> The phase-separated morphologies depend on the volume fraction, the block-block interaction and the length of each block, and can be spheres, gyroids, vesicles, cylinders, lamellae, etc.<sup>46</sup> The desired morphology is the interpenetrating gyroid structure. If one block contains as electron donors while the other block contains electron acceptors, it is possible to form interpenetrating but separated donor and acceptor domains with controllable domain sizes.

### 1.2.2. Characteristics of organic PV devices

The performance of a PV device can be evaluated from the so called  $I$ - $V$  curve as shown in Figure 1-4, from which the most important parameters related to solar cell evaluations can be obtained. The parameters include open circuit voltage  $V_{OC}$ , short circuit current  $I_{SC}$ , fill factor  $FF$ , and power conversion efficiency ( $PCE$  or  $\eta$ ). The power conversion efficiency is defined as the ratio of the maximum output power ( $P_m$ ) to the incident power ( $P_{in}$ ) from the light source.  $P_m$  is the product of  $J_{max}$  and  $V_{max}$  which are the current density and the voltage at the maximum power point.<sup>20</sup>

$$PCE = \frac{P_m}{P_{in}} = \frac{J_m \times V_m}{P_{in}} \quad (1-1)$$

$$J_m \times V_m = FF \times J_{SC} \times V_{OC} \quad (1-2)$$

$J_{SC}$  is short circuit current density which is often used instead of  $I_{SC}$  for the convenience of comparison of different solar cells.  $J_{SC} = I_{SC}/A$ , where  $A$  is the active area of PV device. Apparently, high  $FF$ ,  $J_{SC}$  and  $V_{OC}$  give high power conversion efficiency.

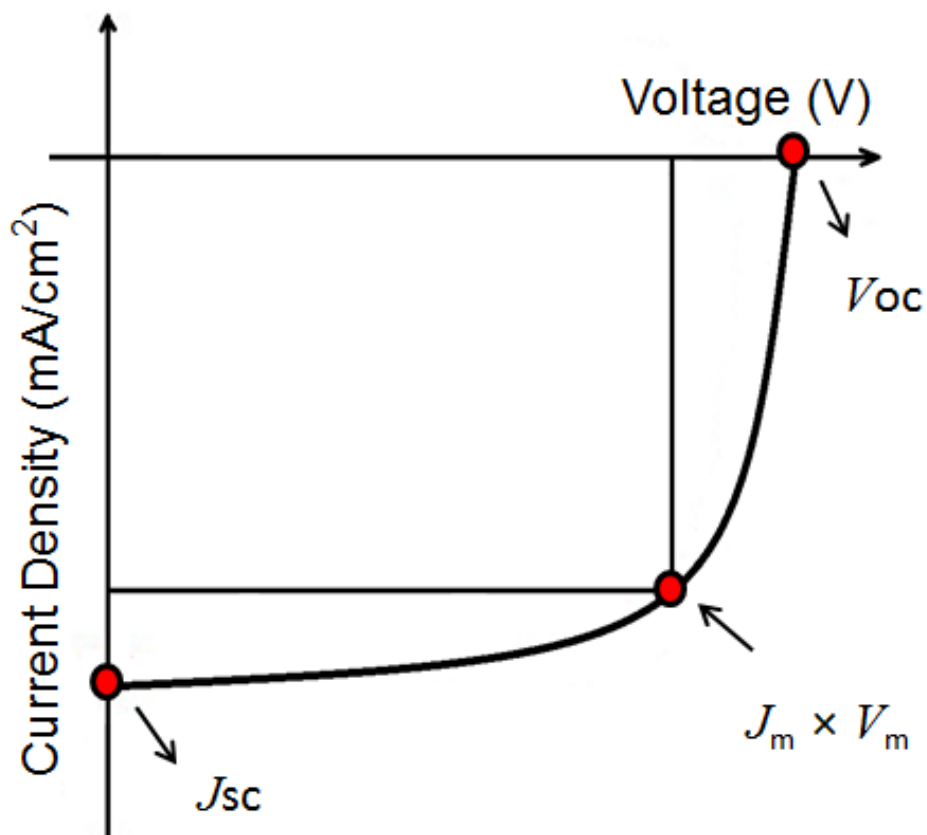


Figure 1-4 Typical current density-voltage ( $J$ - $V$ ) curve.

*The fill factor (FF)*

The fill factor describes the rectangle-like shape of the  $J$ - $V$  curve and reflects the quality of the diode. The more rectangle-like the  $J$ - $V$  curve is, the higher the fill factor will be. The fill factor depends on the carrier transportation and charge recombination which corresponds to series resistance ( $R_s$ ) and shunt resistance ( $R_{sh}$ ), respectively. A large series resistance and a small shunt resistance will lower the fill factor.<sup>47,48</sup> One of the causes of series resistance is the resistance at the contact between organic active layer and the electrodes. The series resistance mainly affects the fill factor but not the short-circuit

current unless the resistance is very large.<sup>49</sup> The shunt resistance decreased the output power by building another current flow path. This resistance is mainly caused by defects and has a stronger effect at low voltages.<sup>48</sup> The following equations are used to estimate  $R_s$  and  $R_{sh}$  of a PV device,<sup>50</sup>

$$R_s = \frac{\partial V}{\partial J} \Big|_{V=V_{oc}+0.2} \quad (1-3)$$

$$R_{sh} = \frac{\partial V}{\partial J} \Big|_{V=0} \quad (1-4)$$

The ideal contact between each adjacent layers or regions in a device is the Ohmic contact where no rectifying occurs. The ideal Ohmic contact will reduce the series resistance especially the portion caused by contact resistance and decrease the power loss caused by shunt resistance. Also, it has been proved that combining the donor and acceptor materials with similar hole mobility and electron mobility can increase fill factor.<sup>51</sup> For example, the combination of PPV/PCBM shows lower photocurrent and efficiency than that of P3HT/PCBM pair, which is due to the unbalanced charge transporting rate leading to a space charge limited (SCL) behavior.<sup>51</sup> When the mobility of holes and electrons are mismatched, charge carriers will accumulate near one of the electrodes without recombination, resulting in a change in the field. This is called  $\mu\tau$  -limited process ( $\mu$  represents mobility, and  $\tau$  represents the life time of the carriers), where the small  $\mu\tau$

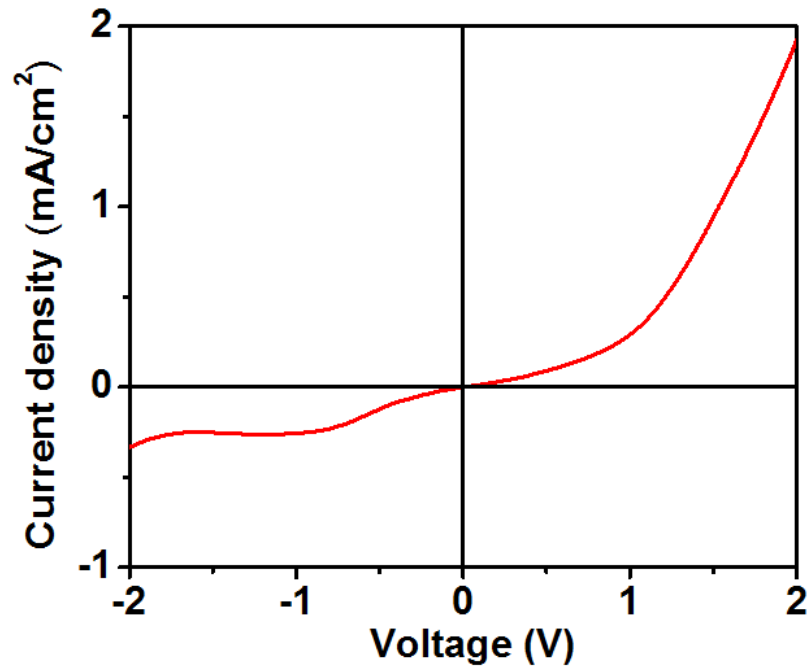


Figure 1-5  $J$ - $V$  curve obtained in space charge limited current mobility measurement. S-shape curve appeared when charge accumulated.

dominates the thickness of the accumulation region.<sup>18</sup> In the extreme situation, a space charge limited current may occur with an internal field building up. This leads to a lower fill factor. An S-shaped  $J$ - $V$  curve is an indicator of carrier accumulation.<sup>51</sup>

*The open circuit voltage ( $V_{OC}$ )*

Open circuit voltage ( $V_{OC}$ ) is the maximum voltage that a solar cell can produce.

Theoretically, it can be estimated by the following equation,<sup>20</sup>

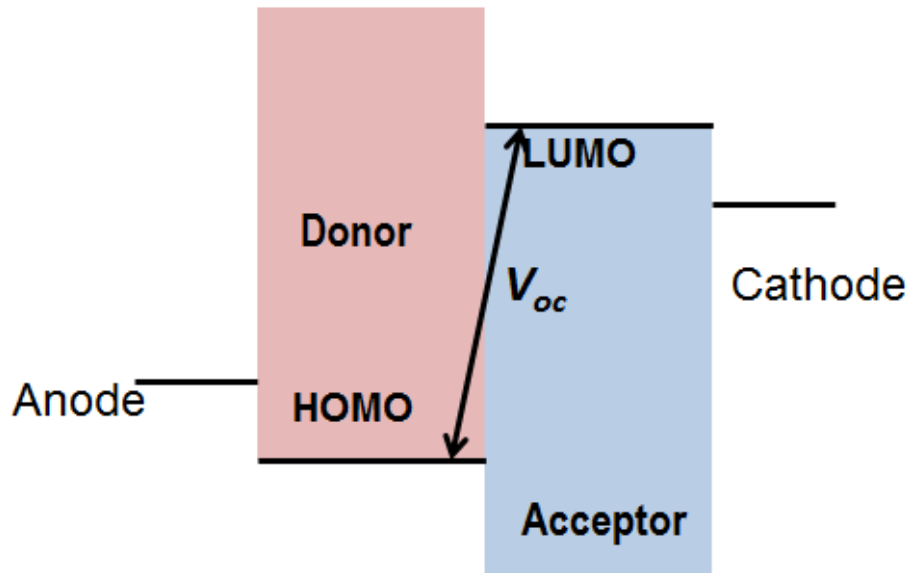


Figure 1-6 Energy diagram of open circuit voltage.

$$V_{oc} \approx \left(\frac{1}{e}\right)(E_{A(LUMO)} - E_{D(HOMO)}) + k_B / e (\ln(n_e n_h / N_c^2)) \quad (1-5)$$

where  $E_{A(LUMO)}$  and  $E_{D(HOMO)}$  are LUMO level of the acceptor and HOMO level of the donor, respectively.  $N_c$  is the corresponding states near the LUMO of acceptor and HOMO of the donor,  $k_B$  is the Boltzmann constant,  $e$  is elementary electron,  $n_e$  &  $n_h$  are the electron density and hole density, respectively. This equation describes the difference between two Fermi distributions of the two opposite charge carriers, which is an upper limit for  $V_{OC}$ . Scharber et al. reported a relationship between energy level of donor/acceptor blends and  $V_{OC}$ .<sup>52</sup> A linear relationship between the HOMO level and the  $V_{OC}$  based on twenty-six donor materials has been observed. A simpler expression was found as:<sup>52</sup>

$$V_{OC} = \left(\frac{1}{e}\right) (|E_{HOMO}^{Donor}| - |E_{LUMO}^{Acceptor}|) - 0.3 V \quad (1-6)$$

This suggests that,  $V_{OC}$  is simply the difference between the HOMO of the donor and LUMO of the acceptor with 0.3 V offset.  $V_{OC}$  can also be influenced by the morphology of the active layer and the contact of metal/organic film. A few nanometer buffer layer is usually deposited between the active layer and metal electrodes which help make the active layer and the electrode compatible.<sup>19</sup> PEDOT:PSS is the most commonly used buffer layer for anode. Its lamellar orientation can be modified by post-deposition treatments.<sup>19</sup>

*The short circuit current density ( $J_{SC}$ )*

The short circuit current can be calculated from photon flux and external quantum efficiency (EQE) under a specific wavelength.<sup>21</sup> EQE is described as a ratio of the number of charge carriers collected by a solar cell over the total number of photon from an input power.<sup>21</sup> It can be estimated from the product of efficiencies in photon absorption  $\eta_{abs}$ , exciton diffusion  $\eta_{diff}$ , hole-electron pair separation  $\eta_{tc}$ , charge carrier transport  $\eta_{tr}$ , and charge carrier collection  $\eta_{cc}$ .<sup>21</sup>

$$J_{SC} = q \int_{\lambda_{min}}^{\lambda_{max}} \Phi(\lambda) \times EQE(\lambda) d\lambda \quad (1-7)$$

$$EQE = \eta_{abs} \eta_{diff} \eta_{tc} \eta_{tr} \eta_{cc} \quad (1-8)$$

It can be noticed that the value of  $J_{SC}$  is related to the entire process from photon absorption to charge collection.

a) *Photon absorption efficiency  $\eta_{abs}$*

The photon absorption efficiency dictates the number of excitons that can be produced. The number of photon absorbed by the active layer is dependent upon the

absorption wavelength range and the absorbance of the resulting device film. For the absorbing wavelength range, it is better overlap as much as possible with the solar flux spectrum. The solar flux is not evenly distributed across the solar spectrum. The strongest solar irradiance is in the visible region (300-700 nm).<sup>19</sup> There are significant solar flux in the UV and near IR region as well. For most organic materials, their wavelength range is usually in the range of 300 - 600 nm.<sup>19</sup> Increasing in  $\pi$ -conjugation length and  $\pi$ - $\pi$  interaction between molecules may result in an enhanced absorption range.

Photon absorption efficiency can also be affected by the thickness of an active layer.<sup>53</sup> The thicker the film is, the higher its absorbance may be.<sup>21</sup> For solution processing techniques, such as spin-coating, doctor blading and screen printing, the film thickness may be controlled by varying the concentration, solvent, spin rate, etc.<sup>54</sup> Taking spin-coating method as an example, the film thickness  $d$  can be estimated by the empirical equation:<sup>54</sup>

$$d = k\omega^\alpha \quad (1-9)$$

where  $\omega$  is the angular velocity,  $k$  and  $\alpha$  are constant related to the properties of the solution, such as viscosity, and the substrate. Thus, decreasing the spin rate or increasing the solution viscosity can resulting thicker films. Addition of an optical spacer in the system can also help photon absorbance through a better distribution of light intensity.<sup>54</sup>

b) *Exciton diffusion  $\eta_{diff}$*

The exciton diffusion efficiency relates to the number of exciton that can reach a donor-acceptor interface. It depends on the exciton diffusion length and the resistance of diffusion pathways. As mentioned earlier, one limitation of organic semiconductors is the short exciton diffusion length. Organic excitons have a diffusion length of only around 10

nm.<sup>19,26</sup> It is, therefore, critical that, donor domains has sizes smaller than 10 nm in at least one dimension. To facilitate exciton diffusion, it is important to limit traps as well.

*c) Hole-electron pair separation  $\eta_{ic}$*

In organic semiconductor, due to the low dielectric constant, the photogenerated electron-hole pair cannot be separated into free charge carriers until it reaches the interface of the donor and the acceptor. The separation of electron-hole pair requires sufficient driving force that is at least larger than the exciton binding energy. The downhill driving force required, which is the difference between the LUMO energy levels of the donor and the acceptor, is 0.3 eV at the minimum.<sup>21,55-57</sup>

*d) Charge carrier transport  $\eta_{tr}$*

Charge carrier transportation efficiency reflects the ability of charge transportation carrier migrating through the active layer. The charge transport is often through a hopping mechanism and can be hindered by the traps on the charge transporting pathway.<sup>21,55,56</sup>

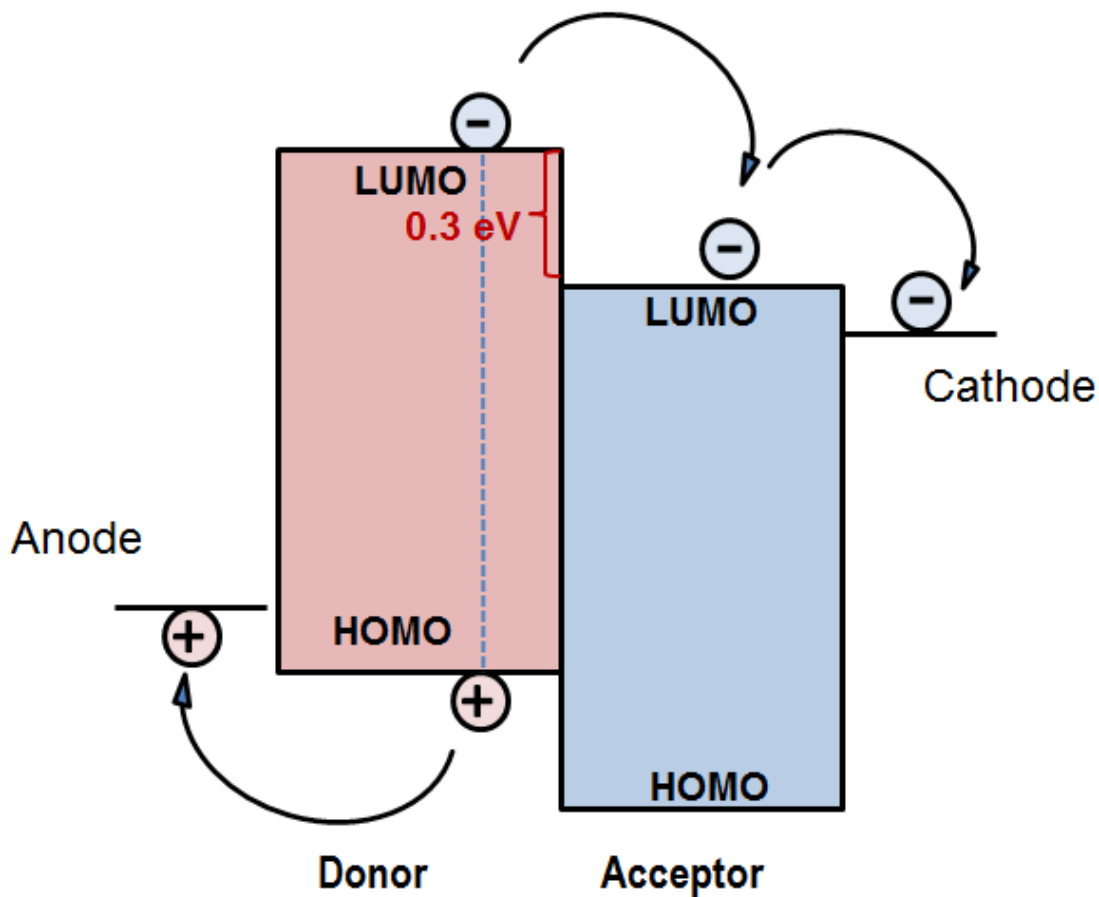


Figure 1-7 Energy level diagram of charge separation and transportation.

Efficient transportation of charge carriers must be an energy favorable process. A downhill driving force is needed for electron transporting to cathode while uphill driving force is needed for hole transporting to anode. The ideal difference between an adjacent energy levels is  $\sim 0.3$  eV for efficient charge hopping.<sup>21</sup> Energy mismatches among the donor, the acceptor and the electrodes can lead to a serious drop in quantum yield and the power conversion efficiencies.

Efficient charge transport requires separate charge transporting pathways for electrons and holes to minimize charge recombination.<sup>58</sup>

Efficient charge transport also calls for high mobility for both charge carriers. Charge mobility of organic/polymeric materials depends on molecular packing and long range order. If the molecules are randomly packed, defects can be brought into the film that can serve as charge carrier trapping sites. Highly ordered molecular arrangement can facilitate the charge carrier transport. Desired molecular packing may be realized through thermal annealing,<sup>34,59,60</sup> solvent annealing,<sup>34,40</sup> or by adding adducts which can facilitate molecule packing.<sup>19</sup>

An ideal configuration is to have donor and acceptor regions interpenetrating to each other with phase segregation domains in the exciton diffusion length scale of  $\sim 10$  nm as shown in Figure 1-8.<sup>61</sup>

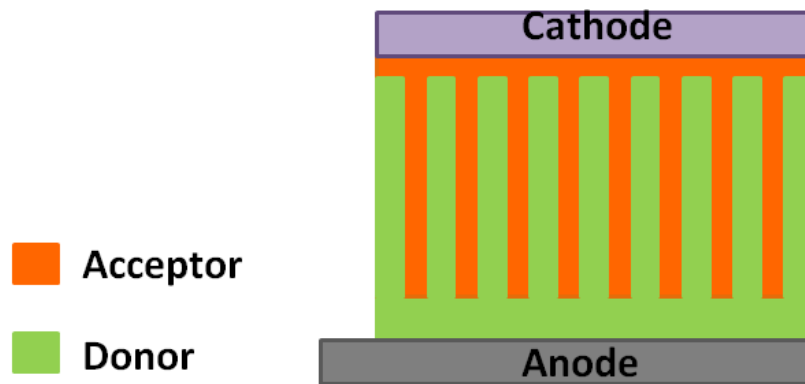


Figure 1-8 Architecture of ideal donor-acceptor organic solar cell.

e) *Charge carrier collection  $\eta_{cc}$*

The charge carrier collection efficiency represents how successful the electrons and holes can be transferred to the respective electrodes. As mentioned earlier, efficient charge transfer requires a downhill driving force for negative charges and an uphill force for positive charges. In other word, to ensure a successful collection of charges, the work function of anode material should be higher than the HOMO of the donor and the work function of the cathode material should be lower than the LUMO of the acceptor.<sup>21</sup>

Ideal Ohmic contact is the most preferred in the charge collecting process. The mechanism of charge collection for organic solar cells has not yet been well understood. It is known that interface inhomogeneity can trap electrons and holes.<sup>18,21,34,51</sup> Accumulation of charge carriers may lower fill factor and the value of  $J_{SC}$ .<sup>51</sup> A buffer layer such as PEDOT:PSS at the anode side and Ca at cathode side can improve the interface of the active layer/electrode.<sup>19,51</sup> Better crystallinity of the buffer layer will enhance the charge injection.<sup>18,19</sup>

In summary, in order to get realize an efficient PV device, the following factors need to be considered: proper absorption wavelength range, high absorbance of the active layer, matched HOMO/LUMO energy levels for donors and acceptors, high charge carrier mobility, efficient exciton separation, efficient charge transport and effective charge collection at electrodes.

### 1.3. Objective

The objectives of this dissertation research are to evaluate the PV performance of various materials newly developed in our laboratory. These materials include organic-inorganic hybrids, new conjugated polymers, and organic discotic compounds. The following three chapters document our efforts in the three different kinds of materials as

the following: Chapter 2 studies the PV properties of organic-inorganic hybrids; Chapter 3 focuses on the studies of conjugated polymers with NIR absorptions while Chapter 4 concentrates on the studies of small organic molecules with high mobilities.

## CHAPTER 2

### POLYOXOMETALATE CONTAINING ORGANIC-INORGANIC HYBRID MATERIALS FOR PHOTOVOLTAIC APPLICATIONS

(A part of the results and discussion in this chapter are reproduced from *Journal of Polymer Science Part B: Polymer Physics*, **2014**, 52, 122-133 with permission from John Wiley and Sons)

#### 2.1 Introduction

Fullerene derivatives are the most commonly used electron transporting and electron accepting materials due to their good electron affinity and high electron mobility ( $\sim 1 \text{ cm}^2 \text{ V}^{-1} \text{ s}^{-1}$ ).<sup>19</sup> They are often blended with conjugated polymers to form BHJ structures. The classical and well-studied architecture in polymer solar cells is the BHJ of polythiophene/fullerene. To form continuous transportation pathways for both electrons and holes, the weight percentage of fullerene in the composite is often at least 50%.<sup>38</sup> Fullerene derivatives are, however, expensive to synthesize.<sup>62</sup> They also have high tendency for aggregation which results in morphological instability and lowers device performance.<sup>34,38</sup> There is thus an urgent need to find alternative acceptor materials.

Many fullerene substitutes have been explored, among which inorganic materials, such as ZnO, TiO<sub>2</sub>, and CdSe, etc.,<sup>63-69</sup> have drawn significant attention. These hybrid solar cells maintain the benefits of organic PV devices but also bring some other advantages. The inorganic materials help improve environmental stability (better photostability, for example) of the system.<sup>21</sup> Some of them have much stronger light absorption than PCBM does.<sup>21</sup> Some of them are able to form well-aligned nanostructures such as nanowires and nanorods which may form an efficient charge transporting pathways while maintaining

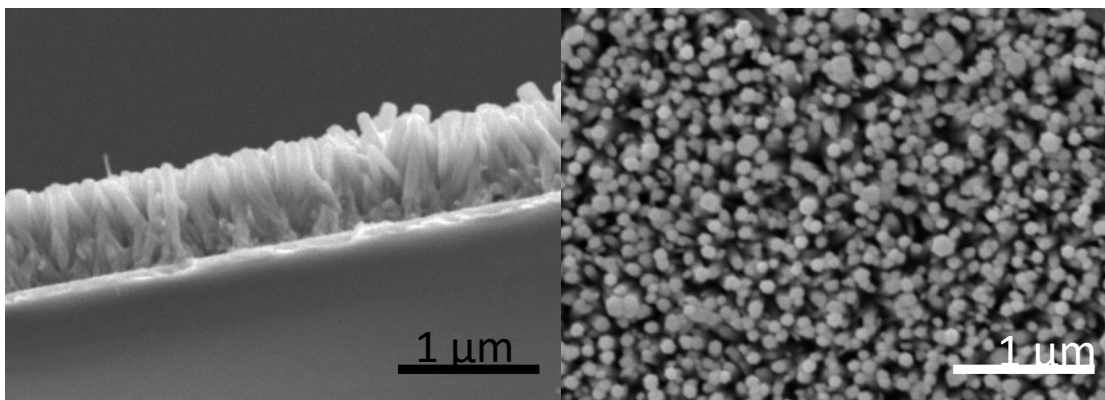


Figure 2-1 SEM of ZnO nanorods cross-section (left) and top view (right).

large donor-acceptor interface for exciton dissociation.<sup>21</sup> Their reported power conversion efficiencies have been steadily increasing but thus far are still significantly lower than those of all organic solar cells such as polymer/fullerene blends, not to mention all-inorganic solar cells such as crystalline Si and CdTe thin films.<sup>21</sup> One reason has to do with the incompatibility between inorganic and organic materials. As mentioned above, donor-acceptor blends often require high loading ratio of both donor and acceptor components.<sup>65,70–72</sup> Such high loading blends exhibit unstable morphologies. For blends involving both organic and inorganic components, it is even harder to control the morphology of the blending films due to the stark structural and property differences between the organic and inorganic components. To improve the compatibility and to ensure close interaction between the two components, one can resort to surface modification, such as attaching inorganic-binding ligands to the organic component.<sup>70,73</sup> A more ultimate solution is to covalently link the two components through chemical bonds.<sup>71,72,74,75</sup>

Covalently bonded donor-acceptor systems (molecules or polymers) are attractive PV materials. With covalent connection between organic and inorganic systems, it is

possible to achieve controllable morphologies, improvement of the compatibility between organic and inorganic components and ensure the close interaction between the organic donor and the inorganic acceptor.<sup>74,75</sup> One requirement to fulfill this concept is to find an inorganic material that can be covalently bonded to an organic material.

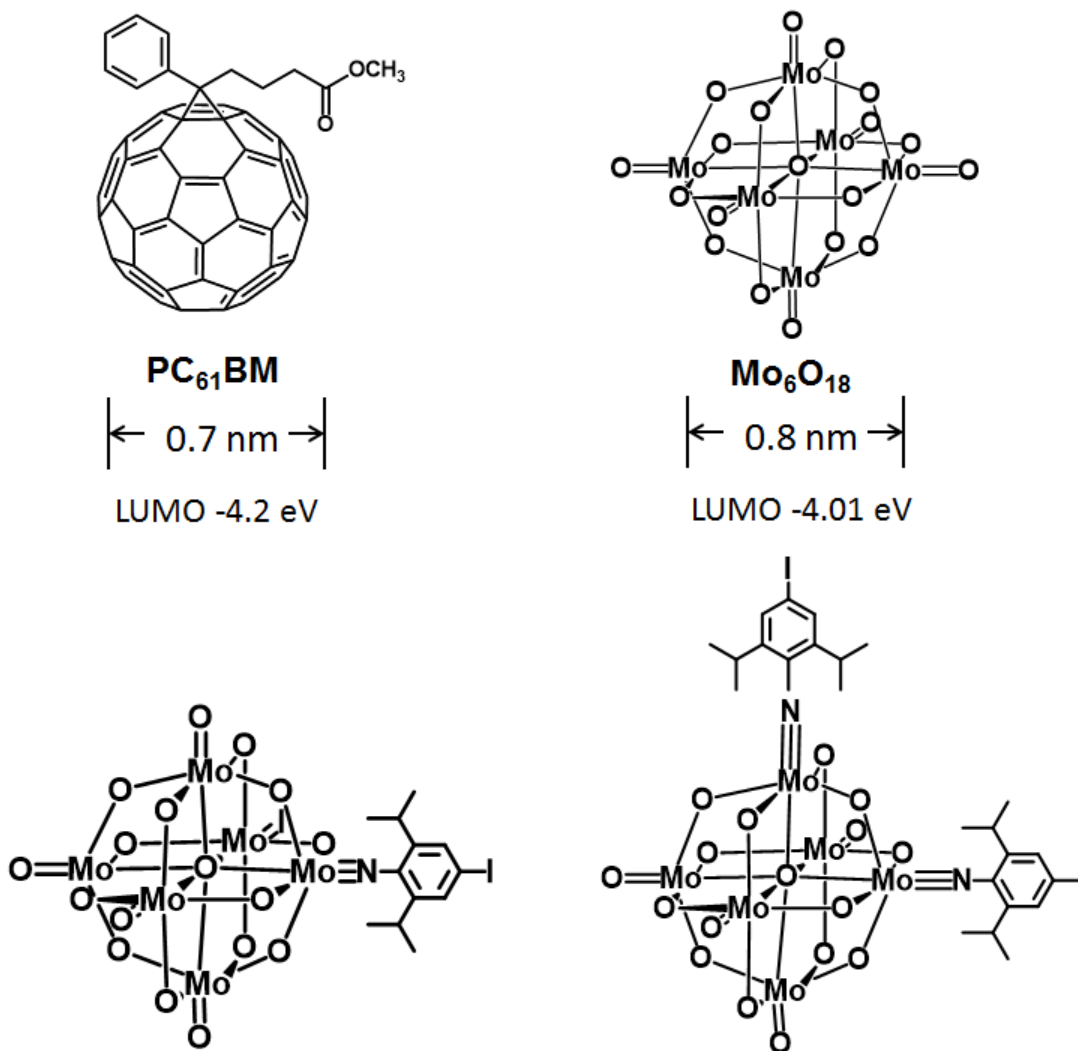


Figure 2-2 Molecule structures of PC<sub>61</sub>BM (top left), hexamolybdate cluster (top right), monofunctionalized (bottom left) and bifunctionalized (bottom right) clusters.

Among various inorganic electron acceptors, polyoxometalates (POM), early transition metal oxygen anion clusters, are especially attractive. POMs are well known oxidants and can accept multiple electrons.<sup>76</sup> They are robust and structurally stable. Furthermore, POMs have unmatched structural and compositional diversity. Their many properties, ranging from molecular shape to solubility, charge density to redox potentials can be easily tuned.<sup>77</sup> One of the POMs, the hexamolybdate cluster, is particularly appealing. It has roughly spherical shape with a diameter around 0.8 nm which is close to that of C<sub>60</sub> (0.7 nm); it has a reversible one electron reduction process at potentials (-4.01 eV in LUMO) close to that of fullerene (-4.20 eV in LUMO).<sup>77</sup> It is easy and inexpensive to synthesize. More importantly, the hexamolybdate cluster can be conveniently and efficiently functionalized with one or two organo imido groups.<sup>76-84</sup> The terminal O atom can be replaced by N atom, allowing the preparation of covalently-bonded organic-inorganic hybrids and POM-containing polymer hybrids.

## 2.2 Objective

Three POM-containing hybrid systems are studied. As shown in Figure 2-3, the POM-containing hybrid systems to be explored include, 1) charge transfer hybrids based on neutral organic donor and POM clusters with a conjugated linkage; 2) POM-containing rod-coil diblock copolymers, where POM clusters are covalently attached as pendants to the coil block. 3) POM-containing main-chain conjugated polymers, where POM clusters

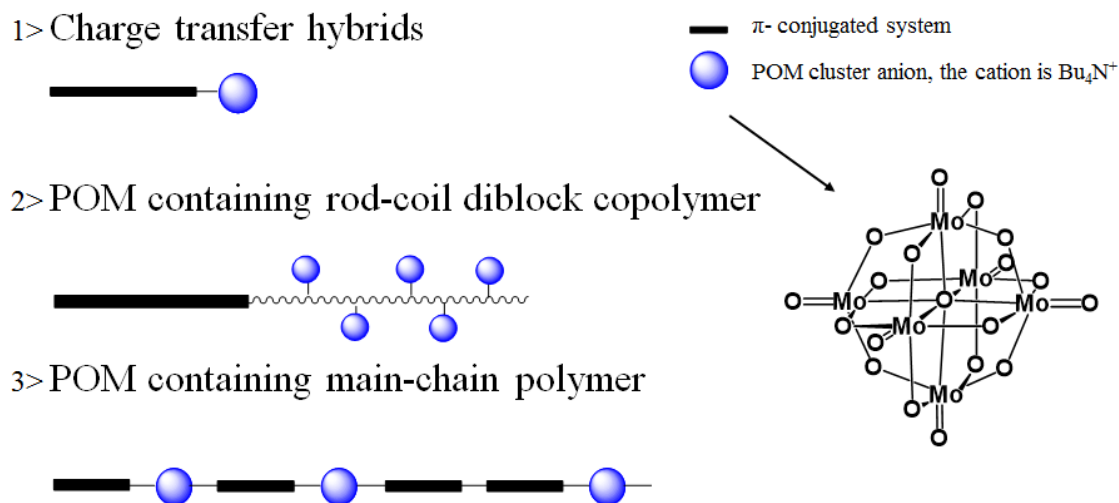


Figure 2-3 Models of the three hybrid POM systems.

are embedded into the conjugated backbone. In these systems, the organic  $\pi$ -conjugated segments serve simultaneously as the light absorbing chromophores, photoexcited electron donors, and hole transporters, while the POM clusters play the roles of electron acceptors and electron transporters.

The specific research objectives are:

- 1) To study the electrochemical properties of these hybrids.
- 2) To fabricated PV devices from the POM containing hybrids with various fabrication conditions including annealing temperature and time, thickness of the active layer, etc.
- 3) To study the incident photon to charge carrier efficiency of the POM containing hybrid materials by measuring external quantum efficiency.
- 4) To understand the relationship of polymer structure and device performances by varying POM and polymer connection and POM loading concentrations.

### 2.3 Small molecular POM-containing hybrid

Charge-transfer hybrids containing organic and inorganic materials have been the focus of studies for many years. The potential applications for superconductor and photovoltaic cells are major driving forces. POM clusters have been used in preparing charge-transfer hybrids with neutral or cationic organic donors. This study focuses on a charge transfer hybrid that contains a POM cluster covalently bonded with a ferrocenyl unit via an extended  $\pi$ -conjugated bridge as shown in Figure 2-4. The conducting bridge ensures facile charge transfer from the organic donor to the POM acceptor. Direct charge-transfer transition from the ferrocenyl donor to the cluster acceptor has been observed in the UV-vis absorption spectrum, showing as a tail extending beyond 500 nm (Figure 2-5).<sup>79</sup>

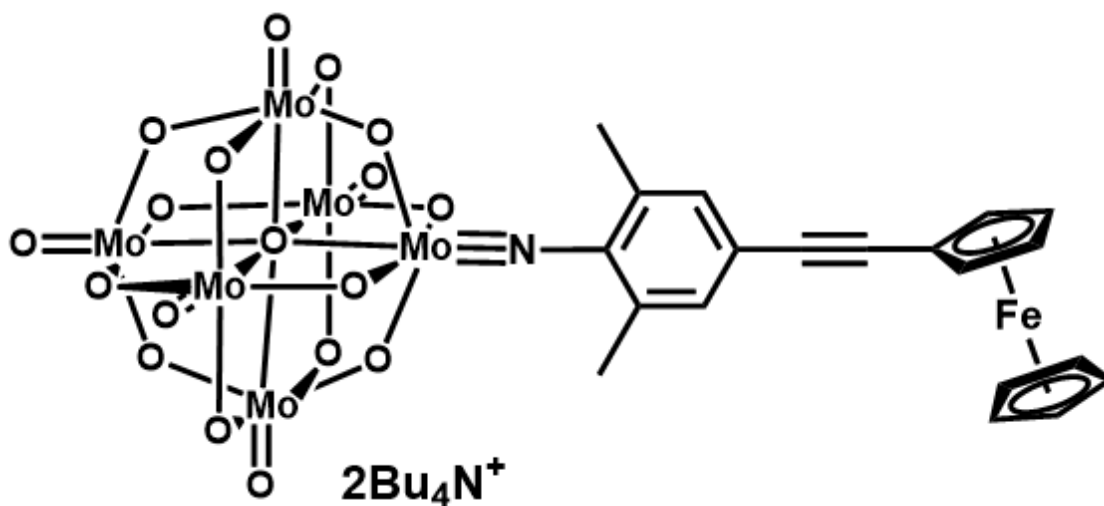


Figure 2-4 Molecule structure of **Mo<sub>6</sub>-Fe**.

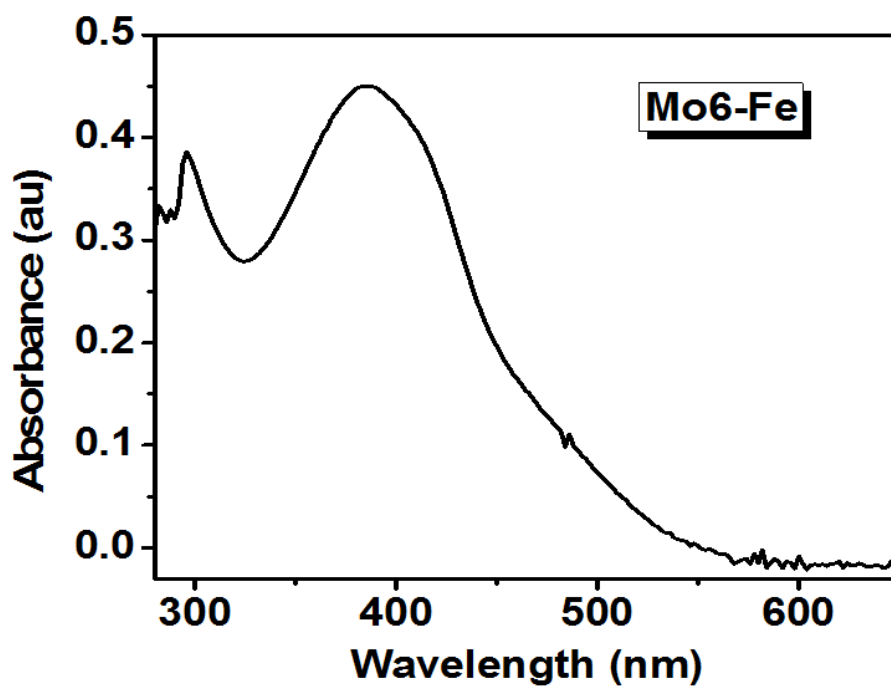


Figure 2-5 UV-vis spectrum of **Mo6-Fe** in *o*-dichlorobenzene solution.

Electrochemical properties of **Mo6-Fe** were investigated by CV measurements in acetonitrile solution with 0.1 M TBAPF as electrolyte. As shown in Figure 2-6, there is one reversible reduction wave in the cathodic scan with a half wave potential of -1.5 V and one reversible oxidation wave in the anodic scan with a half wave potential of -0.1 V, which is corresponding to the reduction of POM cluster and oxidation of linked ferrocene, respectively. The HOMO and LUMO energy levels are calculated to be -4.7 eV and -3.3 eV, respectively. The bandgap of the hybrid is calculated to be 1.4 eV.

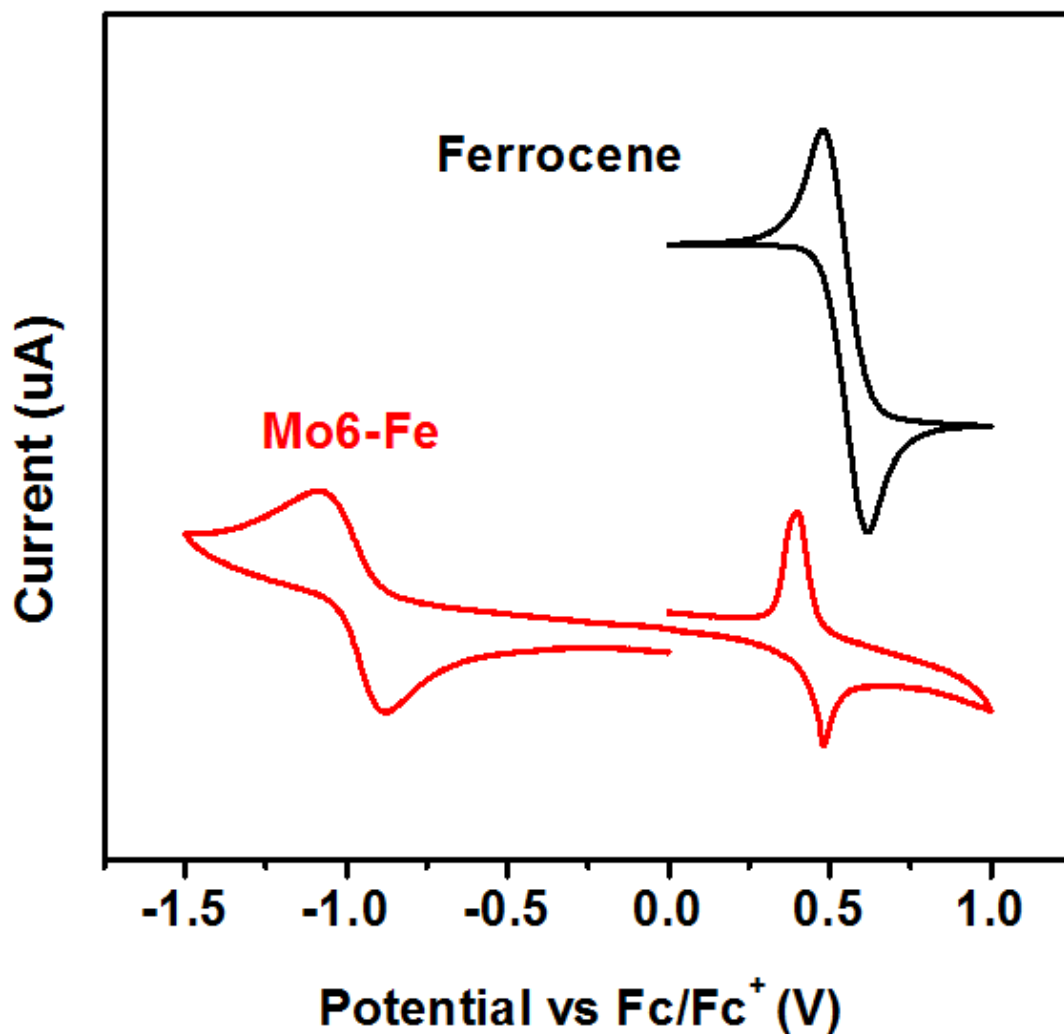


Figure 2-6 Cyclic voltammograms of **Mo6-Fe** in acetonitrile solution.

Figure 2-7 shows UV-vis absorption spectra of **Mo6-Fe** and **Mo6-Fe/PC<sub>61</sub>BM** in solution and in film on ITO substrates. In solution, **Mo6-Fe** shows a major absorption band at 384 nm, while the blend solution shows a major absorption at 330 nm with a shoulder at ~384 nm. The band at 330 nm may be assigned to the sum of both POM and PC<sub>61</sub>BM. Compared to its solution spectrum, the absorption spectrum of the **Mo6-Fe** film shows

again a maximum absorption wavelength around 384 nm but also a much broader absorption hump extending from 450 nm to beyond 650 nm. The prominent absorption hump in the spectrum of **Mo6-Fe** film may be caused by the stronger inter- and intramolecular charge transfer between clusters and ferrocenes. The absorption spectrum of the composite film shows one main peak at 350 nm, a shoulder around 400 nm and a tail extending beyond 600 nm, which indicates a close interaction among hybrid molecules in the blend film as compared to those in blend solution.<sup>85</sup> However, this interaction is weaker in the blend film than that in the pure **Mo6-Fe** film. After thermal treatment, the absorption spectrum of the blend film shows an enhanced tail from 450 nm to beyond 600 nm, which may be a result of the rearrangement of hybrid molecules and the PCBM, leading to enhanced interaction among hybrid molecules.

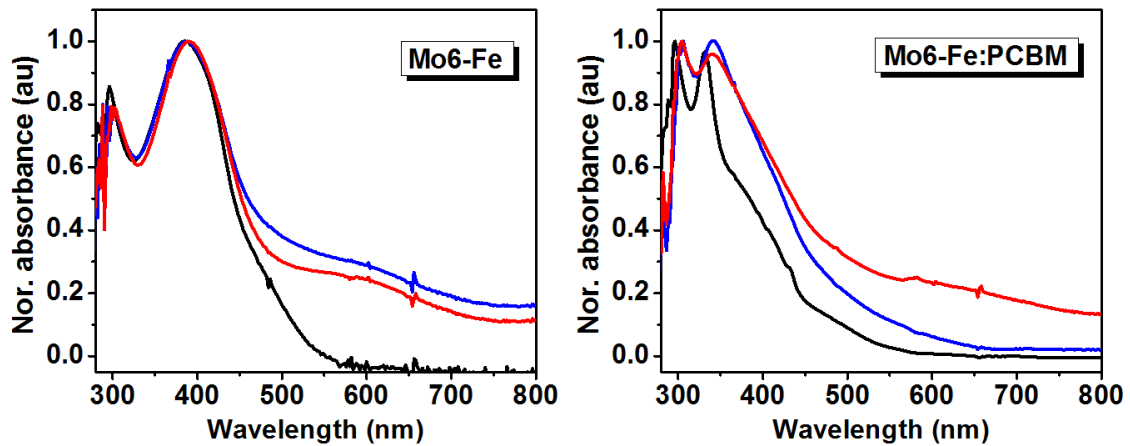


Figure 2-7 UV-vis absorption spectra of **Mo6-Fe** (right) and **Mo6-Fe/PC<sub>61</sub>BM** (1:1 wt. ratio, left) in *o*-dichlorobenzene solutions (black) and films before (blue) and after (red) thermal annealing.

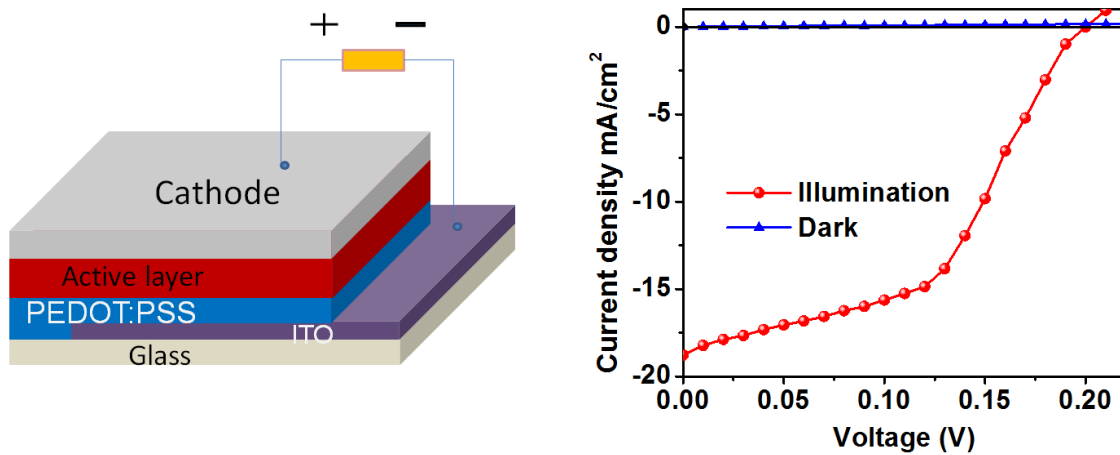


Figure 2-8 Device architecture (left) and  $J$ - $V$  curve (right, blue triangle: in dark; red ball: under illuminated) of the photovoltaic devices of ITO/PEDOT:PSS/**Mo6-Fe**:PCBM/Ca/Al with post thermal annealing treatment under 1-sun air mass 1.5 global illumination.

PV devices were fabricated in a device configuration of ITO/PEDOT:PSS/**Mo6-Fe** or **Mo6-Fe**:PC<sub>61</sub>BM (1:1 wt. ratio)/Ca/Al. The active layer was spin-coated at 600 rpm from **Mo6-Fe** or **Mo6-Fe**/PC<sub>61</sub>BM *o*-dichlorobenzene solution (with **Mo6-Fe** concentration of 10 mg mL<sup>-1</sup>) onto PEDOT:PSS coated ITO substrates. Thermal annealing either before or after deposition of the top metal electrodes was performed at 140 °C for ten minutes.

Figure 2-8 shows the architecture and *J-V* characteristics of a PV devices based on **Mo6-Fe**/PC<sub>61</sub>BM composites. Before thermal annealing, all devices showed very poor performance. The power conversion efficiency is in the order of 10<sup>-6</sup> % for pristine films and 10<sup>-4</sup> % for blended films before post annealing. After post annealing, the **Mo6-Fe** based devices show no dramatic improvement. However, the performance of PV devices based on **Mo6-Fe**/PC<sub>61</sub>BM composites was drastically improved with an efficiency as high as 1.8%. As shown in Figure 2-8, the device shows a *V<sub>OC</sub>* of 0.2 V, a *J<sub>SC</sub>* of 18.77 mA/cm<sup>2</sup>, and a fill factor of 0.48. It should be noted that all device evaluations were done under ambient conditions where cells deteriorated rather quickly.

#### 2.4 Dendrimer-PDI charge transfer molecule

Donor-acceptor charge transfer molecules combining dendritic triphenyleneacetylenes (TPA)-based donor and a perylenediimide (PDI) acceptor were also studied. The structures of such system are shown in Figure 2-10. While the dendritic  $\pi$ -system extended its conjugation to PDI in **G0-PDI** and **G1-PDI**, the donor and the acceptor are linked through a non-conjugated ether bond for **G1-O-PDI**. Both PDI and TPA have a

strong tendency for aggregation which may drive the formation of columnar aggregates with PDI cores surrounded by TPA dendrons as shown in Figure 2-9.<sup>86,87</sup>

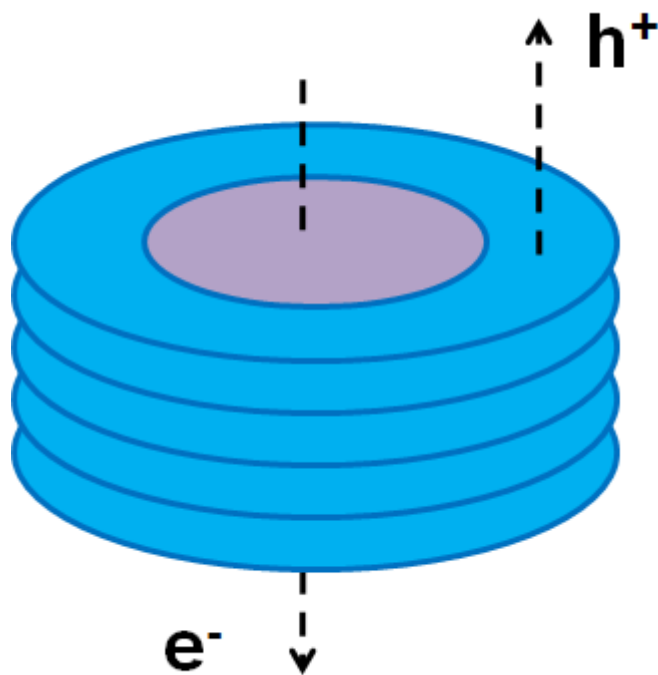


Figure 2-9 Hypothetic module of molecule stacking in **G0-PDI**, **G1-PDI** and **G1-O-PDI** (center grey core: PDI cores; outside blue circles: TPA dendrons).

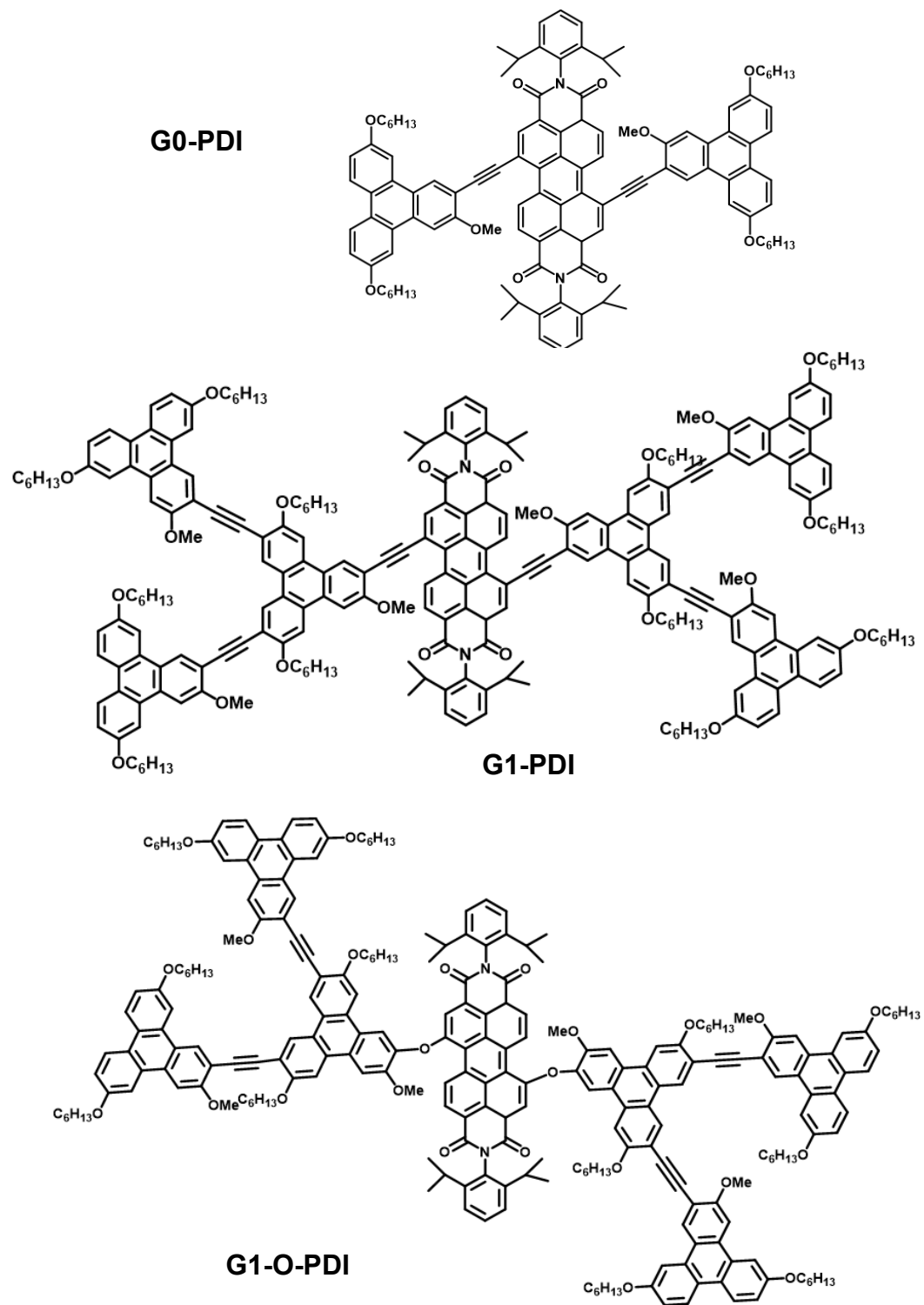


Figure 2-10 Molecule structures of **G0-PDI**, **G1-PDI** and **G1-O-PDI**.

Electrochemical properties were investigated as thin film via cyclic voltammetry measurements as shown in Figure 2-11. All three molecules show an irreversible reduction process in cathodic scan with an onset of  $\sim -2.4$  V and two semi-reversible or irreversible oxidation processes in anodic scan with an onset of  $\sim 0.6$  V, which is corresponding to the reduction and oxidation process of TPA dendrons. The HOMO/LUMO energy levels for

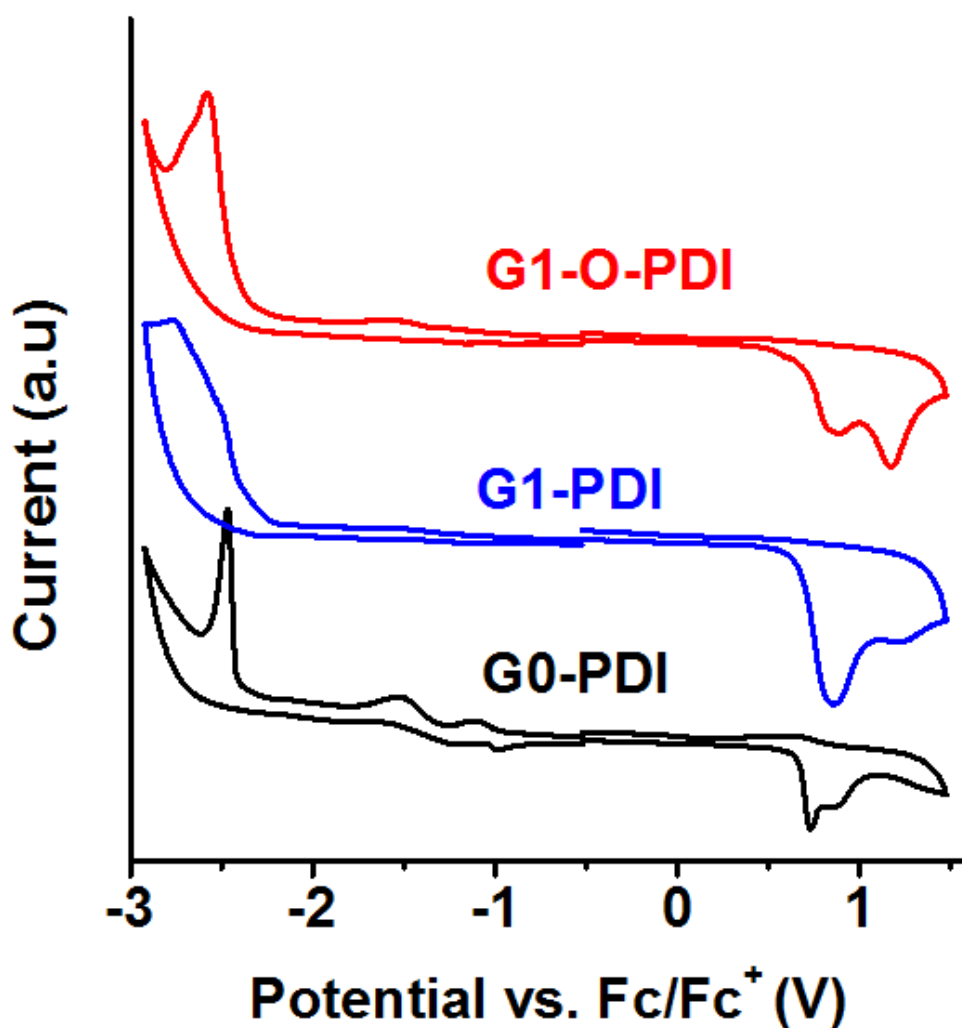


Figure 2-11 Cyclic voltammograms of G0-PDI, G1-PDI and G1-O-PDI thin films.

the TPA dendrons of **G0-PDI**, **G1-PDI** and **G1-O-PDI** are thus calculated to be -5.45/-2.39 eV, -5.35/-2.42 eV and -5.48/-2.38 eV, respectively. The bandgaps of the TPA dendrons are calculated to be 3.06 eV, 2.93 eV and 3.10 eV. There are two clear semi-reversible reduction waves in the cathodic scan with an onset of -0.98 V for **G0-PDI**. This reduction process can be assigned to the reduction of the PDI core.<sup>86</sup> This reduction wave can also be observed in **G1-PDI** and **G1-O-PDI**, but is not as clear as in **G0-PDI**. The LUMO level of the PDI core calculated from the onset of -0.98 V is -3.82 eV. The LUMO levels of the PDI core and the TPA dendrons differ by about 1.42 eV. According to Marcus theory, photoinduced charge transfer from TPA dendrons to the PDI core is thermodynamically favored.<sup>88-90</sup>

Devices with **G0-PDI**, **G1-PDI** and **G1-O-PDI** as active layer were fabricated with the device configuration of ITO/PEDOT:PSS/ **G0-PDI** or **G1-PDI** or **G1-O-PDI** /Ca/Al. Active layers were spin-coated from their chloroform solution with a concentration at 10 mg mL<sup>-1</sup> at a spin rate of 450 rpm for 30 s, followed by thermal evaporation of 25 nm Ca and 100 nm Al. Figure 2-12 (a-c) show the UV-vis spectra of the resulting films before or after thermal treatment at 120 °C for 10 min. **G0-PDI** shows two peaks at 378 nm and 410 nm, while **G1-PDI** and **G1-O-PDI** show a peak with a shoulder at 382/402 nm and 370/402 nm which are attributed to the TPA dendrons. A broad peak at ~550 nm is observed for all pristine films, which is attributed to the PDI core.<sup>86,87</sup> The optical bandgaps calculated from the unannealed films are 2.87 eV, 2.68 eV and 2.88 eV for **G0-PDI**, **G1-PDI** and **G1-O-PDI**, respectively. However, the absorbance values for all the films are very low (< 0.5) due to the limited solubility of the materials.

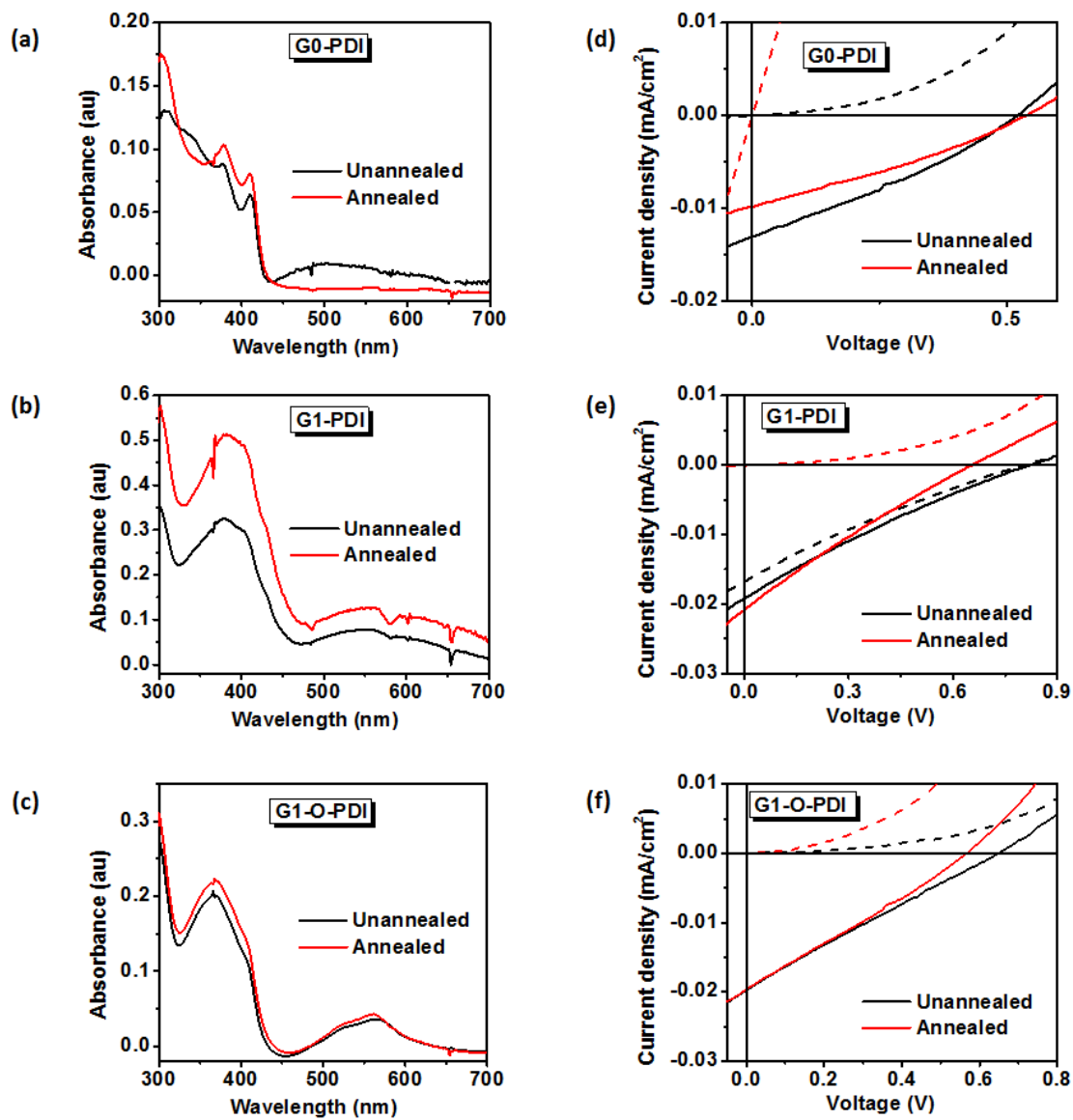


Figure 2-12 (a-c) UV-vis absorption spectra and (d-f)  $J-V$  curves (dash lines: in dark; solid lines: under illumination) of the devices based on **G0-PDI**, **G1-PDI** and **G1-O-PDI** before (black) and after thermal annealing (red).

The  $J$ - $V$  curves of the devices are shown in Figure 2-12 (d-f) and the parameters are summarized in Table 2-1. Even though they all show a good  $V_{OC}$  in the range of 0.5–0.9 V, the  $J_{SC}$  and fill factor are both rather low, leading to poor power conversion efficiencies. The following factors likely contribute to the poor device performance: 1) the low absorbance of the active layer;<sup>53</sup> 2) the inability of the PDI core to co-facial stack, leading to poor electron transport;<sup>86,87</sup> 3) the lack of control in phase-separated morphologies.<sup>82</sup> Thermally annealing did not improve device performance.

Table 2-1 Parameters of the photovoltaic cells under 1-sun air mass 1.5 global illumination

Compounds		$V_{OC}$ (V)	$J_{SC}$ (mA cm <sup>-2</sup> )	$FF$	$\eta$ (%)
<b>G0-PDI</b>	Unannealed <sup>a</sup>	0.52	0.013	0.31	0.0021
	Annealed <sup>a,b</sup>	0.54	0.010	0.30	0.0016
<b>G1-PDI</b>	Unannealed <sup>a</sup>	0.82	0.019	0.22	0.0035
	Annealed <sup>a,b</sup>	0.65	0.021	0.23	0.0031
<b>G1-O-PDI</b>	Unannealed <sup>a</sup>	0.67	0.020	0.23	0.0031
	Annealed <sup>a,b</sup>	0.55	0.020	0.27	0.0030

<sup>a</sup> Films are spin-coated from chloroform solutions at the spin speed of 450 rpm and dried in air. <sup>b</sup> Annealed films are heated at 120 °C for 10 min in glove box.

## 2.5 POM-containing rod-coil diblock copolymers

As mentioned in Chapter 1, morphology plays a critical role in achieving high device performance. In this regard, block copolymers are appealing because they can form various phase-separated morphologies. Rod-coil diblock copolymers are consisted of a conjugated rod block and a flexible coil block. The rod-blocks can align along their long axes showing liquid crystalline-like behavior and facilitate the formation of thermodynamically stable nano-scaled morphologies.<sup>91</sup> The self-assembly of rod-coil diblock copolymers is dominated by interaction between rod blocks, the ratio between the radius of gyration of the coil block and the length of the rod block, the interaction between the rod and coil blocks.<sup>42,46,57,92,93</sup> By tuning these parameters, it is possible to achieve phase domains that are desirable for PV devices. For example, phase separation has been observed in a rod-coil diblock copolymer with MEH-PPV rod block and a fullerene-attached polystyrene as the coil block.<sup>94</sup> A noticeable phase segregation has also been observed in diblock copolymers composed of a P3HT rod block and a fullerene pended coil block.<sup>42</sup>

In this study, POM clusters are introduced into the coil block as side chain pendants while the rod block is P3HT. Polythiophene is used as the rod block because it is the most studied polymer system for solar cells and strong  $\pi$ - $\pi$  stacking between P3HT block may help in stabilizing the morphology of the copolymer films.<sup>42</sup> With  $\pi$ - $\pi$  stacking interaction among the rod blocks and the aggregation of POM clusters in the coil block, phase separation forming POM rich domains and  $\pi$ -stacking conjugated domains is expected. P3HTs with three different lengths were studied for the purpose of achieving proper phase-separated domain sizes.

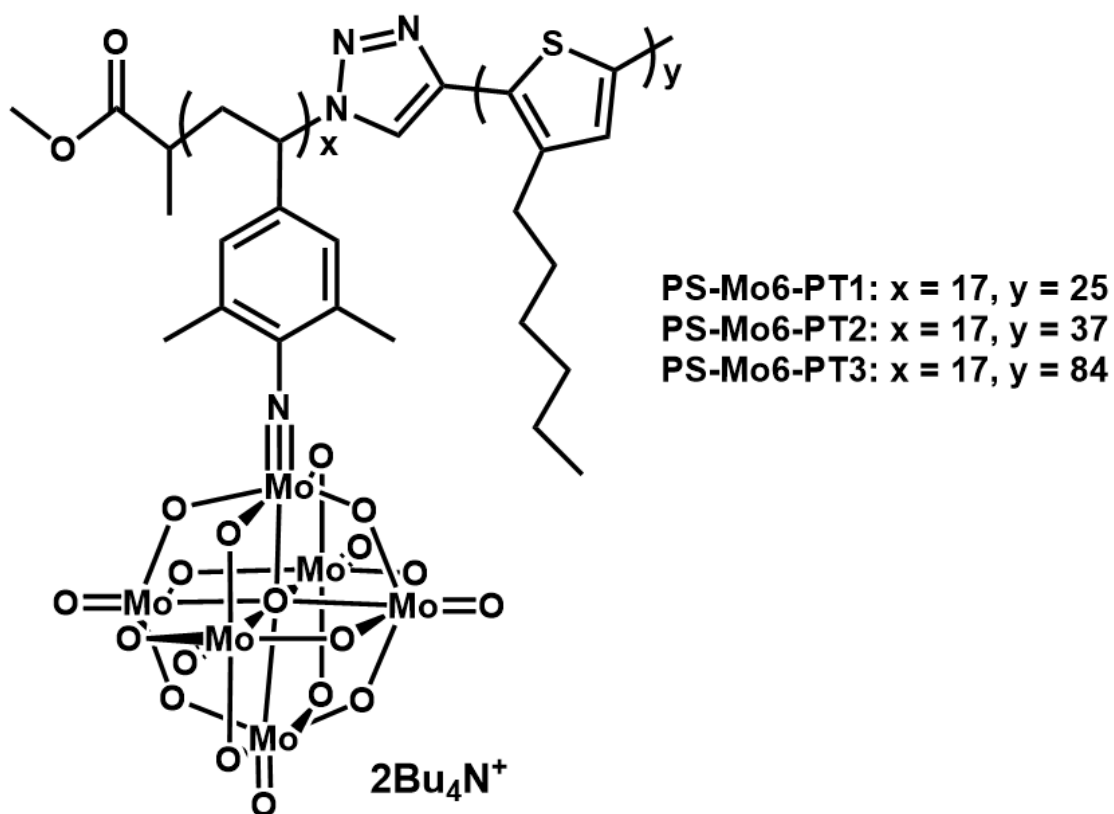


Figure 2-13 Molecule structures of **PS-Mo6-PT1-3**.

Figure 2-13 shows the structure of the three hybrid diblock copolymers. Their synthesis and structural characterizations have been previously reported.<sup>84</sup> The sizes of the coil and the P3HT rod blocks ( $x$  and  $y$  in Figure 2-13) were obtained from MALDI-TOF mass spectrometry measurements.<sup>84</sup> The amount of POM cluster attachment was estimated based on elemental analysis.<sup>84</sup> Among the three hybrid diblock copolymers, **PS-Mo6-PT1** has the shortest rod block **PT1** (25 repeat units) and the highest POM concentration (17

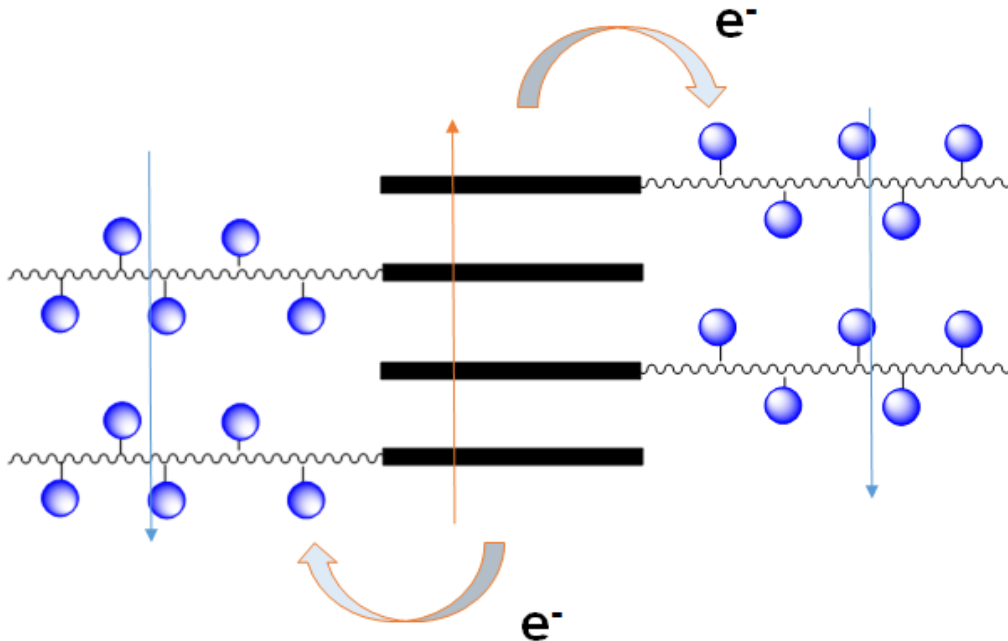


Figure 2-14 Hypothetic module of polymer stacking and charge transfer process in **PS-Mo6-PT1-3**

clusters per chain). **PS-Mo6-PT2** has the medium length of rod block **PT2** (37 repeat units) with an average POM loading of 14 clusters per chain, while **PS-Mo6-PT3** contains the longest rod block **PT3** (84 repeat units) and the lowest POM concentration (2 clusters per chain).<sup>84</sup> Our previous topographical AFM studies of the **PS-Mo6-PT1-3** films revealed a distinct morphological transformation from a nanofibrillar structure to a nanogranular one upon thermal annealing.<sup>83,84</sup> The phase separation after thermal annealing is further confirmed by CS-AFM studies. While the pristine films show only sporadic isolated conducting domains, the film after thermal annealing shows widespread worm-like conducting networks, which are more suitable for photovoltaic applications.<sup>83,84</sup> For

comparison purpose, rod blocks **PT1-3** and diblock copolymers without clusters attached **PS-PT1-3** were also studied in this research.

### 2.5.1 Electrochemistry study

To validate the feasibility of charge transfer between the P3HT block and the POM clusters, the redox properties of both **PT1-3** and **PS-Mo6-PT1-3** were investigated as thin films using CV measurements. As shown in Figure 2-15, the cyclic voltammogram of **PS-Mo6-PT1** shows clearly two reduction processes in the range of -1.2 to -2.0 V which do not exist in that of **PT1**. The reduction process with onset of  $\sim -1.32$  V is attributed to the imido-POM clusters which is cathodically shifted compared to that of free [Mo6].<sup>81</sup> This result is consistent with our previous observations in other hybrid diblock copolymers (HDCP) containing the same imido-POM clusters.<sup>81</sup> It is worth noting that this reduction process in **PS-Mo6-PT2** and **PS-Mo6-PT3** is not as prominent as in **PS-Mo6-PT1** because of their decreased POM content. Both **PT1-3** and **PS-Mo6-PT1-3** show a semi-reversible reduction process with onset of  $\sim -2.13$  V and strongly overlapping oxidation waves with onset of  $\sim 0.31$  V, which are due to the reduction and oxidation of the P3HT block.<sup>95</sup> The LUMO energy levels of the P3HT block and the imido-POM were calculated to be  $\sim -2.67$  eV and  $\sim -3.48$  eV, respectively. In other words, the LUMO of the imido-functionalized POM is 0.81 eV lower than that of P3HT. The HOMO energy level and bandgap of the P3HT block are determined to be  $\sim -5.11$  eV and  $\sim 2.44$  eV, respectively. The optical bandgap of POM was calculated to be  $\sim 3.00$  eV by

$$E_g^{opt} = 1240/\lambda_{onset}^{abs} \quad (2-1)$$

where  $\lambda_{onset}^{abs}$  is the UV-visible absorption onset of POM ( $\sim 414$  nm). The HOMO energy level of imido-POM was therefore estimated to be  $\sim -6.48$  eV by

$$HOMO = LUMO - E_g^{opt} \quad (2-2)$$

The driving forces for the charge transfer between the P3HT moiety and the imido-POM moiety can be estimated by the Rehm–Weller equation,<sup>55,88–90</sup>

$$\Delta G = e[E_{ox}(D) - E_{red}(A)] - E_g - C \quad (2-3)$$

where  $\Delta G$  is the free energy change (in eV) associated with the photoinduced charge transfer process,  $E_{ox}(D)$  and  $E_{red}(A)$  are the oxidation potential of the donor (P3HT) and the reduction potential of the acceptor (imido-POM), respectively,  $E_g$  is the bandgap of the donor or acceptor, and  $C$  is the Coulomb term which is about 0.06 eV in acetonitrile.<sup>55,88</sup> According to the Rehm–Weller equation, the free energy changes for the electron transfer process from the excited P3HT moiety to the LUMO of the imido-POM moiety and for the hole transfer process from the excited imido-POM moiety to the HOMO of the P3HT moiety are -0.87 eV and -1.43 eV, respectively. Therefore, the charge transfer at the P3HT/imido-POM interface is thermodynamically feasible.

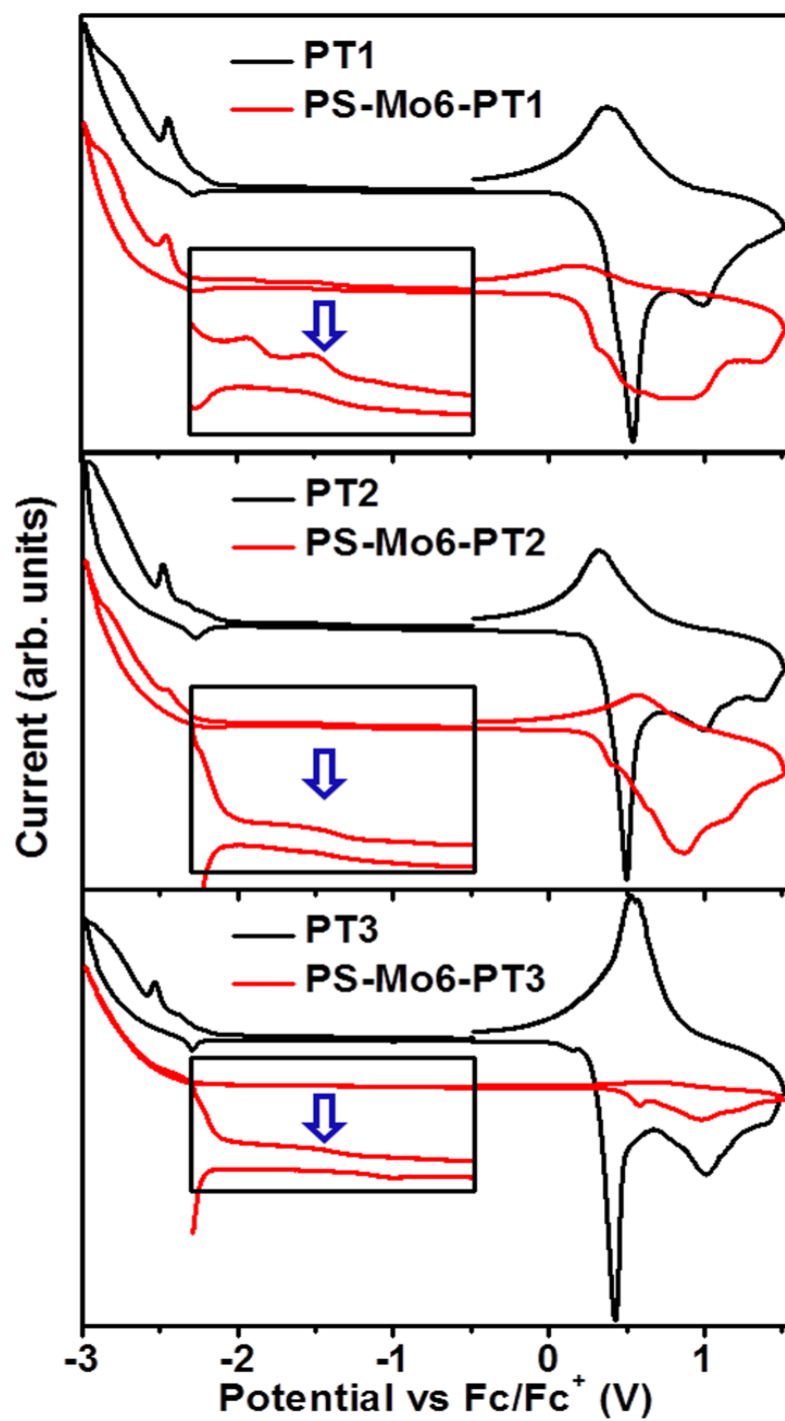


Figure 2-15 Cyclic voltammograms of PS-PT1-3 and PS-Mo6-PT1-3 in films.

### 2.5.2 Photovoltaic devices

Among the three hybrid diblock copolymers, **PS-Mo6-PT2** is most interesting because of an intermediate rod block length and a relatively high cluster loading ratio. Devices of **PS-PT2** and **PS-Mo6-PT2** with or without blending with PC<sub>61</sub>BM were studied in the configuration of ITO/PEDOT:PSS/Active layer/Ca/Al. The active layers were deposited by spin coating from the respective chloroform solutions (2 mg mL<sup>-1</sup>) on top of the PEDOT:PSS layer at 200 rpm for 60 s. Half of the devices were thermally annealed at 120 °C for 10 min. A top electrode including 25 nm thick Ca and 100 nm thick Al was sequentially deposited by thermal evaporation. For comparison, device based on **PT1**/PC<sub>61</sub>BM blends were also fabricated.

Optical properties were investigated for **PS-PT2** and **PS-Mo6-PT2** in solution and as thin films on ITO substrates as shown in Figure 2-16. In solution, both **PS-PT2** and **PS-Mo6-PT2** show one broad absorption band at ~ 450 nm. Careful comparison shows that **PS-Mo6-PT2** gives stronger absorption in the short wavelength side (300-450 nm), likely due to the ligand-to-metal charge-transfer transition (LMCT) of the covalent bonded imido-POM clusters. The film absorption spectra of **PS-PT2** and **PS-Mo6-PT2** show more drastic difference. While both spectra show a red-shifted absorption band at ~550 nm and a shoulder band at ~600 nm, only **PS-Mo6-PT2** shows two additional well defined absorption bands at 330 nm and 410 nm. The red-shifted long wavelength absorption is attributed to the  $\pi$ -stacked P3HT segments, while the absorption band at 410 nm corresponds mainly to LMCT of imido-functionalized POM clusters.<sup>84</sup> When blended with PC<sub>61</sub>BM, the solution spectra of both **PS-PT2** and **PS-Mo6-PT2** show a new peak at ~330 nm which is attributed to the absorption of PC<sub>61</sub>BM.

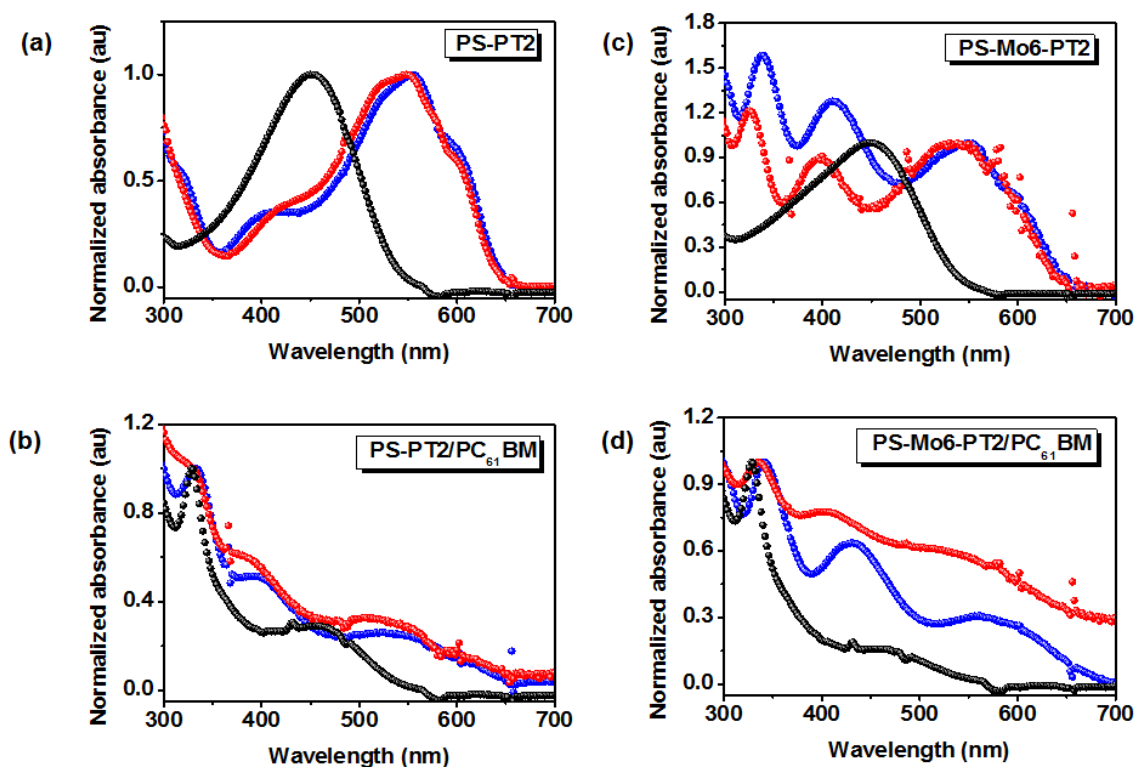


Figure 2-16 UV-vis absorption spectra of (a) **PS-PT2**, (b) **PS-PT2/PC<sub>61</sub>BM**, (c) **PS-Mo6-PT2** and (d) **PS-Mo6-PT2/PC<sub>61</sub>BM** in solutions (black) and in films (blue: unannealed film; red: annealed film).

For pristine films, **PS-PT2** shows a peak at 550 nm with a shoulder at 600 nm, while **PS-Mo6-PT2** shows three well defined bands at 338 nm, 410 nm and 550 nm with a shoulder at 600 nm. After thermal annealing, all absorption bands are blue-shifted. For **PS-PT2**, the blue-shift is only a few nanometer ( $\sim 6$  nm). For the hybrid system, the blue shift is more significant ( $\sim 20$  nm). For the blending films, the blue shift is even more prominent ( $\sim 50$  nm) for thermally annealing. The blue shift may be due to the formation of H-aggregates of the P3HT block or it may be caused by the slight backbone twisting of the P3HT block due to POM cluster aggregation.<sup>96</sup>

Figure 2-17 through 2-19 show  $J$ - $V$  characteristics of resulting devices before or after thermal annealing at 120 °C . The parameters of  $V_{OC}$ ,  $J_{SC}$ , fill factor ( $FF$ ) and efficiency ( $\eta$ ) are summarized in Table 2-2. For **PT1**/ $PC_{61}BM$ , only annealed film were studied. **PT1**/ $PC_{61}BM$  solar cells show a power conversion efficiency of 0.593% with a  $V_{OC}$  of 0.46 V, a  $J_{SC}$  of 4.32 mA/cm<sup>2</sup> and a  $FF$  of 31%. **PT1**, consisted of only ~ 25 repeat thiophene units, has a much lower molecule weight than commercially purchased P3HT, which may account for its inferior performance.<sup>95</sup>

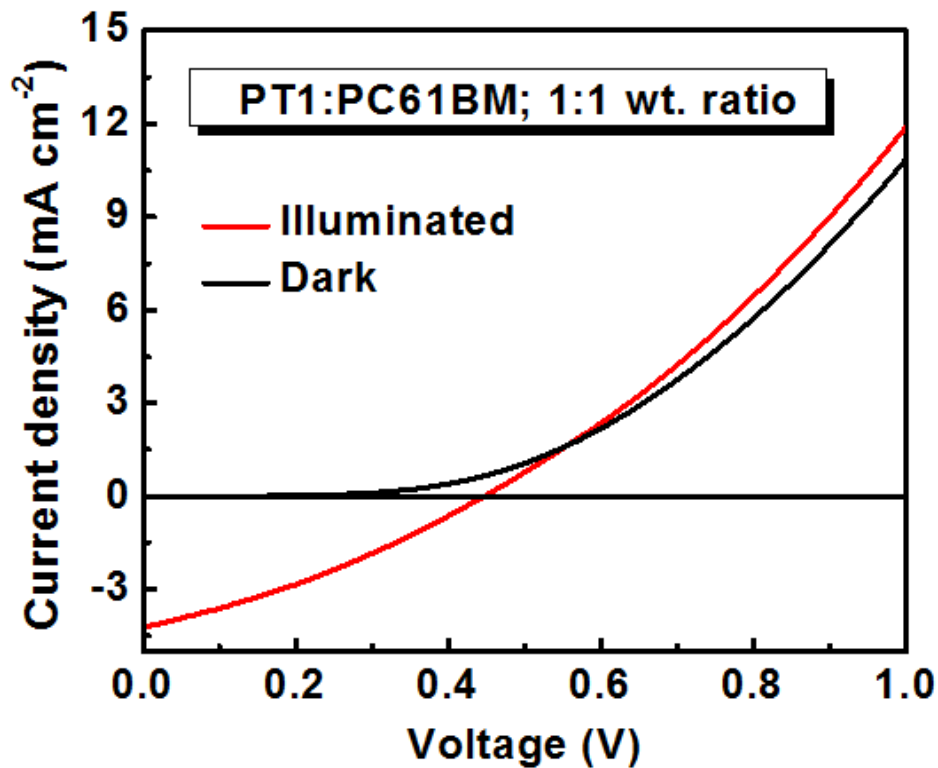


Figure 2-17  $J$ - $V$  curve of device fabricated from **PT1**/ $PC_{61}BM$  solution after thermally annealed, under 1-sun air mass 1.5 global illumination and in dark.

For **PS-PT2**, as shown in Figure 2-18, devices without thermal annealing, a  $\sim 0.01\%$  efficiency is achieved with a  $V_{OC}$  of 0.37 V, a  $J_{SC}$  of 0.083 mA/cm<sup>2</sup> and a  $FF$  of 32%. After thermally annealing, the device performance is even poorer. When **PS-PT2** was blended with PC<sub>61</sub>BM, in the device efficiency was improved to 0.12%, mainly due to the enhanced  $J_{SC}$ .

Devices based on **PS-Mo6-PT2** showed very high  $V_{OC}$  of 1.25 V but dismal  $J_{SC}$  of only 0.0062 mA/cm<sup>2</sup> and low  $FF$  of 17%. As seen in Figure 2-19, annealing improves the photocurrent by one order of magnitude and also the fill factor, presumably due to the formation of desired phase-separated domains. The overall photocurrent is however still very low, likely due to the poor photo-induced charge transfer from the PT backbone to the POM cluster. Adding PC<sub>61</sub>BM into the hybrid system again only slightly improves the device performance.

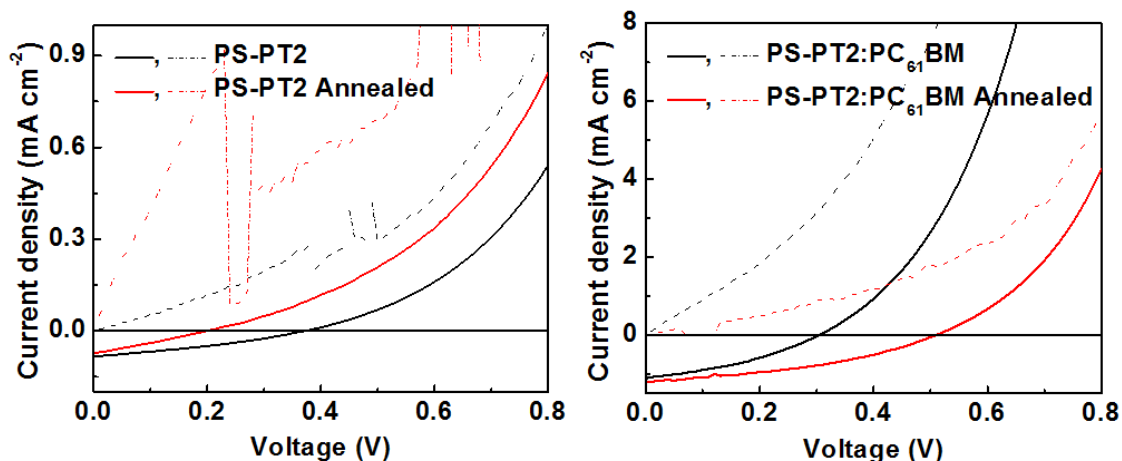


Figure 2-18  $J$ - $V$  curve of the device based on **PS-PT2** (left) and **PS-PT2/PC<sub>61</sub>BM** (right) before (black) or after (red) thermal annealed at 120 °C for 10 min, under 1-sun air mass 1.5 global illumination (solid lines) and in dark (dash lines).

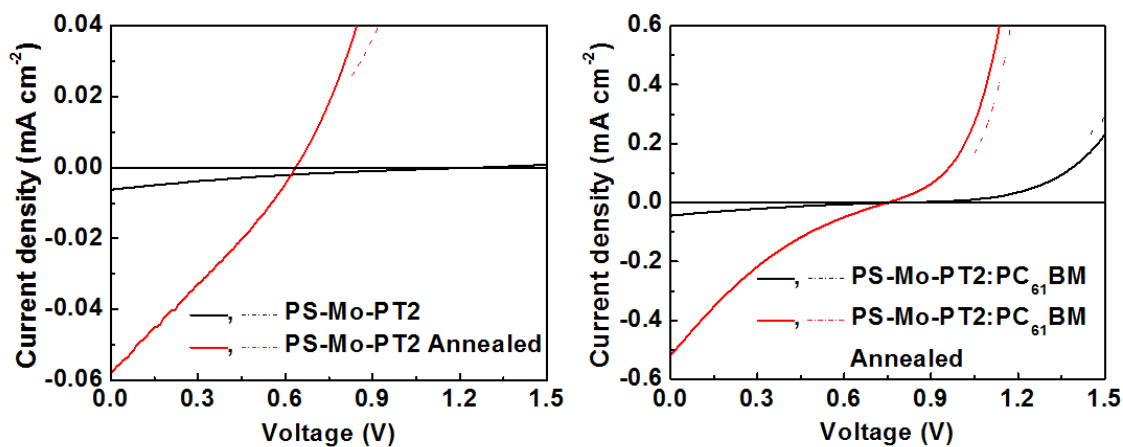


Figure 2-19  $J$ - $V$  curve of the device based on **PS-Mo6-PT2** (left) and **PS-Mo6-PT2/PC<sub>61</sub>BM** (right) before (black) or after (red) thermal annealed at 120 °C for 10 min, under 1-sun air mass 1.5 global illumination (solid lines) and in dark (dash lines).

Table 2-2 Parameters of the photovoltaic cells under 1-sun air mass 1.5 global illumination.

Active Materials		<i>I-V</i> Parameters			
		$V_{oc}$ (V)	$J_{sc}$ (mA cm <sup>-2</sup> )	FF	PCE (%)
<b>PT1:PC<sub>61</sub>BM</b>	Annealed <sup>a,b</sup>	0.45	4.23	0.311	0.593
<b>PS-PT2</b>	Unannealed <sup>a</sup>	0.37	0.0827	0.324	0.0099
	Annealed <sup>a,b</sup>	0.20	0.072	0.274	0.0039
<b>PS-PT2:</b>	Unannealed <sup>a</sup>	0.30	1.106	0.367	0.122
<b>PC<sub>61</sub>BM</b>	Annealed <sup>a,b</sup>	0.51	1.200	0.387	0.237
<b>PS-Mo6-PT2</b>	Unannealed <sup>a</sup>	1.248	0.00621	0.168	0.0013
	Annealed <sup>a,b</sup>	0.63	0.058	0.278	0.0102
<b>PS-Mo6-PT2:</b>	Unannealed <sup>a</sup>	0.797	0.0438	0.181	0.0063
<b>PC<sub>61</sub>BM</b>	Annealed <sup>a,b</sup>	0.75	0.517	0.166	0.0645

<sup>a</sup> Films are spin-coated from respective chloroform solutions and dried in air.

<sup>b</sup> Annealed films are heated at 120 °C for 10 min in glove box.

### 2.5.3 Steady fluorescence

Figure 2-20 shows the steady-state emission and excitation spectra of **PS-Mo6-PT1-3** in anhydrous  $\text{CHCl}_3$  ( $0.5 \text{ mg mL}^{-1}$  concentration). Under the excitation of 400 nm, all three hybrid diblock copolymers (HDCPs) show an emission maximum at  $\sim 575 \text{ nm}$ . A shoulder at 620 nm is discernible for **PS-Mo6-PT2**, which can be attributed to aggregation-enhanced excimer emission.<sup>97,98</sup> It is known that the intensity of excimer emission can be enhanced by both inter- and intramolecular aggregation.<sup>99</sup> The excimer emission of **PS-Mo6-PT3** is more prominent than that of **PS-Mo6-PT2**, indicating stronger propensity for excimer formation between higher molecular weight P3HT blocks. The excitation spectra, whether measured at the emission wavelength of 580 nm (black curves) or 620 nm (blue curves), exhibit one broad peak and generally resemble the absorption spectra of the P3HT block. The band from the ligand-to-metal charge transfer transition associated with imido-POM cluster was not observed in the excitation spectra,<sup>84</sup> indicating the absence of energy transfer from the excited clusters to the P3HT block in these HDCPs.

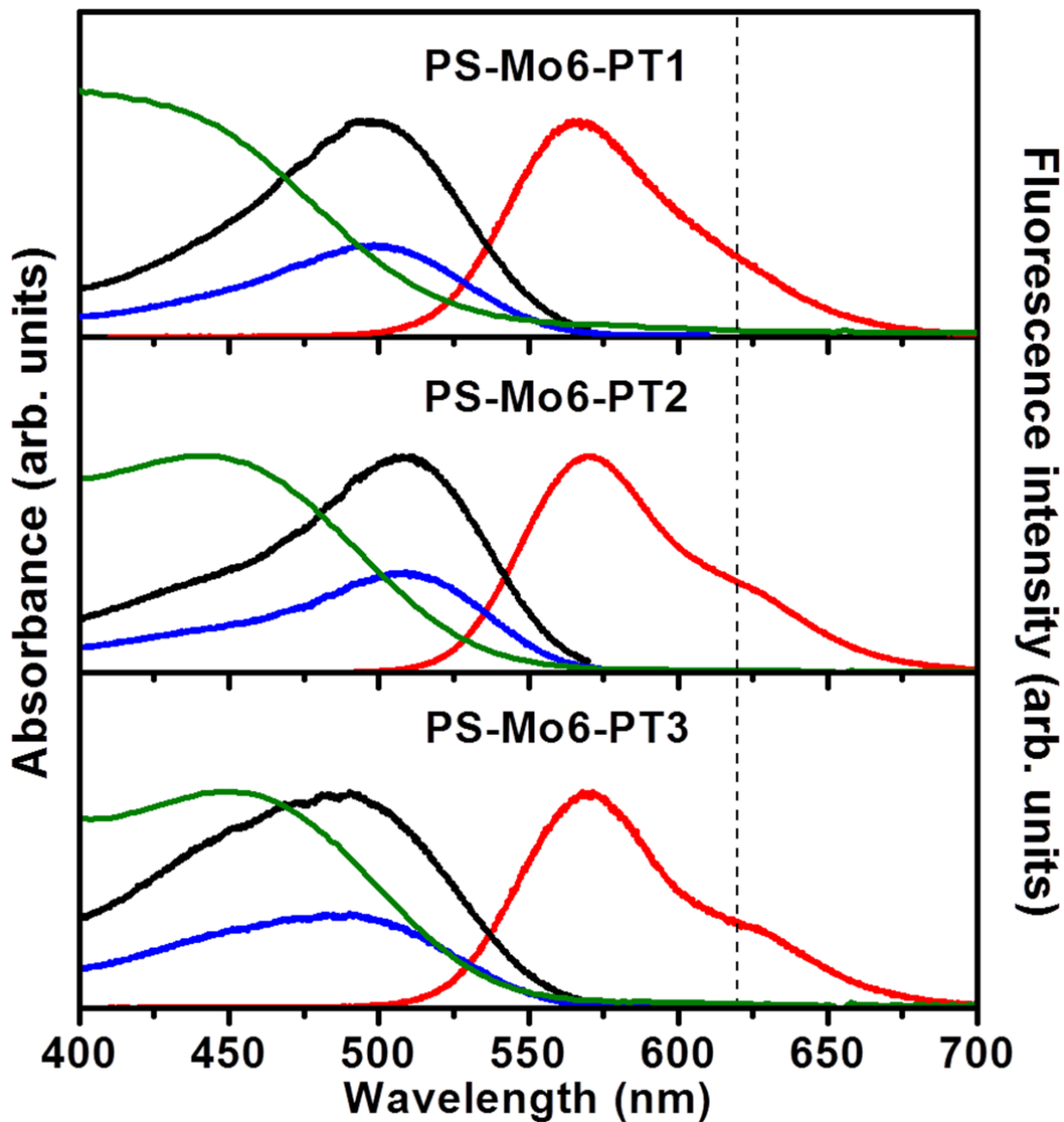


Figure 2-20 Absorption (olive lines) and emission spectra (red lines) with excitation wavelength at 400 nm and excitation spectra with emission wavelengths at 580 nm (black lines) and 620 nm (blue lines) of **PS-Mo6-PT1-3** solutions ( $0.5 \text{ mg mL}^{-1}$  concentration) in  $\text{CHCl}_3$ . The vertical black dashed line serves as an eye-guiding line through the data points at 620 nm.

#### 2.5.4 Dynamic fluorescence study

The fluorescence decay dynamics of the **PS-Mo6-PT1-3** solutions ( $\sim 0.5 \text{ mg mL}^{-1}$  in  $\text{CHCl}_3$ ) were studied at the emission wavelength of 580 nm or at the shoulder peak of 620 nm upon excitation at 400 nm ( $\sim 3.1 \text{ eV}$ ). Each trace was fitted to a sum of two exponentials using a convolute-and-compare algorithm which took into account the instrument response function. The resulting fitting parameters are shown in Figure 2-21 summarized in Table 2-3. The fluorescence dynamics are quite different for the three HDCPs, and are also dependent on the detection (emission) wavelengths. For **PS-Mo6-PT1**, the fluorescence dynamics at both detection wavelengths shows an initial ultrafast decay component with sub-picosecond time constants and a slower decay process with time constants around 10 ps. It is known that under the low power photoexcitation, the excited state of P3HT may undergo self-trapping (dynamic localization), vibrational relaxation, energetically downhill excitation energy transfer (EET), torsional relaxation, and intra- or interchain EET between segments with comparable energy.<sup>70,100</sup> The first two processes (self-trapping and vibrational relaxation) often occur in a time scale of  $\sim 100 \text{ fs}$  or lower,<sup>100–104</sup> and thus cannot be directly observed because they are much shorter than the instrument response function ( $\sim 255 \text{ fs}$ ) of the setup.<sup>100</sup> The fast decay component of **PS-Mo6-PT1** can be assigned to the energetically downhill EET, i.e., the relaxation of excitons from higher-energy localized sites to lower energy conjugated segments. EET with a downhill gradient typically occurs in a time scale from sub-picosecond to  $\sim 1 \text{ ps}$  in conjugated polymers/oligomers.<sup>104–106</sup> The slower component ( $\sim 10 \text{ ps}$ ) can be assigned to the EET between segments with comparable energy, which is known to occur in a time scale of tens of picoseconds.<sup>100,105–107</sup> The time constants for both processes vary little with the probing

wavelength, indicating that there is insignificant P3HT-P3HT aggregation (intra or inter) in the  $\sim 0.5 \text{ mg mL}^{-1}$  **PS-Mo6-PT1** solution.

Table 2-3 Biexponential fitting parameters for the fluorescence dynamics of the **PS-Mo6-PT1-3** solutions ( $\sim 0.5 \text{ mg mL}^{-1}$ ) in  $\text{CHCl}_3$  with excitation of 400 nm.

HDCP	Emission (nm)	$\tau_1$ (fs)	$A_1$ (%)	$\tau_2$ (ps)	$A_2$ (%)	$\tau_3$ (ps)	$A_3$ (%)
<b>PS-Mo6-PT1</b>	580	692	37.5	11	62.5	–	–
	620	804	51.4	8.5	48.6	–	–
<b>PS-Mo6-PT2</b>	580	$40 \pm 20$	-15.5	–	–	34	84.5
	620	153	-56.6	–	–	33	43.4
<b>PS-Mo6-PT3</b>	580	–	–	6.3	40.0	67	60.0
	620	–	–	–	–	496	100.0

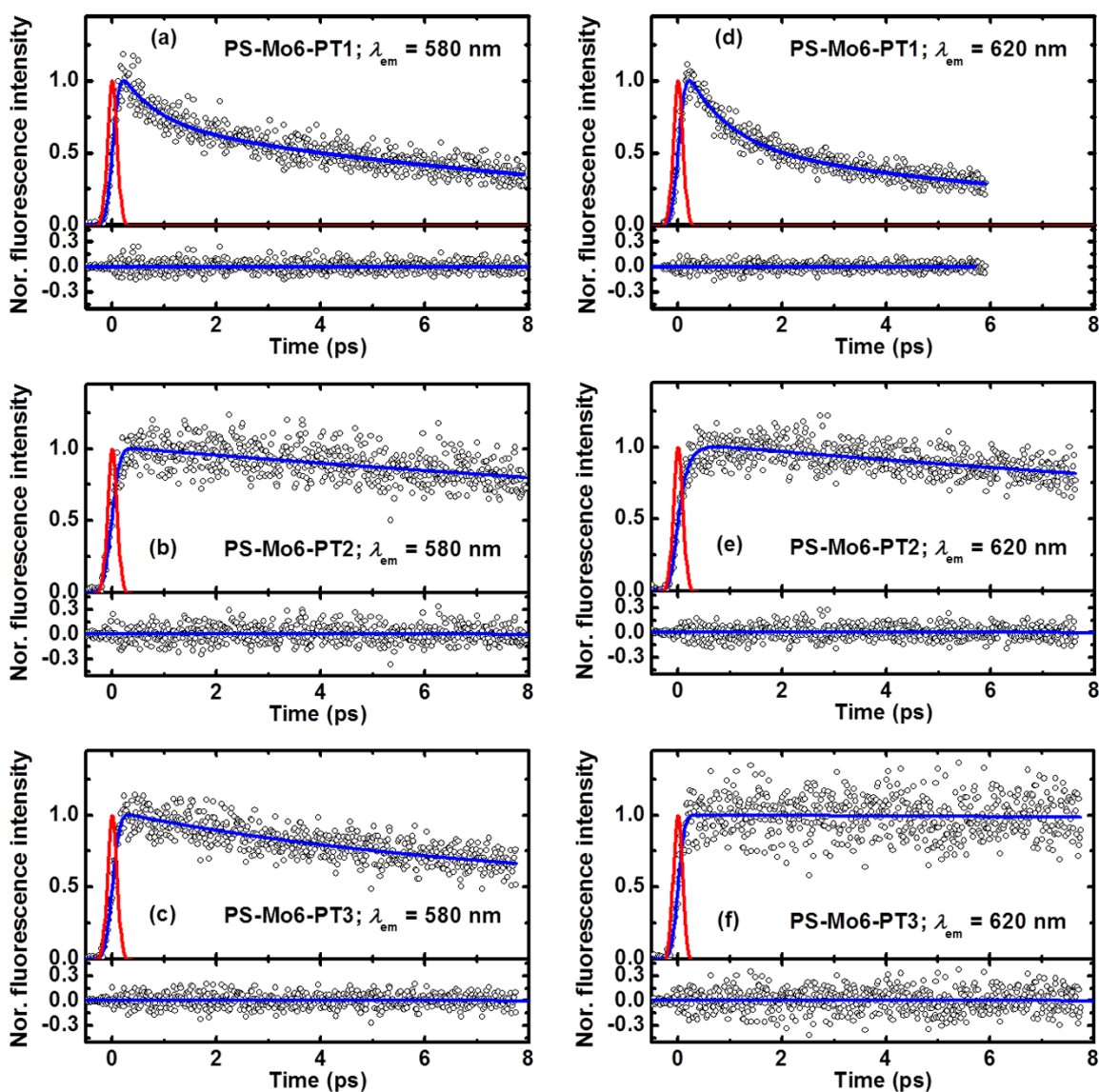


Figure 2-21 Fluorescence dynamics of the **PS-Mo6-PT1-3** solutions ( $\sim 0.5 \text{ mg mL}^{-1}$ ) in  $\text{CHCl}_3$  with excitation at 400 nm and emission at (a-c) 580 nm and (d-f) 620 nm, respectively. The red lines are the plotted instrument response function, and the blue ones are the fitted curves.

The fluorescence dynamics of **PS-Mo6-PT2** is very different where a rising component and a decay component are observed at both 580 and 620 nm. The time constant of the decay process (corresponding to the EET between segments with comparable energy) is identical at both probing wavelengths, indicating that the major exciton leading to 580 and 620 nm emissions must be the same. There are however clear differences in fluorescence dynamics at the two probing wavelengths: The rise time increases from  $40 \pm 20$  fs to 153 fs as the emission wavelength changes from 580 to 620 nm. Note that these two deconvoluted lifetimes are within the instrument response function and thus may cause much uncertainty. The corresponding amplitude increases significantly from 15.5 to 56.6%. Such a difference indicate that the 620 nm emission may come from different excitons one of which is likely excimer formed by the association of excited P3HT segment with another ground-state P3HT segment in the same chain or a different chain (dynamic excimer formation). It is noted that sub-picosecond excimer formation dynamics has been observed on organic systems.<sup>108–110</sup>

The difference in fluorescence dynamics at different detecting wavelengths is even more striking for **PS-Mo6-PT3**, where a biexponential decay is observed at 580 nm but an essentially monoexponential decay is seen at 620 nm. At 580 nm, the first decay component (6.3 ps) for **PS-Mo6-PT3** can be attributed to torsional relaxations. Photoexcitation changes the thiophene conformation from an aromatic structure to a quinoid structure, creating torsional defects (conformational disorders) in the backbone.<sup>107</sup> The torsional relaxation that typically happens in a time scale of a few ps can help reduce the conformational disorders of the long chain.<sup>100,111</sup> The second decay process (67 ps) can be assigned to the EET between segments with comparable energy. The lack of any fast decay

process for **PS-Mo6-PT3** at 620 nm indicates that the 620 nm emission is presumably dominated by the excimer emission. The long time constant (496 ps) thus corresponds to the fluorescence lifetime of the excimers.

To recap, **PS-Mo6-PT1** which has the shortest P3HT block (number of repeating thiophene unit = 25) shows biexponential fluorescence decay dynamics with insignificant emission wavelength dependence. The exciton decay is dominated by EET between segments with a downhill gradient (ultrafast, in subpicosecond) or with comparable energy (slower, in  $\sim 10$  ps). Considering the short P3HT block in **PS-Mo6-PT1**, energy transfer among intra-chain segments is unlikely. Thus, inter-chain energy transfer has to be the prevailing process. A  $\sim 0.5$  mg mL<sup>-1</sup> **PS-Mo6-PT1** solution has a concentration around  $2 \times 10^{-5}$  M. For such a relatively dilute solution to show significant ultrafast interchain energy transfer, some polymer association which brings the short P3HT blocks in close proximity has to occur. It is believed that counterion-mediated POM anion aggregation drives the

HDCP association as shown in Figure 2-22(a). Similar aggregation has recently been observed on a POM-containing conjugated polymer.<sup>112</sup>

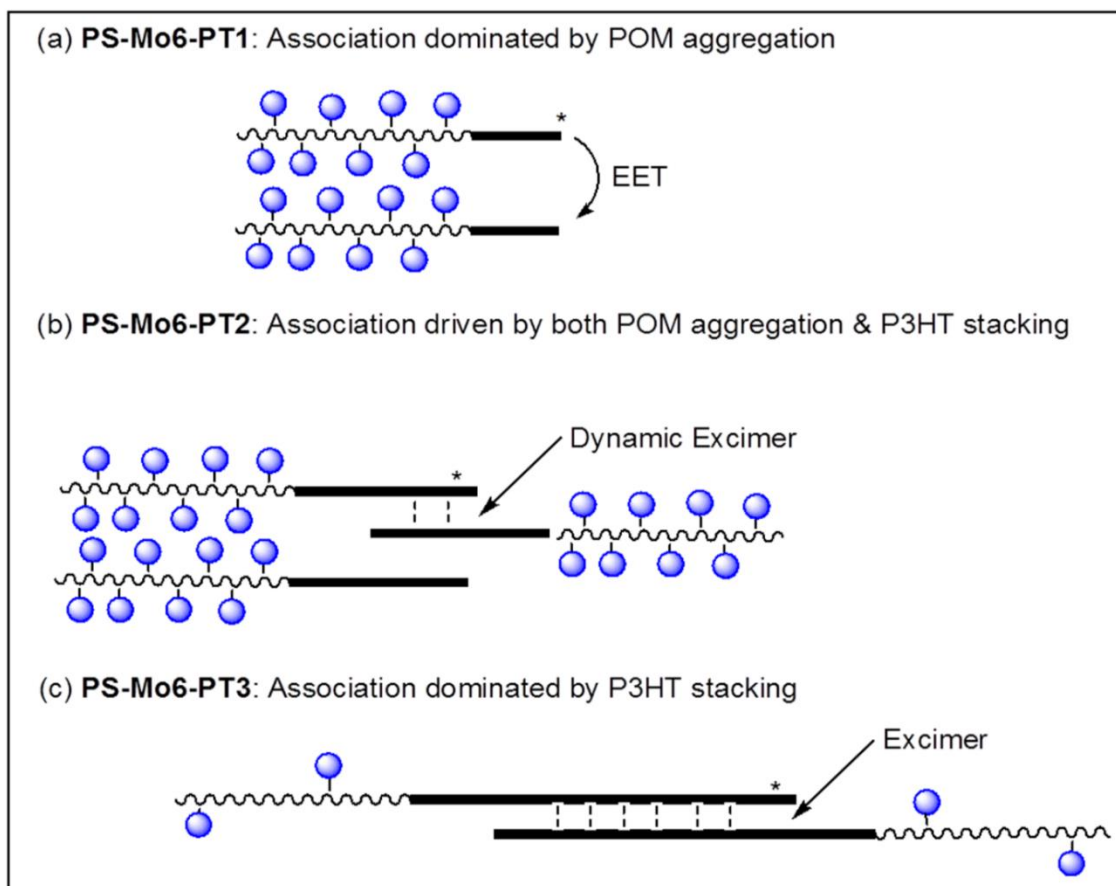


Figure 2- 22 Schematic illustration of the association mechanisms of **PS-Mo6-PT1-3** molecules in solution.

For **PS-Mo6-PT2**, whose P3HT block has an intermediate length (37 repeating units), its fluorescence dynamics is clearly probing wavelength dependent. It shows a rise component at 620 nm and identical decay constants at 580 nm and 620 nm. The clear rise component at 620 nm indicates the formation of dynamic excimers which contribute partly

to the emission at 620 nm. It is suspected that **PS-Mo6-PT2** forms aggregates in chloroform solution as well but the aggregation is driven by both POM association and P3HT-P3HT  $\pi$ -stacking as shown in Figure 2-22(b). The  $\pi$ -stacking, presumably only weakly in the ground state, facilitates the ultrafast dynamic excimer formation. The nearly identical decay time constants, though, indicate that singlet exciton emission, instead of excimer emission, dominates even at 620 nm.<sup>108,109</sup>

When the P3HT block is further significantly elongated as in **PS-Mo6-PT3** (84 repeating units), the HDCP aggregation in solution is now dominated by P3HT-P3HT  $\pi$ -stacking as shown in Figure 2-22(c). The counterion-mediated POM cluster associate takes the back seat not only because the  $\pi$ - $\pi$  stacking interaction is stronger among longer regioregular P3HT blocks, but also due to the fact that **PS-Mo6-PT3** has much lower cluster loading (only two clusters per chain) in the flexible block than the other two HDCPs do. As a result, the long wavelength emission of **PS-Mo6-PT3** is dominated by the excimer emission.

Fluorescence anisotropy decay profiles for emissions at 580 nm and 620 nm of the **PS-Mo6-PT1-3** solutions ( $\sim 0.5 \text{ mg mL}^{-1}$  in  $\text{CHCl}_3$ ) with excitation at 400 nm. As shown in Figure 2-23, the initial anisotropy values is close to 0.4, the limiting anisotropy for fluorophores with parallel or co-linear excitation and emission dipoles, and decay rapidly within tens to a couple of hundreds of femtoseconds to residual anisotropies of  $\sim 0.19$ ,  $\sim 0.26$ , and  $\sim 0.21$  at 580 nm emission and  $\sim 0.18$ ,  $\sim 0.25$ , and  $\sim 0.16$  at 620 nm emission for **PS-Mo6-PT1-3**, respectively. The residual anisotropies of the three HDCPs are higher than those of a P3HT ( $\sim 0.18$  and  $\sim 0.14$  for emission at 580 nm and 650 nm, respectively) with much higher molecular weights (number of repeating units  $\sim 300$ ) measured under similar

conditions,<sup>100</sup> which indicates that the rotational flexibility of the P3HT block in HDCPs is restricted by the attached heavier POM clusters. It is noted that among the three HDCPs **PS-Mo6-PT2** shows the highest residual anisotropies, presumably due to the strongest inter-chain association in **PS-Mo6-PT2** since both counterion-mediated POM aggregation and P3HT-P3HT  $\pi$ -stacking contribute to the HDCP aggregation.

Imido-functionalized hexamolybdates have a wider bandgap ( $\lambda_{\text{max}}$  around 350 nm) than P3HT does. Thus, energy transfer from P3HT exciton to the attached POM cluster is not expected and not observed. According to the CV study, photoinduced electron transfer from excited P3HT to a POM cluster is thermodynamically feasible. Charge transfer from organic donors to nanostructured inorganic semiconductors usually occurs in subpicosecond time scale and often in tens of femtoseconds.<sup>70,85,113</sup> Fluorescence decay dynamics of all three HDCPs did not reveal such ultrafast decay processes. In conjunction with the high residual polarization anisotropy, it is concluded that charge transfer from P3HT excitons to POM clusters in all three HDCPs is inefficient. This conclusion is consistent with our previous static fluorescence studies where the cluster-attached HDCPs are found to exhibit similar fluorescence quantum yields as the corresponding DCPs without POM clusters.<sup>84</sup>

It would be interesting to further study the fluorescence dynamics of the HDCP thin films because the HDCPs are in thin solid film form in the solar cells. Unfortunately, the weak fluorescence intensity complicates the measurements and leads to unacceptable signal-to-noise ratios. We thus gave up those measurements.

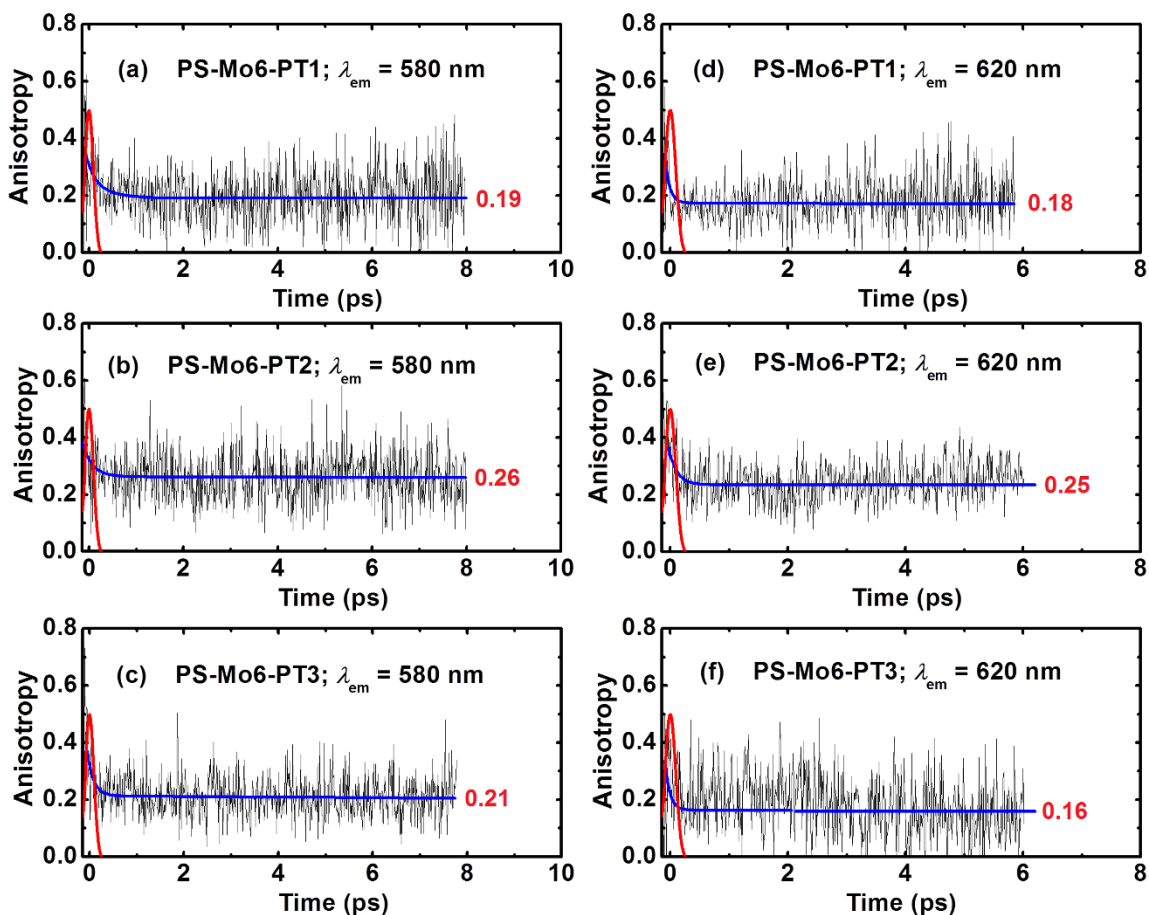


Figure 2-23 Anisotropy decay profiles of the **PS-Mo6-PT1–3** solutions ( $\sim 0.5 \text{ mg mL}^{-1}$ ) in  $\text{CHCl}_3$  for the emission at 580 nm (a-c) and 620 nm (d-f), respectively, under the excitation of 400 nm. The red lines are the plotted instrument response function, and the blue ones are eye-guiding curves for the decay trends.

The poor photovoltaic performance of the HDCPs is likely due to the poor photoinduced charge transfer from the  $\pi$ -conjugated exciton to the POM clusters as observed in the solutions. We have previously shown that when POM clusters are linked to the  $\pi$ -conjugated backbone through a nonconjugated flexible linkage, the charge transfer from the excited  $\pi$ -backbone to the POM clusters is inefficient.<sup>78</sup> When the POM clusters are linked through a conjugated linkage, however, the charge transfer process becomes very efficient.<sup>78,82</sup> Thus, if one introduces POM which is directly conjugated with the organic  $\pi$ -system, one may be able to improve the initial charge transfer process from the photoexcited organic conjugated segment to the POM clusters.

## 2.6 Main chain POM containing donor-acceptor hybrid conjugated polymers

Main-chain POM-containing conjugated polymers with  $\pi$ -conjugation extended directly to the POM clusters show efficient through-bond photoinduced charge transfer and are thus more appealing photovoltaic materials.<sup>78,82</sup> While main-chain POM-containing conjugated polymers are still very rare in the literature, they have indeed shown better photovoltaic performance than other POM hybrid systems.

Our previous POM-containing main-chain conjugated polymers were based on conjugated backbones which are not among the best electron donors and their bulk heterojunction solar cells with PCBM exhibit poor performance.<sup>82</sup> With our recent demonstration that new donor-acceptor conjugated polymer **PBOR** based on 3,3'-didodecyloxy bithiophene and imide-functionalized naphtho[1,2-*b*:4,3-*b'*]dithiophene (INDT) building blocks shows relatively high solar cell performance (up to 6.56%) when mixed with PCBM,<sup>98</sup> we have sought to prepare POM-containing hybrid polymers based on **PBOR** backbone. In this contribution, we design two main-chain POM-containing

conjugated copolymers, namely **P10** and **P11**, as show in Figure 2-24. The synthesis and optoelectronic properties will be reported in this study.

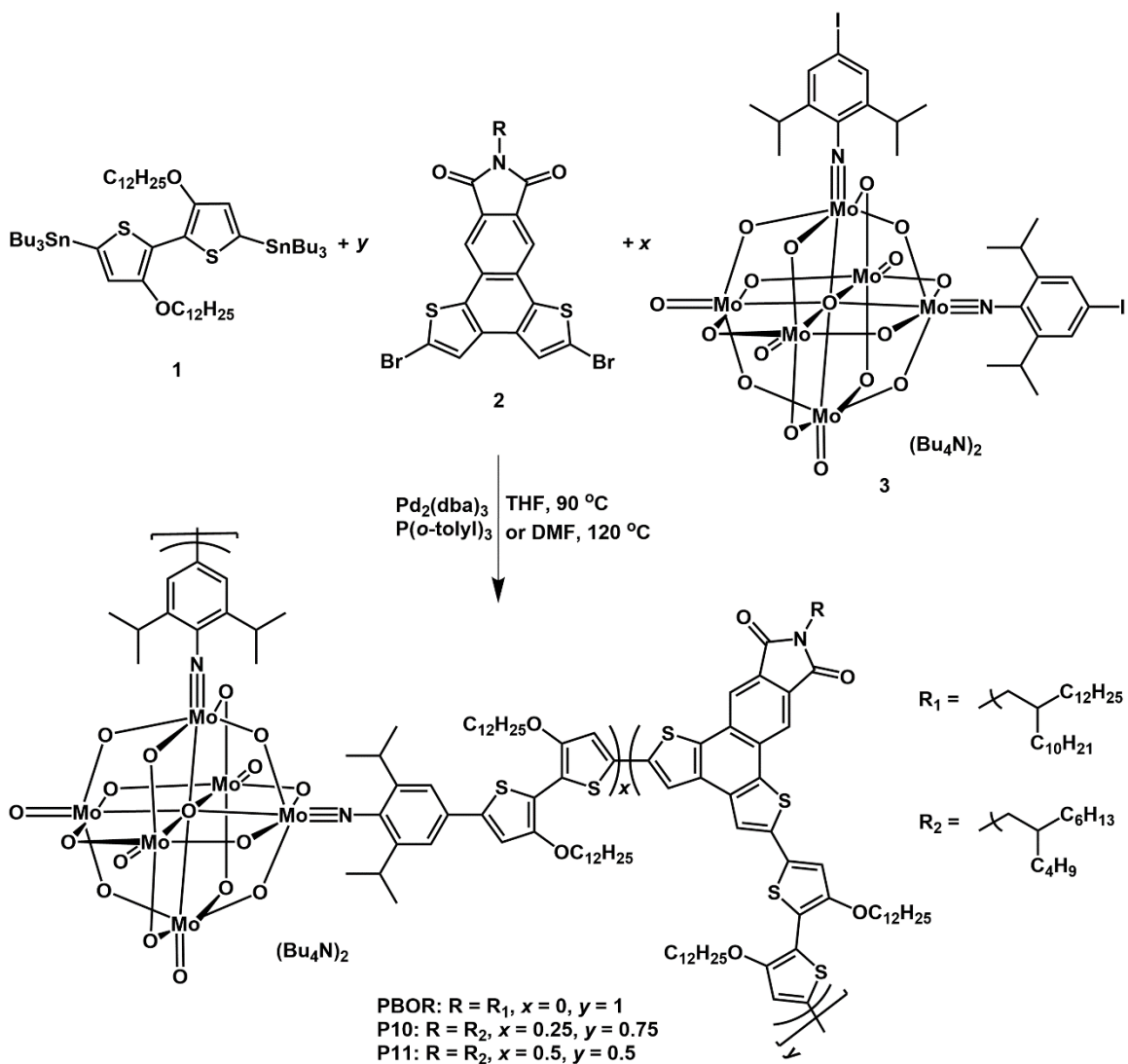


Figure 2-24 Synthesis of main chain POM-containing hybrid conjugated copolymer **P10** and **P11**.

### 2.6.1 Structure characteristics

The synthesis of the two new hybrid polymers **P10** and **P11** are depicted in Figure 2-24. **P10** and **P11** were synthesized using the Stille polycondensation reaction of electron-deficient aryl dihalide monomers, **2** and **3**, with electron-rich distannane monomer **1** in DMF.<sup>114</sup> The selected monomer pairings are favorable for the Stille coupling reaction to yield high-molecular-weight polymers.<sup>115</sup> By changing the feeding ratio of three monomers (1:0.75:0.25 and 1:0.5:0.5, molar ratios), two random copolymers, **P10** and **P11**, containing different content of POMs were obtained. In these polymers, the POMs are covalently embedded into the main chain, replacing some of the INDT units in donor-acceptor alternating copolymer **PBOR**. With a long branched alkyl chain at the imide nitrogen position of INDT and two long dodecyloxy groups at the bithiophene unit, polymer **PBOR** is soluble in common organic solvents such as chloroform and THF. **P10**, with some POM clusters covalently linked to the backbone, also exhibits a decent solubility in these solvents at room temperature. With more embedded POM clusters, **P11**, however, shows rather poor solubility in these solvents. As the cluster loading increases, counterion-mediated POM anion aggregation may occur which decreases the polymer solubility.<sup>83</sup>

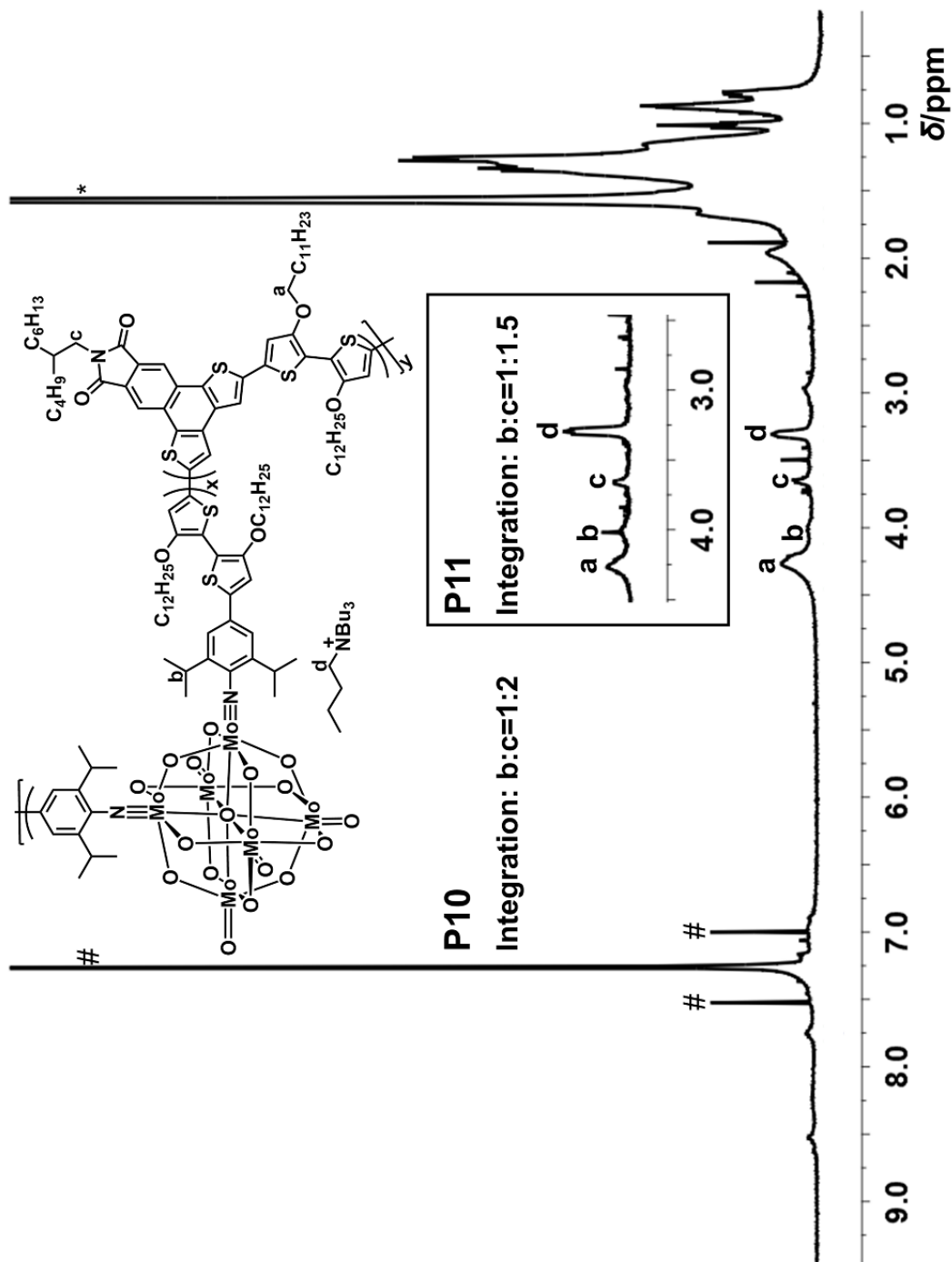


Figure 2-25  $^1\text{H}$  NMR spectrum of **P10** in  $\text{CDCl}_3$  (signals labeled with “#” or “\*” are solvent peaks). The insert in rectangle displays the region of interest of the  $^1\text{H}$  NMR of **P11** in  $\text{CDCl}_3$ .

The  $^1\text{H}$  NMR spectra of the two hybrid polymers were measured in deuterated chloroform and are shown in Figure 2-25. The clear appearance of the characteristic signals associated with the bifunctionalized POM cluster and its tetrabutylammonium counterions, such as the isopropyl CH proton (proton b in Figure 2-25) at  $\delta = 4.00$  ppm,  $N^+-\text{CH}_2$  protons (proton d in Figure 2-25) at  $\delta = 3.30$  ppm, etc., confirms the successful incorporation of POM clusters into polymers **P10** and **P11**. The signals at  $\delta = 4.25$  and 3.65 ppm, corresponding to the *O*- $\text{CH}_2$  protons (proton a in Figure 2-25) in the bithiophene unit and the *N*- $\text{CH}_2$  protons (proton c in Figure 2-25) in the INDT unit, respectively, are also well resolved. Relative to proton c signal, proton b signal has a higher integration ratio in **P11** than that in **P10**, indicating that **P11** indeed has a higher POM loading in the backbone. The integral ratio of proton b signal vs. proton c signal is 1:2 and 1:1.5 for **P10** and **P11**, respectively. From this ratio, the molar ratio of INDT units (corresponding to monomer **2**) vs. POM clusters (corresponding to monomer **3**) is estimated to be 4:1 for **P10** and 3:1 for **P11**. The INDT:POM molar ratio in **P10** (4:1) is slightly higher than its monomer feeding ratio (**2:3** = 3:1). Elemental analysis showed that the weight percentage of Mo in **P10** and **P11** was 10.78% and 16.13%, respectively. On the basis of the elemental analysis data and ignoring the end groups, the molar ratio of INDT units (corresponding to monomer **2**) vs. POM clusters (corresponding to monomer **3**) is estimated to be 3.1:1 for **P10** and 1.3:1 for **P11**. The POM contents in these hybrid copolymers estimated by elemental analysis are only slightly lower than their monomer feeding ratios (**2:3** = 3:1 for **P10** and 1:1 for **P11**), indicating that monomers **3** and **2** have a similar reactivity towards monomer **1** under the applied reaction conditions. It needs to be pointed out that because of the limited solubility of **P11**, its  $^1\text{H}$  NMR spectrum reflects only the structures of the soluble part. This is likely

the reason responsible for the substantial underestimation of POM content in **P11** by its  $^1\text{H}$  NMR spectrum.

Molecular weights of the two hybrid polymers were estimated by GPC with THF as the eluent and polystyrene as the standards. The weight-average molecular weights ( $M_w$ ) of **P10** and **P11** were found to be 5.48 and 3.69 KDa, respectively. Both polymers showed relatively narrow polydispersity indices (PDI = 1.50 and 1.25, respectively). The lower molecular weights of **P11** may be attributed to its poor solubility. When pure hybrid monomer **3** was subjected to the same GPC column, an  $M_w$  of 1.78 KDa with a PDI of 1.24 was obtained.<sup>82,84,116</sup> As shown previously, molecular weights of POM-containing hybrid monomers and polymers based on GPC, relative to polystyrene standards, should not be taken literally. Nevertheless, the GPC traces of **P10** and **P11** are clearly separated from that of monomer **3**, indicating that the POM clusters are covalently attached to the backbone in the hybrid copolymers.

Figure 2-26 shows the FT-IR spectra of **P10** and **P11**. The FT-IR spectra of **PBOR** and monomer **3** are also included in Figure 2-26 for comparison. As can be seen, almost all of the characteristic vibrations of both polymer **PBOR** and monomer **3** can be found in the FT-IR spectra of **P10** and **P11**. The strong band at  $\sim 1708\text{ cm}^{-1}$  is assigned to the stretching vibration of the C=O bond in the INDT units. The strong band at  $\sim 948\text{ cm}^{-1}$  is attributed to  $\nu(\text{Mo}=\text{O})$ , while the clear band/shoulder at  $\sim 969\text{ cm}^{-1}$  corresponds to  $\nu(\text{Mo}\equiv\text{N})$ .<sup>78,82</sup> These results again confirmed the covalent attachment of POM clusters in **P10** and **P11**.

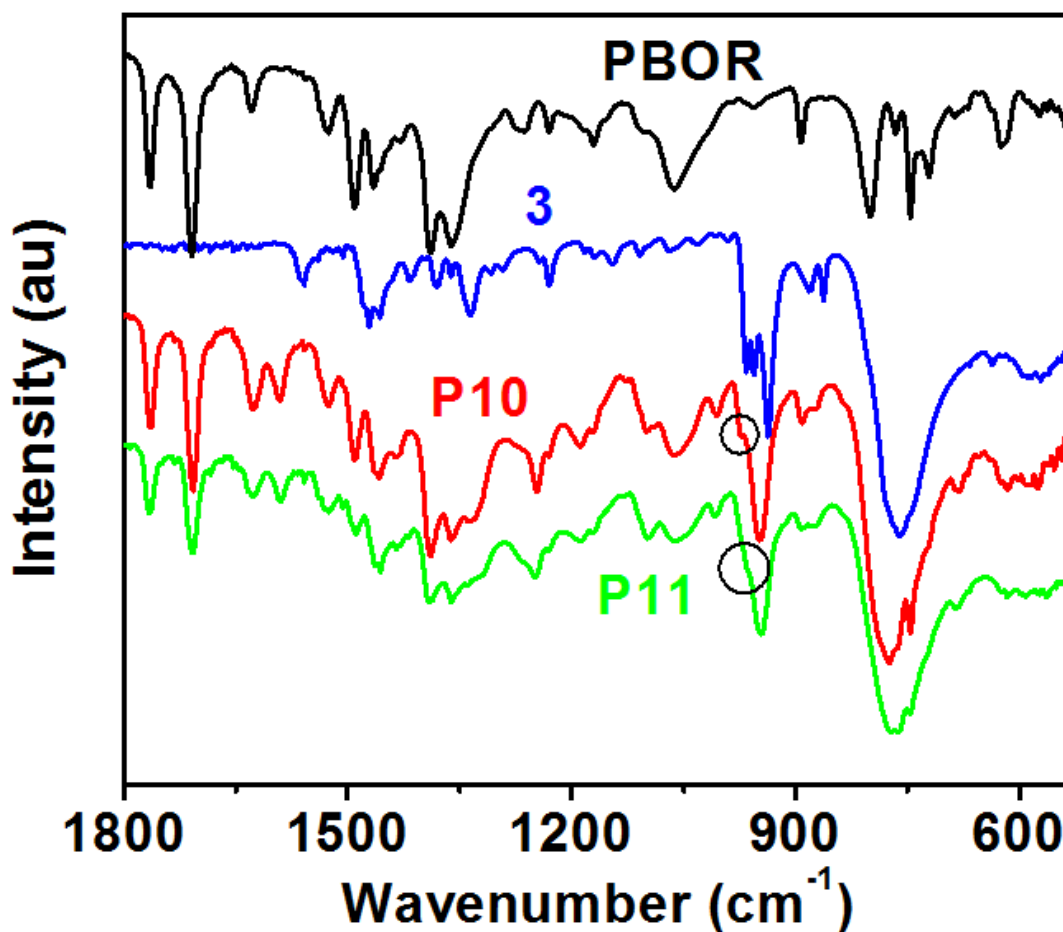


Figure 2-26 FT-IR spectra of **PBOR**, **3**, **P10** and **P11**.

### 2.6.2 Optical properties

The absorption and fluorescence properties of the polymers were studied in dilute THF and CHCl<sub>3</sub> solutions. As shown in Figure 2-27 (a, d), the maximum absorption of **P10** and **P11** in both solutions is at a shorter wavelength (509 ~ 515 nm) than that of **PBOR** (~535 nm) (Table 2-4) as a result of the insertion of POM clusters in the backbone. All three polymers show broad NIR absorptions up to 1600 nm in CHCl<sub>3</sub>. Such NIR absorptions were not observed in their THF solutions. The appearance of NIR absorptions

in chloroform is likely due to the protonation of some 3,3'-didodecyloxy bithiophene end functional units by the residual acid in  $\text{CHCl}_3$  as commercial  $\text{CHCl}_3$  usually contains trace amount of acid as a result of photolysis (details are shown in Chapter 3).<sup>117,118</sup> It is noted that as the POM content in the polymer backbone increases, the NIR absorption decreases. This is understandable since hexamolybdate is an electron acceptor which decreases backbone  $\pi$ -electron density and thus Lewis basicity.

The hybrid copolymers **P10** and **P11** are weakly fluorescent in both THF and  $\text{CHCl}_3$  solutions, Figure 2-27 (b, e). Unlike polymer **PBOR**, which showed two emissions: one from polymer aggregates (excimer emission, at 629 ~ 636 nm) and the other from non-aggregated polymers at a lower wavelength (600 ~ 615 nm),<sup>98</sup> the hybrid copolymers show only the lower wavelength emission with emission  $\lambda_{\text{max}}$  values at 595 ~ 600 nm for both **P10** and **P11** (Table 2-4). The spherical shape and the *ortho*-type bifunctionalization of the POM clusters in **P10** and **P11** likely limited the approaching and thus the  $\pi$ - $\pi$  stacking of the organic  $\pi$ -segments. From fluorescence point of view, embedding POMs into the **PBOR** backbone has thus two opposing effects: decreases  $\pi$ -segment aggregation which increases fluorescence quantum yields, and increases LMCT which results in enhanced fluorescence quenching.<sup>116</sup> As a result, when POM loading in the backbone increases from **PBOR** to **P10** and to **P11**, the fluorescence quantum yield increases initially and then drops. Overall though, all three polymers show weak fluorescence with quantum yields around or lower than 1% (Table 2-4). The excitation spectra of **P10** and **P11** show two maxima around 510 and 540 nm, while those of the **PBOR** exhibit only one at ~550 nm (Figure 2-27(c, f)). The 510 and 540 nm excitations can be assigned to LMCT and  $\pi$ - $\pi^*$  transition, respectively. Comparing with their absorption spectra which show that the absorption  $\lambda_{\text{max}}$

for **P10** and **P11** is both around 510 nm, one can conclude that  $\pi$ - $\pi^*$  transition is much more effective in producing emissive excitons than LMCTs.

Table 2-4 Optical and redox properties of the polymers.

Polymer	$\lambda_{\max}^{\text{abs}}$ (nm) <sup>a</sup>		$\lambda_{\max}^{\text{fl}}$ (nm) <sup>a</sup>		$\phi$ <sup>b</sup>		$E_{\text{ox}}^{\text{onset}}$	$E_{\text{red}}^{\text{onset}}$	$E_{\text{red}}^{\text{onset}}$ (POM)
	THF	CHCl <sub>3</sub>	THF	CHCl <sub>3</sub>	THF	CHCl <sub>3</sub>	(V) <sup>c</sup>	(V) <sup>c</sup>	(V) <sup>c</sup>
<b>PBOR</b>	536	535	636	629	0.004	0.005	0.06	-1.95	–
<b>P10</b>	509	509	596	599	0.006	0.012	0.10	-1.99	-1.42
<b>P11</b>	512	515	595	600	0.003	0.006	-0.06	-1.84	-1.34

<sup>a</sup> in solution. <sup>b</sup> Fluorescence quantum yield. <sup>c</sup> From CV measurements of thin solid film.

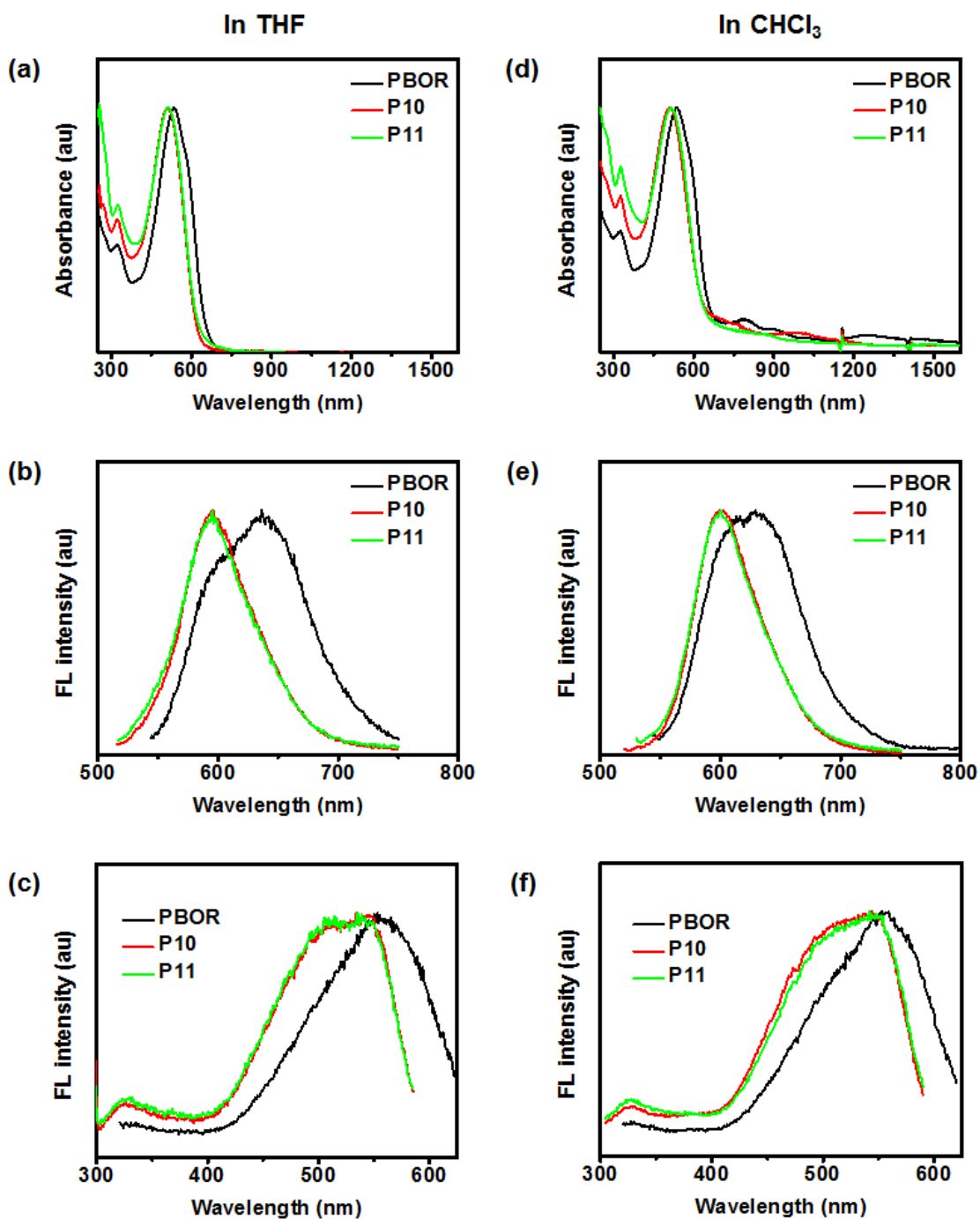


Figure 2-25 Normalized UV-vis-NIR absorption (a, d) and fluorescence emission spectra (c and e, excited at the wavelength of maximum absorption) and excitation spectra (c and f, monitored at the wavelength of maximum emission) of dilute solutions of **PBOR**, **P10** and **P11** in THF (a-c) and  $\text{CHCl}_3$  (d-f).

### 2.6.3 Electrochemical properties

The electrochemical properties of the polymers were investigated as thin films using CV measurements. As shown in Figure 2-28, polymer **PBOR** shows two irreversible reduction waves during the cathodic scan and two reversible or semi-reversible oxidation waves in the anodic scan. Besides these four waves as observed on **PBOR**, both **P10** and **P11** show clearly one additional semi-reversible reduction process as highlighted in Figure 2-28. This reduction process with onset of  $-1.42$  and  $-1.34$  V for **P10** and **P11**, respectively, is attributed to the reduction of the embedded POM clusters. It is noted that the reduction potential decreases (more difficult to reduce) from monomer **3** ( $-1.21$  V) to **P11** and to **P10**, presumably reflecting the good electron-donating property of the polythiophene-based  $\pi$ -system and the strong electronic interaction between the organic  $\pi$ -system and the POM clusters. From the first oxidation onset potential in the anodic scan and the first reduction onset potential in the cathodic scan (Table 2-4),<sup>119</sup> the HOMO/LUMO energy levels of the polymers were calculated to be  $-4.86/-2.85$ ,  $-4.90/-3.38$ , and  $-4.74/-3.46$  eV for **PBOR**, **P10**, and **P11**, respectively.

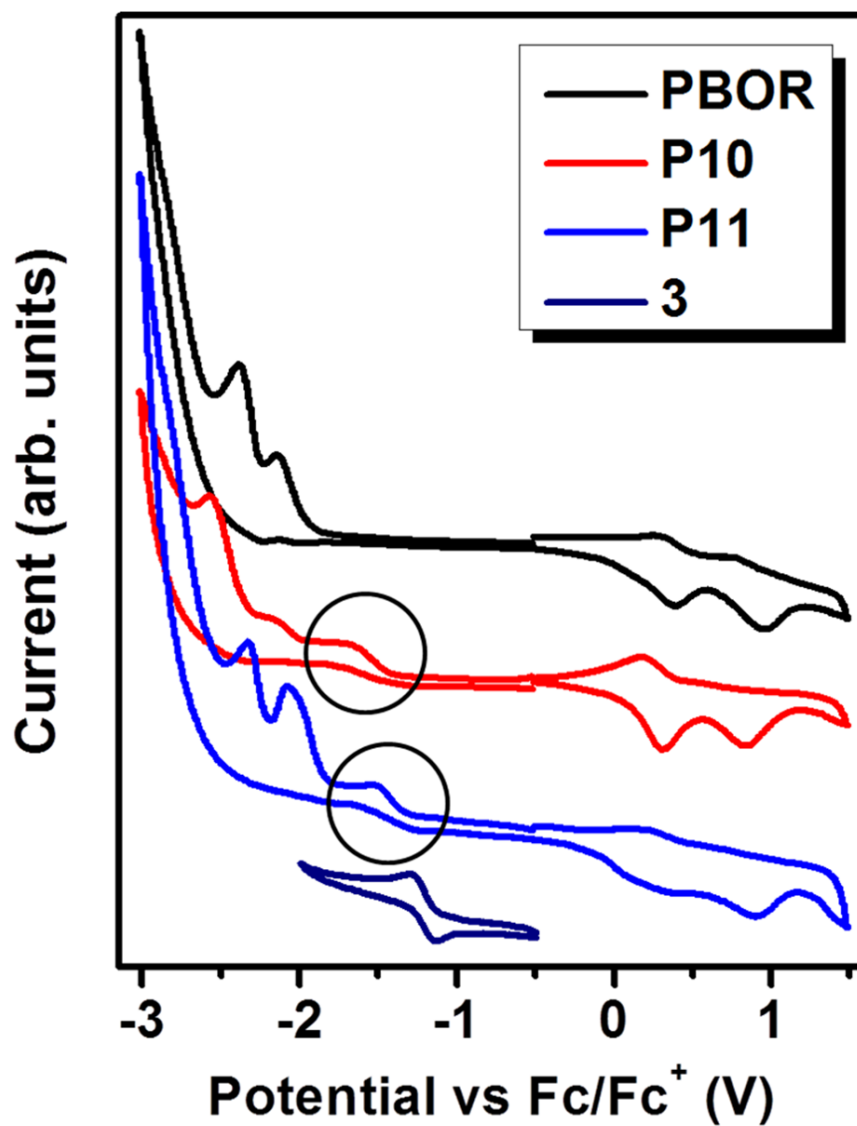


Figure 2-28 Cyclic voltammograms of PBOR, P10, P11 and 3 thin films prepared from CHCl<sub>3</sub> solutions.

#### 2.6.4 Photovoltaic properties

Simple photovoltaic devices with a thin layer of **PBOR**, **P10** or **P11**, sandwiched between a transparent anode (ITO/PEDOT:PSS) and a metal cathode (Ca/Al), were fabricated.  $\text{CHCl}_3$  was used as the solvent to prepare the polymer solutions. As mentioned earlier, all three polymers show NIR absorptions in  $\text{CHCl}_3$ . Thin films spin-coated from their  $\text{CHCl}_3$  solutions ( $20 \text{ mg mL}^{-1}$ ; 900 rpm for **PBOR** and 600 rpm for **P10/P11**; 1 min) showed NIR absorptions as well (Figure 2-29 (a)). Compared to their solution spectra shown in Figure 2-27(d), the spectral shape of **PBOR** in the UV-visible region is essentially the same with only slight redshift (by  $\sim 6 \text{ nm}$ ) in absorption  $\lambda_{\text{max}}$ , whereas the thin-film spectra of **P10** and **P11** are more redshifted (by  $\sim 32 \text{ nm}$ ) and nearly cover the same visible range as **PBOR** does. This indicates that the strong  $\pi$ - $\pi$  stacking among conjugated bridges recovered in the solid state of these hybrid copolymers. Thermal annealing treatment (at  $120 \text{ }^\circ\text{C}$  for 15 min) induced only negligible changes to the absorption spectra of the thin films of three polymers (see Figure 2-29 (a)).

Figure 2-29 (b-d) shows the typical current density–voltage ( $J$ - $V$ ) curves of the devices in dark and under illumination. Corresponding photovoltaic characteristics, including open circuit voltage ( $V_{\text{OC}}$ ), short circuit current density ( $J_{\text{SC}}$ ), fill factor (FF), and PCE, are tabulated in Table 2-5. Without any other added electron acceptors, the devices of pure **PBOR** exhibited a low but normal PCE of 0.009%, whereas the devices based on hybrid copolymer **P10** showed a much more encouraging PCE of 0.222%. The 24 times increase in PCE was brought about by the boost of  $J_{\text{SC}}$  from  $0.062 \text{ mA cm}^{-2}$  to  $2.42 \text{ mA cm}^{-2}$  thanks to the insertion of strong electron-accepting POM clusters in the  $\pi$ -conjugated backbone. The much higher  $J_{\text{SC}}$  and PCE achieved with **P10** than **PBOR** suggests that

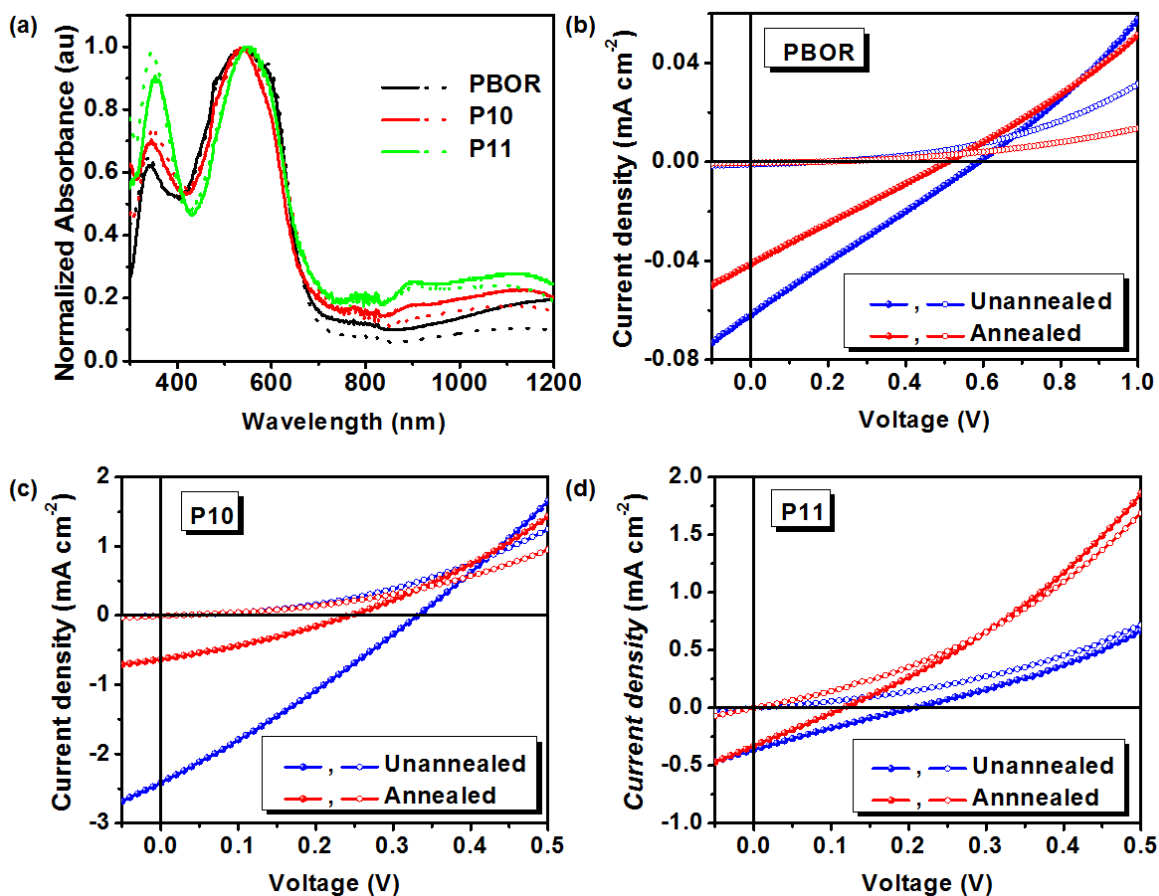


Figure 2- 29 (a) Normalized absorption spectra of **PBOR**, **P10** and **P11** thin films before (solid line) and after (dot line) thermal annealing at 120 °C for 10 min under nitrogen atmosphere; (b-d) Typical  $J$ - $V$  curve (empty circle: in dark; sphere: under 1-sun air mass 1.5 global illumination) of the single –component photovoltaic cells of (b) **PBOR**, (c) **P10** and (d) **P11** with structure of ITO/PEDOT:PSS/polymer/Ca/Al (100nm).

photoinduced charge separation in such main-chain POM-containing hybrid polymers can be rather efficient. Due to the poor solubility of **P11**, the maximum absorbance of its thin films spin-coated from CHCl<sub>3</sub> solutions is only about half of that of **P10**. As a result, devices of **P11** performed not as well as **P10** did, and showed a PCE of only 0.017%. The

above results are all from devices that were not thermally annealed. Thermal annealing of the polymer thin films, in all cases, shows a detrimental effect on the device performances (see Figure 2-29(b-d) and Table 2-5).

Further device optimization by varying polymer concentration, spin rate, etc., yielded a higher PCE from **P10** (Figure 2-30). Although the devices suffer again from low  $V_{OC}$  and poor FF, the 0.31% efficiency is still highly respectable, among the highest PCE values for all reported POM-based hybrid polymers. The device performance, while encouraging, pales in comparison with the best composite hybrid systems.<sup>120-122</sup> This is not surprising as hybrid polymers **P10** and **P11** have POM clusters uniformly distributed in the backbone and thus are not likely to form the required phase-separated bicontinuous donor and acceptor domains necessary for highly efficient devices.

Figure 2-31 shows the IPCE spectra of the photovoltaic cells of **P10** and **P11**. All the IPCE spectra reasonably match the absorption spectra of their corresponding thin films (Figure 2-29(a)) in the UV-visible region (from 300 to 700 nm), confirming the photocurrent contribution of both the organic  $\pi$ -segments and the POM clusters in the polymer backbone. The IPCE spectra in the range of 800 to 1600 nm were also collected (not shown in Figure 2-31), but they showed no quantum efficiency. Apparently, the NIR absorptions of both hybrid polymers, corresponding to intramolecular charge transfer induced by protonation, are unable to produce photocurrent. This is presumably due to the localized nature of the charges generated by the intramolecular charge transfer transition in the protonated species.

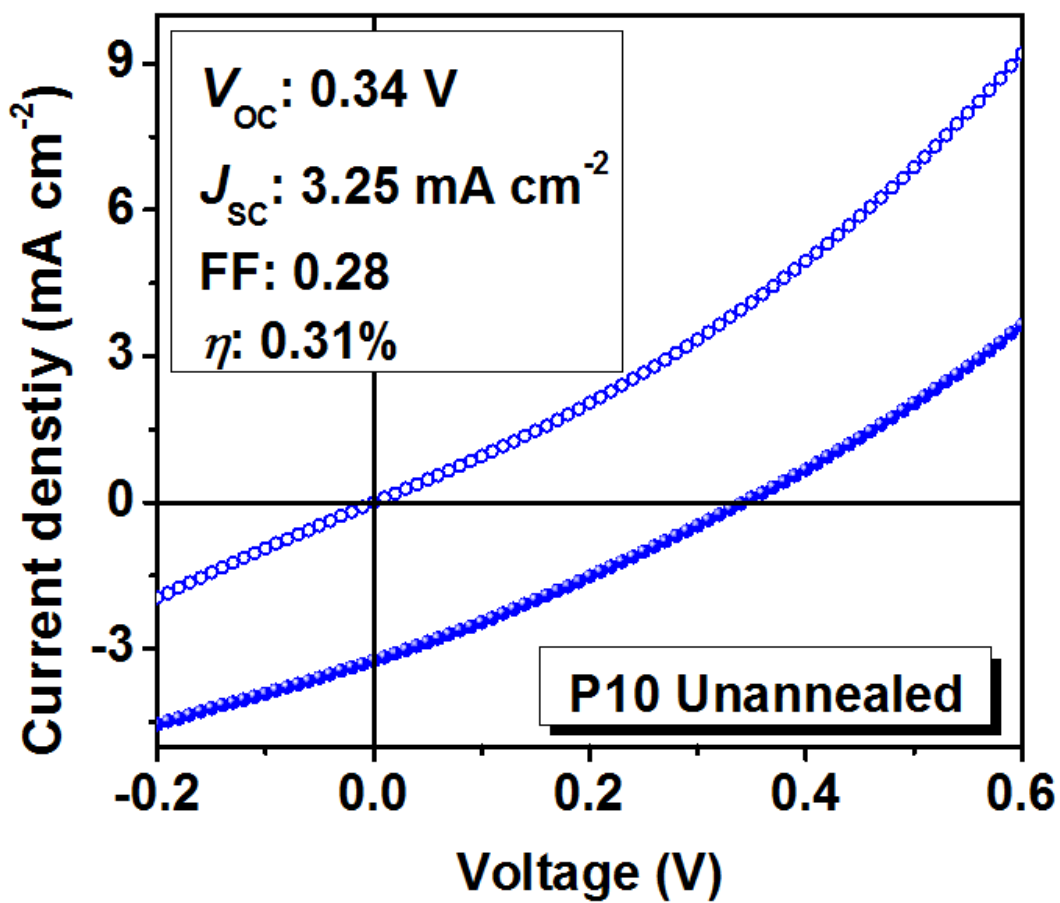


Figure 2-30  $J$ - $V$  curves (empty circles: in dark; spheres: under illumination) of the highest-performing cells of ITO/PEDOT:PSS/P10/Ca (50 nm)/Al (100 nm).

Table 2-5 Photovoltaic Parameters of **PBOR**, **P10** and **P11** under illumination.

Active Materials	<i>I-V</i> Parameters			
	$V_{oc}$ (V)	$J_{sc}$ (mA/cm <sup>2</sup> )	FF	PCE (%)
<b>PBOR</b>	0.59	0.062	0.25	0.009
<b>PBOR</b> Annealed <sup>a</sup>	0.51	0.041	0.25	0.005
<b>P10</b>	0.33	2.42	0.28	0.222
<b>P10</b> highest	0.34	3.25	0.28	0.310
<b>P10</b> Annealed <sup>a</sup>	0.24	0.63	0.31	0.047
<b>P11</b>	0.21	0.36	0.23	0.017
<b>P11</b> Annealed <sup>a</sup>	0.12	0.33	0.24	0.010

<sup>a</sup>Thermally annealed at 120 °C for 15 min in dark under N<sub>2</sub> atmosphere.

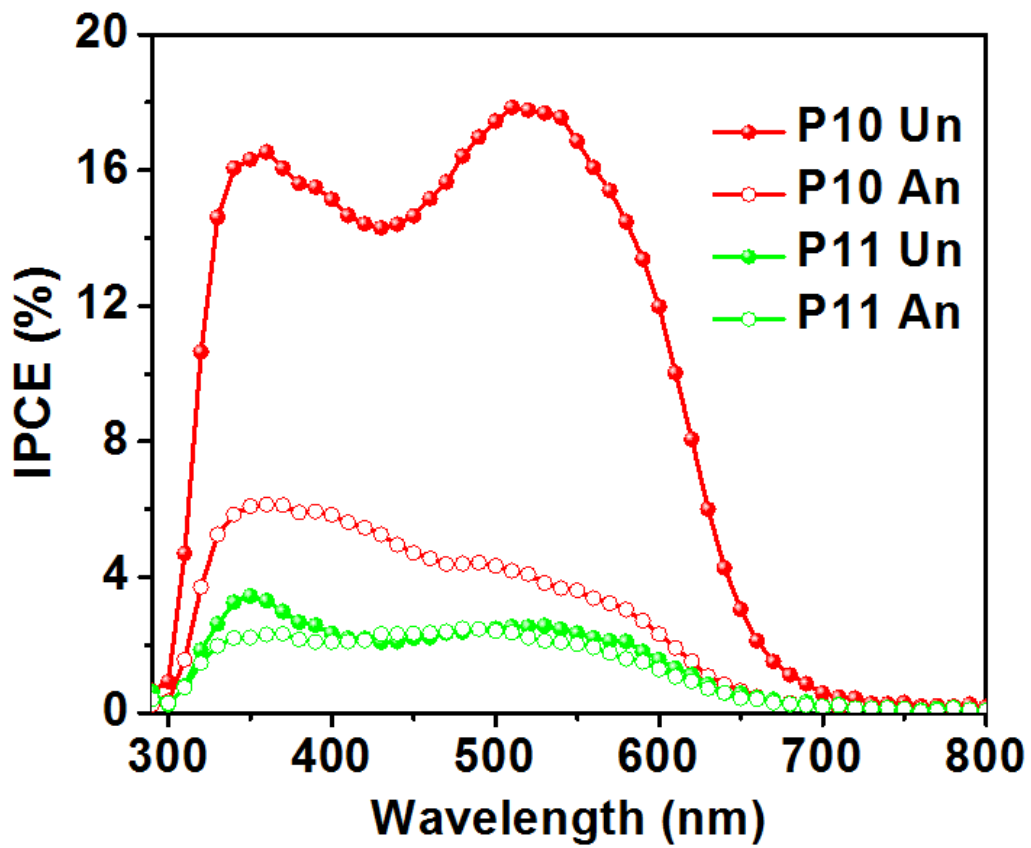


Figure 2-31 IPCE spectra of the devices of **P10** and **P11** with structure of ITO/PEDOT:PSS/polymer/Ca (50 nm)/Al (100 nm) before (sphere) and after (empty circle) thermally annealed at 120 °C for 15 min.

## 2.7 Conclusions

Three POM-containing hybrid systems have been explored for PV applications. The charge transfer hybrids **Mo6-Fe**, when blended with PCBM shows appealing photovoltaic performance. The rod-coil hybrid diblock copolymers show desired phase separated domains but poor device performance (<0.1%). To explore the reason for the poor photovoltaic performances of the HDCPs, FFU technique has been used to study the exciton decay dynamics of the three HDCPs. The three HDCPs show very different exciton decay dynamics. The fluorescence dynamics indicates that all three HDCPs aggregate in solution but do so in different ways. While both cation-mediated POM cluster association and P3HT-P3HT  $\pi$ -stacking contribute significantly to **PS-Mo6-PT2** aggregation, the aggregation of **PS-Mo6-PT1** and that of **PS-Mo6-PT3** is driven predominantly by cluster association and  $\pi$ -stacking, respectively. Although the fluorescence dynamics of the three HDCPs are different, none of them shows ultrafast decay processes attributable to the photoinduced charge transfer processes. In conjunction with the high residual polarization anisotropy, it is concluded that charge transfer from P3HT excitons to POM clusters in all three HDCPs is inefficient. The poor photovoltaic device performance is likely attributed to the poor initial photoinduced charge transfer from the organic exciton to the POM cluster which is intrinsic to the polymer structure where there is no direct  $\pi$ -conjugation between the POM clusters and the rod block.

Main-chain POM-containing conjugated copolymers with IND<sub>2</sub>T and 3,3'-didodecyloxy bithiophene units have been synthesized by using the Stille polycondensation reaction. The structures of the hybrid polymers were confirmed by <sup>1</sup>H NMR, FT-IR, and elemental analysis. These polymers show intense absorption in the visible range with weak

fluorescence emissions in solutions. Noticeably, these polymers were found to have broad NIR absorptions in  $\text{CHCl}_3$  which can be carried forward to their spin-coated thin films. Simple single-layer solar cells based on **P10** showed respectable PCEs up to 0.31%. IPCE measurement revealed that the photocurrent of the solar cells was attributed exclusively by the UV and visible absorptions. The NIR absorptions of both hybrid polymers, assignable to protonation-induced intramolecular charge transfer, are unable to produce photocurrent for photovoltaic applications.

When POM clusters are linked to the  $\pi$ -conjugated backbone through a non-conjugated flexible linkage, the charge transfer from the excited  $\pi$ -system to the POM cluster is inefficient. When the POM cluster is linked through a conjugated linkage the charge transfer process becomes very efficient. Thus, if one introduces a bridging POM which is directly conjugated with the organic  $\pi$ -system as schematically shown in Figure 2-32, one may be able to improve the initial charge transfer process from the photoexcited organic rod block to the POM cluster. In this system, bifunctionalized imido POM cluster is used as the bridge between the organic conjugated rod block and POM-containing flexible coil block.

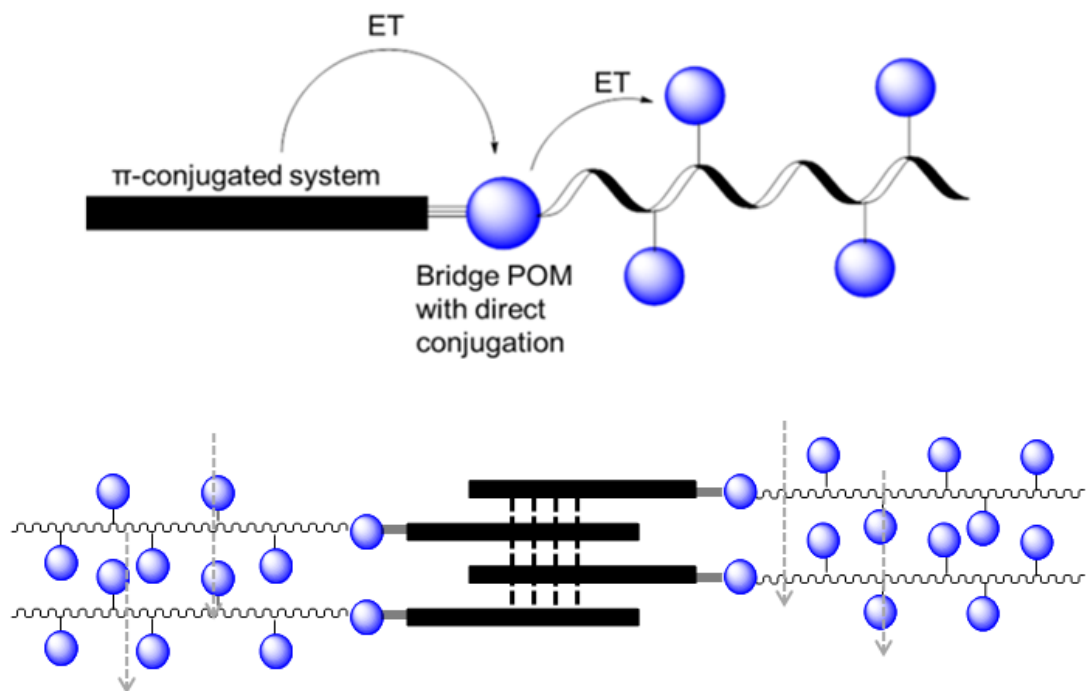


Figure 2-32 Schematic representation of a new hybrid diblock copolymer containing a bridging POM cluster to facilitate initial charge transfer and hypothetical module of polymer stacking.

## 2.8 Methods

### 1) *General remarks*

Solvents were freshly distilled from appropriate drying agents under inert conditions prior to use. All other reagents, unless noted otherwise, were used as received from vendors without further purification. Poly(3,4-ethylenedioxythiophene)-poly(styrenesulfonate) (PEDOT:PSS) (Clevios™ P VP AI 4083) aqueous dispersion was purchased from Heraeus Precious Metals. Indium tin oxide (ITO)-coated glass with sheet resistance of 8–12  $\Omega$  square<sup>-1</sup> was purchased from Delta Technologies. <sup>1</sup>H NMR spectra were recorded on a Varian INOVA 400 MHz FT-NMR spectrometer in deuterated solvents as indicated. Chemical shifts (in ppm) were internally referenced to the signals of residual non-deuterated solvents. Gel permeation chromatography (GPC) data were collected at 30 °C with a Tosoh EcoSEC HLC-8320GPC system equipped with a differential refractometer, a UV detector, a light scattering detector, and a styra gel column with THF as the eluent. The GPC system was calibrated with a set of four polystyrene standards (from 474 to 549000) before test. Elemental analyses for Mo were performed on a PerkinElmer Optima 2000DV ICP-OES spectrometer. FT-IR spectra were measured with a Shimadzu IRAffinity-1 Fourier transform infrared spectrophotometer. UV-vis-NIR absorption spectra were collected with a Shimadzu UV-3600 spectrophotometer. UV-vis absorption spectra were measured in Hewlett Packard 8452A diode array spectrophotometer. Fluorescence spectra were recorded on a Shimadzu RF-5301PC spectrofluorophotometer. Fluorescence quantum yields were determined in dilute solutions (absorption maximum < 0.1) by using quinine sulfate in 1 N H<sub>2</sub>SO<sub>4</sub> ( $\phi_{fl} \approx 0.546$ ) as the standard. Cyclic voltammetry (CV) measurements of the polymer thin films were carried out under argon protection with

a BAS Epsilon EC electrochemical station employing a Pt working electrode, a silver wire reference electrode and a Pt wire counter electrode. In order to prepare a thin film, a drop of polymer solution was evenly spread on the bare surface of the Pt working electrode and air dried. A [Bu<sub>4</sub>N]PF<sub>6</sub> solution (0.1 M in acetonitrile) was used as the supporting electrolyte and the scan rate was 20 mV s<sup>-1</sup>. The potentials were calibrated using a Fc/Fc<sup>+</sup> redox couple whose absolute energy was assigned to be 4.80 eV vs vacuum. Time-resolved fluorescence measurements for **PS-Mo6-PT1-3** in solution were carried out using the same system and procedures as in our previously reported work.<sup>70,85,100</sup> The excitation power was less than 1.0 mW with a spot size of ~1.5 mm in diameter.<sup>100</sup> The instrument response function was estimated to be ~255 fs at full width at half maximum.

## 2) *Synthesis*

Polymers **P10** and **P11** were synthesized using the Stille coupling reactions, Scheme 1. The syntheses of monomers (3,3'-bis(dodecyloxy)-[2,2'-bithiophene]-5,5'-diyl)bis(tributylstannane) (**1**), 2,5-dibromo-9-(2-butyloctyl)-8*H*-dithieno[2',3':3,4;3'',2'':5,6]benzo[1,2-*f*]isoindole-8,10(9*H*)-dione (**2**), and diiodo-functionalized hexamolybdate **3**, as well as polymer **PBOR** have been previously reported.<sup>98,123</sup>

### ***Polymer P10***

To a Schlenk flask were added **1**, **2**, and **3** (with a molar ratio of 1:0.75:0.25). The flask was subjected to three pump-purge cycles with N<sub>2</sub> followed by the addition of anhydrous DMF (3 mL) via syringe. Pd<sub>2</sub>(dba)<sub>3</sub> (5 mol %) and P(*o*-tolyl)<sub>3</sub> (40 mol %) were then added to the flask under N<sub>2</sub> protection. The reaction flask was sealed, and the mixture was stirred at 120 °C for 24 h. After the reaction mixture was cooled to room temperature,

a small amount of tetrabutylammonium fluoride solution (1.0 M; in THF) was added into the reaction flask, and the mixture was stirred for 15 min. After filtration through a filter paper, the filtrate was added to methanol (30 mL) and the mixture was stirred overnight. The polymer precipitates were collected by centrifugation and washed repeatedly with ethanol. After drying at 50 °C in a vacuum oven for 3 d, polymer **P10** was obtained as a black solid (36% yield). <sup>1</sup>H NMR (400 MHz, CDCl<sub>3</sub>, 25 °C): δ 8.52 (br, Ar-H), 7.74 (br, thiophene-H), 4.25 (br, O-CH<sub>2</sub>-), 4.00 (br, Ph-CH<), 3.65 (br, N-CH<sub>2</sub>-), 3.30 (br, N<sup>+</sup>-CH<sub>2</sub>-), 1.95 (br, -CH<), 1.66 (br, -CH<sub>2</sub>-), 1.47-1.03 (m & br, -CH<sub>2</sub>-), 1.01 (m & br, -CH<sub>3</sub>), 0.87 (m & br, -CH<sub>3</sub>), 0.76 (m & br, -CH<sub>3</sub>) ppm. *M<sub>w</sub>* = 5.5 kDa, PDI = 1.50. Elemental analysis (ICP) for Mo: 10.78%.

### ***Polymer P11***

**P11** was synthesized using the same procedure as that for **P10** except that the molar ratio of **1**, **2**, and **3** was 1:0.5:0.5. **P11** was obtained as a black solid (56% yield). <sup>1</sup>H NMR (400 MHz, CDCl<sub>3</sub>, 25 °C): δ 8.52 (br, Ar-H), 7.75 (br, thiophene-H), 4.25 (br, O-CH<sub>2</sub>-), 4.00 (br, Ph-CH<), 3.65 (br, N-CH<sub>2</sub>-), 3.30 (br, N<sup>+</sup>-CH<sub>2</sub>-), 1.95 (br, -CH<), 1.66 (br, -CH<sub>2</sub>-), 1.60-1.03 (m & br, -CH<sub>2</sub>-), 0.98 (m & br, -CH<sub>3</sub>), 0.87 (m & br, -CH<sub>3</sub>), 0.77 (m & br, -CH<sub>3</sub>) ppm. *M<sub>w</sub>* = 3.7 kDa, PDI = 1.25. Elemental analysis (ICP) for Mo: 16.13%.

### ***3) Device Fabrication and Characterization***

ITO glass slides (1.5 cm × 1.5 cm) were patterned and cleaned following previously published procedures and were used as the substrates.<sup>19</sup> After a UV/ozone treatment for a minimum of 45 min, the ITO substrates were coated with a hole-conducting PEDOT:PSS layer (~45 nm thick) and then subjected to thermal annealing on a hotplate (~120 °C, 45 min) in air. Polymer solutions were prepared in glove box. The solutions were heated

overnight at 50 °C with stirring, passed through a 0.45  $\mu\text{m}$  filter and spin-coated on top of the PEDOT:PSS thin films. The resultant devices were dried under petri dishes and then transferred into a glove box full of  $\text{N}_2$ . Half of the devices were thermally annealed on a hot plate at 120 °C for 15 min in the  $\text{N}_2$  atmosphere. Subsequently, through a shadow mask, electrodes composed of 25 or 50 nm thick Ca and 100 nm thick Al were deposited on the top by thermal evaporation under high vacuum ( $< 2 \times 10^{-6}$  Mbar). The active area of the devices ( $0.14 \text{ cm}^2$ ) was defined by the overlap area of the ITO and the deposited Ca/Al electrodes. Current–voltage characteristics of the devices were measured under the illumination of an Oriel xenon arc lamp solar simulator at an intensity of  $100 \text{ mW cm}^{-2}$  (1-sun air mass 1.5 global illumination) using a Keithley 2400 source meter. Incident photon-to-current conversion efficiency (IPCE) spectra were recorded using a Newport QE-PV-SI/Ge QE/IPCE measurement kit.

#### 4) *FFU Measurements*

Time-resolved fluorescence measurements for **PS-Mo6-PT1-3** in solution were carried out using the same system and procedures as in our previously reported work.<sup>70,85,100</sup> The excitation power was less than 1.0 mW with a spot size of  $\sim 1.5 \text{ mm}$  in diameter.<sup>100</sup> The instrument response function was estimated to be  $\sim 255 \text{ fs}$  at full width at half maximum. The isotropic fluorescence was calculated by:  $F_{par} + 2G \cdot F_{per}$ , while fluorescence anisotropy ( $\gamma$ ) can be given by the equation:

$$\gamma = \frac{F_{par} - G \cdot F_{per}}{(F_{par} + 2G \cdot F_{per})} \quad (2-4)$$

where  $F_{par}$  and  $F_{per}$  are the fluorescence intensity for the parallel and perpendicular polarization, respectively;  $G$  factor was calibrated by measuring the polarized fluorescence

decay of perylene in toluene, which gives equal polarized fluorescence intensity after a complete rotational diffusion in tens of picoseconds.

Both the isotropic and anisotropic fluorescence dynamics data were fitted with a multi-exponential decay/rise model via the vFit program (CDP, Russia), in which the fluorescence signal  $F(t)$  can be theoretically expressed by convolution of the instrument response function  $r(t)$  with a molecule response function  $f(\tau)$ ,

$$F(t) = \int_0^{\infty} r(t - \tau)f(\tau)d\tau \quad (2-5)$$

where  $r(t)$  is a Gaussian function with laser pulse width and  $f(s)$  is given by:

$$f(\tau) = \sum_i A_i e^{-\frac{\tau}{\tau_i}} \quad (2-6)$$

where the factor  $A_i$  represents the relative weight (or amplitude) of the corresponding component, whose sign can distinguish the rising or decay process;  $\tau_i$  is the rising or decay time constant.

## CHAPTER 3

### NEAR INFRARED ABSORPTION POLYMERS WITH 3, 3'-DIALKOXY SUBSTITUTED BITHIOPHENE UNITS

#### 3.1. Introduction

Near-infrared (NIR) absorbing conjugated polymers are appealing for a variety of applications such as solar cells,<sup>98,116,124</sup> photodetectors,<sup>125,126</sup> sensors,<sup>127–131</sup> et al. A common and well-adopted approach to lower the bandgap of conjugated polymers is to alternate donor and acceptor segments in a polymer backbone.<sup>132–137</sup> While this approach can in principle achieve any bandgap by modulating the HOMO of the donor and LUMO of the acceptor, it has not yet been able to break the 900 nm absorption window.<sup>133,138</sup>

Other methods have also been explored to realize NIR-absorbing polymers, which include electrochemical oxidation or reduction,<sup>139–141</sup> chemical oxidation,<sup>142</sup> Lewis acid adduct,<sup>143–145</sup> and protonation,<sup>146–149</sup> etc. Conjugated polymers were first found to act as conducting materials when polyacetylene was chemically doped.<sup>140</sup> Meanwhile, the doped polymer showed a new broad absorption band in the NIR range. Electrochemical doping has been applied in many conjugated polymers to produce NIR absorption. The appearance of NIR bands is thought to be the results of the formation of polarons, bipolarons or solitons upon oxidation or reduction process, which forms subgap states.<sup>141</sup>

Lewis acid induced NIR absorption was reported by Gregory C. Welch on polymers containing a benzothiadiazole or a 2,1,3-azabenzothiadiazole unit in the backbone.<sup>143,145</sup> When Lewis acid  $B(C_6F_5)_3$  was added, the polymer absorption was extended to over 900 nm. The N-B Lewis base-acid interaction lowers the electron density

on the polymer backbone and thus the LUMO level, resulting in a decreasing in bandgap.<sup>143,145</sup>

Redshifted absorption can also be achieved for polymers containing Bronsted bases in the backbone through protonation. The above mentioned benzothiadiazol or azabenzothiadiazole based copolymers, for example, were shown to give absorption bands redshifted by 110 nm after protonation with trifluoroacetic acid (TFA).<sup>146-149</sup>

### 3.2. Objective

The objective of this research is to study a series of donor-acceptor conjugated polymers that exhibit well-defined NIR absorption bands. These polymers are based on substituted bithiophene units which act as electron donor and different comonomers from thiophenes to fused polycyclic aromatic hydrocarbons (PAHs) which act as electron acceptor. Their structures are shown in Figure 3-1. Five polymers **PTR**, **PTOR**, **PTD**, **PDR** and **PBOR**, combining different electron acceptors with substituted bithiophene units were studied. **PTR**, **PTOR**, and **PTD** are new polymers not reported previously. So their synthesis, electrochemical properties and application in solar cells are also presented.

The specific research objectives are:

- 1) To design and synthesize new donor-acceptor conjugated copolymers with NIR absorption bands.
- 2) To investigate their optical and electrochemical properties.
- 3) To study their photovoltaic properties.

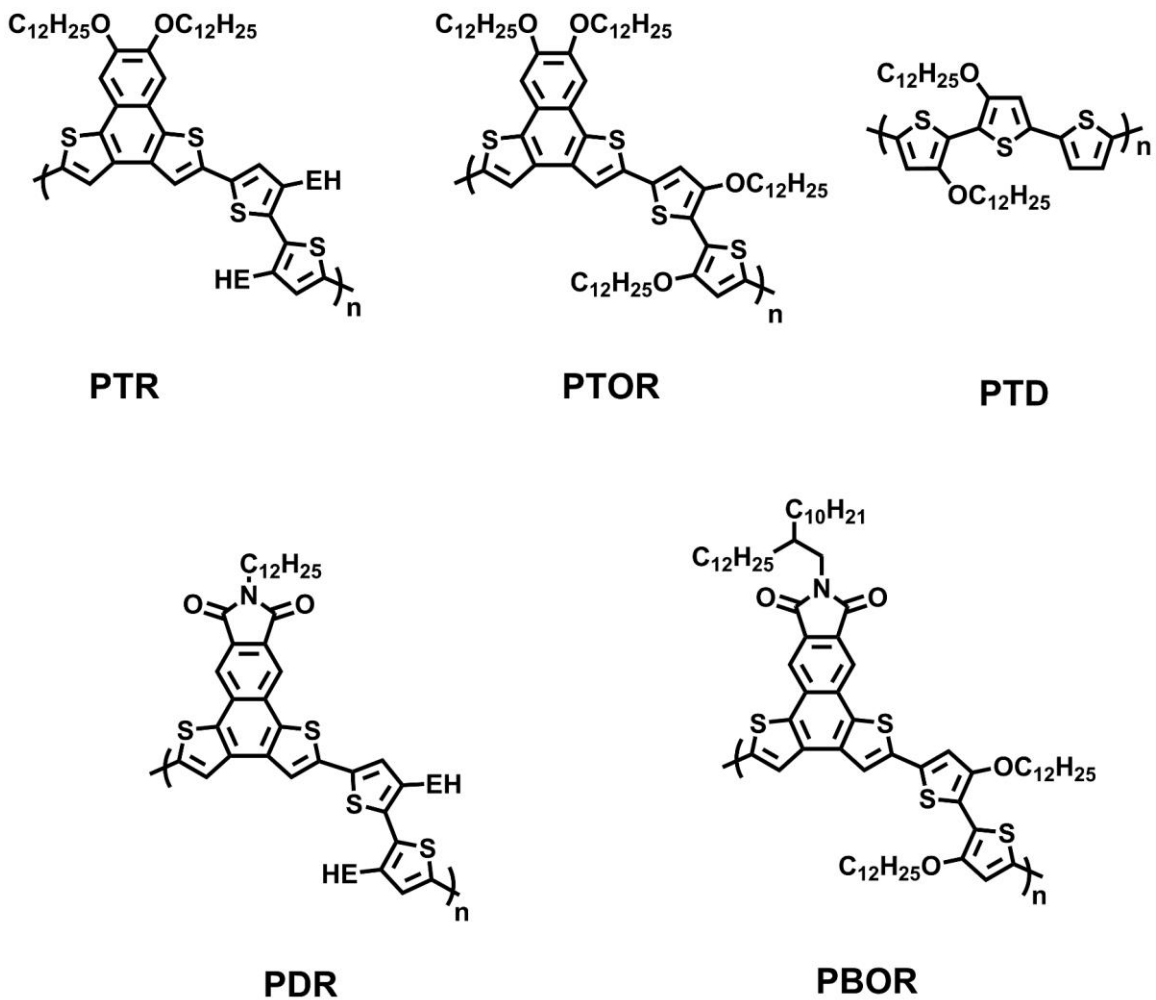


Figure 3-1 Structures of conjugated copolymer **PTR**, **PTOR**, **PTD**, **PDR** and **PBOR** (EH: 2-ethylhexyl group).

### 3.3. Results

#### 3.3.1. Synthesis

The synthesis of **PDR** and **PBOR** has been reported previously.<sup>98</sup> Figure 3-2 shows the synthetic route of the three new conjugated copolymers. All three polymers were synthesized by the Stille Coupling polycondensation reaction. The dibromo-functionalized naphthodithiophene (NDT) monomer **1** and the di(tributyl)tin-functionalized comonomers **2a** (substituted with branched 2-ethylhexyl groups) and **2b** were prepared following published procedures.<sup>98,123</sup> All three polymers have good solubility in common organic solvents such as chloroform, THF and *o*-dichlorobenzene, at room temperature. The <sup>1</sup>H NMR spectrum of **PTR** show clear broadened peaks. The spectra of **PTOR** and **PTD**, however, show only some broad humps in the aromatic region.

Gel permeation chromatography (GPC) was performed to estimate polymer molecular weights with THF as the eluent and polystyrene as the standard. The number average molecular weight (Mn) was found to be 6.0, 6.4 and 5.2 KDa for **PTR**, **PTOR** and **PTD**, respectively, with relatively narrow polydispersity indexes of 1.33, 1.35 and 1.40, respectively.

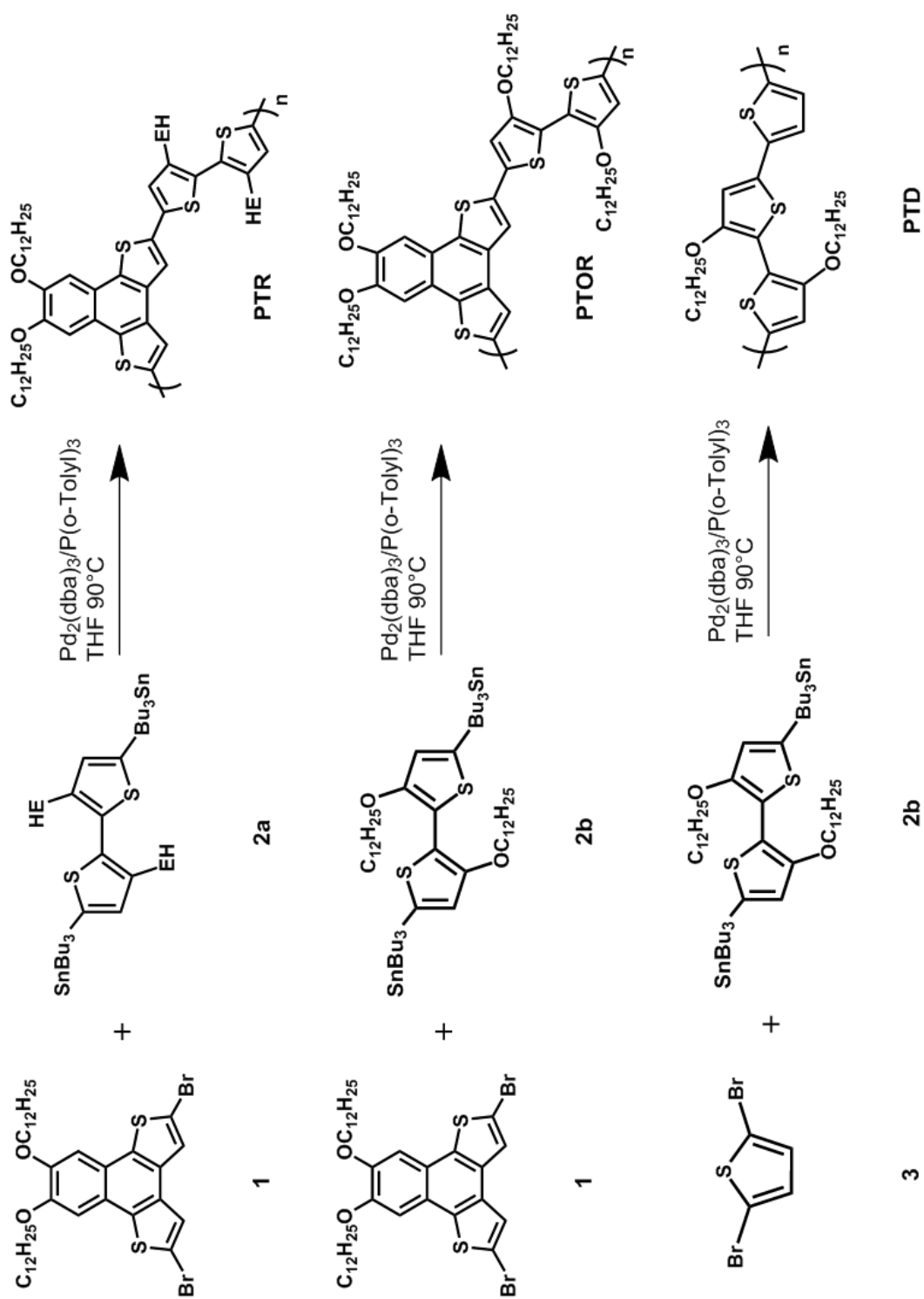


Figure 3-2 Synthetic route of polymers **PTR**, **PTOR** and **PTD**.

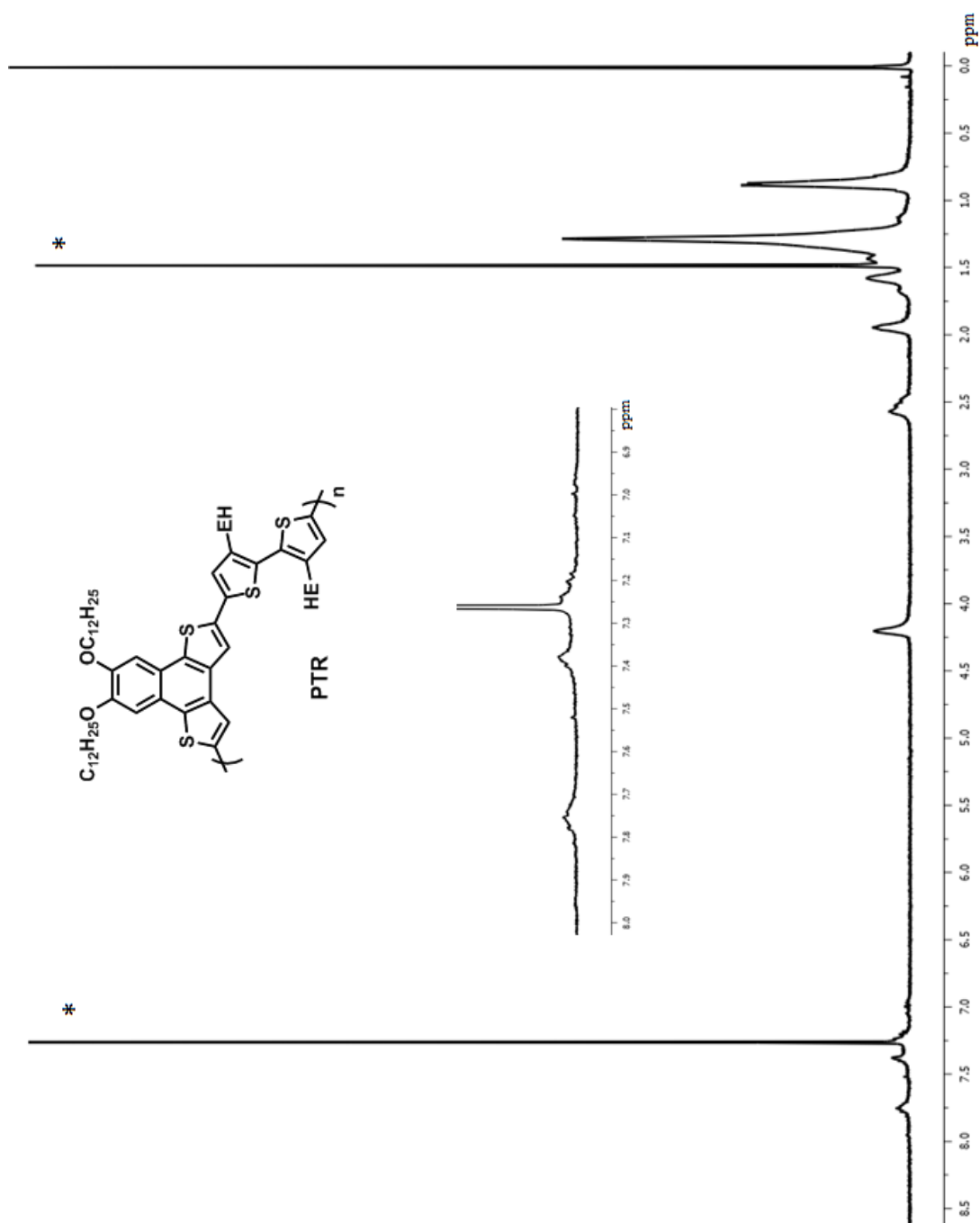


Figure 3-3  $^1\text{H}$  NMR spectra of **PTR** in  $\text{CDCl}_3$  at room temperature.

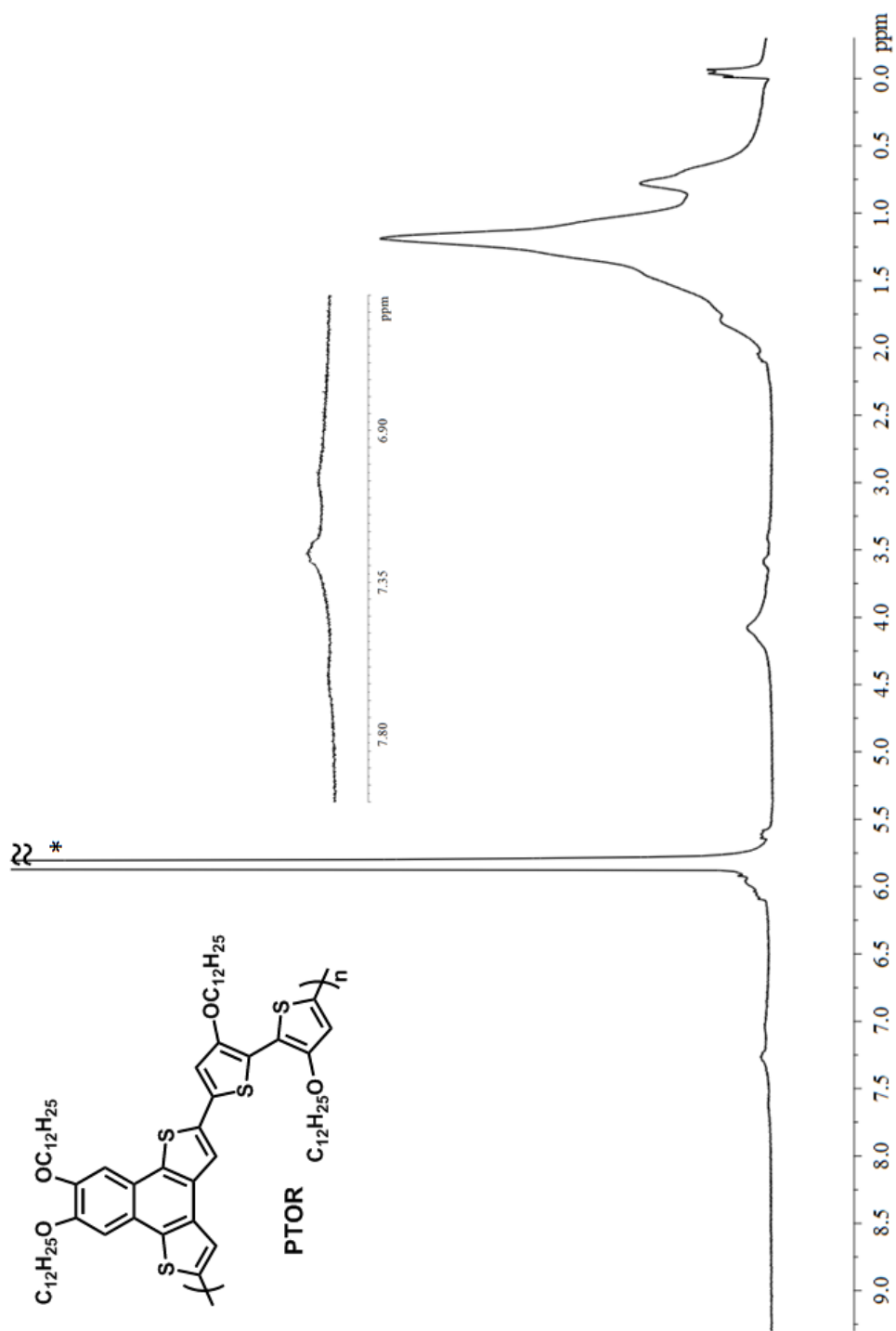


Figure 3-4  $^1\text{H}$  NMR spectra of **PTOR** in  $\text{C}_2\text{D}_2\text{Cl}_4$  measured at 348 K.

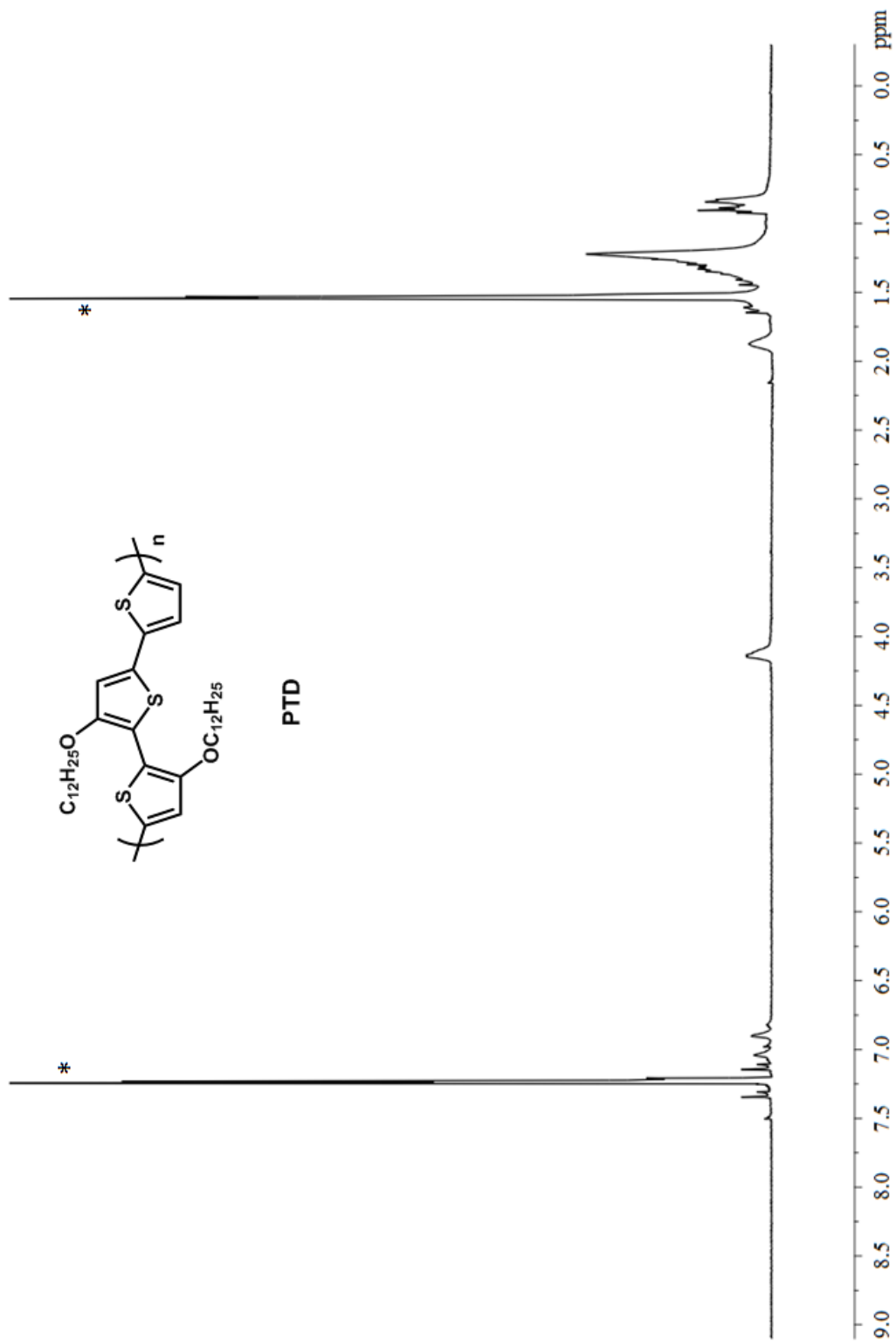


Figure 3-5  $^1\text{H}$  NMR spectra of **PTD** in  $\text{CDCl}_3$  at room temperature.

### 3.3.2. Theoretical calculation

To understand the geometrical structure and electronic states of the polymers, theoretical calculations were carried out on the trimers of all three polymers. In order to simplify the calculation, all the dodecyl groups in the three polymers and long branched alkyl chains in **PTR** were replaced by methoxy and methyl groups, respectively. The geometrical optimization was performed on the Gaussian 03w program with density functional theory (DFT) calculation at the B3LYP 631G(d) level. Figure 3-6 shows the optimized conformers for the three trimers. The dihedral angles between monomers and the S-O distance were summarized in Table 3-1. The dihedral angles between the two thiophene rings in the 3,3'-disubstituted bithiophene is significantly smaller in the alkoxy substituted bithiophene than that of alkyl substituted bithiophene (less than 1° in **PTD** and **PTOR** versus 57° in **PTR**). The near-planar bithiophene orientation in **PTOR** and **PTD** trimer can be attributed to the S-O short contact. The computed S-O distance in the energy minimized structure was found to be 2.85 Å, shorter than the sum of their van der Waals radii (3.32 Å).<sup>98</sup> The dihedral angles between NDT and the adjacent thiophene average around 13° for **PTR** and 11° for **PTOR**. Based on the computation results, the backbone planarity for the three trimers is in the order of **PTD** > **PTOR** >> **PTR**, similar trend was observed in our previous study.<sup>98</sup>

The highest occupied molecular orbital (HOMO) and lowest unoccupied molecule orbital (LUMO) energy levels of **PTD**, **PTOR** and **PTR** were estimated based on the optimized structures of the trimers described above. The HOMO/LUMO distributions on energy minimized structures are shown in Figure 3-8 and the energy levels are summarized in Table 3-2. The HOMO/LUMO energy levels are -4.08/-1.99 eV, -4.30/-1.85 eV and -

4.84/-1.77 eV for **PTD**, **PTOR** and **PTR**, respectively. And the bandgaps are found to be 2.09 eV, 2.45 eV and 3.07 eV, respectively. Detailed discussion on energy levels and bandgaps will be presented in the following sections.

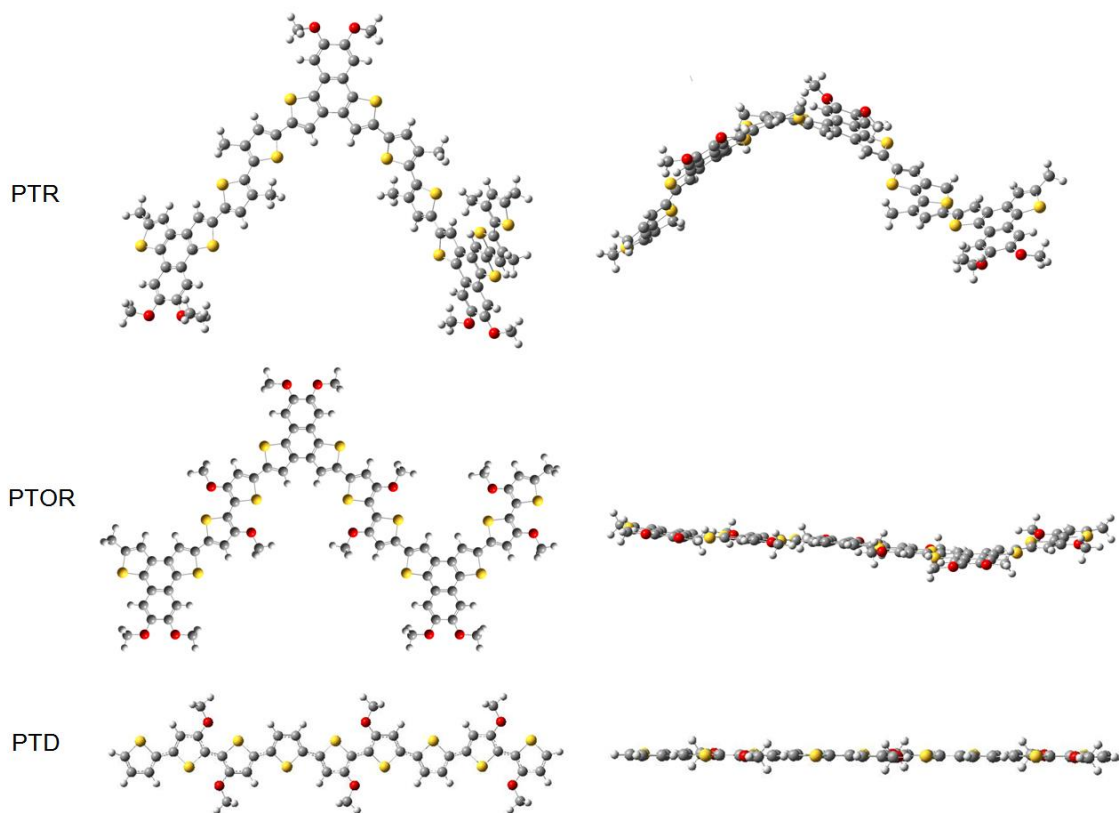


Figure 3-6 Energy minimized structures of **PTR**, **PTOR** and **PTD** from different views obtained from DFT calculations at the B3LYP/6-31G(d) level.

Table 3-1 Calculated dihedral angles and S-O short contact distances.

Compound	Intermonomer twist		Comonomer twist		S---O short contact (Å)
	$\theta_1$	$\theta_1'$	$\theta_2$	$\theta_2'$	
<b>PTR</b>	13.53	13.30	57.03	56.95	N/A
<b>PTOR</b>	4.71	-16.86	0.29	-0.69	2.85
<b>PTD</b>	-0.00029	0.00057	0.00037	0	2.85

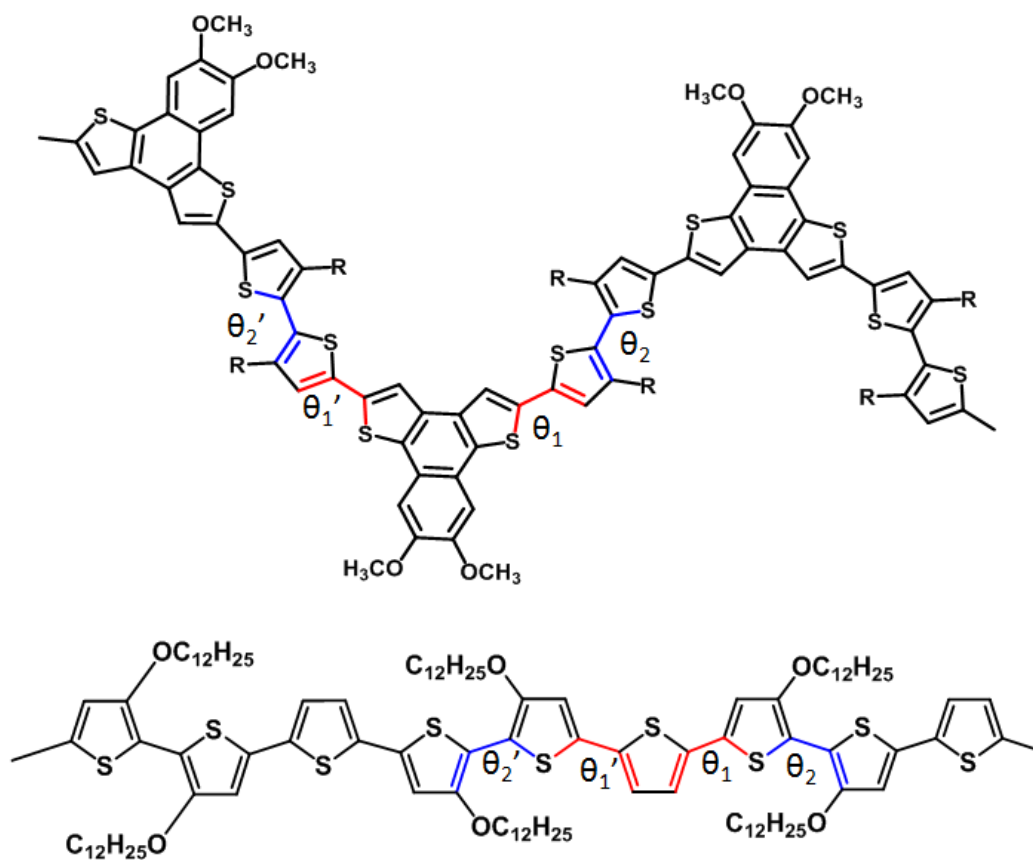


Figure 3-7 Schemes of dihedral angles of trimers.

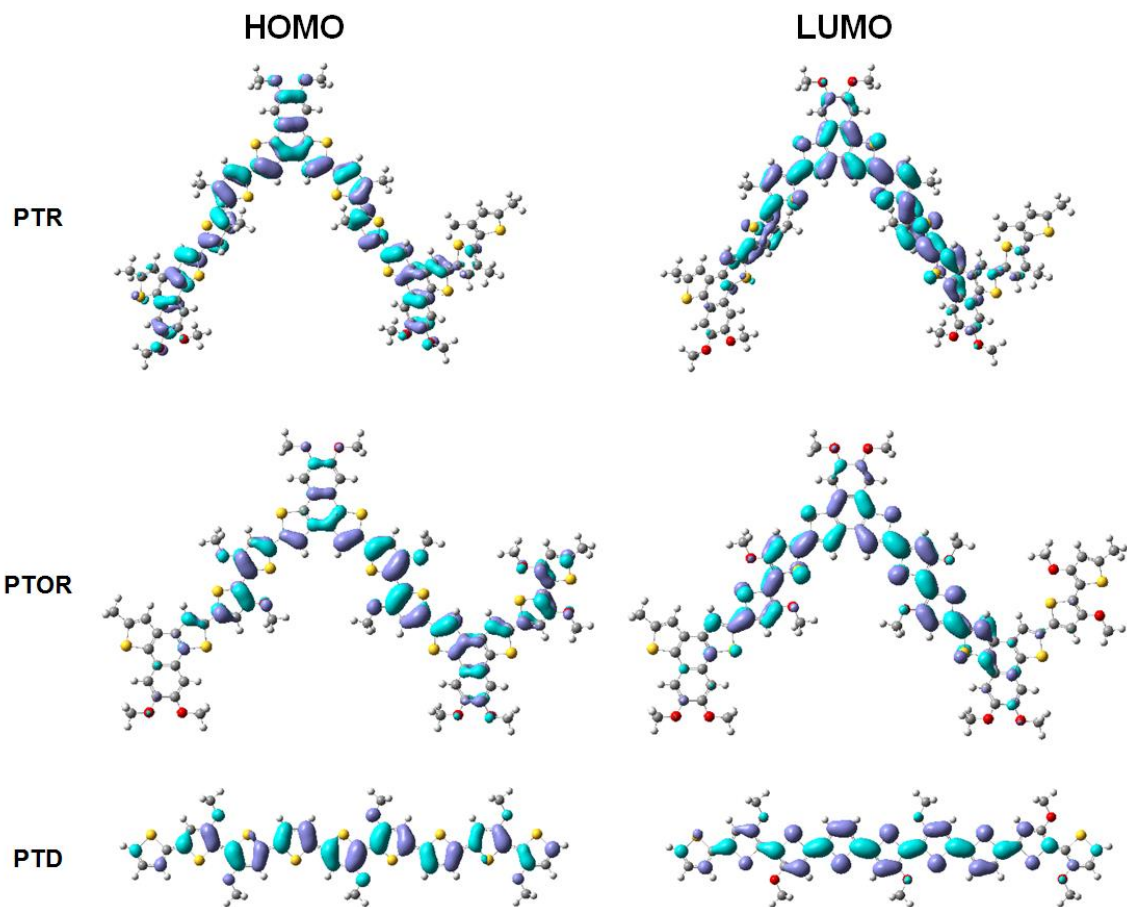


Figure 3-8 Visualized HOM/LUMO orbitals of **PTR**, **PTOR** and **PTD** from different views obtained from Gaussian 03w at the B3LYP/6-31G(d) level.

### 3.3.3. Electrochemical Properties

The electrochemical properties for the three polymers were investigated as thin films using cyclic voltammetry measurements. As shown in Figure 3-9, **PTR** and **PTOR** show an irreversible reduction peak and two reversible or semi-reversible oxidation processes. **PTD** shows a reversible reduction peak with two irreversible oxidation processes. The onset of the first oxidation wave in anodic scan and the onset of the

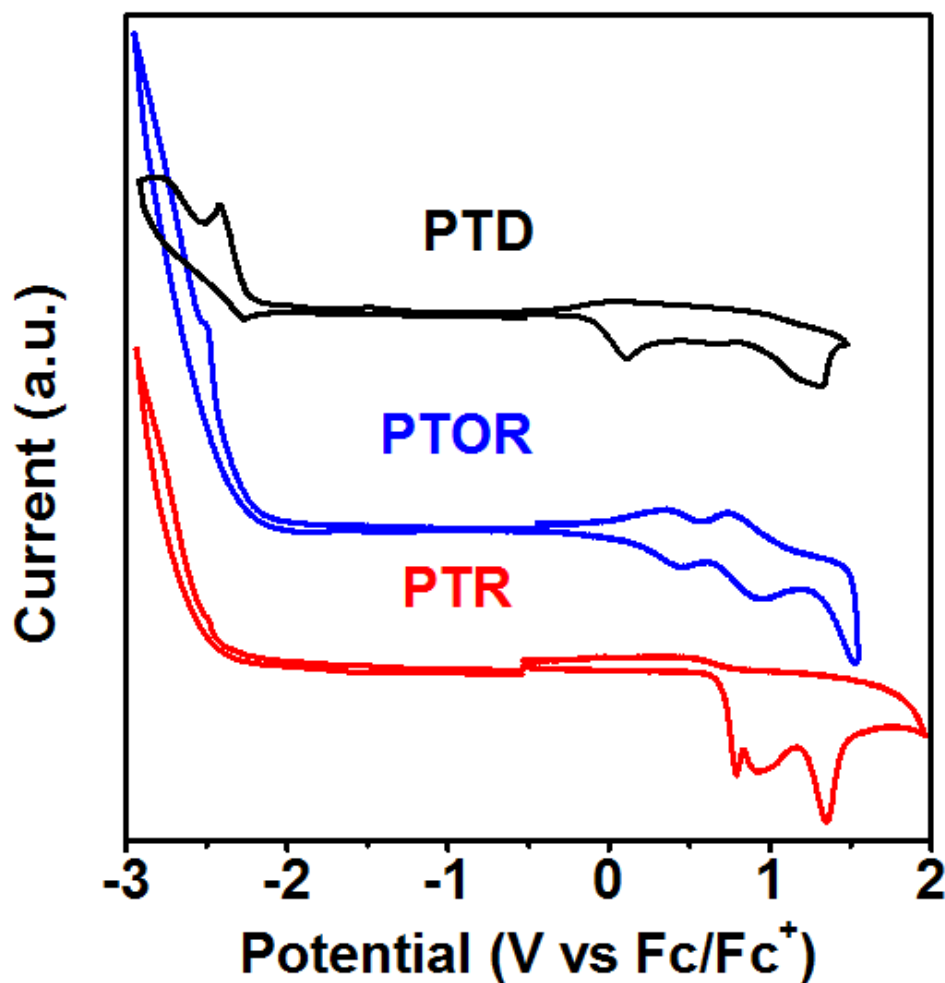


Figure 3-9 Cyclic voltammograms of polymer thin films, scale corrected based on Fc/Fc<sup>+</sup>.

reduction wave in cathodic scan were used in the calculation of HOMO and LUMO energy levels, which were estimated to be -4.70/-2.53, -4.91/-2.60 and -5.50/-2.40 eV for **PTD**, **PTOR**, and **PTR**, respectively. **PTD** and **PTOR** have similar HOMO levels. The alkoxy groups have a stronger electron donating effect than alkyl groups do, which makes the two polymers easier to be oxidized and thus higher HOMO levels. The higher planarity of **PTD** and **PTOR** backbone also helps raise the HOMO levels and decreases the bandgaps due to better  $\pi$ -conjugation. On the other hand, the highly twisted backbone of **PTR** and the weaker electron donating alkyl groups on the bithiophene unit contribute to its lower HOMO and a wider bandgap. The bandgap of **PTD**, **PTOR** and **PTR** are calculated to be 2.17, 2.31, and 3.10 eV, respectively. The values of energy levels and bandgaps obtained from CV measurements closely match those obtained by computational calculations.

#### 3.3.4. Optical properties

The absorption spectra of **PTR**, **PTOR** and **PTD** in both dilute solutions and as thin films are shown in Figure 3-10. All of the solution spectra were measured in chloroform. **PTR** shows only one narrow peak at 387 nm while **PTOR** shows three well-defined absorption bands at 487, 730 and 1095 nm. The NIR absorption has also been observed for **PTD** which shows an absorption band at 546 nm and a broad hump from 700 nm to 1200 nm. The maximum absorption wavelength ( $\lambda_{\text{max}}$ ) of the three polymers increases from **PTR**, **PTOR** and **PTD**, consistent with results obtained from DFT calculations and CV measurements. The optical bandgaps, calculated from the band-edges of the maximum absorption peak of **PTR**, **PTOR** and **PTD** in films, are 2.58, 2.04 and 1.90 eV, respectively. It is noted that these bandgap values are lower than those obtained from CV measurements. The larger bandgap values obtained from CV studies may be

caused by the barrier at the interface between the polymer film and the electrode. Similar phenomenon has been observed in other polymer systems.<sup>150</sup>

When absorption spectra of the polymer films are compared with their respective solution spectra, one notices only a slight red-shift/broadening in  $\lambda_{\text{max}}$  for **PTR** (6 nm) and **PTOR** (11 nm), but a significant redshift (46 nm) for **PTD**. NIR absorptions observed on **PTOR** and **PTD**, on the other hand, show a slight blue shift. The larger red-shift observed on **PTD** is likely due to its more planar backbone structure resulting in stronger  $\pi$ - $\pi$  interchain stacking interactions.

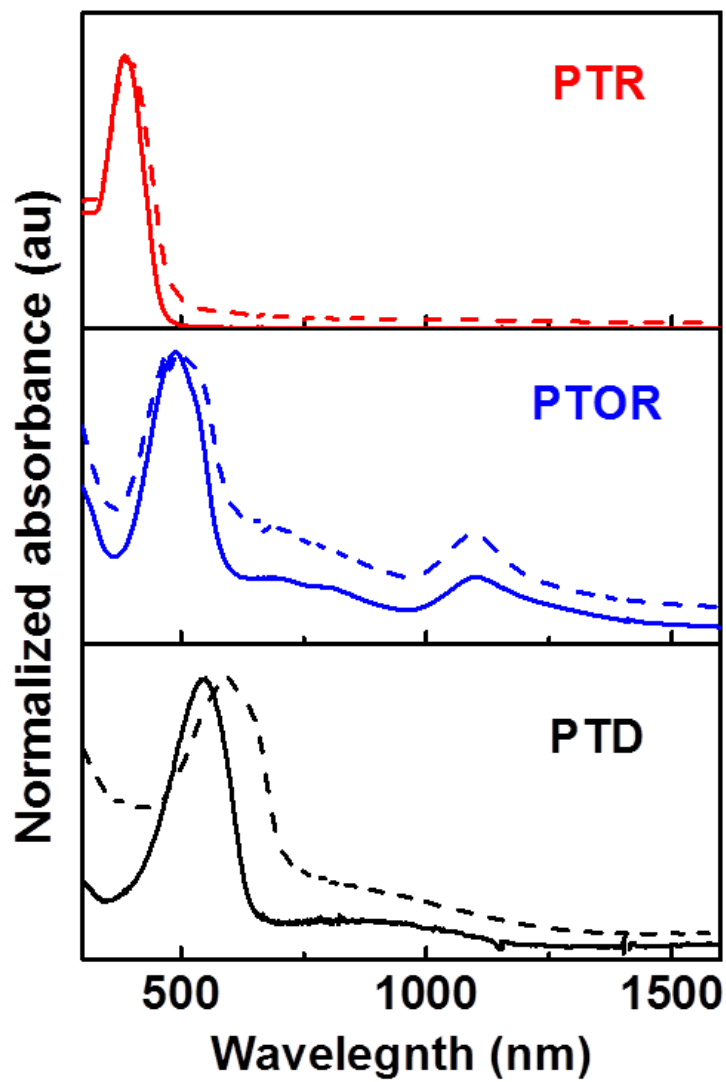


Figure 3-10 Normalized UV-vis-NIR absorption spectra in chloroform solutions (solid lines) and as thin films (short dots).

Table 3-2 Optoelectronic properties of **PTR**, **PTOR** and **PTD**

Polymer	$\lambda_{max}^{abs}$ (nm)		$\lambda_{max}^{fl}$ (nm)		$E_g^{opt}$ (eV) <sup>a</sup>	$\Phi^b$	Experimental <sup>c</sup>			Calculated <sup>d</sup>			
	CHCl <sub>3</sub>	THF	Film	CHCl <sub>3</sub>			Film	$E_{HOMO}$ (eV)	$E_{LUMO}$ (eV)	$E_g^{CV}$ (eV)	$E_{HOMO}$ (eV)	$E_{LUMO}$ (eV)	$E_g^{DFT}$ (eV)
<b>PTR</b>	387	386	393	505	524	2.53	0.093	-5.50	-2.40	3.10	-4.84	-1.77	3.07
<b>PTOR</b>	487	484	498	542	-	1.91	0.030	-4.91	-2.60	2.31	-4.30	-1.85	2.45
<b>PTD</b>	546	548	592	629	-	1.68	0.024	-4.70	-2.53	2.17	-4.08	-1.99	2.09

<sup>a</sup>The optical band gap was calculated by  $E_g^{opt} = 1240/\lambda_{onset}^{abs}$  (eV),  $\lambda_{onset}^{abs}$  is absorption onset of polymer film. <sup>b</sup>Fluorescence quantum yield was calculated for dilute CHCl<sub>3</sub> solutions for **PTOR**, **PTR** and **PTD**. <sup>c</sup>CV measurement for thin film. <sup>d</sup>DFT calculation at the B3LYP 631G(d) level for trimers.

All three polymers are weakly fluorescent in solutions while only **PTR** and **PTOR** show detectable fluorescence in thin films. As shown in Figure 3-11, **PTR** gives one relatively narrow emission band with a shoulder band in both solution and solid state. The emission spectra are independent of the excitation wavelength and the excitation spectra are independent of the emission wavelength, indicating that there is only one kind of emitting excitons corresponding to the non-aggregated backbone emission.<sup>98</sup> Among the three polymers, **PTR** is most fluorescent with a solution fluorescence quantum yield of 0.093. Both **PTOR** and **PTD** exhibit weak fluorescence in solutions and are nearly non-fluorescent in the solid state. The fluorescence emission spectrum of **PTD** solution shows one broad featureless emission band ( $\lambda_{\text{max}}^{\text{fl}}$ ) at 629 nm. The emission spectrum of **PTOR**, on the other hand, show two emission bands at 542 and 586 nm. The intensity ratio of emissions at 586 nm over 542 nm decreased when the solution is further diluted, indicating that the emission at 586 nm is likely due to polymer aggregates (intramolecular excimer emission) while that at 542 nm comes from non-aggregated polymers.<sup>98</sup> The fact that even in extremely dilute solutions (concentration lower than  $10^{-5}$  M) the emission intensity at 586 nm is comparable to that at 542 nm confirms that there is strong inter-chain aggregation even in extremely dilute solution. The aggregation likely accounts for its lower fluorescence quantum yields.<sup>98</sup>

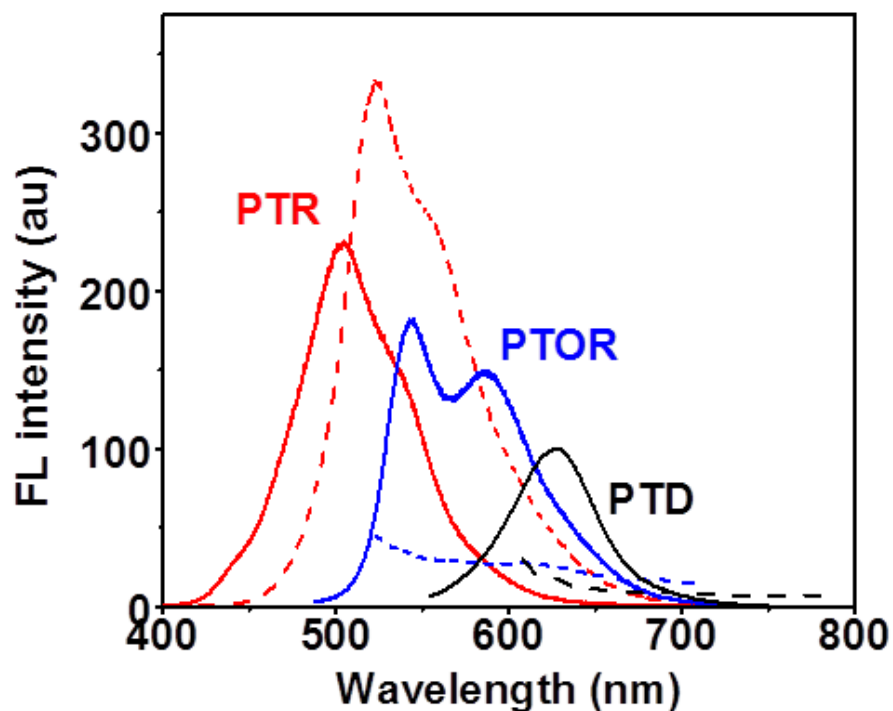


Figure 3-11 Emission spectra of **PTR**, **PTOR** and **PTD** (excited at 544/594, 386/390, and 480/494 nm for **PTD**, **PTR** and **PTOR** solution/film, respectively) in solutions (solid line) and as films (dash line).

The UV-vis-NIR absorption of **PTOR** and **PTD** has been studied in different solvents, as shown in Figure 3-12. For **PTOR**, three solvents including chloroform, THF and *o*-dichlorobenzene have been used. There are prominent absorption bands in the NIR range only in chloroform solution. It is noted that the NIR absorbance is stronger when **PTOR** was dissolved in chloroform that has been set on shelf for a longer time. For **PTD**, the UV-vis-NIR spectrum has been examined in chloroform and THF solutions. As mentioned earlier, a hump from around 700 nm to 1200 nm is observed in chloroform solutions, while no NIR absorption is observed in the THF solutions.

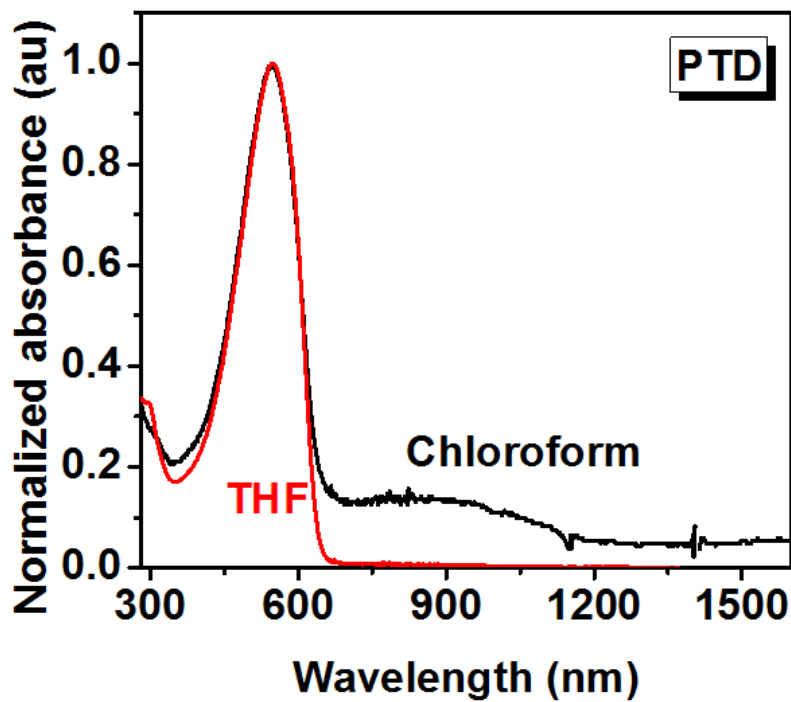
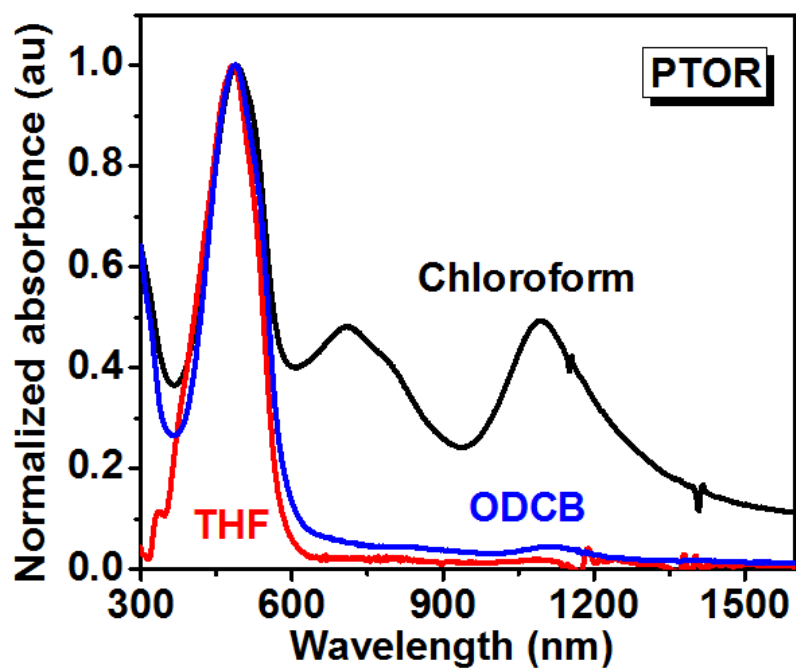


Figure 3-12 UV- vis- NIR absorption spectra of **PTOR** (up) and **PTD** (down) in different solvents.

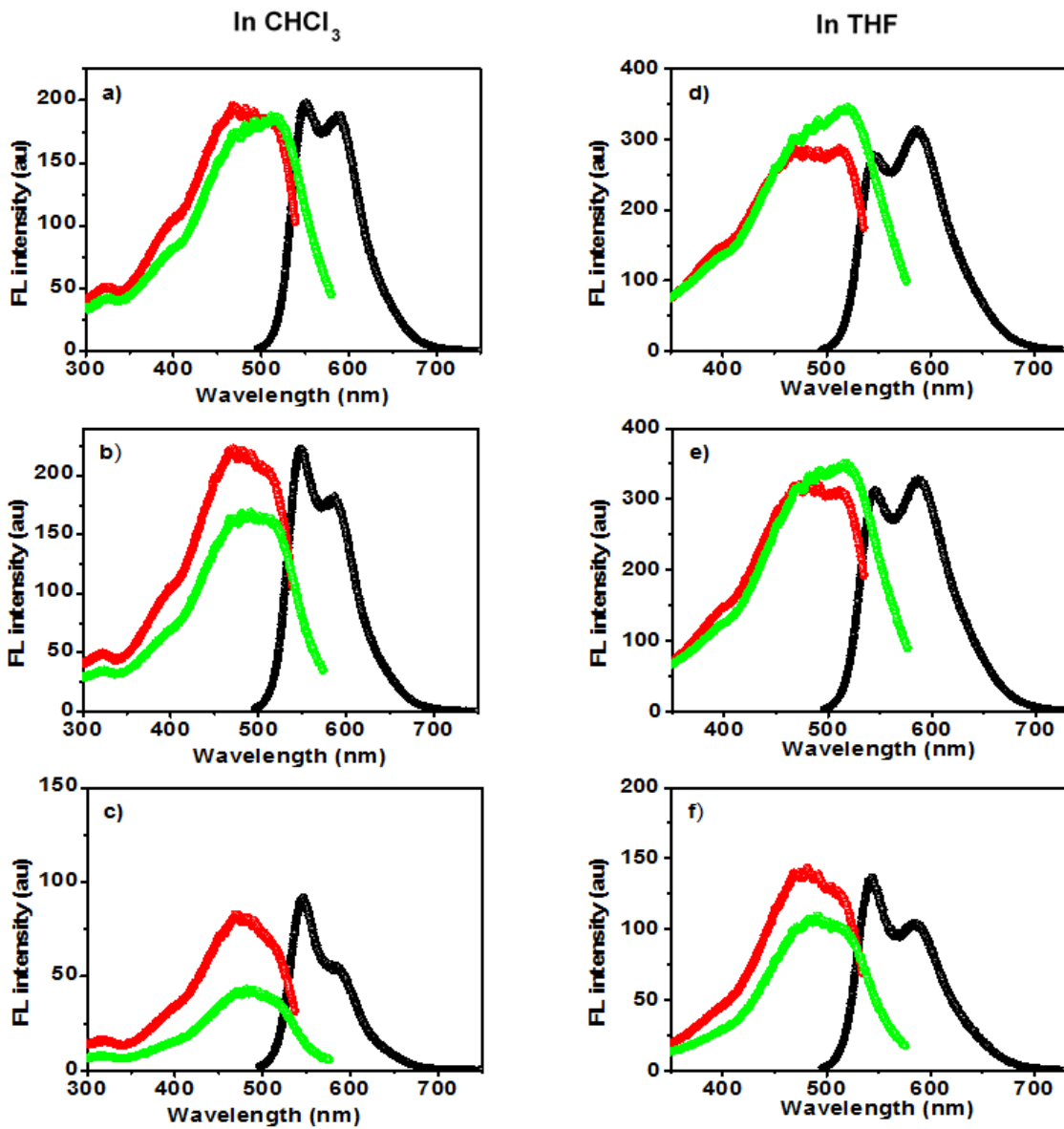


Figure 3-13 Emission and excitation spectra of **PTOR** in  $\text{CHCl}_3$  (a-c) and THF (d-f), corresponding absorbance at  $\lambda_{\text{max}}$  for (a, d), (b, e) and (c, f) is 0.9, 0.7 and 0.1 respectively.

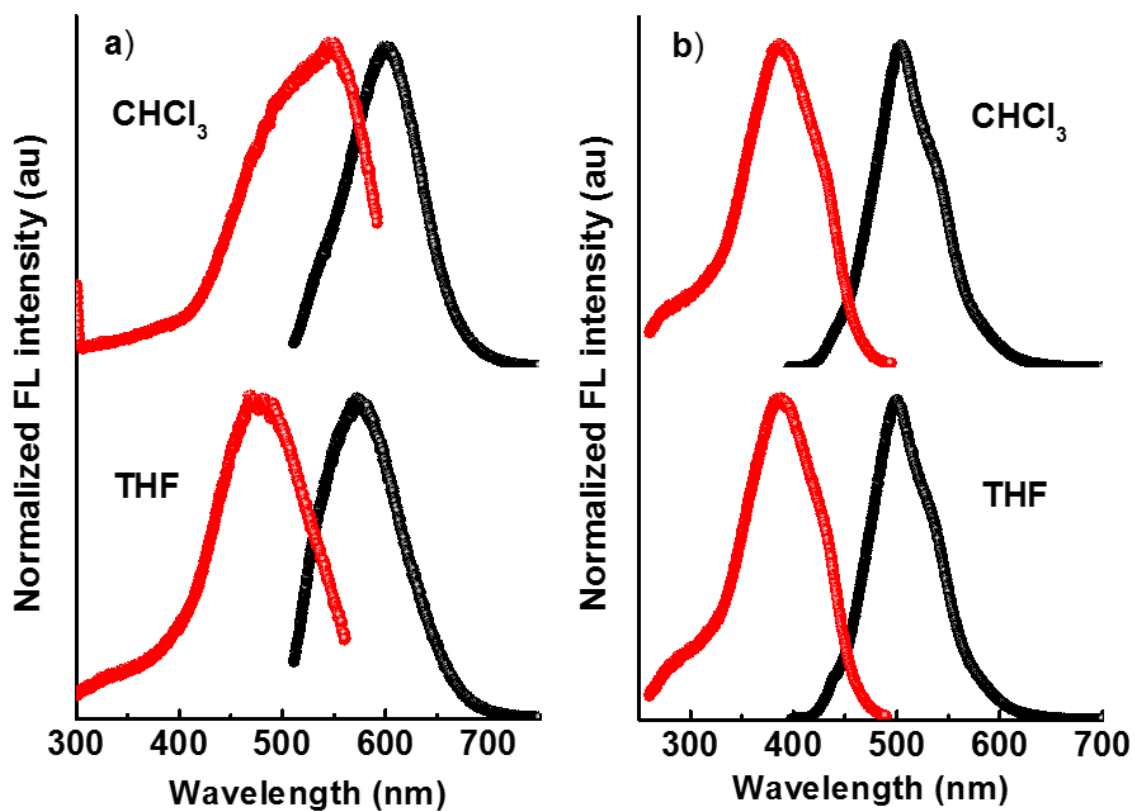


Figure 3-14 Emission (black) and excitation (red) spectra of **PTD** (a) and **PTR** (b) in THF or CHCl<sub>3</sub> solutions. Emission spectra were excited at 511/511 nm and 386/388 nm in THF/CHCl<sub>3</sub> solutions for **PTD** and **PTR**, respectively. Excited spectra were emitted at 571/602 nm for **PTD** and 500/504 nm for **PTR** in THF/CHCl<sub>3</sub> solutions, respectively.

The appearance of NIR absorptions in chloroform is likely due to the protonation of some 3,3'-didodecyloxy bithiophene end functional units by the residual acid in chloroform as commercial chloroform usually contains trace amount of acid as a result of photolysis.<sup>117,151</sup> This explanation is corroborated by the observation of similar NIR absorption when *p*-toluenesulfonic acid is added to the THF solution of the **PTOR** polymer. As shown in Figure 3-15, **PTOR** in THF has no absorption bands in NIR range. When *p*-toluenesulfonic acid is added, however, two new absorption bands with  $\lambda_{\text{max}}$  at 730 nm and 1078 nm appeared. When the above solution was neutralized with triethylamine, the absorbance in the NIR range is decreased. Similar phenomenon was observed for **PTD**, a new band at  $\lambda_{\text{max}}$  of 895 nm and another band (or tail) beyond 1500 nm appeared after the addition of *p*-toluenesulfonic acid. These results confirm that the NIR absorption is indeed due to the protonation of the polymers.

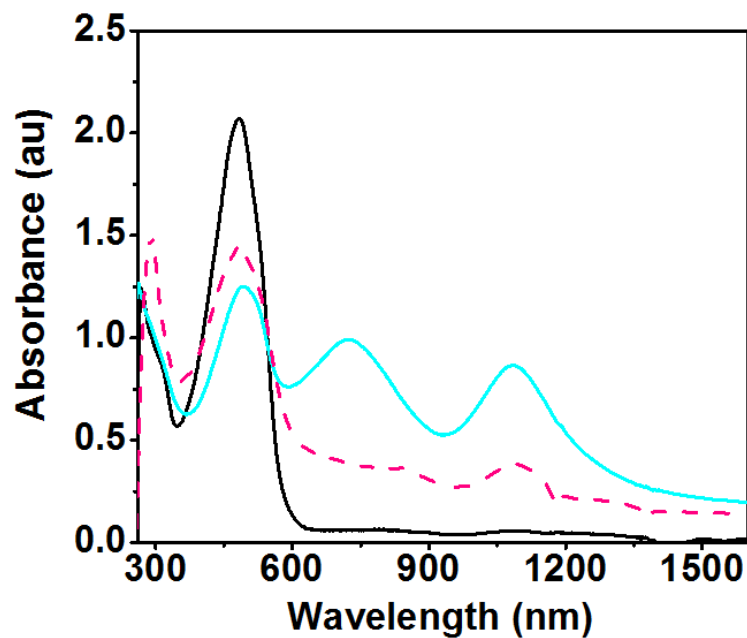


Figure 3-15 UV-vis-NIR absorption spectra of **PTOR** (black), **PTOR** with addition of TSOH (blue) and then neutralized with base (red dash).

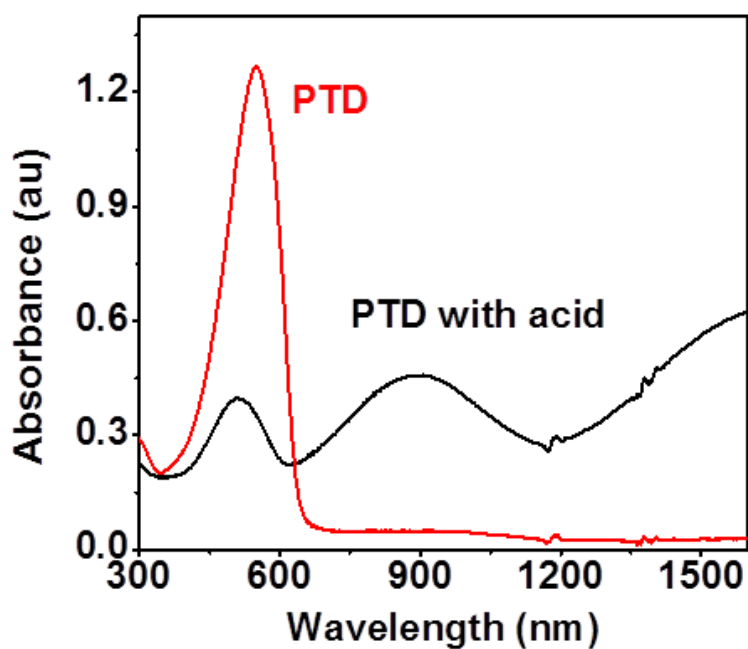


Figure 3-16 UV-vis-NIR absorption spectra of **PTD** before (red) and after addition of TSOH (black).

To study quantitatively the protonation effect, THF solutions of **PTOR** and **PTD** with known concentrations were prepared. A THF solution of *p*-toluenesulfonic acid (TSOH) with the concentration of  $7.63 \times 10^{-3} \text{ mol L}^{-1}$  was then added in small portions. The UV-vis-NIR spectra of the solutions after each acid addition were recorded. For each solution, the mole ratio of TSOH added versus polymer repeating unit was calculated. As shown in Figure 3-17, **PTR** and **PDR**, both of which contain the highly twisted 3,3'-diakylbithiophene monomer units, show no changes in absorption when acid even up to 16 equiv. is added. The other three polymers (**PTOR**, **PBOR** and **PTD**), all containing the planar 3,3'-diakoxy-substituted bithiophene, show new NIR absorption bands when acid is added. As the amount of acid increased, the NIR absorption bands increase while the initial absorption band in the visible range decreased. A clear isosbestic point is observed for all three polymers, indicating a protonation-induced transition between two structural forms.<sup>152</sup> As sufficient TSOH is added, the NIR absorption saturates. The TSOH concentrations for NIR saturation are 10, 4 and 2 equiv. for **PBOR**, **PTOR** and **PTD**, respectively. This order is consistent with the  $\pi$ -electron density and the HOMO levels of the three polymers.<sup>98</sup> **PBOR** has an electron-withdrawing imido-substituted NDT repeating unit while the NDT unit in **PTOR** has two electron-donating alkoxy substituents. As a result, **PTOR** has a higher electron density, making it easier to be protonated. As discussed earlier, **PTD** has an even higher electron density and thus higher HOMO than that of **PTOR** due to its more planar backbone structure.

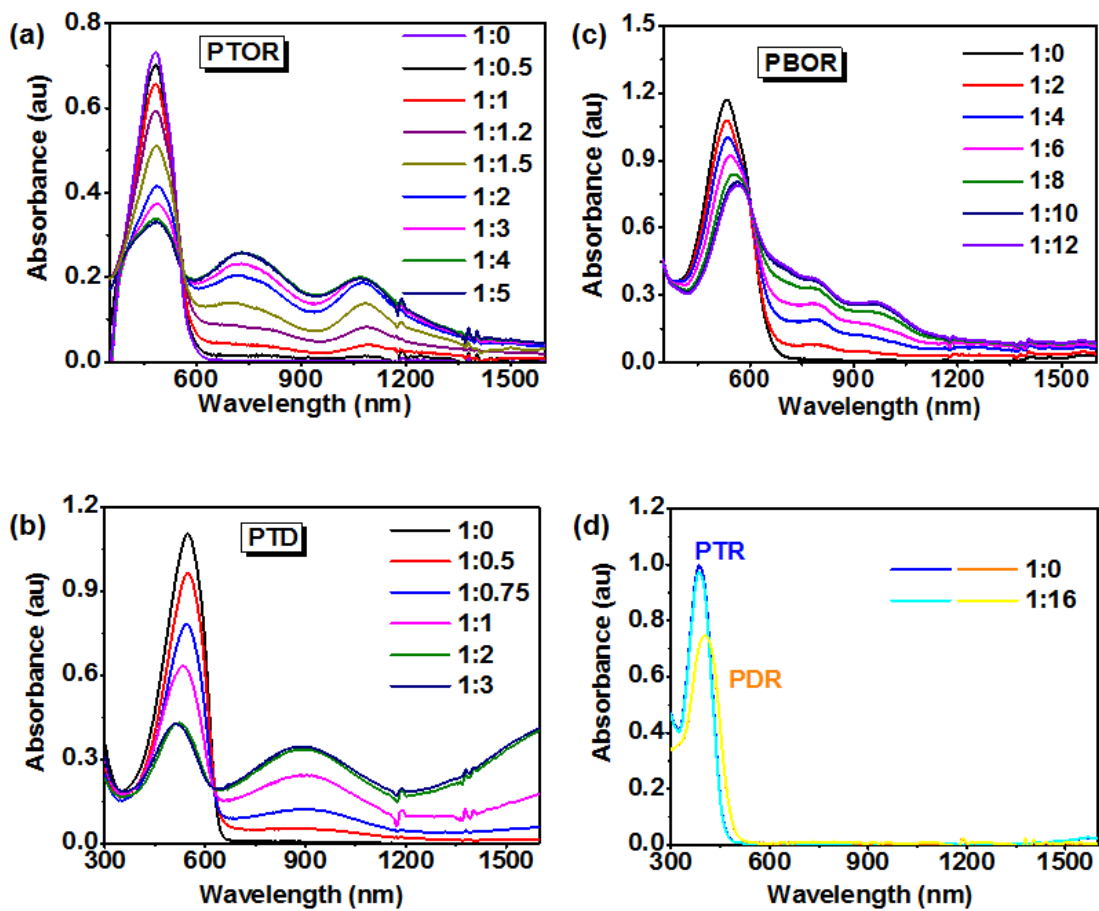


Figure 3-17 UV-vis-NIR absorption spectra of **PTOR**, **PBOR**, **PTD**, **PTR** and **PDR** with different polymer: acid ratio.

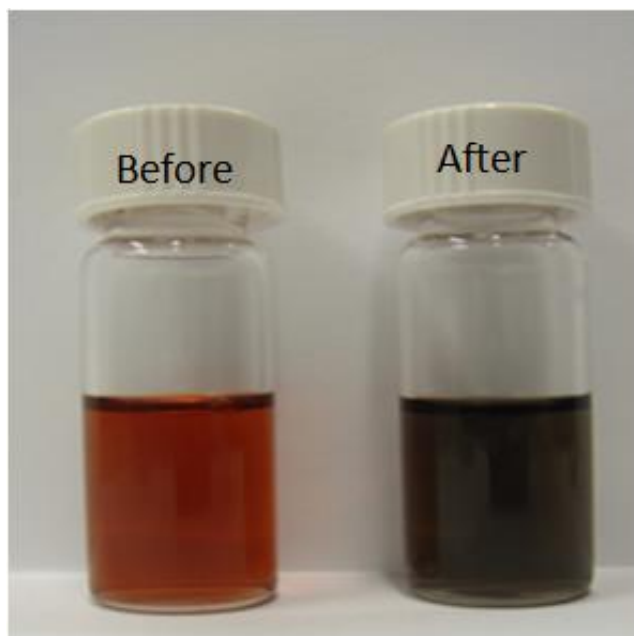
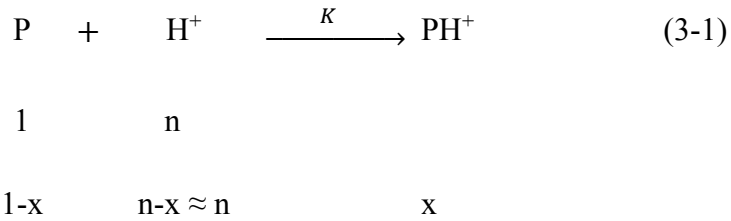


Figure 3-18 Color change in **PTOR** dilute THF solutions before (left) and after (right) addition of TSOH.



Figure 3-19 Color change in **PTD** dilute THF solutions before (left) and after (right) addition of TSOH.

Clearly, the 3,3'-dialkoxy substituted bithiophene plays a critical role in the protonation-induced NIR absorption. It is plausible that under acidic conditions, the end bithiophene unit undergoes electrophilic addition of  $H^+$  to the  $\alpha$ -carbon (or C-2) of the end thiophene ring (see Figure 3-20). The resulting carbocation can be resonance stabilized by the backbone  $\pi$ -system, leading to intra-chain charge transfer transitions that give rise to NIR absorptions. The equilibrium between the neutral polymer form (P) and the end-protonated form ( $PH^+$ ) (see Equation 3-1) depends mostly on the stability of the resulting carbocation. Thus, electron donating groups can facilitate protonation while electron withdrawing groups destabilize it. In other words, the equilibrium constant  $K$  is the largest for **PTD** and lowest for **PBOR**.



$$K = \frac{x}{n(1-x)} \quad (3-2)$$

$$x = \frac{Kn}{1+Kn} \quad (3-3)$$

Assuming the initial neutral polymer concentration of 1, the amount of acid added is  $n$  equivalent of the polymer concentration, the equilibrium concentration of the protonated form is  $x$ , the equilibrium concentration of the neutral polymer form is  $1-x$  and the equilibrium proton concentration ( $[H^+]$ ) is  $n-x \approx n$  (since  $x \leq 1$  while  $n \gg 1$ ). The protonated form concentration  $x$  can then be expressed as  $Kn/(Kn+1)$ . When  $Kn \gg 1$ ,  $x = 1$  and is independent of  $n$ . The larger the  $K$  is, the lower the  $n$  is required to realize  $x = 1$

(saturation), which is what has been observed in the previously described experiments. Based on the acid ratio of 1:2, 1:4 and 1:10 for **PTD**, **PTOR** and **PBOR**, respectively, one can estimate that the protonation equilibrium constant ratio of  $K_{PTD} : K_{PTOR} : K_{PBOR}$  is about 10:4:2 (5:2:1). It also worth noting that from **PBOR** to **PTOR** and to **PTD**, the NIR absorption wavelengths shift further into longer wavelengths. While the longest wavelength absorption band for **PBOR** is at 971 nm, it is at 1078 nm for **PTOR** and beyond 1600 nm for **PTD**.

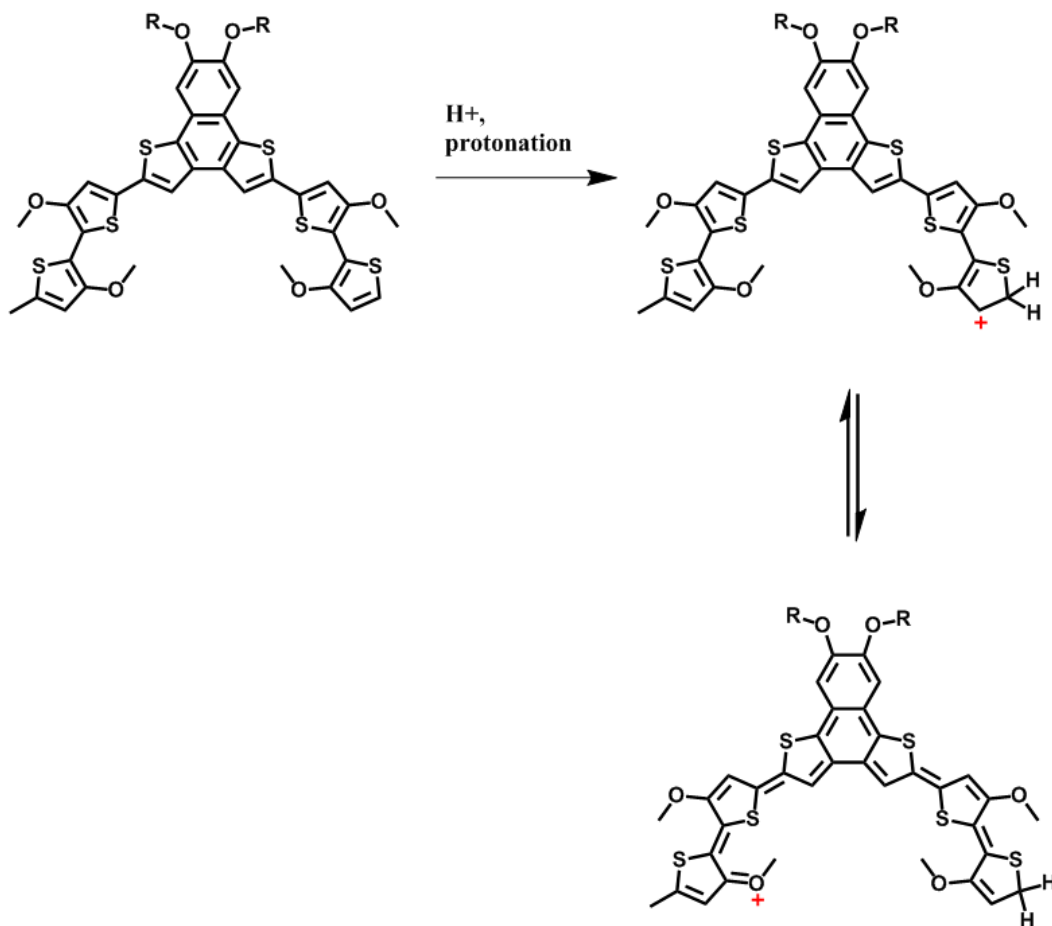


Figure 3- 20 Scheme of protonation in **PTOR**.

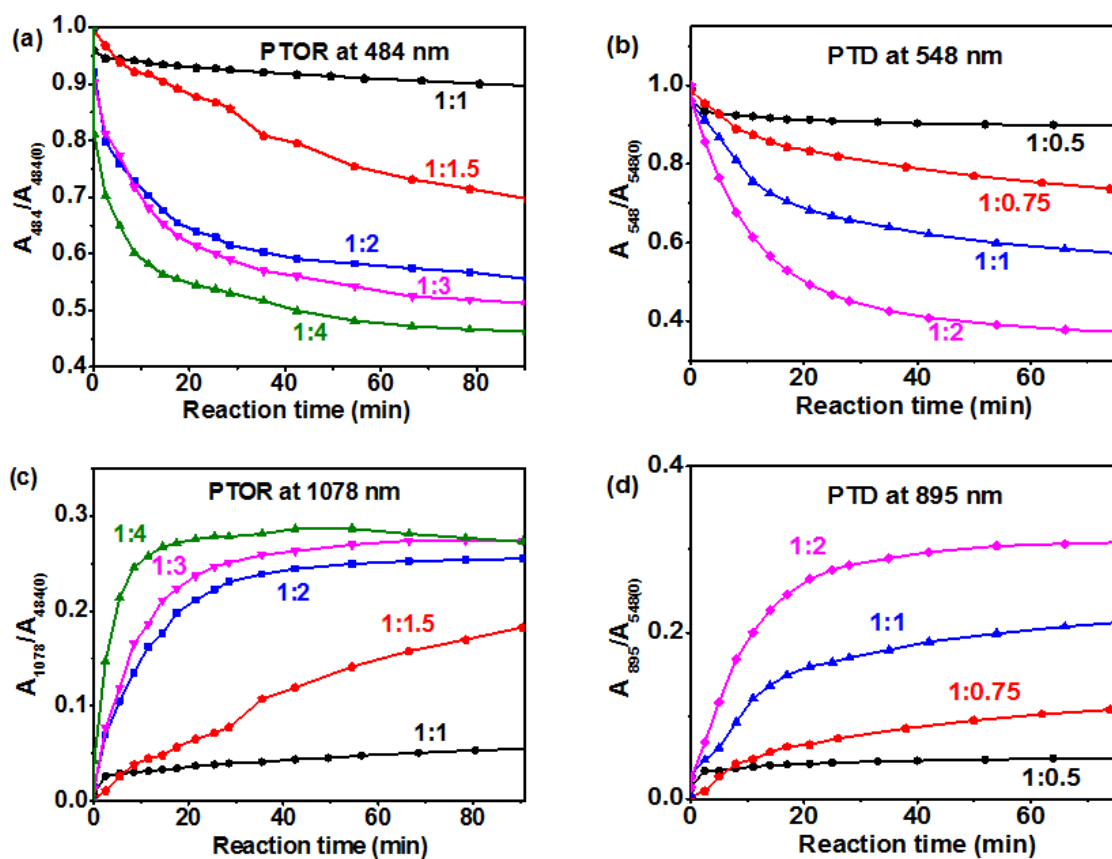


Figure 3- 21 UV-vis-NIR absorbance ratio as a function of the reaction time at selected wavelengths in protonation process of **PTOR** (a,  $A_{484}/A_{484(0)}$ ; c,  $A_{1078}/A_{484(0)}$ ) and **PTD** (b,  $A_{548}/A_{548(0)}$ ; d,  $A_{895}/A_{548(0)}$ ) at different polymer: acid ratio.  $A_{484(0)}$  and  $A_{548(0)}$  are the absorbance of initial neutral **PTOR** and **PTD**, respectively.

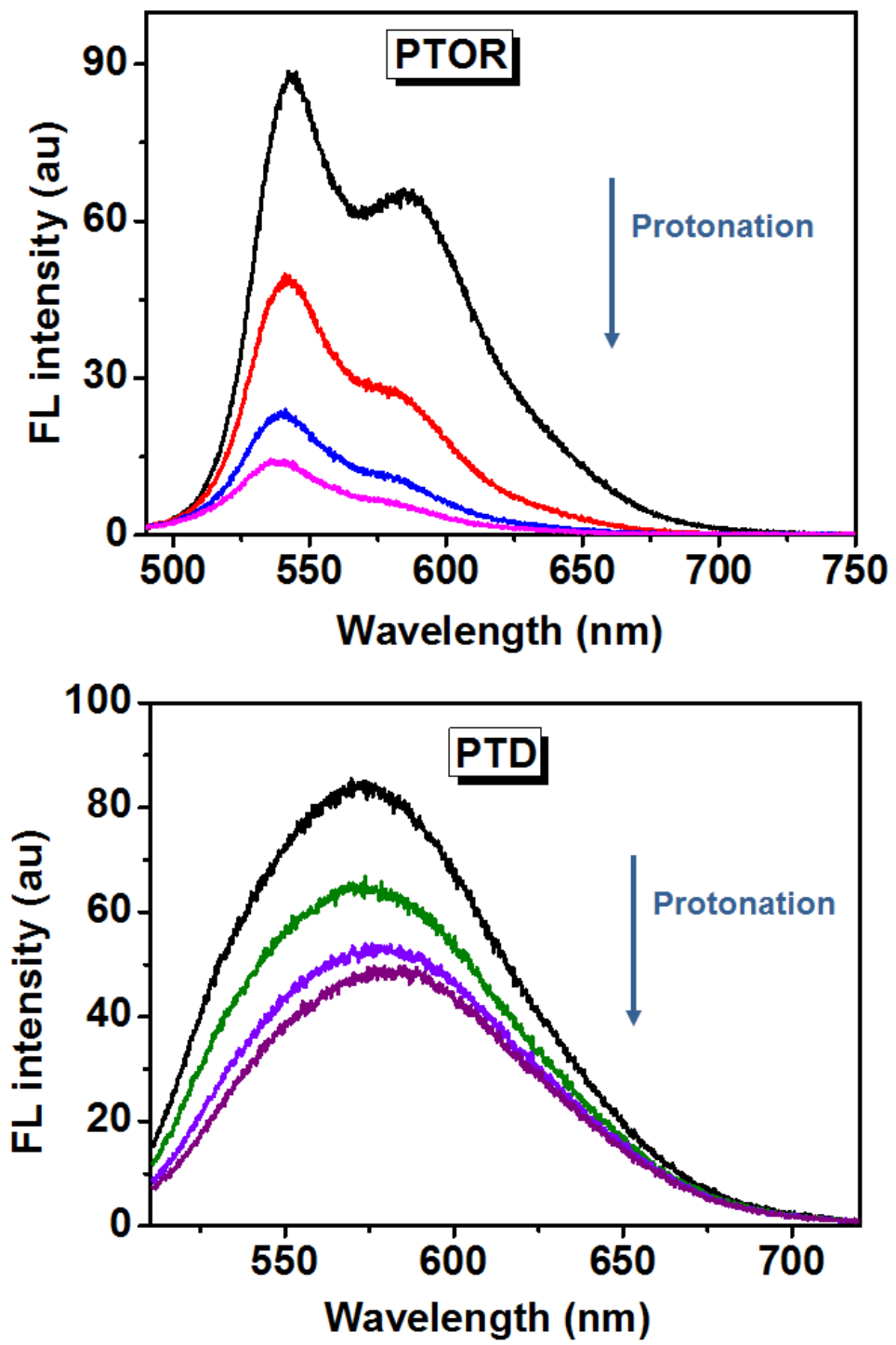


Figure 3- 22 Fluorescence intensity vs. time of PTOR (top) and PTD (bottom) at certain acid concentrations.

The dynamics of the protonation reaction has also been studied for **PTD** and **PTOR** by monitoring the UV-vis-NIR spectra versus time after the addition of specific amount of acid. As shown in Figure 3-21 the concentration of the neutral polymer [P] decreases exponentially while the concentration of the protonated form [PH<sup>+</sup>] increases exponentially, indicating a first order reaction kinetics.

The electrophilic aromatic addition reaction is first order to both the electrophile (H<sup>+</sup> in this case) and the aromatic substrate (P in this case). The reaction rate, expressed as the decreasing rate of the neutral polymer concentration [P] or the increasing rate of the production concentration [PH<sup>+</sup>] can be described as the following:



$$-\frac{d[P]}{dt} = \frac{d[PH^+]}{dt} = k[P][H^+] \quad (3-5)$$

Where  $k$  is the reaction rate constant. Under the condition of excess [H<sup>+</sup>] (note that the acid ratios shown in Figure 3-21 are equivalent numbers to the polymer repeating unit. Therefore, for all the experimental conditions, [H<sup>+</sup>] is at least one order of magnitude higher than [P]), [H<sup>+</sup>] can be regarded as a constant.  $k[H^+] = k'$ . The concentration of [P] or [PH<sup>+</sup>] versus time can then be expressed as:<sup>153</sup>

$$\frac{[P]}{[P]_0} = e^{-k't} \quad (3-6)$$

where [P] is the neutral polymer concentration at time  $t$  while [P]<sub>0</sub> is the initial neutral polymer concentration before the addition of acid. Assuming each polymer has by average one end bithiophene group, then the [PH<sup>+</sup>] can be expressed as:

$$[PH^+] = [P]_0 - [P] = [P]_0(1 - e^{-k't}) \quad (3-7)$$

When half of the polymer is protonated,  $[P] = [PH^+] = 0.5[P]_0$ , the time  $t$  is  $t_{1/2}$ , based on which  $k'$  can be estimated as following:

$$k' = \frac{\ln 2}{t_{1/2}} \quad (3-8)$$

From Figure 3-21 (a, c), for **PTOR**, the  $t_{1/2}$  is obtained to be 35.5 min (2130 s) and  $k'$  and  $k$  are calculated to be  $3.25 \times 10^{-4} \text{ s}^{-1}$  and  $2.32 \text{ L mol}^{-1} \text{ s}^{-1}$ , respectively. For **PTD**, the  $t_{1/2}$  is obtained to be 21 min (1260 s) and  $k'$  and  $k$  are calculated to be  $5.5 \times 10^{-4} \text{ s}^{-1}$  and  $4.20 \text{ L mol}^{-1} \text{ s}^{-1}$ , respectively.

### 3.3.5. Photostability

The photostability of **PTOR** was studied in both THF and chloroform solutions. The THF or chloroform solution of **PTOR** was exposed to a xenon arc lamp solar simulator. The UV-vis-NIR absorption of the solution was monitored versus time. As shown in Figure 3-23, the NIR absorptions in chloroform increased initially (in the first few minutes) and then dropped continuously as the time of exposure is extended. Even after continuous exposure for an hour, the NIR absorption bands are still significant, indicating the good photostability of the protonated form. In THF solution, no NIR absorption is observed before or after being exposed to a solar simulator.

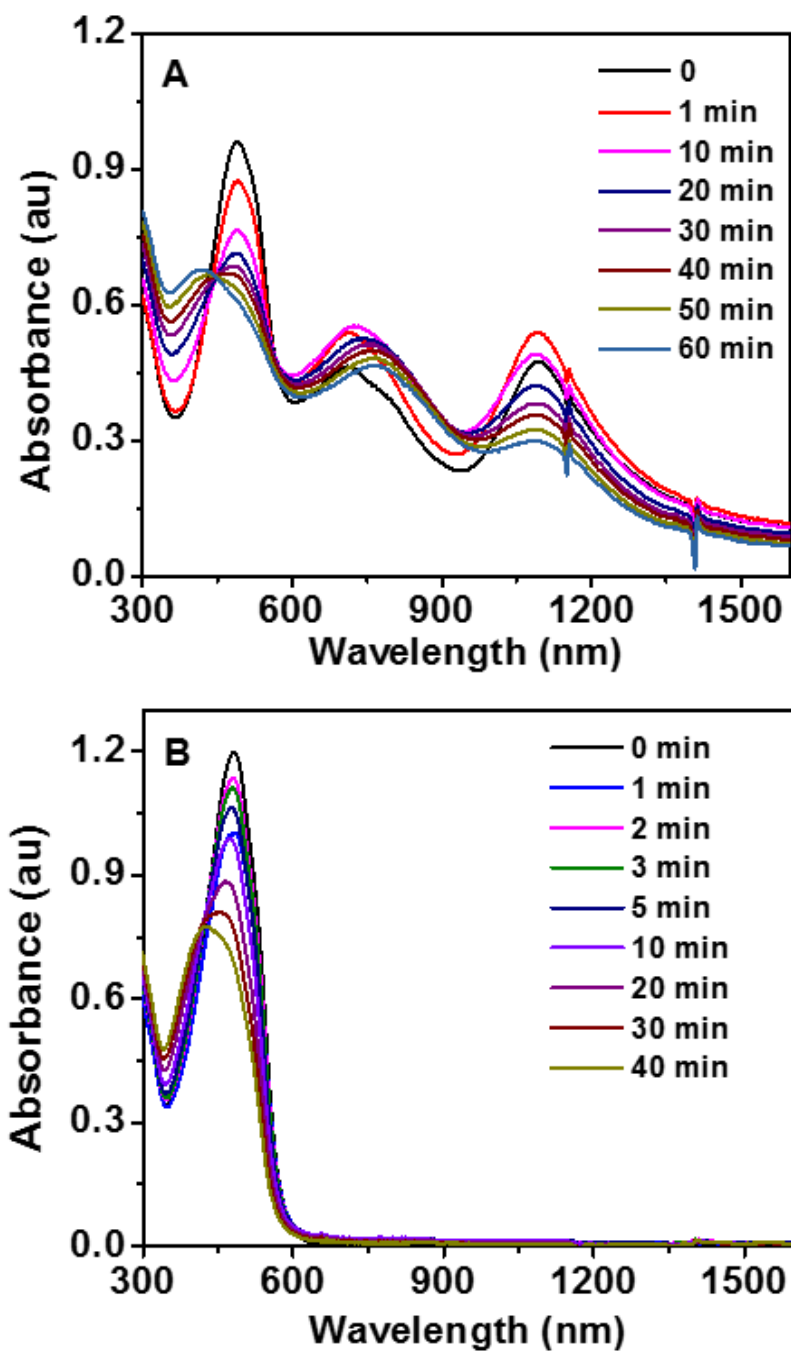


Figure 3-23 UV-vis-NIR absorption spectra of **PTOR** in chloroform (A) and THF (B) solutions illuminated by a solar simulator.

### 3.3.6. Photovoltaic properties

Bulk heterojunction (BHJ) solar cells were fabricated to investigate the photovoltaic properties. **PTOR** was chosen due to its suitable absorption wavelength range and matched energy levels with fullerene where **PTOR** acted as the electron donor and [6,6]-phenyl-C<sub>71</sub>-butyric acid methyl ester (PC<sub>71</sub>BM) was used as the electron acceptor. The device structure, as shown in Figure 3-24(b), consisted of indium tin oxide (ITO)/PEDOT:PSS/polymer:PC<sub>71</sub>BM/Ca/Al. With an initial 1:1 **PTOR**/PC<sub>71</sub>BM weight ratio, the mixture was spin-casted onto a PEDOT:PSS coated ITO substrates from either an *o*-dichlorobenzene (ODCB) solution or a chloroform solution. Some of the devices fabricated from chloroform solutions had *p*-toluenesulfonic acid (TSOH) added for the purpose of increasing the absorbance in the NIR range. Top Ca/Al electrode was then deposited onto the active layer through thermal evaporation. All device performance evaluations were done under ambient conditions. Thermal annealing has been performed on half of the devices before depositing the top electrode. Unfortunately, all thermally annealed devices spin-coated from chloroform solutions failed. It is possible that the residual or added acid reacted with the top electrode. Figure 3-25 shows the UV-vis-NIR absorption spectrum of the device films drop-casted from respective solutions on quartz substrates in order to avoid the interference of NIR absorptions from ITO substrates. All films show NIR absorption on quartz substrates. With the addition of TSOH, enhanced absorption in the NIR range is observed. Films spin-coated from *o*-dichlorobenzene show similar NIR absorptions to those from chloroform solutions.

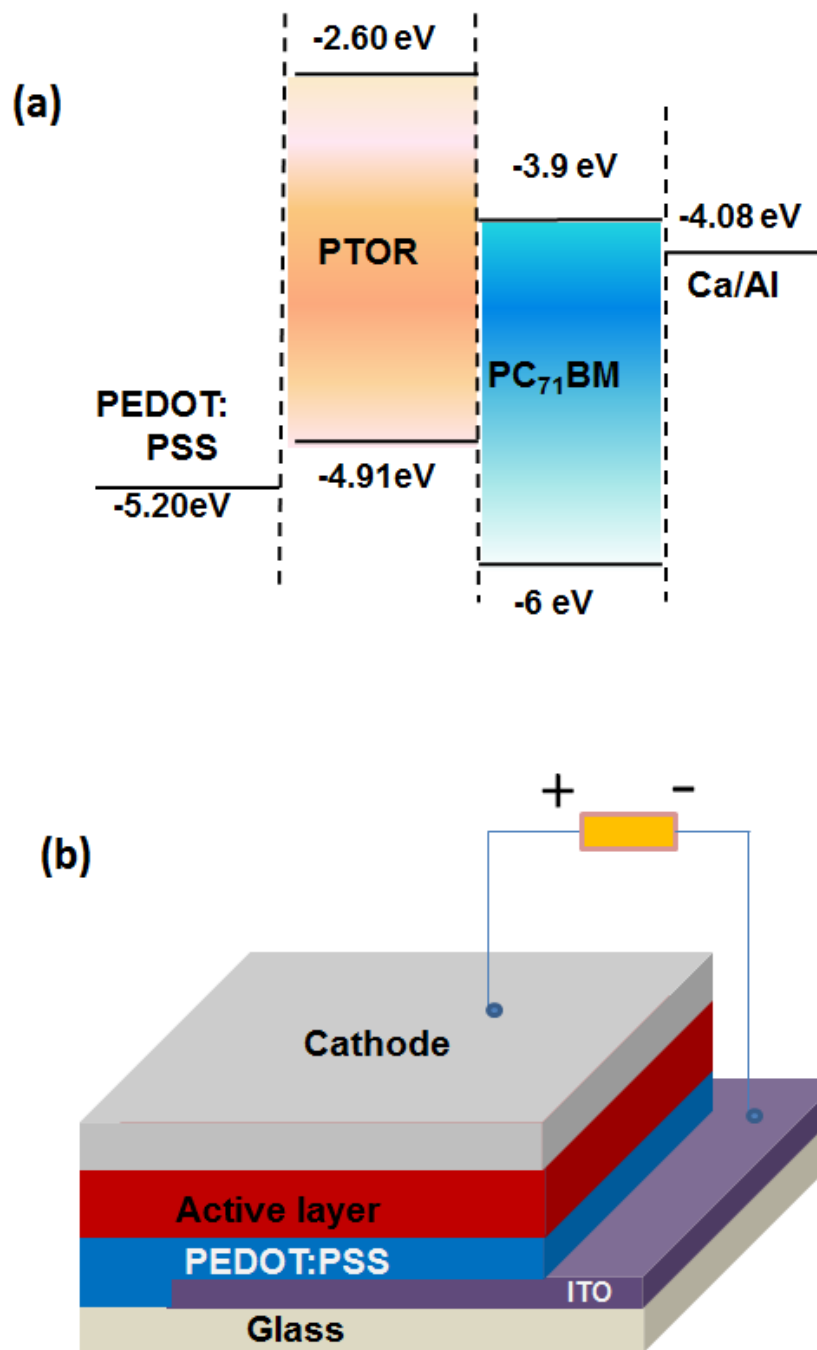


Figure 3-24 Energy level diagram (a) and device structure (b) of blend films of **PTOR** :PC<sub>71</sub>BM (1:1 wt. ratio).

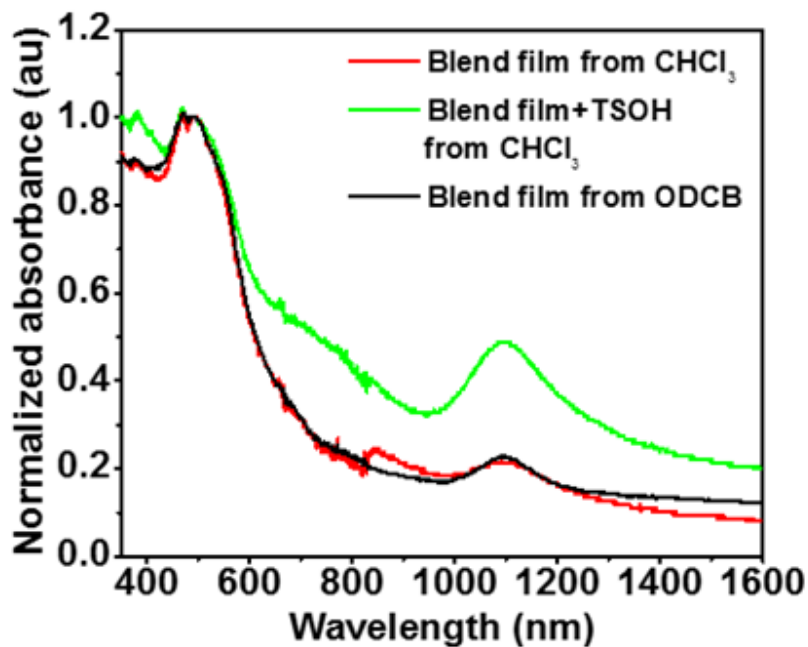


Figure 3-25 UV-vis-NIR absorption spectra of blend films of **PTOR/PC<sub>71</sub>BM** (1:1 wt. ratio) fabricated from CHCl<sub>3</sub> and ODCB solutions with or without acid.

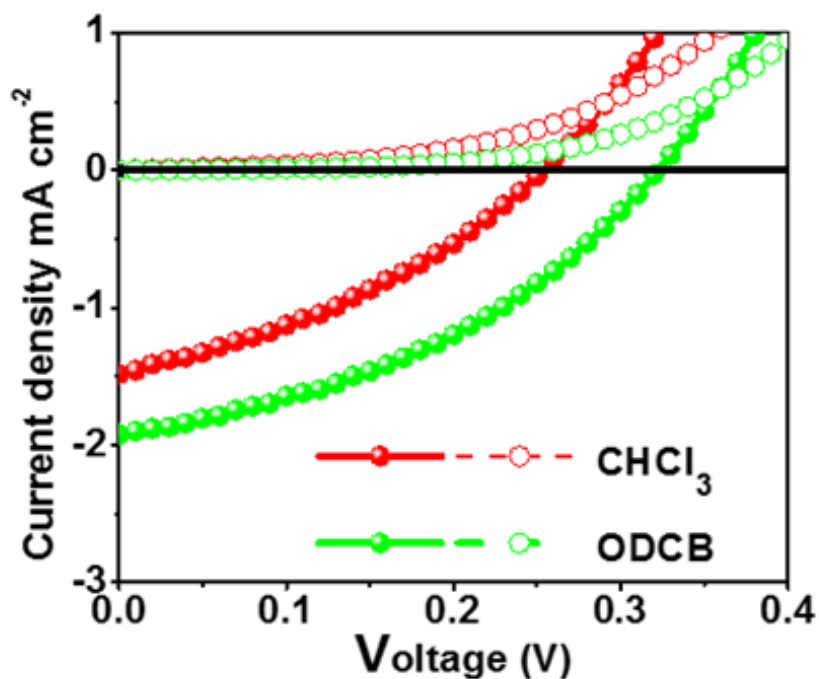


Figure 3-26 *J-V* curve of device fabricated from **PTOR/PC<sub>71</sub>BM** (1:1 wt. ratio) CHCl<sub>3</sub> and ODCB solutions in dark (empty circle) and under illumination (sphere).

Figure 3-26 shows the photovoltaic performance of the resulting devices. The illuminated curves were measured under 1-sun air mass 1.5 global illumination. The best performance was obtained from devices spin-coated from *o*-dichlorobenzene solutions and after thermal annealing. A  $V_{OC}$  of 0.32 V, a  $J_{SC}$  of 1.92 mA cm<sup>-2</sup> and a fill factor of 0.39 and a power conversion efficiency of 0.24% were obtained. The best performance for the device fabricated from chloroform solutions has 0.13% power conversion efficiency.

Figure 3-27 shows the external quantum efficiency (EQE) spectra of the various photovoltaic cells. All the EQE spectra reasonably match the absorption spectra of their corresponding thin films in the UV-visible region (from 300 to 750 nm). However, no photocurrent response is observed in the NIR range for all devices. Apparently, the NIR absorptions, corresponding to intramolecular charge transfer induced by protonation, are unable to produce photocurrent. This is presumably due to the localized nature of the charges generated by the intramolecular charge transfer transition in the protonated form.

Table 3-3 Photovoltaic device performance under 1-sun air mass 1.5 global illumination.

	$V_{OC}$ (V)	$J_{SC}$ (mA cm <sup>-2</sup> )	PCE (%)	Fill Factor (%)
From CHCl <sub>3</sub> <sup>a</sup>	0.25	1.484	0.13	35.04
From ODCB <sup>b</sup>	0.32	1.92	0.24	39.06

<sup>a</sup> Device were fabricated from chloroform solution without thermal treatment.

<sup>b</sup> Devices fabricated from ODCB solution and annealed at 120 °C for 10 min.

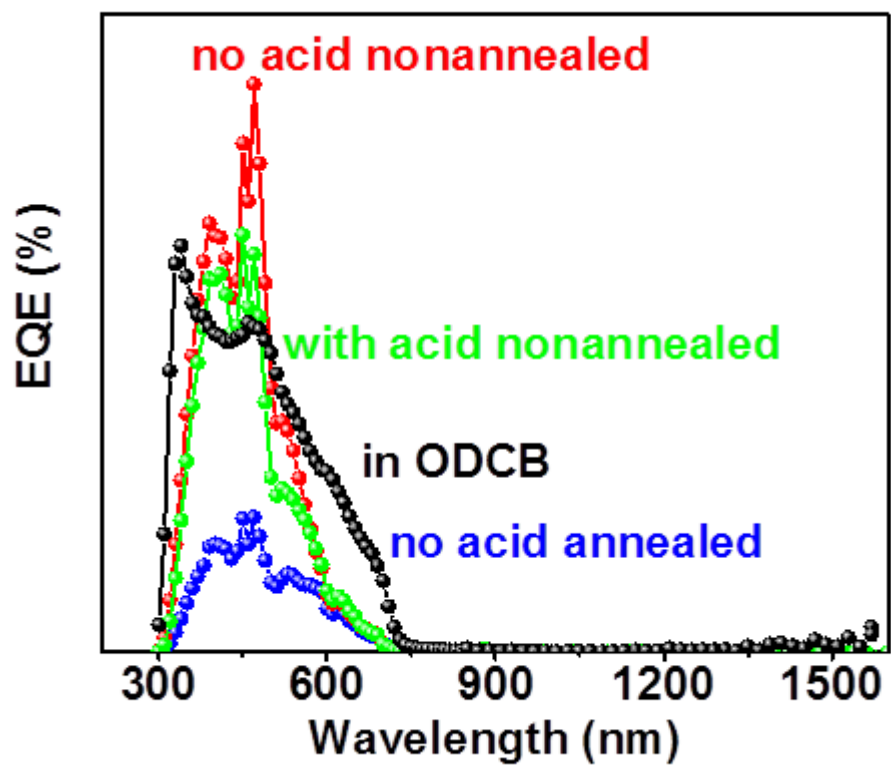


Figure 3- 27 External quantum efficiency of **PTOR**: PC<sub>71</sub>BM blends in ODCB (black, thermal annealed film), in CHCl<sub>3</sub> before (red) or after (blue) thermal annealing at 120 °C for 10 min, and in CHCl<sub>3</sub> with acid addition (green).

### 3.3.7. Mobility

Hole mobility of thermally annealed films of **PTOR**/PB<sub>71</sub>CM was measured via the space charge limited current (SCLC) technique. Hole only devices were fabricated with the configuration of ITO/PEDOT:PSS/**PTOR**:PC<sub>71</sub>BM/MoO<sub>3</sub>/Au. The fabrication procedures are similar to those of solar cells. The blend solution was spin-coated on to PEDOT:PSS coated ITO substrates. MoO<sub>3</sub> (10 nm)/Au (50 nm) electrodes were then sequentially deposited through thermal evaporation under high vacuum. The area of the active device was the same as those of photovoltaic devices (0.14 cm<sup>2</sup>). MoO<sub>3</sub> and PEDOT:PSS are chosen to be hole transporting/electron-blocking layers. Figure 3-28a shows the *J-V* curve of the hole-only devices. Assuming it is Ohmic contact between each layer, the thin film hole mobility can be estimated by fitting the curve in the SCLC area with the following equation:<sup>154</sup>

$$J = \frac{9}{8} \epsilon_0 \epsilon_r \mu \frac{(V_{app} - V_{bi})^2}{d^3} \quad (3-9)$$

Where *J* is the current density, *V<sub>app</sub>* is the applied voltage, *V<sub>bi</sub>* is the built-in voltage,  $\epsilon_0$  is the electric constant ( $8.854 \times 10^{-12}$  F/m),  $\epsilon_r$  is the relative dielectric constant,  $\mu$  is the charge carrier mobility, and *d* is the thickness of the thin film. For an organic semiconductor, the relative dielectric constant can be assigned to be 3.<sup>155</sup> The thickness of the blend films is around 300 nm (ranged from 250- 400 nm). The built-in voltage is estimated to be 0.33 V. The hole mobility of the blend film is calculated to be  $3.98 \times 10^{-3}$  cm<sup>2</sup> V<sup>-1</sup> s<sup>-1</sup> which is comparable to that of P3HT: PCBM blend films using SCLC mobility measurements.<sup>19</sup>

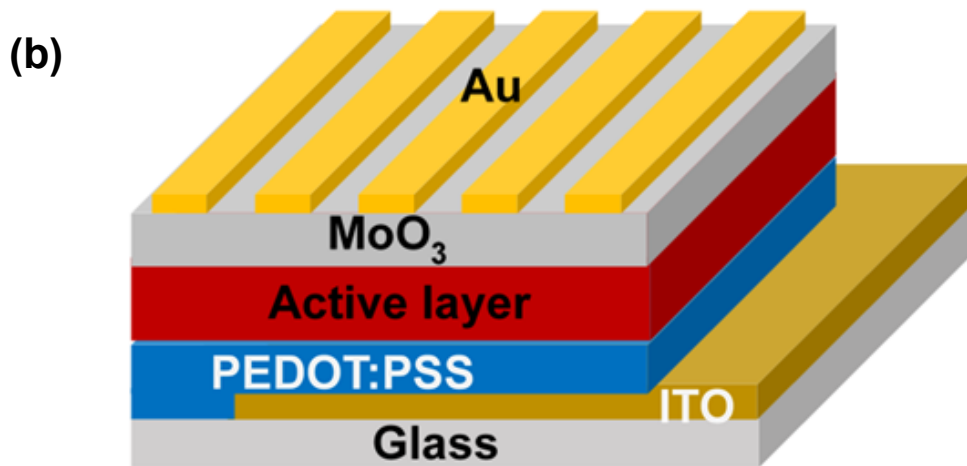
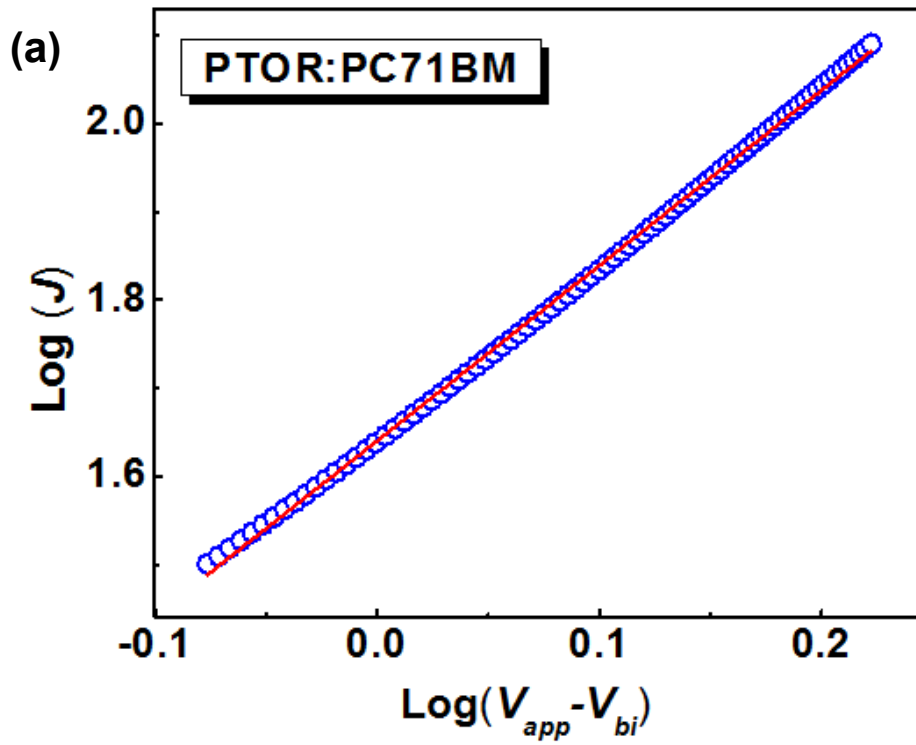


Figure 3-1 (a) Experimental (blue circle) and fitted (red line) current density-voltage curve of ITO/PEDOT:PSS/PTOR:PC<sub>71</sub>BM/MoO<sub>3</sub>/Au, (b) device architecture for mobility test.

### 3.4. Conclusions

In conclusion, we have synthesized three new conjugated copolymers containing 3-3'-substituted bithiophene units, and studied their optical, electrochemical and photovoltaic properties. Due to the electron-donating properties of the alkoxy substituents and the near planar structure of the bithiophene unit (due to the short S-O contacts), conjugated polymers containing 3,3'-dialkoxybithiophene units show strong propensity towards electrophiles such as  $H^+$ . The protonated polymers show strong NIR absorptions due to intra-chain charge transfer. The strength and the wavelengths of the NIR absorption depend on the comonomers as well. Comonomers with stronger electron-donating properties (such as NDT over INDT) lead to more intense NIR absorptions and longer NIR absorption wavelengths. The protonation process is found to follow the first order reaction kinetics. While the NIR-absorbing polymers, when blended with PC<sub>71</sub>BM, show photovoltaic properties, only the absorptions in the UV-visible range are able to produce photocurrent. The NIR absorption is found to be unable to yield photocurrent.

### 3.5. Methods

#### 1) General remarks

Solvents were purified following literature procedures prior to use. All chemicals were purchased from commercial sources and were used without further purification unless otherwise stated. **PBOR** and **PDR** were synthesized from previous work.<sup>98</sup> All reactions were run using standard Schlenk techniques under argon atmosphere. The <sup>1</sup>H NMR spectra were measured in deuterated solvents on a Varian 400 MHz FTNMR spectrometer. Gel permeation chromatography (GPC) measurements were performed at 30 °C on a Tosoh EcoSec HLC8320GPC system consisted of a differential refractometer, a UV detector, and a styra gel column. THF was used as the eluent and a set of polystyrenes with known molecular weights were used as standards. UV-vis-NIR absorption spectra were measured on a Shimadzu UV3600 UV-vis-NIR spectrophotometer. Fluorescence spectra were recorded on a Shimadzu RF-5301PC spectro fluorophotometer. Fluorescence quantum yields for solutions were calculated using quinine sulfate in 1 N H<sub>2</sub>SO<sub>4</sub> ( $\phi_{fl} \sim 0.58$ ) as the standard. For protonation studies, five polymers **PTOR**, **PTR**, **PTD**, **PBOR** and **PDR** were each dissolved in THF. All the solutions were stirred at 40 °C in a glove box overnight. Solution of *p*-toluenesulfonic acid was added at certain polymer: acid molar ratios. Photostability was performed by illuminating the polymer solutions under an Oriel xenon arc lamp solar simulator at an intensity of 100 mW cm<sup>-2</sup> (1-sun air mass 1.5 global illumination). Cyclic voltammetry studies were carried out in acetonitrile at room temperature under the protection of argon using BAS Epsilon EC electrochemical station employing a 1 mm<sup>2</sup> Pt disk as the working electrode, an Ag wire as the reference electrode and a Pt wire as the counter electrode. A 0.1 M tetra-*n*-

butylammoniumhexafluorophosphate solution was used as the supporting electrolyte and the scan rate was 20 mV/s. Fc/Fc<sup>+</sup> was used as an internal reference and assigned an absolute energy of -4.8 eV vs vacuum.

## 2) *Synthesis*<sup>98,123</sup>

Monomer **1** and **2a/2b** were synthesized following published procedures.<sup>98,123</sup> Monomer **3** was purchased from Sigma Aldrich.

### ***Polymer PTOR***

Monomer **1** (100 mg, 0.13 mmol), **2b** (145 mg, 0.13 mmol), Pd<sub>2</sub>(dba)<sub>2</sub> (6 mg, 0.0065 mmol) and P(o-Tolyl)<sub>3</sub> (15.8 mg, 0.05 mmol) were added to an air free flask followed by three times of vacuum/argon cycling. Then 6 ml of freshly distilled THF was added to the flask. The reaction mixture was stirred at 90 °C for 48 h. After cooled to room temperature, 2-bromo thiophene was added to the mixture and the resulting mixture was stirred for 30 min. Then 2-tributyltin thiophene was added and the mixture was stirred for another 30 min. The mixture was poured in 30 mL methanol and then stirred for 4 h. The precipitates were collected by centrifugation. The collected polymers were dissolved in THF and then re-precipitated out from methanol. The precipitates were collected by centrifugation and dried under reduced pressure. The final products were purple-colored solid, yield 85%. <sup>1</sup>H NMR (400 MHz, C<sub>2</sub>D<sub>2</sub>Cl<sub>4</sub>, 75 °C) δ: 7.5-6.5 (br, 6H, aromatic-H's), 4.49-3.66 (br, 8H, O-CH<sub>2</sub>-), 2.17-0.52 (br, 103H, aliphatic-H's). Molecular weights from GPC measurements: Mn, 6.36 KDa; Mw, 8.55 KDa; PDI, 1.35.

The synthetic procedures for polymers **PTR** and **PTD** are similar to those of **PTOR**.

### ***Polymer PTR***

Yield 90%. <sup>1</sup>H NMR (400 MHz, CDCl<sub>3</sub>, 20 °C) δ: 7.88-7.63 (br, 2H, Ar-H), 7.45-

7.33 (br, 2H, thiophene-H's), 4.2 (br, 4H, O-CH<sub>2</sub>-), 2.5 (br, 4H, -CH<sub>2</sub>-), 1.9 (br, 4H, -CH<sub>2</sub>-), 1.21-1.71 (br, 56H, -CH<sub>2</sub>-), 0.92-0.72 (br, 22H, -CH<sub>3</sub>). Molecular weights from GPC measurements: Mn, 5.96 KDa; Mw, 7.93 KDa; PDI, 1.33.

### ***Polymer PTD***

<sup>1</sup>H NMR (400 MHz, CDCl<sub>3</sub>, 20 °C) δ: 7.05 (br, 2H, thiophene-H's), 6.85 (br, 2H, comonomer thiophene-H's), 4.22-4.03 (br, 4H, O-CH<sub>2</sub>-), 1.96-1.79 (br, 4H, -CH<sub>2</sub>-), 1.44-1.08 (br, 36H, -CH<sub>2</sub>-), 0.93-0.74 (br, 9H, -CH<sub>3</sub>). Molecular weights from GPC measurements: Mn, 5.23 KDa; Mw, 7.31 KDa; PDI, 1.40.

### ***3) Device Fabrication and Characterization***

ITO glass (purchased from Delta Technologies, 8–12 Ω/square sheet resistance) was used as substrates. ITO glass was cut into 1.5 cm by 1.5 cm pieces, and was patterned by etching with aqua regia vapor. The patterned ITO glass substrates were cleaned in an ultrasonic bath by detergent, water, deionized water, toluene, acetone, and isopropyl alcohol, sequentially, each for 15 min. Then they were dried with compressed air. Cleaned ITO substrates were then treated with UV ozone for 45 min. A thin layer of PEDOT:PSS (purchased from Heraeus Precious Metals, Clevis P VP AI4083) was spin-coated onto the ITO substrates from an aqueous solution at 4000 RPM for 30 s. The substrates were then dried at 120 °C for 45 min on a hotplate in air. **PTOR**/PC<sub>71</sub>BM(1:1, wt. ratio) blend solutions were prepared in a glove box by dissolving **PTOR** and PC<sub>71</sub>BM (purchased from Nano-C) in nitrogen-degassed chloroform or *o*-dichlorobenzene. The solutions were stirred at 50 °C overnight and filtered before use. The blend solution was spin-coated on top of the PEDOT:PSS layer at certain RPM for 60 s. The wet films were covered with a petri-dish for solvent annealing. For comparison, half of the devices were annealed at 120 °C for

10 min in a glove box. Subsequently, an electrode consisting of 25 nm thick Ca and 100 nm thick Al was deposited on top of the active layer by thermal evaporation under high vacuum ( $< 2 \times 10^{-6}$  Mbar) through a shadow mask which defined the active area of  $0.14 \text{ cm}^2$  of the devices. For hole-only devices, instead of Ca/Al, 10 nm  $\text{MoO}_3$  and 50 nm Au were deposit sequentially onto the films through the shadow mask. The thickness for hole only devices were determined using a Tencor Alphastep 200 automatic step profiler.

*J-V Curve Measurement:* Devices for solar cell measurement were illuminated with an Oriel xenon arc lamp solar simulator at an intensity of  $100 \text{ mWcm}^{-2}$  (1-sun airmass 1.5 global illumination). Current–voltage characteristics were measured using a Keithley 2400 source meter.  $J_{\text{SC}}$ ,  $V_{\text{OC}}$ , and maximum output power density ( $J_{\text{max}}V_{\text{max}}$ ) were obtained from the *J-V* curves under illumination. The PCE was calculated by  $\eta = (J_{\text{SC}}V_{\text{OC}}FF)/P_{\text{in}}$ , where  $P_{\text{in}}$  is the incident power density; and *FF* is the fill factor which is given by  $(J_{\text{max}}V_{\text{max}})/(J_{\text{SC}}V_{\text{OC}})$ .

*EQE Measurement:* EQEs were determined by illuminating the device with monochromatic light from an Oriel xenon arc lamp solar simulator at an intensity of  $100 \text{ mWcm}^{-2}$ . Incident light was chopped by a monochromator (Newport 74004). The AC photocurrent from the devices was converted to an AC voltage and measured with a lock-in amplifier. The light spot area was around  $2 \text{ mm}^2$ . A calibrated crystalline silicon diode (Newport 79356) and Ge diode (Newport 79359) were used as a reference before each measurement.

## CHAPTER 4

### HOLE MOBILITY STUDIES OF SELECTED POLYCYCLIC AROMATIC HYDROCARBONS

#### 4.1. Introduction

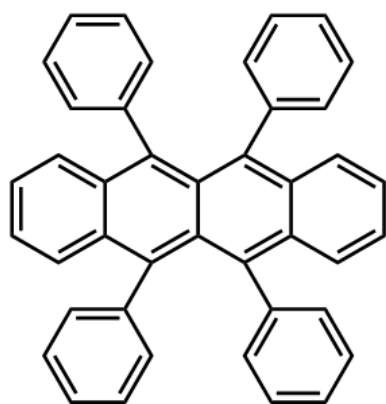
Organic semiconductors with high charge carrier mobility are attractive due to their application in numerous electronic and optoelectronic devices. As discussed in Chapter 1, charge carrier mobility is important in improving photovoltaic performance, especially in multilayer or BHJ systems.

The charge carrier mobility, an ability of a charge carrier to move in a solid film, is a bulk property which depends not only on the molecular structure of the material but also on the processing conditions and measurement techniques.<sup>119,123</sup> The molecule packing order, orientation, grain size and crystal alignment, etc. all affect the charge mobility.<sup>156-159</sup> Extensive studies have uncovered a number of organic and polymeric systems with high charge carrier mobilities.<sup>119,123,156,157,159</sup> For example, high hole mobility of  $15 \text{ cm}^2 \text{ V}^{-1} \text{ s}^{-1}$  has reported on a highly ordered rubrene single crystal.<sup>160</sup>

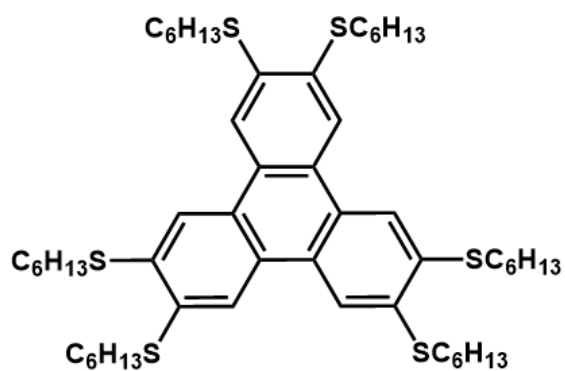
Among various organic materials, polycyclic aromatic hydrocarbons (PAHs) are the most appealing. The aromatic core of a PAH offers a planar extended  $\pi$ -conjugation building block which can drive the intermolecular packing through the strong  $\pi$ - $\pi$  stacking interaction. Solubilizing groups can be introduced to the periphery of the PAH core to allow solution processability without affecting the core electronic structure.

PAHs are common discotic mesogens which have a propensity to pack into column-like structures at a certain temperature range. The  $\pi$ -stacked column may allow efficient

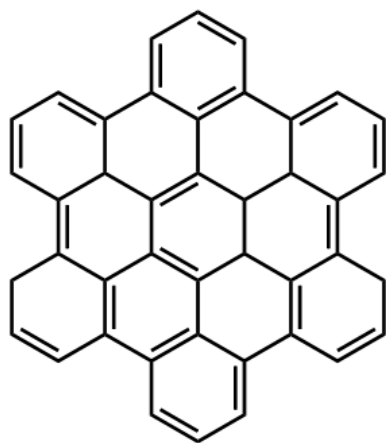
charge transport. Depending on the order of the columnar structure and the size of the aromatic core, the charge carrier mobilities for discotic PAHs reported so far range from  $10^{-3}$  to  $1 \text{ cm}^2 \text{ V}^{-1} \text{ s}^{-1}$ .<sup>35</sup> The carrier mobility reaches  $\sim 10^{-1} \text{ cm}^2 \text{ V}^{-1} \text{ s}^{-1}$  for a triphenylene derivatives **C6STP** in a highly ordered columnar phase.<sup>161</sup> Charge carrier mobility as high



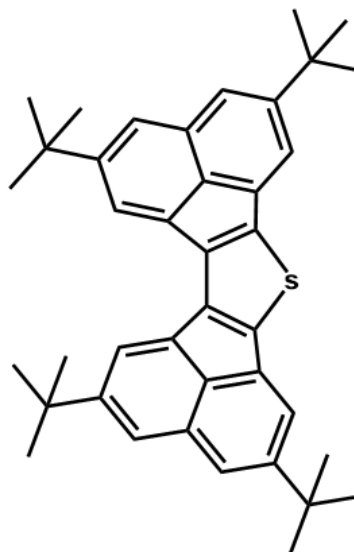
**Rubrene**



**C6STP**



**Hexabenzocoronene**



**DAT**

Figure 4-1 Structures of rubrene, **C6STP**, hexabenzocoronene, and **DAT**.

as  $1.1 \text{ cm}^2 \text{ V}^{-1} \text{ s}^{-1}$  has been reported on a hexabenzocoronene derivative which has a much large aromatic core.<sup>162</sup> PAHs containing heteroatoms in the aromatic core have also been explored. Films spin-coated from **DAT** as shown in Figure 4-1, for example, have mobility up to  $8.72 \times 10^{-2} \text{ cm}^2 \text{ V}^{-1} \text{ s}^{-1}$  upon thermal annealing.<sup>119</sup>

#### 4.2. Methods in organic semiconductor mobility measurement

There are many methods that have been developed for solution processed hole mobility devices, such as time of flight (TOF) measurements,<sup>163–166</sup> organic field effect transistor (FET) measurements,<sup>167–169</sup> space charge limited current (SCLC) measurements,<sup>119,123,170–172</sup> Hall effect measurements,<sup>173–175</sup> the equilibrium charge carrier extraction measurements,<sup>176</sup> conductivity/concentration ( $\sigma/n$ ) methods,<sup>177</sup> and charge extraction in a linearly increasing voltage (CELIV) measurements,<sup>178</sup> etc. The first three techniques are the most commonly applied ones and are described in more detail.

##### *Time of flight (TOF) measurements*

TOF measurement is the most direct method in measuring charge mobility. By measuring the time  $t$  required for a sheet of charge to move across the sample with thickness of  $d$  under an applied voltage  $V$ , the charge carrier mobility can be calculated by the following equation:<sup>166</sup>

$$\mu = \frac{d^2}{Vt} \quad (4-1)$$

In the measurement set up, a thick organic film up to a few microns is sandwiched between two electrodes as shown in Figure 4-2. A thin sheet of charge carriers is injected into the surface of the sample film on the top electrode with a pulsed laser light at a highly absorbing wavelength. The charges then drift across the film resulting in a transient current response. The transition time, corresponding to the time needed for the sheet of charges to

cross through the film, can be determined. Experimentally, the transition time is the time at which the current abruptly drops to zero. Depending on the direction of the applied electric field, hole mobility or electron mobility can be obtained.

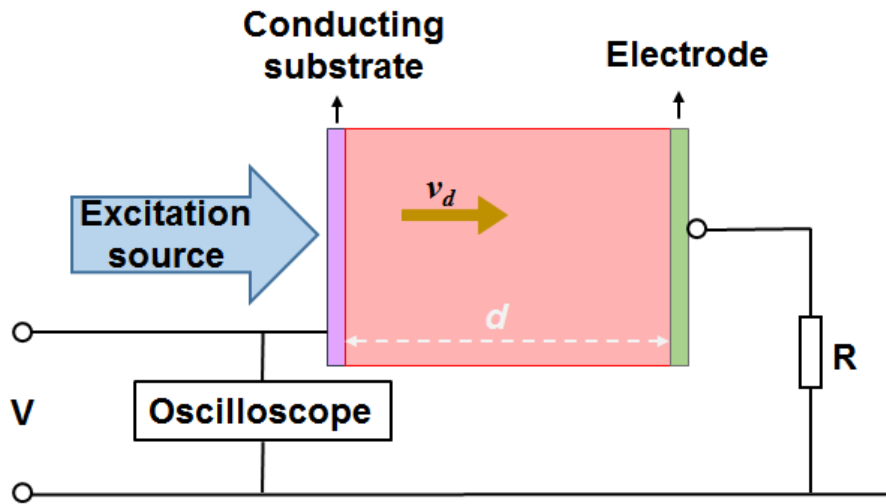


Figure 4-2 Setup of time of flight charge carrier mobility measurements

*Organic field effect transistor (OFET) measurements*

A FET device usually consists of four major parts, a conducting channel, a source, a drain and a gate, as shown in Figure 4-3. The conducting channel sets apart the source and the drain electrodes. Both contacts are required to be Ohmic contact. The charge travels from the source to the drain. A gate may be on the top or bottom of the conducting channel. Many types of FET devices have been investigated, such as metal-insulator-semiconductor field-effect transistors (MISFET), metal-semiconductor field-effect transistors (MESFET) and thin film transistors (TFFET).<sup>167</sup> Organic FET is a FET using organic semiconductor as the channel material. Figure 4-3 (b, c) shows the common architectures of the OFETs.

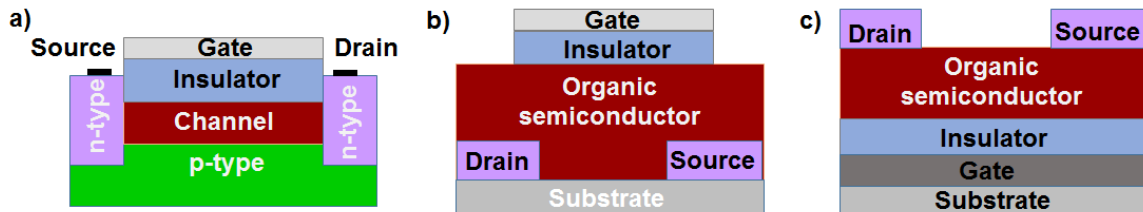


Figure 4-3 Device structures of metal-insulator-semiconductor field-effect transistor (a) and Organic field effect transistors with bottom contact (b) or top contact (c).<sup>167</sup>

Several working mechanisms in understanding charge carrier mobility in an OFET have been developed, including the hopping model, the field dependent mobility model, small polaron model, etc.<sup>167</sup> The most commonly adopted method use the drain current  $I_D$  in the saturated regime, by plotting  $I_{D,sat}$  versus the applied gate voltage  $V_G$  in the saturated regime with the following equation,<sup>167</sup>

$$I_{D,sat} = \frac{W\mu C_i}{2L} (V_G - V_T)^2 \quad (4-2)$$

Where  $I_{D,sat}$  is the drain current in the saturated regime,  $W$  and  $L$  are the channel width and length, respectively.  $C_i$  is the capacitance density of the insulating layer and  $V_T$  is the threshold voltage.

*Space charge limited current (SCLC) measurements*

SCLC measurement is another popular method in mobility study of organic semiconductors. Space charge is described as excess positive or negative charges distributed over a region of space like a continuous stream instead of a distinct point.<sup>154</sup> It normally occurs in dielectric materials. In a semiconductor material, there are immobile ionized dopants and free charges in the solid film.<sup>179</sup> In the neutral state, the concentrations of free charges are equal to the dopants concentrations. When one kind of free charge carriers are injected into the system, the concentration of the free charge carrier increases

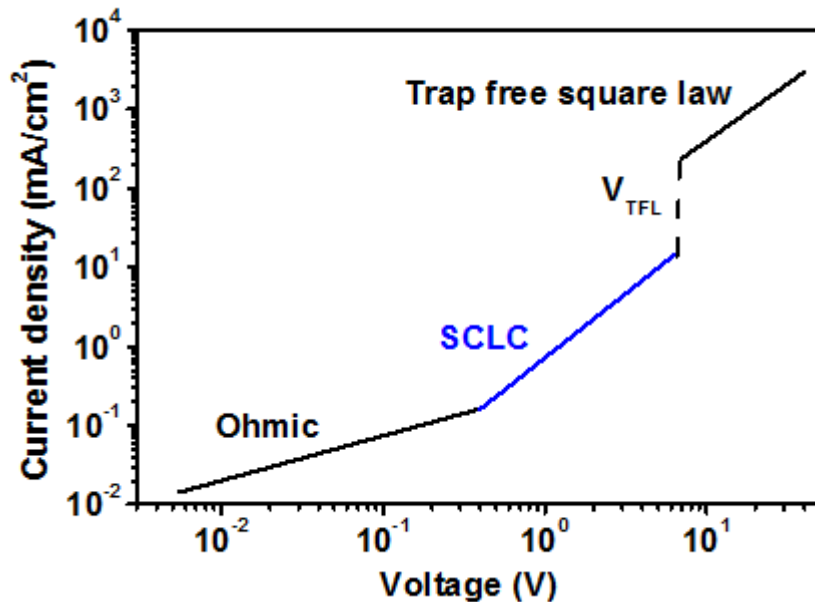


Figure 4-4 Typical current density-voltage curve in Ohmic and SCLC regions.<sup>180</sup>

while the dopants concentration remains the same. At some point, this equilibrium is broken and results in a space-charge effect. In other words, SCLC will occur when the dopant concentrations are much lower than the injected free charge density. The equilibrium charge concentration, in this case, can be negligible. Large gradient of free carrier density causes charge diffusion and affects the electric field in this region, this electron field also determines the entire current. This current is called space charge limited current (SCLC). The excess charge injected into the active region move in the direction that parallel to the electric field.<sup>35,180</sup>

Figure 4-4 shows a typical  $J$ - $V$  curve of a semiconducting material. In the low voltage region, charge concentration is balanced. This region is so-called Ohmic regime where the current is following Ohm's law, being proportional to the electric field. When the applied voltage increases, the charge concentration equilibrium is broken, the current becomes space charge limited current and is proportional to the square of the voltage. As described in the Mott-Gurney Law,<sup>154</sup> the SCLC current density  $J$  of the measured thin film can be expressed as following equation,

$$J = \frac{9}{8} \epsilon \mu \frac{V^2}{d^3} \quad (4-3)$$

Where  $V$  is the voltage crossed the film,  $\epsilon$  is the permittivity of the material,  $\mu$  is the charge carrier mobility, and  $d$  is the thickness of the thin film. When the voltage keeps increases, all traps are filled resulting a nearly vertical increasing in current, which is called trap-free voltage limit ( $V_{TFL}$ ).<sup>180</sup> After that, the current reaches trap-free SCLC region, the current here follows trap free square rule.<sup>180</sup>

In SCLC measurement, the current is considered to be determined by the injected carrier density which completely overwhelms the free carrier density of a film. In this case,

the free carrier density of the film is negligible in the above equations. The advantage of the SCLC measurement is that the mobility can be calculated without knowing the film's free carrier density. However, in most of the cases, the mobility measured by SCLC measurement is lower than from FET devices. One difference is that, in FET measurement, all the carriers presented in the system is assumed to be induced by the applied field.<sup>181</sup> If this is not the case, there are other carriers present, then the value of mobility will be overestimated.<sup>35</sup> For SCLC measurement, the situation is opposite. The mobility is usually underestimated because the current in SCLC measurement is thought to be contributed by the maximum possible number of carriers.<sup>35</sup>

#### 4.3. Device design for SCLC measurements

The Mott-Gurney equation is derived based on several assumptions.<sup>154</sup> It assumes that the material itself does not show intrinsic conductivity and there is only one kind of charge carries presented in the system. This kind of charge carrier is injected from one electrode and received by the other. Moreover, the mobility and dielectric constant are considered to the same throughout the film.<sup>154</sup>

In order to ensure only one type of charge carrier drifts in the system, hole-only or electron-only devices are designed for SCLC measurements. The active layer is sandwiched between two conducting layers which allow only one type of charge carriers to transport. Ohmic contact is required in order to ensure smooth charge transfer between layers. For hole only devices, the two hole transporting layers have similar HOMO levels to that of the measured material. Commonly used electron-blocking materials include MoO<sub>3</sub> and PEDOT:PSS.<sup>119,182,183</sup> For electron-only devices, the active layer is sandwiched between two electron transporting layers which have similar LUMO level to the applied material. Metal calcium and aluminum are usually applied in electron-only devices for electron mobility measurement. As seen in the device structures (Figure 4-5), the charge drifting direction is vertical to the substrate. This is different from FET measurements

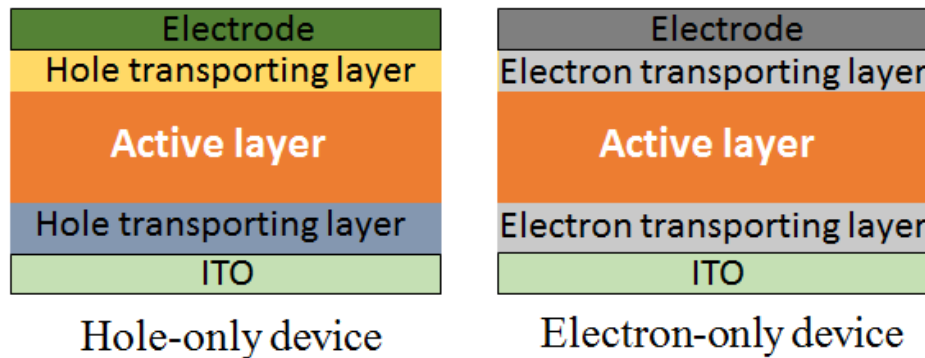


Figure 4-5 Device structures of hole-only device and electron-only device in SCLC mobility measurements.

where charges travel along a horizontal path from source to drain. Another requirement for SCLC measurements is an evenly spread active layer. The film thickness is also an important factor. Proper thickness can ensure the transporting of charge carriers to the receiving electrode without overlap between the depletion layers of the top and bottom metal/organic contacts. The suitable thickness is ranged from several hundred nanometers to a few micrometers.

For solution-based processing, the simplest way to obtain a uniform thin film is spin-coating. The normal operation of spin-coating follows procedures of applying solution onto a substrate and then accelerating the substrate to a designed rotation speed for a certain time.<sup>54</sup> As a result, only a thin film will be left on the substrate with most of the solution discarded during the rotational process. The drying process of spin-coating technique allows to form homogenous film in a diameter up to 30 cm.<sup>54</sup> The film thickness and morphology of spin-coated films are highly reproducible, if they are obtained from a solution of a certain material in the same solvent with the same concentration.<sup>54</sup> The thickness and morphology of resulting film is dependent on the molecule weight, solution viscosity, solution concentration, and rotation speed.<sup>54</sup> By varying solution concentration and spin-coating parameters, it is possible to achieve relatively uniform thin film with suitable film thickness.<sup>54</sup>

For the calculation of charge carrier mobility of organic semiconducting materials, the permittivity  $\epsilon$  can be estimated from electric constant  $\epsilon_0$  and relative dielectric constant  $\epsilon_r$ ,

$$\epsilon = \epsilon_0 \epsilon_r \quad (4-4)$$

where  $\epsilon_0$  is  $8.854 \times 10^{-12}$  F/m, and the relative dielectric constant  $\epsilon_r$  is around 3 for most organic materials.<sup>155</sup> The electric field across the film is affected by two opposite voltages, one is the applied voltage  $V_{app}$  and the other is a built-voltage,  $V_{bi}$ , existed in the device.

The voltage across the system can be expressed as:

$$V = V_{app} - V_{bi} \quad (4-5)$$

Combining the Equation (4-3) - (4-5), the current density can be rewritten as,

$$J = \frac{9}{8} \epsilon_0 \epsilon_r \mu \frac{(V_{app} - V_{bi})^2}{d^3} \quad (4-6)$$

The charge carrier mobility can then be estimated by fitting the  $J$ - $V$  curve, plotted in logarithmic scale, in the SCLC region with Equation (4-6).<sup>119</sup>

#### 4.4. Objective

In this chapter, a new set of PAHs based on the tribenzopentaphene (TBP) core have been studied on their thin film hole mobilities. The specific aims in this study are:

- 1) To study the molecular packing in thin films before and after thermal annealing using X-ray diffraction
- 2) To study the electrochemical properties and to calculate the HOMO/LUMO energy levels of the materials.
- 3) To fabricate hole-only devices and evaluate the hole mobility of thin films spin-coated from selected PAHs.

## 4.5. Materials

Three TBP derivatives with different alkoxy substituents are shown in Figure 4-6. Two long dodecyloxy groups are introduced at the bay position to ensure good solubility. We have previously shown that the TBP rings exhibit strong  $\pi$ - $\pi$  stacking interactions in **1a** and **1b** but not so much in **1c** due to the steric effect of the four bulky isopropoxy groups.<sup>184</sup> Driven by the strong  $\pi$ - $\pi$  stacking interaction, **1a** and **1b** self-assemble into microfibrils. Compound **1c**, on the other hand, fails to assemble into well-defined structures under similar conditions. Photovoltaic cells using **1b** as the electron donor and PDI as the electron acceptor showed photovoltaic performance and a power conversion efficiency of 0.12% has been obtained.<sup>184</sup> This research focuses on the mobility studies of thin films spin-coated from these compounds. It is hoped that thin films of **1a** and **1b** exhibit high hole mobilities as they form columnar stacks.

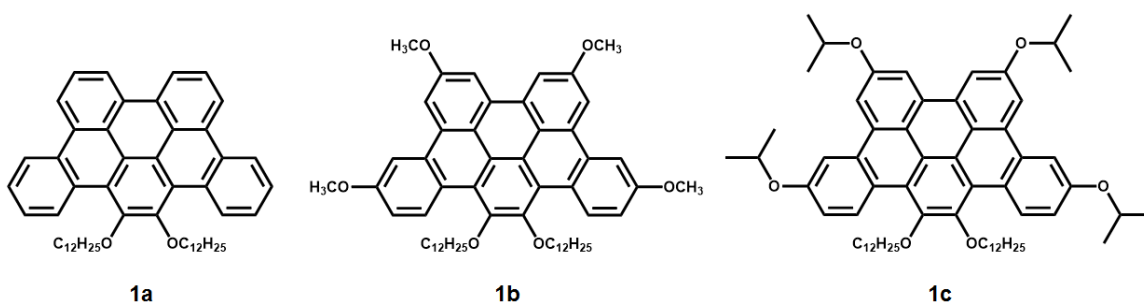


Figure 4- 6 Structures of compounds **1a-c**.

## 4.6. Result and discuss

### 4.6.1 Theoretical calculation

In order to understand the geometrical structure and electronic states of the three compounds, theoretical calculations were carried out. In order to simplify the calculation, all the dodecyl groups were replaced by ethoxy groups. The geometrical optimization were performed on Gaussian 03w program with density functional theory (DFT) calculation at the B3LYP 631G(d) level. Figure 4-8 depicts the energy minimized geometry of compounds **1a-c**. The TBP cores in all three molecules is somewhat distorted from planarity. The twisting was described by the dihedral angles labeled as  $\alpha$ ,  $\beta$  and  $\gamma$  as shown in Figure 4-7. The three dihedral angles of the TBP core in **1a** are  $15.48^\circ$ ,  $8.01^\circ$  and  $13.00^\circ$  for  $\alpha$ ,  $\beta$  and  $\gamma$ , respectively. For **1b**, they are  $13.99^\circ$ ,  $7.71^\circ$  and  $11.87^\circ$ ; while for **1c** they are

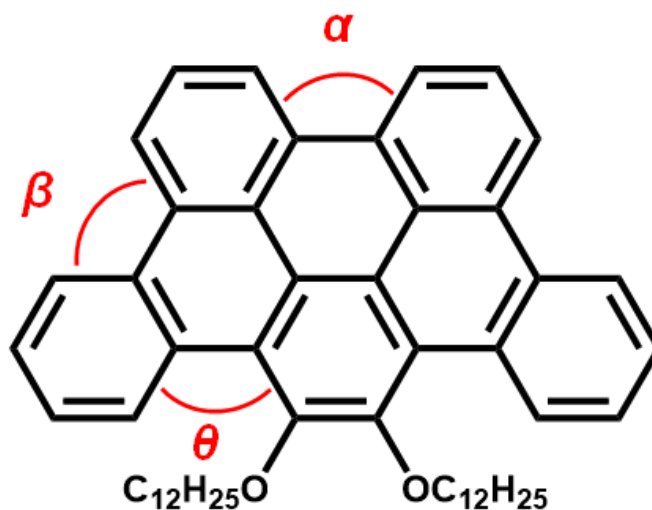


Figure 4-7 Model structure used for describing molecular twist.

14.32°, 7.51° and 11.82°. The twist in TBP core is similar for **1b** and **1c** with **1a** showing a slightly larger twist.

The HOMO and LUMO energy levels of the three compounds were estimated based on the energy minimized structure obtained from DFT calculations. The HOMO/LUMO distributions on energy minimized structures are depicted in Figure 4-9 and the energy levels are summarized in Table 4-1. The HOMO/LUMO energy levels are calculated to be -5.28/-1.47, -4.93/-1.22 and -4.81/-1.31 eV for **1a**, **1b** and **1c**, respectively. And the bandgaps are 3.81, 3.71 and 3.50 eV, respectively. Compared to **1a**, compounds **1b** and **1c** have four additional electron-donating alkoxy substituents, which raise both the HOMO and LUMO levels.

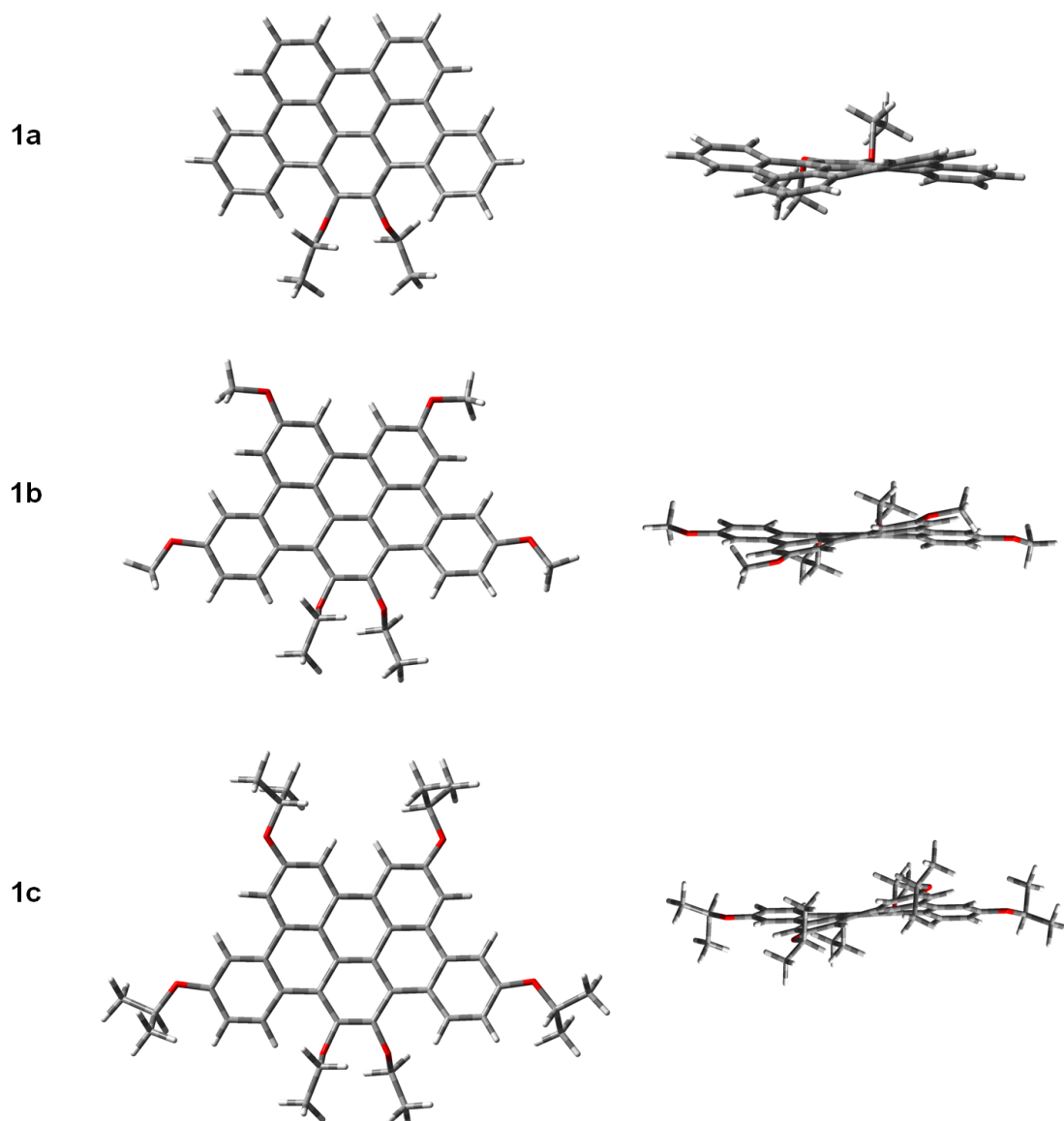


Figure 4-8 The energy minimized structures of **1a-1c** from different views obtained from Gaussian 03w at B3LYP 631G(d) level.

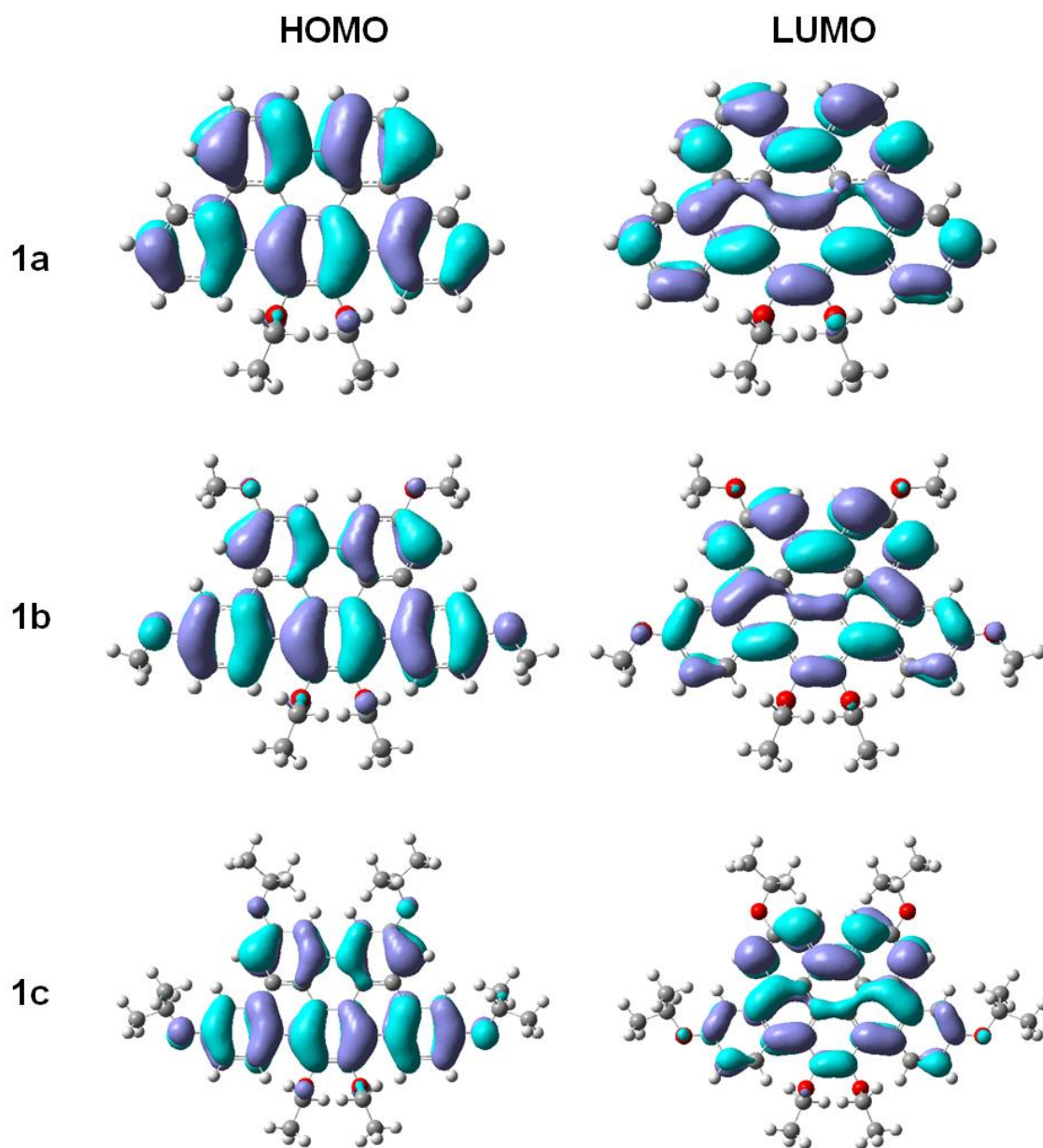


Figure 4-9 Visualized HOMO/LUMO orbitals of **1a-1c** obtained from Gaussian 03w at B3LYP 631G(d) level.

#### 4.6.2 Electrochemical properties

Cyclic voltammetry (CV) measurements were performed for **1a-c** as thin films drop-casted from their respective chloroform solutions. As shown in Figure 4-10 compound **1a** shows one reversible oxidation waves in the anodic scan with the onset of 0.90 V, while **1b** and **1c** exhibit two semi-reversible or irreversible oxidation waves with the first wave onset potential of 0.57 V and 0.51 V, respectively. Since there is no obvious reduction wave obtained from cathodic scans for all three compounds, the HOMO/LUMO energy levels were calculated based on their first oxidation onset potentials and their optical bandgaps (3.08, 2.71 and 2.83 eV for **1a-1c**, respectively) based on previous studies,<sup>184</sup> which are estimated to be -5.70/-2.62, -5.37/-2.66 and -5.31/-2.48 eV for **1a**, **1b** and **1c**, respectively. The gradually increasing in HOMO levels reflects the enhanced electron donating effect from **1a** to **1b** to **1c**.

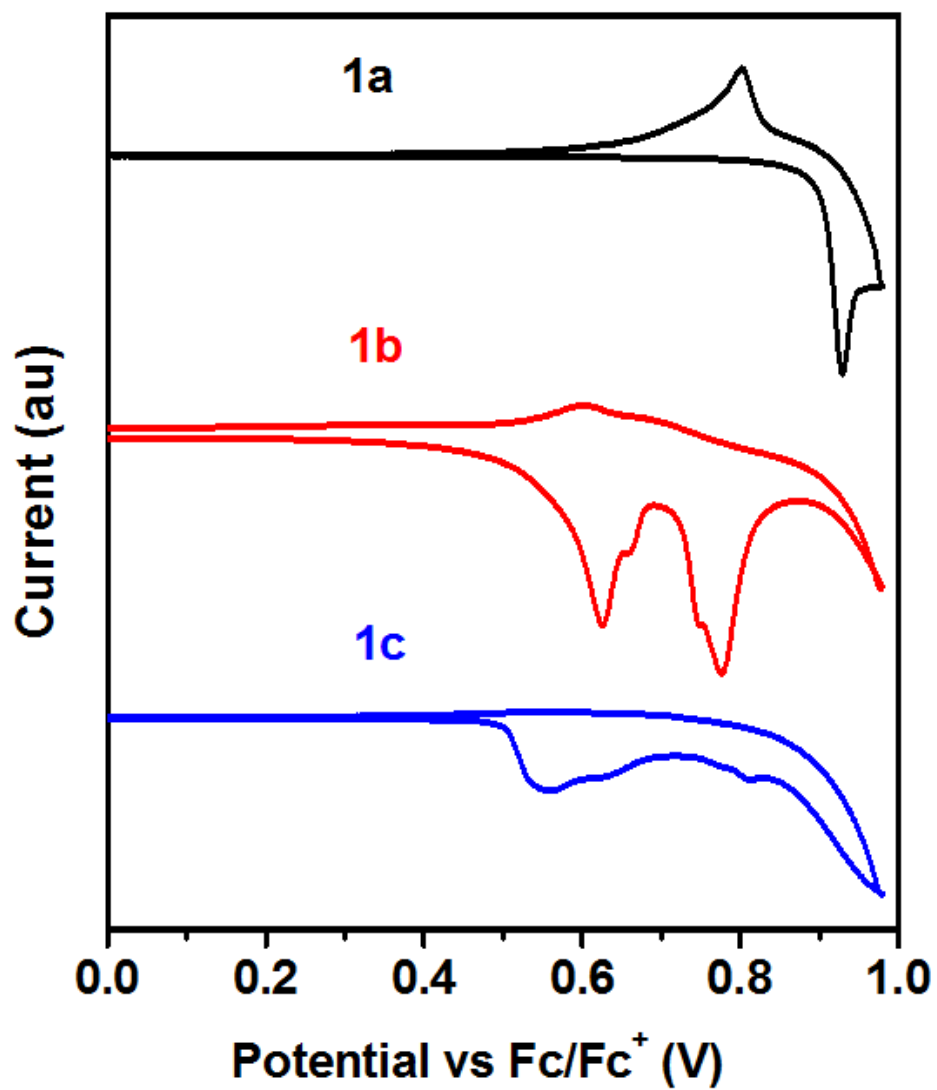


Figure 4-10 Cyclic voltammograms of **1a-1c** thin films drop-casted on Pt plate.

Table 4-1 Electrochemical properties of **1a**, **1b** and **1c**.

Compound	Experimental				Calculated <sup>e</sup>		
	$E_{ox}^{onset}$ (V) <sup>a</sup>	$E_{HOMO}$ (eV) <sup>b</sup>	$E_g^{opt}$ (eV) <sup>c</sup>	$E_{LUMO}$ (eV) <sup>d</sup>	$E_{HOMO}$ (eV)	$E_{LUMO}$ (eV)	$E_g^{DFT}$ (eV)
<b>1a</b>	0.90	-5.70	3.08	-2.62	-5.28	-1.47	3.81
<b>1b</b>	0.57	-5.37	2.71	-2.66	-4.93	-1.22	3.71
<b>1c</b>	0.51	-5.31	2.83	-2.48	-4.81	-1.31	3.50

<sup>a</sup> CV measurement for thin film. <sup>b</sup> Calculated from  $E_{HOMO} = -(E_{ox}^{onset} + 4.80)$  (eV). <sup>c</sup>

The optical band gap was estimated by  $E_g^{opt} = 1240/\lambda_{onset}^{abs}$  (eV),  $\lambda_{onset}^{abs}$  is absorption onset of thin films obtained from previous work.<sup>184</sup> <sup>d</sup> Calculated from  $E_{LUMO} = E_{HOMO}$

+  $E_g^{opt}$ . <sup>e</sup> DFT calculation at the B3LYP 631G(d) level.

### 4.6.3 Mobility

The hole mobilities of **1a-1c** were examined using the steady-state SCLC method by fabricating hole-only devices with the configuration of ITO/PEDOT:PSS/(**1a**, **1b** or **1c**)/MoO<sub>3</sub>/Au. Half of the devices were thermally annealed at the temperature determined via differential scanning calorimetry (DSC).<sup>184</sup> The annealing temperature was selected to be between the crystalline/liquid crystal phase transition temperature and the isotropic transition (melting) temperature in order to rearrange the molecule packing without melting. The annealing temperatures are 70 °C, 90 °C and 50 °C for **1a**, **1b** and **1c**, respectively.<sup>184</sup> There were five individual devices with an active area of 0.14 cm<sup>2</sup> on each slide, and at least three batches of devices were fabricated for each condition. It is assumed that the organic/metal contacts are Ohmic. The  $J$ - $V$  curves of the hole-only devices, plotted in logarithmic scales, are shown in Figure 4-11. The hole mobilities were derived by fitting the  $J$ - $V$  curves in the SCLC region using Equation (4-6). The thickness  $d$  of the thin film is measured to be ~800 nm for **1a**, ~400 nm for **1b** and ~200 nm for **1c**. The calculated SCLC hole mobility of the unannealed and annealed thin films of **1a-1c** are summarized in Table 4-2.

The pristine films of the three compounds give mobility values of  $8.58 \times 10^{-4} \text{ cm}^2 \text{ V}^{-1} \text{ s}^{-1}$ ,  $5.42 \times 10^{-3} \text{ cm}^2 \text{ V}^{-1} \text{ s}^{-1}$ , and  $2.30 \times 10^{-4} \text{ cm}^2 \text{ V}^{-1} \text{ s}^{-1}$ , respectively, which are in the typical mobility range of spin-coated organic films. After thermal annealing, all three compounds show some improvement in mobility. Compounds **1a** and **1b** see close to one order of magnitude higher hole mobility after thermal annealing. Compound **1c** also shows an increase in hole mobility. Thin film of compound **1b** after thermal annealing shows the highest hole mobility of  $3.63 \times 10^{-2} \text{ cm}^2 \text{ V}^{-1} \text{ s}^{-1}$ .

It is surprising that the mobility of **1a** is comparable to that of **1c** even though one (**1a**) forms intermolecular  $\pi$ - $\pi$  stacks and the other (**1c**) does not. This may be due to the non-Ohmic contact in the **1a** devices, which results in underestimating its mobility. As mentioned earlier. The validity of Equation (4-6) requires Ohmic contact between interfaces. The work functions of MoO<sub>3</sub> and PEDOT:PSS are 5.4 eV and 5.2 eV, respectively. The HOMO levels obtained from CV measurements are -5.70, -5.37 and -5.30 eV for **1a**, **1b** and **1c**, respectively. The HOMO levels of **1b** and **1c** closely match those of MoO<sub>3</sub> and PEDOT:PSS, ensuring Ohmic contact between them. However, the HOMO level of **1a** is 0.5 eV off that of PEDOT:PSS, likely making the **1a**/PEDOT:PSS interface non-Ohmic (an Ohmic contact requires less than 0.3 eV mismatch). Therefore, the mobility obtained for **1a** may be underestimated.

Table 4-2 SCLC hole mobility of compound **1a**, **1b** and **1c**

Compound	$\mu$ (cm <sup>2</sup> V <sup>-1</sup> S <sup>-1</sup> )	
	Unannealed	Annealed <sup>a</sup>
<b>1a</b>	$8.58 \times 10^{-4}$	$3.15 \times 10^{-3}$
<b>1b</b>	$5.42 \times 10^{-3}$	$3.63 \times 10^{-2}$
<b>1c</b>	$2.30 \times 10^{-4}$	$8.45 \times 10^{-4}$

<sup>a</sup> Thermal annealed were performed in glove box in dark for 10 min at 70 °C, 90 °C and 50 °C for **1a**, **1b** and **1c**, respectively.

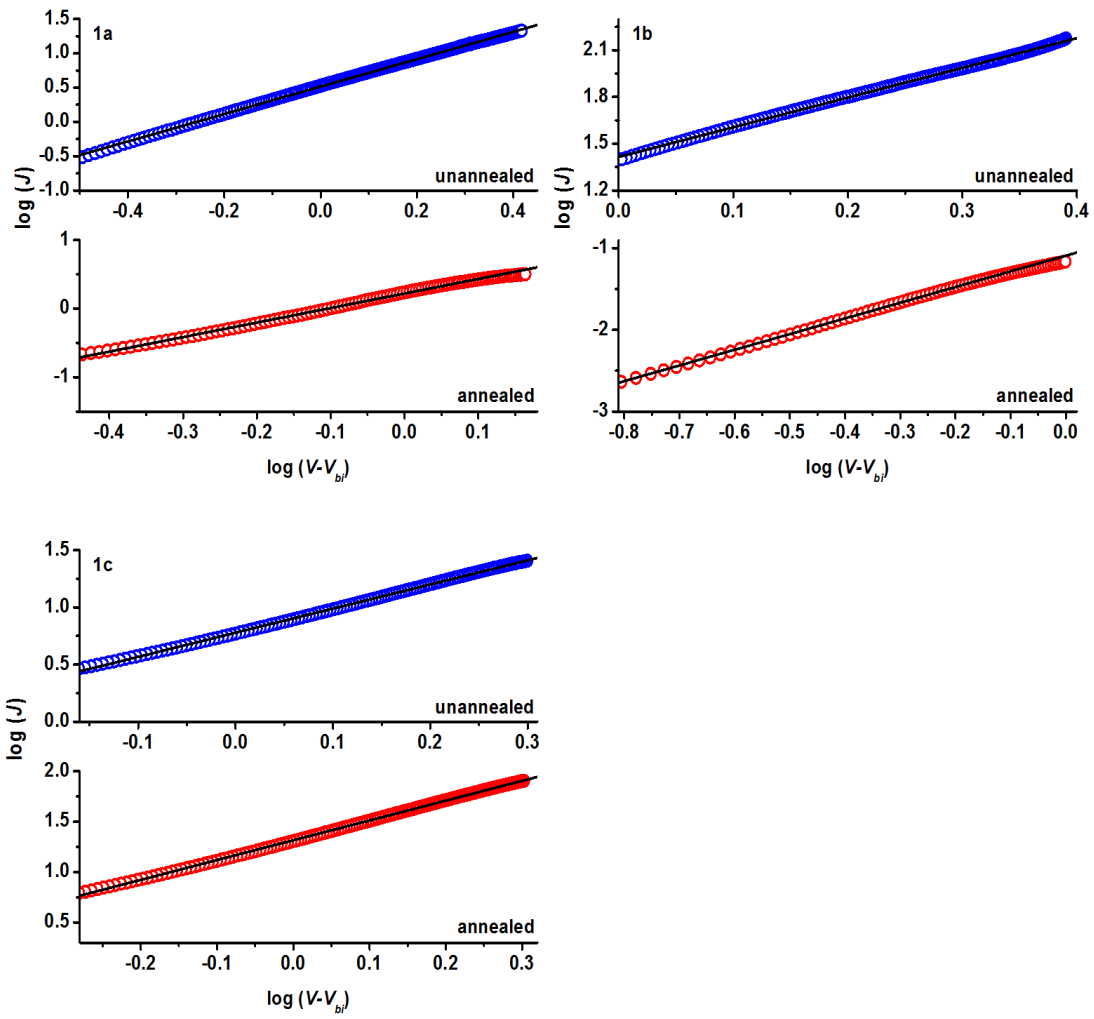


Figure 4- 11 Current density -voltage curves of hole only devices for **1a-1c** before (blue) or after (red) thermal annealing process. (Experimental data: empty circles; fitting curve: black line)

#### 4.6.4 X-ray diffraction pattern

To understand the change in molecule packing and hole mobility improvement after thermal annealing, powder X-ray diffraction (XRD) studies were performed for all three compounds in spin-coated thin films before and after thermal annealing. As it shown in Figure 4-12, all three compounds show one broad peak with a centre at  $2\theta = \sim 6.65^\circ$  (d spacing: 13.29 Å) for **1a**,  $2\theta = \sim 7.55^\circ$  (d spacing: 11.71 Å) for **1b**, and  $2\theta = \sim 7.55^\circ$  (d spacing: 11.71 Å) for **1c**. After thermal annealing, compound **1a** shows one sharp peaks on the top of the original broad peak with  $2\theta = \sim 8.05^\circ$  (d spacing: 10.98 Å),  $\sim 11^\circ$  (d spacing: 8.04 Å),  $\sim 12.15^\circ$  (d spacing: 7.28 Å) and  $\sim 13.1^\circ$  (d spacing: 6.76 Å). New sharp peaks, although not as many and as strong as those in **1a**, have also appeared in the diffractogram of **1b** after thermal annealing. These peaks include  $2\theta = \sim 7.65^\circ$  (d spacing: 11.56 Å),  $\sim 9.9^\circ$  (d spacing: 8.93 Å),  $\sim 7.2^\circ$  (d spacing: 12.33 Å) and  $\sim 15.25^\circ$  (d spacing: 5.81 Å). Compound **1c**, however, shows no clear new peaks after thermal annealing. These results indicate that thermal annealing does improve the molecular packing of **1a** and **1b**, but not **1c**.

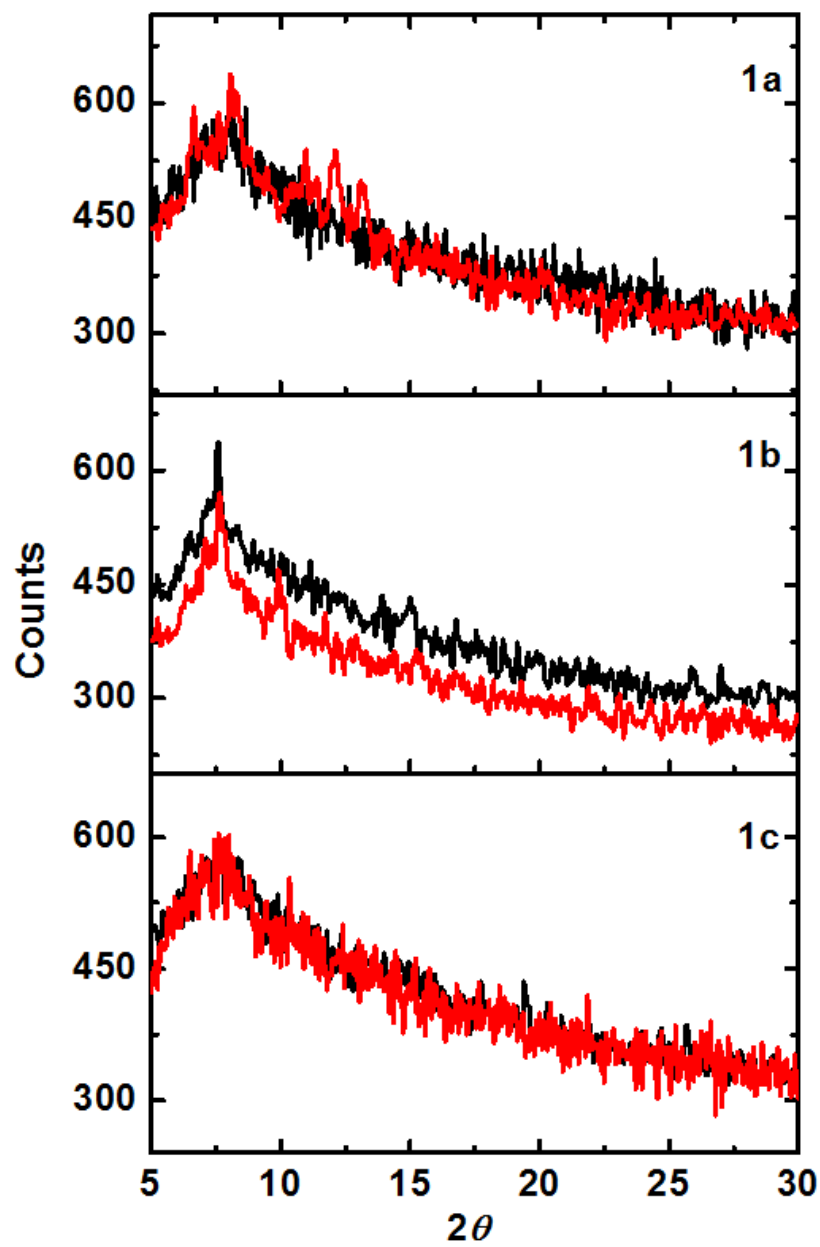


Figure 4- 12 XRD patterns of **1a-1c** thin films spin-coated on Si zero-diffraction plates.

#### 4.7. Conclusions

Three PAH molecules, all based on the TBP core but with different peripheral substituents, have been studied as hole transporting materials. Their electrochemical properties have been explored as well. DFT calculations indicate that all three molecules have a somewhat twisted TBP core with compound **1a** showing the largest twist. The SCLC hole mobility of **1a-1c** pristine films deposited by spin-coating were measured to be  $8.58 \times 10^{-4} \text{ cm}^2 \text{ V}^{-1} \text{ s}^{-1}$ ,  $5.42 \times 10^{-3} \text{ cm}^2 \text{ V}^{-1} \text{ s}^{-1}$ , and  $2.30 \times 10^{-4} \text{ cm}^2 \text{ V}^{-1} \text{ s}^{-1}$ , respectively, which are typical for solution-processed organic films. Thermal annealing improved the mobility of all three compounds with compound **1b** showing the largest increase and an appealing SCLC hole mobility of  $3.63 \times 10^{-2} \text{ cm}^2 \text{ V}^{-1} \text{ s}^{-1}$  was obtained. The XRD studies of thin films before and after annealing suggest better molecule orders for both **1a** and **1b** after thermal annealing, which is likely responsible for their improved hole mobility.

#### 4.8 Methods

##### 1) *General remarks*

All chemicals are commercially purchased and used without further purification unless otherwise stated. Acetonitrile used for CV measurements was freshly distilled prior to use and degassed with dry argon. Compound **1a-c** were prepared following a previous publication.<sup>184</sup> UV-vis absorption spectra were measured with a Hewlett-Packard 8452A diode array spectrophotometer, and fluorescence spectra were collected on a Shimadzu RF-5301PC spectrofluorophotometer. CV measurements were performed under argon atmosphere on a BAS Epsilon EC electrochemical station with the scan rate of  $20 \text{ mV s}^{-1}$ . A  $1 \text{ mm}^2$  Pt disk, an Ag wire and a Pt wire were applied as the working electrode, the

reference electrode and the counter electrode, respectively. A tetra-n-butylammoniumhexafluorophosphate solution (0.1 M in acetonitrile) was used as supporting electrolyte. The thin films of the three compounds were drop-casted from respective chloroform solutions onto the Pt disk and dried with air flow. All measurements were calibrated with Fc/Fc<sup>+</sup> redox couple whose absolute energy was assigned to be -4.8 eV vs vacuum. XRD patterns of the thin films were analysed on a Rigaku MiniFlex automated powder X-ray diffractometer (Cu K $\alpha$ , 30 kV, 15 mA, Ni filter,  $\lambda = 1.54178 \text{ \AA}$ ). The thin films were spin-coated on Si zero diffraction plates from their chloroform solutions and dried in air.

## 2) *Hole only devices fabrication and characterization*

ITO glass with a sheet resistance of 8–12  $\Omega$ /square was used as substrates. ITO glass was cut into 1.5 cm by 1.5 cm pieces, and the ITO was patterned by etching with aqua regia vapor. The patterned ITO glass substrates were cleaned in an ultrasonic bath sequentially by detergent, water, deionized water, toluene, acetone, and isopropyl alcohol, each for 15 min, and then dried by compressed air. Cleaned ITO substrates were treated with UV ozone for 1h before use. PEDOT:PSS thin layer was spin coated [4000 rotations per minute (RPM), 30s] onto the ITO substrates from an aqueous solution. The substrates were then dried at 120 °C for 45 min on a hotplate in air. The compound under study was dissolved in degassed chloroform in a glove box and the resulting solution were heated at 40 °C with stirring overnight. The active layer was deposited by spin-coating the solution on top of the PEDOT:PSS layer at certain RPM for 30 s. Then the resulted devices were dried by covering the wet films with petri dishes. For comparison, half of the devices were annealed at certain temperature for 10 min in glove box under dark. Subsequently, an

electrode including 10 nm thick MoO<sub>3</sub> and 50 nm thick Au was deposited on top of the active layer by thermal evaporation under high vacuum ( $< 2 \times 10^{-6}$  Mbar). The active area of 0.14 cm<sup>2</sup> of the devices was defined by the area of deposited electrode through a shadow mask. Current-voltage characteristics were measured using a Keithley 2400 source meter. The film thickness was measured with a Tencor Alphastep 200 automatic step profiler.

## REFERENCES

- (1) Fahrenbruch, A. L.; Bube, R. H. *Fundamentals of Solar Cells*; Academic Press, 1983.
- (2) Loferski, J. J. *Prog. Photovoltaics Res. Appl.* **1993**, *1*, 67–78.
- (3) Razykov, T. M.; Ferekides, C. S.; Morel, D.; Stefanakos, E.; Ullal, H. S.; Upadhyaya, H. M. *Sol. Energy* **2011**, *85*, 1580–1608.
- (4) Becquerel, A. E. *Acad. des Sci.* **1839**, *9*, 561–567.
- (5) Tao, M. *Electrochem. Soc. Interface* **2008**, *17*, 30–35.
- (6) Masuko, K.; Shigematsu, M.; Hashiguchi, T.; Fujishima, D.; Kai, M.; Yoshimura, N.; Yamaguchi, T.; Ichihashi, Y.; Mishima, T.; Matsubara, N.; Yamanishi, T.; Takahama, T.; Taguchi, M.; Maruyama, E.; Okamoto, S. *IEEE J. Photovoltaics* **2014**, *4*, 1433–1435.
- (7) Swanson, R. M. *Conf. Rec. Thirty-first IEEE Photovolt. Spec. Conf. 2005.* **2005**, 0–5.
- (8) Gribov, B. G.; Zinov'ev, K. V. *Inorg. Mater.* **2003**, *39*, 653–662.
- (9) Swanson, R. M. *Prog. Photovoltaics Res. Appl.* **2006**, *14*, 443–453.
- (10) Ferry, V. E.; Verschuuren, M. A.; Lare, C. Van; Schropp, R. E. I.; Atwater, H. A.; Polman, A. *Nano Lett.* **2011**, *11*, 4239–4245.
- (11) Sites, J.; Pan, J. *Thin Solid Films* **2007**, *515*, 6099–6102.
- (12) Chopra, K. L.; Paulson, P. D.; Dutta, V. *Prog. Photovoltaics Res. Appl.* **2004**, *12*, 69–92.
- (13) Green, M. A.; Emery, K.; Hishikawa, Y.; Warta, W.; Dunlop, E. D. *Prog. Photovoltaics Res. Appl.* **2011**, *19*, 565–572.

- (14) Abdulrazzaq, O. a.; Saini, V.; Bourdo, S.; Dervishi, E.; Biris, A. S. *Part. Sci. Technol.* **2013**, *31*, 427–442.
- (15) Wohrle, D.; Meissner, D. *Advanced Materials*. 1991, pp 129–138.
- (16) Chamberlain, G. a. *Sol. Cells* **1983**, *8*, 47–83.
- (17) Li, G.; Zhu, R.; Yang, Y. *Nat. Photonics* **2012**, *6*, 153–161.
- (18) Hoppe, H.; Sariciftci, N. S. *J. Mater. Res.* **2004**, *19*, 1924–1945.
- (19) Cai, W.; Gong, X.; Cao, Y. *Sol. Energy Mater. Sol. Cells* **2010**, *94*, 114–127.
- (20) Heeger, A. J. *Adv. Mater.* **2014**, *26*, 10–28.
- (21) Wright, M.; Uddin, A. *Sol. Energy Mater. Sol. Cells* **2012**, *107*, 87–111.
- (22) Nazeeruddin, M. K.; Baranoff, E.; Grätzel, M. *Sol. Energy* **2011**, *85*, 1172–1178.
- (23) Hains, A. W.; Liang, Z.; Woodhouse, M. a.; Gregg, B. a. *Chem. Rev.* **2010**, *110*, 6689–6735.
- (24) Coakley, K. M.; McGehee, M. D. *Chemistry of Materials*. 2004, pp 4533–4542.
- (25) Tang, C. W. *Appl. Phys. Lett.* **1986**, *48*, 183–185.
- (26) Sariciftci, N. S.; Smilowitz, L.; Heeger, a J.; Wudl, F. *Science* **1992**, *258*, 1474–1476.
- (27) Yu, G.; Gao, J.; Hummelen, J. C.; Wudl, F.; Heeger, A. J. *Science (80-. )*. **1995**, *270*, 1789–1791.
- (28) Haugeneder, a.; Neges, M.; Kallinger, C.; Spirkl, W.; Lemmer, U.; Feldmann, J.; Scherf, U.; Harth, E.; Gügel, A.; Müllen, K. *Phys. Rev. B* **1999**, *59*, 15346–15351.

- (29) Nenashev, a. V.; Wiemer, M.; Jansson, F.; Baranovskii, S. D. *J. Non. Cryst. Solids* **2012**, *358*, 2508–2511.
- (30) Knupfer, M. *Appl. Phys. A Mater. Sci. Process.* **2003**, *77*, 623–626.
- (31) Stübinger, T.; Brütting, W. *J. Appl. Phys.* **2001**, *90*, 3632–3641.
- (32) Lunt, R. R.; Giebink, N. C.; Belak, A. a.; Benziger, J. B.; Forrest, S. R. *J. Appl. Phys.* **2009**, *105*, 053711.
- (33) Gommans, H.; Schols, S.; Kadashchuk, A.; Heremans, P.; Meskers, S. C. J. *J. Phys. Chem. C* **2009**, *113*, 2974–2979.
- (34) Hoppe, H.; Sariciftci, N. S. *J. Mater. Chem.* **2006**, *16*, 45–61.
- (35) Sun, S.-S.; Sariciftci, N. S. *Organic photovoltaics: Mechanisms, Materials, and Devices*; CRC Press (Taylor & Francis Group), 2005.
- (36) Gao, J.; Yu, G.; Heeger, A. J. *Adv. Mater.* **1998**, *10*, 692–695.
- (37) Kim, J. Y.; Lee, K.; Coates, N. E.; Moses, D.; Nguyen, T.-Q.; Dante, M.; Heeger, A. J. *Science* **2007**, *317*, 222–225.
- (38) Dennler, G.; Scharber, M. C.; Brabec, C. J. *Adv. Mater.* **2009**, *21*, 1323–1338.
- (39) Chen, L. M.; Hong, Z.; Li, G.; Yang, Y. *Adv. Mater.* **2009**, *21*, 1434–1449.
- (40) Li, G.; Yao, Y.; Yang, H.; Shrotriya, V.; Yang, G.; Yang, Y. *Adv. Funct. Mater.* **2007**, *17*, 1636–1644.
- (41) Sivula, K.; Ball, Z. T.; Watanabe, N.; Frechet, J. M. J. *Adv. Mater.* **2006**, *18*, 206–210.
- (42) Yang, C.; Lee, J. K.; Heeger, A. J.; Wudl, F. *J. Mater. Chem.* **2009**, *19*, 5416–5423.
- (43) Zhang, Q.; Cirpan, A.; Russell, T. P.; Emrick, T. *Macromolecules* **2009**, *42*, 1079–

1082.

- (44) Sun, S. S. *Sol. Energy Mater. Sol. Cells* **2003**, *79*, 257–264.
- (45) Topham, P. D.; Parnell, A. J.; Hiorns, R. C. *J. Polym. Sci. Part B Polym. Phys.* **2011**, *49*, 1131–1156.
- (46) Olsen, B. D.; Segalman, R. A. *Mater. Sci. Eng. R Reports* **2008**, *62*, 37–66.
- (47) El-Adawi, M. K.; Al-Nuaim, I. a. *Vacuum* **2001**, *64*, 33–36.
- (48) Bowden, S.; Rohatgi, A. In *17th European Photovoltaic Solar Energy Conference*; 2001.
- (49) Wolf, M.; Rauschenbach, H. *Adv. Energy Convers.* **1963**, *3*, 455–479.
- (50) Nelson, J. *The physics of solar cells*; Imperial College Press, 2003.
- (51) Gupta, D.; Mukhopadhyay, S.; Narayan, K. S. *Sol. Energy Mater. Sol. Cells* **2010**, *94*, 1309–1313.
- (52) Scharber, M. C.; Mühlbacher, D.; Koppe, M.; Denk, P.; Waldauf, C.; Heeger, A. J.; Brabec, C. J. *Adv. Mater.* **2006**, *18*, 789–794.
- (53) Li, G.; Shrotriya, V.; Yao, Y.; Yang, Y. *J. Appl. Phys.* **2005**, *98*, 1–6.
- (54) Krebs, F. C. *Sol. Energy Mater. Sol. Cells* **2009**, *93*, 394–412.
- (55) Brédas, J.-L.; Norton, J. E.; Cornil, J.; Coropceanu, V. *Acc. Chem. Res.* **2009**, *42*, 1691–1699.
- (56) Weickert, J.; Dunbar, R. B.; Hesse, H. C.; Wiedemann, W.; Schmidt-Mende, L. *Adv. Mater.* **2011**, *23*, 1810–1828.
- (57) He, M.; Qiu, F.; Lin, Z. *J. Mater. Chem.* **2011**, *21*, 17039–17048.

- (58) Mihailetchi, V. D.; Xie, H.; De Boer, B.; Koster, L. J. A.; Blom, P. W. M. *Adv. Funct. Mater.* **2006**, *16*, 699–708.
- (59) Verploegen, E.; Mondal, R.; Bettinger, C. J.; Sok, S.; Toney, M. F.; Bao, Z. *Adv. Funct. Mater.* **2010**, *20*, 3519–3529.
- (60) Yang, X.; Uddin, A. *Renew. Sustain. Energy Rev.* **2014**, *30*, 324–336.
- (61) Mayer, A. C.; Scully, S. R.; Hardin, B. E.; Rowell, M. W.; McGehee, M. D. *Mater. Today* **2007**, *10*, 28–33.
- (62) Murayama, H.; Tomonoh, S.; Alford, J. M.; Karpuk, M. E. *Fullerenes, Nanotub. Carbon Nanostructures* **2005**, *12*, 1–9.
- (63) Huang, J.; Yin, Z.; Zheng, Q. *Energy & Environmental Science*. 2011, pp 3861–3877.
- (64) Lim, D. C.; Shim, W. H.; Kim, K.-D.; Seo, H. O.; Lim, J.-H.; Jeong, Y.; Kim, Y. D.; Lee, K. H. *Sol. Energy Mater. Sol. Cells* **2011**, *95*, 3036–3040.
- (65) Greene, L. E.; Law, M.; Yuhas, B. D.; Yang, P. *J. Phys. Chem. C* **2007**, *111*, 18451–18456.
- (66) Li, Y.; Li, S.; Jin, L.; Murowchick, J. B.; Peng, Z. *RSC Adv.* **2013**, *3*, 16308–16312.
- (67) Lira-Cantu, M.; Chafiq, A.; Faissat, J.; Gonzalez-Valls, I.; Yu, Y. *Sol. Energy Mater. Sol. Cells* **2011**, *95*, 1362–1374.
- (68) Huynh, W. U.; Dittmer, J. J.; Alivisatos, a P. *Science* **2002**, *295*, 2425–2427.
- (69) Celik, D.; Krueger, M.; Veit, C.; Schleiermacher, H. F.; Zimmermann, B.; Allard, S.; Dumsch, I.; Scherf, U.; Rauscher, F.; Niyamakom, P. *Sol. Energy Mater. Sol. Cells* **2012**, *98*, 433–440.
- (70) Li, Y.; Lu, P.; Jiang, M.; Dhaka, R.; Thapaliya, P.; Peng, Z.; Jha, B.; Yan, X. *J. Phys. Chem. C* **2012**, *116*, 25248–25256.

- (71) Zhao, L.; Pang, X.; Adhikary, R.; Petrich, J. W.; Jeffries-El, M.; Lin, Z. *Adv. Mater.* **2011**, *23*, 2844–2849.
- (72) Zhao, L.; Pang, X.; Adhikary, R.; Petrich, J. W.; Lin, Z. *Angew. Chemie - Int. Ed.* **2011**, *50*, 3958–3962.
- (73) Hsu, S.-C.; Liao, W.-P.; Lin, W.-H.; Wu, J.-J. *J. Phys. Chem. C* **2012**, *116*, 25721–25726.
- (74) Yan, J.; Ye, Q.; Han, X.; Zhou, F. *RSC Adv.* **2012**, *3*, 166–171.
- (75) Briseno, A. L.; Holcombe, T. W.; Boukai, A. I.; Garnett, E. C.; Shelton, S. W.; Fréchet, J. J. M.; Yang, P. *Nano Lett.* **2010**, *10*, 334–340.
- (76) Gouzerh, P.; Proust, A. *Chem. Rev.* **1998**, *98*, 77–112.
- (77) Peng, Z. *Angew. Chem. Int. Ed. Engl.* **2004**, *43*, 930–935.
- (78) Xu, B.; Lu, M.; Kang, J.; Wang, D.; Brown, J.; Peng, Z. *Chem. Mater.* **2005**, *17*, 2841–2851.
- (79) Kang, J.; Nelson, J. a; Lu, M.; Xie, B.; Peng, Z.; Powell, D. R. *Inorg. Chem.* **2004**, *43*, 6408–6413.
- (80) We, Y.; Xu, B.; Barnes, C. L.; Peng, Z. *J. Am. Chem. Soc.* **2001**, *123*, 4083–4084.
- (81) Chakraborty, S.; Keightley, A.; Dusevich, V.; Wang, Y.; Peng, Z. *Chem. Mater.* **2010**, *22*, 3995–4006.
- (82) Lu, M.; Xie, B.; Kang, J.; Chen, F. C.; Yang, Y.; Peng, Z. *Chem. Mater.* **2005**, *17*, 402–408.
- (83) Li, Y.; Jin, L.; Chakraborty, S.; Li, S. H.; Lu, P. F.; Zhu, D. M.; Yan, X. Z.; Peng, Z. H. *J. Polym. Sci. Part B-Polymer Phys.* **2014**, *52*, 122–133.
- (84) Chakraborty, S.; Jin, L.; Li, Y.; Liu, Y.; Dutta, T.; Zhu, D. M.; Yan, X.; Keightley, A.; Peng, Z. *Eur. J. Inorg. Chem.* **2013**, *10-11*, 1799–1807.

- (85) Li, Y.; Lu, P.; Yan, X.; Jin, L.; Peng, Z. *RSC Adv.* **2012**, *3*, 545–558.
- (86) Bagui, M.; Dutta, T.; Zhong, H.; Li, S.; Chakraborty, S.; Keightley, A.; Peng, Z. *Tetrahedron* **2012**, *68*, 2806–2818.
- (87) Bagui, M.; Dutta, T.; Chakraborty, S.; Melinger, J. S.; Zhong, H.; Keightley, A.; Peng, Z. *J. Phys. Chem. A* **2011**, *115*, 1579–1592.
- (88) Rand, B. P.; Burk, D. P.; Forrest, S. R. *Phys. Rev. B - Condens. Matter Mater. Phys.* **2007**, *75*, 1–11.
- (89) Dissanayake, D. M. N. M.; Zhong, Z. *Nano Lett.* **2011**, *11*, 286–290.
- (90) Nelson, J.; Kirkpatrick, J.; Ravirajan, P. *Phys. Rev. B* **2004**, *69*, 1–11.
- (91) Sary, N.; Richard, F.; Brochon, C.; Leclerc, N.; Lévêque, P.; Audinot, J. N.; Berson, S.; Heiser, T.; Hadziioannou, G.; Mezzenga, R. *Adv. Mater.* **2010**, *22*, 763–768.
- (92) Pryamitsyn, V.; Ganesan, V. *J. Chem. Phys.* **2004**, *120*, 5824–5838.
- (93) Sary, N.; Rubatat, L.; Brochon, C.; Hadziioannou, G.; Mezzenga, R. *Macromol. Symp.* **2008**, *268*, 28–32.
- (94) de Boer, B.; Stalmach, U.; van Hutten, P. F.; Melzer, C.; Krasnikov, V. V.; Hadziioannou, G. *Polymer (Guildf)*. **2001**, *42*, 9097–9109.
- (95) Trznadel, M.; Pron, A.; Zagorska, M.; Chrzaszcz, R.; Pielichowski, J. *Macromolecules* **1998**, *31*, 5051–5058.
- (96) Spano, F. C. *Acc. Chem. Res.* **2010**, *43*, 429–439.
- (97) Rathnayake, H.; Binion, J.; McKee, A.; Scardino, D. J.; Hammer, N. I. *Nanoscale* **2012**, *4*, 4631–4640.
- (98) Dutta, T.; Li, Y.; Thornton, A. L.; Zhu, D.-M.; Peng, Z. *J. Polym. Sci. Part A*

*Polym. Chem.* **2013**, *51*, 3818–3828.

- (99) Conlon, P.; Yang, C. J.; Wu, Y.; Chen, Y.; Martinez, K.; Kim, Y.; Stevens, N.; Marti, A. a.; Jockusch, S.; Turro, N. J.; Tan, W. *J. Am. Chem. Soc.* **2008**, *130*, 336–342.
- (100) Xie, Y.; Li, Y.; Xiao, L.; Qiao, Q.; Dhakal, R.; Zhang, Z.; Gong, Q.; Galipeau, D.; Yan, X. *J. Phys. Chem.* **2010**, *114*, 14590–14600.
- (101) Yang, X. J.; Dykstra, T. E.; Scholes, G. D. *Phys. Rev. B* **2005**, *71*, 045203.
- (102) Tretiak, S.; Saxena, A.; Martin, R. L.; Bishop, a R. *Phys. Rev. Lett.* **2002**, *89*, 097402.
- (103) Grage, M.; Zaushitsyn, Y.; Yartsev, A.; Chachisvilis, M.; Sundström, V.; Pullerits, T. *Phys. Rev. B* **2003**, *67*, 205207.
- (104) Kobayashi, T.; Yoshizawa, M.; Stamm, U.; Taiji, M.; Hasegawa, M. *J. Opt. Soc. Am. B* **1990**, *7*, 1558–1578.
- (105) Scheblykin, I. G.; Yartsev, A.; Pullerits, T.; Gulbinas, V.; Sundstroem, V. *J. Phys. Chem. B* **2007**, *111*, 6303–6321.
- (106) Westenhoff, S.; Daniel, C.; Friend, R. H.; Silva, C.; Sundström, V.; Yartsev, A. *J. Chem. Phys.* **2005**, *122*, 094903.
- (107) Westenhoff, S.; Beenken, W. J. D.; Friend, R. H.; Greenham, N. C.; Yartsev, A.; Sundström, V. *Phys. Rev. Lett.* **2006**, *97*, 166804.
- (108) Johnson, J. M.; Chen, R.; Chen, X.; Moskun, A. C.; Zhang, X.; Hogen-Esch, T. E.; Bradforth, S. E. *J. Phys. Chem. B* **2008**, *112*, 16367–16381.
- (109) Dhar, L.; Rogers, J. A.; Nelson, K. A. *Chem. Rev.* **1994**, *94*, 157–193.
- (110) Williams, L.; Nelson, K. *J. Chem. Phys.* **1987**, *87*, 7346–7347.
- (111) Nakamura, T.; Araki, Y.; Ito, O.; Takimiya, K.; Otsubo, T. *J. Phys. Chem. A* **2008**,

112, 1125–1132.

- (112) Yin, P.; Jin, L.; Li, D.; Cheng, P.; Vezenov, D. V.; Bitterlich, E.; Wu, X.; Peng, Z.; Liu, T. *Chem. - A Eur. J.* **2012**, *18*, 6754–6758.
- (113) Anderson, N. a; Lian, T. *Annu. Rev. Phys. Chem.* **2005**, *56*, 491–519.
- (114) Stille, J. K. *Angew. Chemie* **1986**, *25*, 508–524.
- (115) Carsten, B.; He, F.; Son, H. J.; Xu, T.; Yu, L. *Chem. Rev.* **2011**, *111*, 1493–1528.
- (116) Wang, R.; Li, Y.; Shetye, K.; Dutta, T.; Jin, L.; Li, S.; Peng, Z. *Eur. J. Inorg. Chem.* **2015**, *2015*, 656–663.
- (117) Yu, W. H. S.; Wijnen, M. H. J. *J. Chem. Phys.* **1970**, *52*, 2736.
- (118) Tang, T.; Lin, T.; Wang, F.; He, C. *J. Phys. Chem. B* **2015**, *119*, 8176–8183.
- (119) Li, Y.; Clevenger, R. G.; Jin, L.; Kilway, K.; Peng, Z. *J. Mater. Chem. C* **2014**, *2*, 7180–7183.
- (120) MacLachlan, A. J.; Rath, T.; Cappel, U. B.; Dowland, S. A.; Amenitsch, H.; Knall, A.-C.; Buchmaier, C.; Trimmel, G.; Nelson, J.; Haque, S. A. *Adv. Funct. Mater.* **2015**, *25*, 409–420.
- (121) Moulé, A. J.; Chang, L.; Thambidurai, C.; Vidu, R.; Stroeve, P. *J. Mater. Chem.* **2012**, *22*, 2351–2368.
- (122) Gao, F.; Ren, S.; Wang, J. *Energy Environ. Sci.* **2013**, *6*, 2020–2040.
- (123) Li, Y.; Dutta, T.; Gerasimchuk, N.; Wu, S.; Shetye, K.; Jin, L.; Wang, R.; Zhu, D.-M.; Peng, Z. *ACS Appl. Mater. Interfaces* **2015**, *7*, 9372–9384.
- (124) Qian, G.; Wang, Z. Y. *Chem. - An Asian J.* **2010**, *5*, 1006–1029.
- (125) Gong, X.; Tong, M. H.; Park, S. H.; Liu, M.; Jen, A.; Heeger, A. J. *Sensors* **2010**, *10*, 6488–6496.

- (126) Gong, X.; Tong, M.; Xia, Y.; Cai, W.; Moon, J. S.; Cao, Y.; Yu, G.; Shieh, C.-L.; Nilsson, B.; Heeger, A. J. *Science* **2009**, *325*, 1665–1667.
- (127) Ho, H. a.; Leclerc, M. *J. Am. Chem. Soc.* **2003**, *125*, 4412–4413.
- (128) Chen, L. X.; Jaeger, W. J. H.; Gosztola, D. J.; Niemczyk, M. P.; Wasielewski, M. R. *J. Phys. Chem. B* **2000**, *104*, 1950–1960.
- (129) Plante, M. P.; Bérubé, E.; Bissonnette, L.; Bergeron, M. G.; Leclerc, M. *ACS Appl. Mater. Interfaces* **2013**, *5*, 4544–4548.
- (130) Lange, U.; Roznyatovskaya, N. V.; Mirsky, V. M. *Anal. Chim. Acta* **2008**, *614*, 1–26.
- (131) Wang, Y.; Zhu, H.; Yang, X.; Dou, Y.; Liu, Z. *Analyst* **2013**, *138*, 2085–2089.
- (132) Fu, B.; Baltazar, J.; Hu, Z.; Chien, A. T.; Kumar, S.; Henderson, C. L.; Collard, D. M.; Reichmanis, E. *Chem. Mater.* **2012**, *24*, 4123–4133.
- (133) Havinga, E. E.; ten Hoeve, W.; Wynberg, H. *Synth. Met.* **1993**, *55*, 299–306.
- (134) Havinga, E. E.; ten Hoeve, W.; Wynberg, H. *Polym. Bull.* **1992**, *29*, 119–126.
- (135) Wu, P. T.; Kim, F. S.; Champion, R. D.; Jenekhe, S. a. *Macromolecules* **2008**, *41*, 7021–7028.
- (136) Wu, P.-T.; Bull, T.; Kim, F. S.; Luscombe, C. K.; Jenekhe, S. a. *Macromolecules* **2009**, *42*, 671–681.
- (137) Zhu, Y.; Champion, R. D.; Jenekhe, S. A. *Macromolecules* **2006**, *39*, 8712–8719.
- (138) Bundgaard, E.; Krebs, F. C. *Sol. Energy Mater. Sol. Cells* **2007**, *91*, 954–985.
- (139) Heeger, A. J. *Polym. J.* **1985**, *17*, 201–208.

- (140) Patil, a O.; Heeger, a J.; Wudl, F. *Chem. Rev.* **1988**, *88*, 183–200.
- (141) Bredas, J.; Street, G. *Accounts of Chemical Research.* 1985, pp 309–315.
- (142) Yamamoto, J.; Furukawa, Y. *J. Phys. Chem. B* **2015**, *119*, 4788–4794.
- (143) Welch, G. C.; Coffin, R.; Peet, J.; Bazan, G. C. *J. Am. Chem. Soc.* **2009**, *131*, 10802–10803.
- (144) Poverenov, E.; Zamoshchik, N.; Patra, A.; Ridelman, Y.; Bendikov, M. *J. Am. Chem. Soc.* **2014**, *136*, 5138–5149.
- (145) Welch, G. C.; Bazan, G. C. *J. Am. Chem. Soc.* **2011**, *133*, 4632–4644.
- (146) Fukumoto, H.; Yamamoto, T. *J. Polym. Sci. Part A Polym. Chem.* **2008**, *46*, 2975–2982.
- (147) Tang, T.; Chi, H.; Lin, T.; Wang, F.; He, C. *Phys. Chem. Chem. Phys.* **2014**, *16*, 20221–20227.
- (148) Tang, T.; Ding, G.; Lin, T.; Chi, H.; Liu, C.; Lu, X.; Wang, F.; He, C. *Macromol. Rapid Commun.* **2013**, *34*, 431–436.
- (149) Wang, F.; Lin, T. T.; He, C.; Chi, H.; Tang, T.; Lai, Y.-H. *J. Mater. Chem.* **2012**, *22*, 10448–10451.
- (150) Sirringhaus, H.; Friend, R. H.; Wang, C.; Leuninger, J.; Müllen, K. *J. Mater. Chem.* **1999**, *9*, 2095–2101.
- (151) Maudens, K. E.; Wille, S. M. R.; Lambert, W. E. *J. Chromatogr. B. Analyt. Technol. Biomed. Life Sci.* **2007**, *848*, 384–390.
- (152) Sanjeev, R.; Jagannadham, V.; Vrat, R. V. *Chem. New Zeal.* **2012**, *76*, 133–135.
- (153) Corbett, J. F. *J. Chem. Educ.* **1972**, *49*, 663–663.
- (154) Murgatroyd, P. N. *J. Phys. D. Appl. Phys.* **1970**, *3*, 151–156.

- (155) Blom, P. W. M.; De Jong, M. J. M.; Vleggaar, J. J. M. *Appl. Phys. Lett.* **1996**, *68*, 3308–3310.
- (156) Olivier, Y.; Niedzialek, D.; Lemaire, V.; Pisula, W.; Müllen, K.; Koldemir, U.; Reynolds, J. R.; Lazzaroni, R.; Cornil, J.; Beljonne, D. *Adv. Mater.* **2014**, *26*, 2119–2136.
- (157) Chen, Z.; Cai, P.; Chen, J.; Liu, X.; Zhang, L.; Lan, L.; Peng, J.; Ma, Y.; Cao, Y. *Adv. Mater.* **2014**, *26*, 2586–2591.
- (158) Yassar, A. *Polym. Sci. Ser. C* **2014**, *56*, 4–19.
- (159) Günther, A. A.; Widmer, J.; Kasemann, D.; Leo, K. *Appl. Phys. Lett.* **2015**, *106*, 233301.
- (160) Sundar, V. C.; Zaumseil, J.; Podzorov, V.; Menard, E.; Willett, R. L.; Someya, T.; Gershenson, M. E.; Rogers, J. a. *Science* **2004**, *303*, 1644–1646.
- (161) Monobe, H.; Awazu, K.; Shimizu, Y. *Thin Solid Films* **2009**, *518*, 762–766.
- (162) Ruiz, C.; García-Frutos, E. M.; Hennrich, G.; Gómez-Lor, B. *J. Phys. Chem. Lett.* **2012**, *3*, 1428–1436.
- (163) de Boer, R. W. I.; Jochemsen, M.; Klapwijk, T. M.; Morpurgo, A. F. *J. Appl. Phys.* **2004**, *95*, 1196–1202.
- (164) Kotani, M.; Kakinuma, K.; Yoshimura, M.; Ishii, K.; Yamazaki, S.; Kobori, T.; Okuyama, H.; Kobayashi, H.; Tada, H. *Chem. Phys.* **2006**, *325*, 160–169.
- (165) Li, H.; Duan, L.; Zhang, D.; Dong, G.; Qiao, J.; Wang, L.; Qiu, Y. *J. Phys. Chem. C* **2014**, *118*, 6052–6058.
- (166) Choulis, S. a.; Nelson, J.; Kim, Y.; Poplavskyy, D.; Kreouzis, T.; Durrant, J. R.; Bradley, D. D. C. *Appl. Phys. Lett.* **2003**, *83*, 3812–3814.
- (167) Malachowski, M. J.; Zmija, J. *Opto-Electronics Rev.* **2010**, *18*, 121–136.

- (168) Pfattner, R.; Mas-Torrent, M.; Bilotti, I.; Brillante, A.; Milita, S.; Liscio, F.; Biscarini, F.; Marszalek, T.; Ulanski, J.; Nosal, A.; Gazicki-Lipman, M.; Leufgen, M.; Schmidt, G.; Laurens, W. M.; Laukhin, V.; Veciana, J.; Rovira, C. *Adv. Mater.* **2010**, *22*, 4198–4203.
- (169) Mas-Torrent, M.; Durkut, M.; Hadley, P.; Ribas, X.; Rovira, C. *J. Am. Chem. Soc.* **2004**, *126*, 984–985.
- (170) Zheng, Y.-Q.; Dai, Y.-Z.; Zhou, Y.; Wang, J.-Y.; Pei, J. *Chem. Commun. (Camb)*. **2014**, *50*, 1591–1594.
- (171) Foster, S.; Deledalle, F.; Mitani, A.; Kimura, T.; Kim, K.-B.; Okachi, T.; Kirchartz, T.; Oguma, J.; Miyake, K.; Durrant, J. R.; Doi, S.; Nelson, J. *Adv. Energy Mater.* **2014**, *4*, 1400311.
- (172) Zhou, N.; Lin, H.; Lou, S. J.; Yu, X.; Guo, P.; Manley, E. F.; Loser, S.; Hartnett, P.; Huang, H.; Wasielewski, M. R.; Chen, L. X.; Chang, R. P. H.; Facchetti, A.; Marks, T. J. *Adv. Energy Mater.* **2014**, *4*, 1300785.
- (173) Heurlin, M.; Hultin, O.; Storm, K.; Lindgren, D.; Borgström, M. T.; Samuelson, L. *Nano Lett.* **2014**, *14*, 749–753.
- (174) Jang, J.; Liu, W.; Son, J. S.; Talapin, D. V. *Nano Lett.* **2014**, *14*, 653–662.
- (175) Dong, Q.; Fang, Y.; Shao, Y.; Mulligan, P.; Qiu, J.; Cao, L.; Huang, J. *Science (80-. )*. **2015**, *347*, 967–970.
- (176) Juska, G.; Arlauskas, K.; Österbacka, R.; Stubb, H. *Synth. Met.* **2000**, *109*, 173–176.
- (177) Nguyen, P. H.; Paasch, G.; Brütting, W.; Riess, W. *Phys. Rev. B* **1994**, *49*, 5172–5181.
- (178) Mozer, a. J.; Sariciftci, N. S.; Lutsen, L.; Vanderzande, D.; Österbacka, R.; Westerling, M.; Juška, G. *Appl. Phys. Lett.* **2005**, *86*, 1–3.
- (179) Islam, S. S. *Semiconductor physics and devices*; Oxford University Press, 2006.

- (180) Lampert, M. A.; Mark, P. *Current Injection in Solids*; Academic Press: New York, 1970.
- (181) Yasuda, T.; Yamaguchi, Y.; Zou, D. C.; Tsutsui, T. *Japanese J. Appl. Physics, Part 1 Regul. Pap. Short Notes Rev. Pap.* **2002**, *41*, 5626–5629.
- (182) Tse, S. C.; Tsang, S. W.; So, S. K. *J. Appl. Phys.* **2006**, *100*, 063708.
- (183) Matsushima, T.; Kinoshita, Y.; Murata, H. *Appl. Phys. Lett.* **2007**, *91*, 2005–2008.
- (184) Chou, C. E.; Li, Y.; Che, Y. K.; Zang, L.; Peng, Z. H. *Rsc Adv.* **2013**, *3*, 20666–20672.

## VITA

Lu Jin was born on December 6, 1987 in Anhui, China, where she attended elementary school, middle school, high school and college. Her interest in chemistry was promoted by her chemistry teacher in high school. In 2005, Lu went to Anhui Medical University studying Clinical Pharmacology. She received her bachelor's degrees in Medicine in 2010. In order to further extend her knowledge in chemistry, she decided to go abroad for higher education. Lu joined the Department of Chemistry in UMKC in July 2010 for her Ph.D. degree in chemistry.

During her Ph.D. study in Professor Zhonghua Peng's group, Lu had devoted her effort in research of conjugated small molecules, polymers and organic-inorganic hybrid materials for photovoltaic applications. She has received SGS research grant and K. L. Cheng award in 2014. She has co-authored the following publications and presentations:

1. Y. Li, T. Dutta, N. Gerasimchuk, S. Wu, K. Shetye, **L. Jin**, R. Wang, D. Zhu, Z. Peng. "Conjugated Foldamers with Unusually High Space-Charge-Limited Current Hole Mobilities", *ACS Appl. Mater. Interfaces*, **2015**, 7, 9372–9384.
2. R Wang, Y. Li, K. Shetye, T. Dutta, **L. Jin**, S. Li, Z Peng, "Luminescent Polythiophene-Based Main-Chain Polyoxometalate-Containing Conjugated Polymers with Improved Solar-Cell Performance", *Eur. J. Inorg. Chem.* **2015**, 2015, 656–663.
3. Y. Li,\* **L. Jin**,\* S. Chakraborty, S. Li, P. Lu, D. Zhu, X. Yan, Z. Peng. "Photovoltaic Properties and Femtosecond time - Resolved Fluorescence Study of Polyoxometalate - Containing Rod-Coil Diblock Copolymers", *J. Polym. Sci., Part B: Polym. Phys*, **2014**, 2, 122-133. (Contribution equally).

4. S. Li, Y. Li, C. Wisner, **L. Jin**, N Leventis, Z. Peng, "Synthesis, optical properties and photovoltaic applications of hybrid rod-coil diblock copolymers with coordinatively attached CdSe nanocrystals", *RSC Adv.*, **2014**, *4*, 35823-35832.
5. F. Haso, R. Wang, P. Yin, J Zhou, **L. Jin**, Z Peng, T. Liu, "Supramolecular Assemblies of Polyoxometalate-Tethered Diblock Copolymers with Tunable Sizes in *N*-Methyl-2-pyrrolidone/Toluene Mixed Solvents", *Eur. J. Inorg. Chem.* **2014**, *2014*, 4589–4592.
6. Y. Li, R. Clevenger, **L. Jin**, K. Kilway, Z. Peng. "Unusually high SCLC hole mobility in solution-processed thin films of a polycyclic thiophene-based small-molecule semiconductor" *J. Mater. Chem. C*, **2014**, *2*, 7180-7183.
7. S. Chakraborty, **L. Jin**, Y. Li, Y. Liu, T. Dutta, D. Zhu, X. Yan, A. Keightley Z. Peng. "Synthesis, Characterizations, and Morphological Studies of Polyoxometalate - Containing Rod-Coil Diblock Copolymers," *Eur. J. Inorg. Chem.*, **2013**, *10-11*, 1799-1807.
8. Y. Li, S. Li, **L. Jin**, J. Murowchick, Z. Peng. "Carbon nanoparticles as an interfacial layer between TiO<sub>2</sub>-coated ZnO nanorod arrays and conjugated polymers for high-photocurrent hybrid solar cells", *RSC Adv.*, **2013**, *3*, 16308–16312.
9. P. Yin, **L. Jin**, D. Li, P. Cheng, D. Vezenov, E Bitterlich, X Wu, Z. Peng, T Liu. "Supramolecular Assembly of Conjugated Polymers Containing Polyoxometalate Terminal Side Chains in Polar and Nonpolar Solvents," *Chem. Eur. J.* **2012**, *22*, 6754-6758

Oral and poster presentations:

1. **L. Jin**, T. Dutta, Y. Li, Z. Peng. "Near infrared absorbing polymers based on substituted bithiophene units," *2015 Fall ACS National Meeting, Boston.*

2. **L. Jin**, Y. Li, Z. Peng. "Photovoltaic Properties of a Polyoxometalate-Ferrocene Charge-Transfer Molecular Hybrid," *2014 Fall ACS National Meeting, San Francisco*.
3. **L. Jin**, T. Dutta, Y. Li, Z. Peng. "Strong Near-Infrared-Absorbing Conjugated Polymers for Solar Cells and Broad Spectral Photodetectors," *2013 ACS Midwest Regional Meeting, Springfield*.
4. **L. Jin**, Y. Li, S. Chakraborty, Y. Liu, D. Zhu, Z Peng. "Evaluations of Photovoltaic Properties of Polyoxometalate-containing Rod-coil Diblock Copolymers with Poly(3-hexylthiophene) as the Rod Block," *2012 ACS Midwest Regional Meeting, Omaha*.